OPIS

Listă 10 publicaţii relevante

Candidat pentru obţinerea atestatului de abilitare în Domeniul Medicină:

CAROLINA MARIA SOLOMON

1. Dulgheriu IT, Solomon C, Ciuce C, Dudea SM. The ultrasonographic diagnosis of lymph node varicose veins in the groin - an overlooked missing link in chronic venous disease? Med Ultrason. 2024 Sep 16;26(3):270-276. doi: 10.11152/mu-4390. Epub 2024 Jun 6. PMID: 38909378 Pag. 3

2. Muntean DD, Dudea SM, Băciuț M, Dinu C, Stoia S, Solomon C, Csaba C, Rusu GM, Lenghel LM. The Role of an MRI-Based Radiomic Signature in Predicting Malignancy of Parotid Gland Tumors. Cancers (Basel). 2023 Jun 23;15(13):3319. doi: 10.3390/cancers15133319. PMID: 37444429; PMCID: PMC10340186. Pag. 8

3. Petea-Balea DR, Solomon C, Muntean DD, Dulgheriu IT, Silaghi CA, Dudea SM. Viscosity Plane-Wave UltraSound (Vi PLUS) in the Evaluation of Thyroid Gland in Healthy Volunteers-A Preliminary Study. Diagnostics (Basel). 2022 Oct 13;12(10):2474. doi: 10.3390/diagnostics12102474. PMID: 36292163; PMCID: PMC9600479 Pag. 25

4. Dulgheriu IT, Solomon C, Muntean DD, Petea-Balea R, Lenghel M, Ciurea AI, Dudea SM. Shear-Wave Elastography and Viscosity PLUS for the Assessment of Peripheric Muscles in Healthy Subjects: A Pre- and Post-Contraction Study. Diagnostics (Basel). 2022 Sep 2;12(9):2138. doi: 10.3390/diagnostics12092138. PMID: 36140536; PMCID: PMC9497738 Pag. 35

5. Manole S, Pintican R, Palade E, Duma MM, Dadarlat-Pop A, Schiau C, Bene I, Rancea R, Miclea D, Manole V, Molnar A, Solomon C. Primary Pericardial Synovial Sarcoma: A Case Report and Literature Review. Diagnostics (Basel). 2022 Jan 10;12(1):158. doi: 10.3390/diagnostics12010158. PMID: 35054325; PMCID: PMC8774691 Pag. 48

6. Săftoiu A, Gilja OH, Sidhu PS, Dietrich CF, Cantisani V, Amy D, Bachmann-Nielsen M, Bob F, Bojunga J, Brock M, Calliada F, Clevert DA, Correas JM, D'Onofrio M, Ewertsen C, Farrokh A, Fodor D, Fusaroli P, Havre RF, Hocke M, Ignee A, Jenssen C, Klauser AS, Kollmann C, Radzina M, Ramnarine KV, Sconfienza LM, Solomon C, Sporea I, Ștefănescu H, Tanter M, Vilmann P. The EFSUMB Guidelines and Recommendations for the Clinical Practice of Elastography in Non-Hepatic Applications: Update 2018. Ultraschall Med. 2019 Aug;40(4):425-453. English. doi: 10.1055/a-0838-9937. Epub 2019 Jun 25. PMID: 31238377 Pag. 57

7. Micu M, Bolboaca SD, Rusu GM, Crivii CB, Solomon CM. Musculoskeletal ultrasound versus MRI of the hands in healthy subjects - a pilot study. Med Ultrason. 2019 May 2;21(2):117-124. doi: 10.11152/mu-1775. PMID: 31063513 Pag. 86

8. Botar-Jid CM, Cosgarea R, Bolboacă SD, Şenilă SC, Lenghel LM, Rogojan L, Dudea SM. Assessment of Cutaneous Melanoma by Use of Very- High-Frequency Ultrasound and Real-Time Elastography. AJR Am J Roentgenol. 2016 Apr;206(4):699-704. doi: 10.2214/AJR.15.15182. Epub 2016 Feb 11. PMID: 26866335 Pag. 94

9. Marina ME, Solomon C, Bolboaca SD, Bocsa C, Mihu CM, Tătaru AD. High-frequency sonography in the evaluation of nail psoriasis. Med Ultrason. 2016 Sep;18(3):312-7. doi: 10.11152/mu.2013.2066.183.hgh. PMID: 27622407. (IF 1.118) Pag. 100
10. Botar Jid C, Bolboacă SD, Cosgarea R, Şenilă S, Rogojan L, Lenghel M, Vasilescu D, Dudea SM. Doppler ultrasound and strain elastography in the assessment of cutaneous melanoma: preliminary results. Med Ultrason. 2015 Dec;17(4):509-14. doi: 10.11152/mu.2013.2066.174.dus. PMID: 26649347 Pag. 106

Original papers

Med Ultrason 2024, Vol. 26, no. 3, 270-276
DOI: 10.11152/mu-4390

The ultrasonographic diagnosis of lymph node varicose veins in the groin – an overlooked missing link in chronic venous disease?

Ioana-Teofana Dulgheriu[1], Carolina Solomon[1], Constantin Ciuce[2], Sorin M. Dudea[1]

[1]Radiology Department, "Iuliu Hațieganu" University of Medicine and Pharmacy Cluj-Napoca, [2]Regina Maria Hospital, Cluj-Napoca, Romania

Abstract

Aim: Chronic venous disease is a common pathology characterized by valvular incompetence and venous hypertension. The venous network of the lymph nodes at the Scarpa triangle connects the superficial and the deep venous systems. This study aimed to describe infrainguinal intranodal venous dilatations and to evaluate the connection with peripheral venous disease. **Material and methods:** The study included 183 subjects (116 women, 67 men) who underwent Doppler ultrasound examinations of the venous system of the inferior limb in the context of chronic venous disease. The diagnosis of lymph node varices was based on well-defined criteria and the severity of the lymph node varices was established using an original classification. **Results:** There was a statistically significant, moderately strong association, between the presence of intranodal varices and the great saphenous vein reflux ($\varphi=0.341$, $p=0.000$). There was a moderate-to-high positive correlation between intranodal varices and the chronic venous disease stage ($rrb=0.457$, $p=0.000$). **Conclusions:** Patients with more advanced stages of chronic venous insufficiency have a higher probability of presenting intranodal varices. Lymph node venous network identification could considerably impact clinical decision-making and treatment choices.

Keywords: Doppler ultrasound; chronic venous disease; lymph node venous network

Introduction

Chronic venous disease (CVD) is a common pathology characterized by valvular incompetence and venous hypertension. The obstruction of the lower extremity venous system results in a great spectrum of clinical symptoms. A standardized classification system (CEAP) is used for homogenous, reproducible reporting. The CEAP system was introduced in 1996 and revised in 2004 and 2020. It addresses the clinical manifestations (C), etiology (E), anatomy (A), and the underlying pathophysiology (P) of CVD [1].

The term chronic venous disease has been defined as "(any) morphological and functional abnormalities of the venous system of long duration manifested either by symptoms and/or signs indicating the need for investigation and/or care" [2]. The same publication states that the term "chronic venous insufficiency" (CVI) should only be used for advanced CVD, which is applied to the functional abnormalities of the venous system corresponding with stages C3 to C6 of the CEAP classification.

A recent systematic review found that this pathology represents a global issue, with important heterogeneity in prevalence: C2 disease was highest in Europe (21%) and lowest in Africa (5.5%) [3].

Ultrasonography (US) is currently the gold-standard imaging modality for the assessment of CVD. By providing a "venous mapping" it is also a useful tool for the guidance of percutaneous treatment of CVD and postprocedural follow-up [4,5]. Duplex US provides anatomic and hemodynamic diagnostic information concerning venous course, patency, wall alterations, and flow. By using straining methods such as the Valsalva maneuver, the sonographer can assess the presence and record the duration of the venous reflux.

Received 10.12.2023 Accepted 18.04.2024
Med Ultrason
2024, Vol. 26, No 3, 270-276

Corresponding author: Carolina Solomon
Radiology Department, Cluj County
Emergency Hospital, 2-4 Clinicilor Street,
400012, Cluj-Napoca, Romania
E-mail: carolinasolomon12@gmail.com

The venous network in the lymph nodes at the Scarpa triangle connects the superficial and the deep venous systems in normal subjects [6]. The lymph node venous network (LNVN) has small, filiform veins, with a transganglionar, subaponevrotic course, usually connecting the great saphenous vein (GSV) to the anterior accessory saphenous vein (AASV). Few studies [6-10] characterized the morphology of the LNVN. In patients with CVD, the LNVN may dilate and become a cause of primary CVD or more frequently, of variceal recurrence [6]. A more detailed morphological and hemodynamic assessment of the LNVN could lead to a better understanding of a different, new pathway of the varicose veins formation or recurrence.

The aims of this study were to provide an US anatomical description of intranodal varix, to present an original classification of its severity and to evaluate the correlation between peripheral venous disease and infrainguinal intranodal venous dilatation.

Materials and methods

A retrospective, monocentric study was performed by reviewing the patients evaluated between January 2008 and December 2014 in the Ultrasound Department of the host institution. This was an observational, cohort-type study, that comprised records of patients admitted in the Dermatology, General Surgery, and Vascular Surgery departments investigated for CVD work-up. Due to the retrospective design of the study, the necessity of informed consent was waived. The study was approved by the Ethics Committee of the University (protocol code DEP43/22.11.2021).

The recorded information included: patient age and gender, clinical C grading (the presence/absence of skin changes and the quantification of the skin changes, according to the CEAP classification [1]), the US report, the presence/absence of intranodal varicose veins and the grading of lymph node varix.

The US studies were performed with a HITACHI EUB 8500 scanner, using a 6-13 MHz, 50 mm linear probe (EUP L54M). US examinations were performed by a single operator. All images were anonymized. The US images and reports were a part of the standard evaluation of the lower limb venous system. Inclusion criteria: patients assessed for peripheral venous disease, with complete clinical assessment, US reports, and image recordings. Exclusion criteria: patients with systemic diseases (lymphoma, tuberculosis, lymphoproliferative disease, HIV, sarcoidosis), lymphedema of or edema of systemic etiology (renal insufficiency, hypoalbuminemia, cardiac disease), patients with incomplete data (absent or incomplete: demographic data, record of the clinical assessment, record of the US report or images).

The US report included the following: 1) the common femoral vein (CFV) and the femoral vein (FV) patency and reflux. Signs of chronic proximal (thigh/femoral) lower limb deep venous thrombosis were quantified as present or absent; 2) The Valsalva maneuver to assess the saphenous-femoral junction (SFJ). The reflux >1 sec was considered significant (present), otherwise absent; 3) The great saphenous vein (GSV), small saphenous vein (SSV), and other relevant superficial veins patency and thrombosis (present or absent): 4) The popliteal vein (POPV) and the anterior and posterior tibial veins (ATV, PTV) patency and thrombosis (present or absent).

The diagnosis of lymph node varix was based on the following criteria: 1) the presence in the lymph node hilum of an anechoic structure with the following characteristics: compressibility with the transducer; communication with extranodal venous vessels, draining in the main venous trunks in the groin, slow/absent spontaneous flow, modulated by respiration or stress maneuvers; 2) the lymph nodes had to be localized inferior to the inguinal ligament, in the Scarpa triangle. The presence of transfixiant veins through the lymph node cortex was also noted.

The infrainguinal lymph node varix were graded as [11]: grade I (mildly dilated veins in the hilum, with visible echogenic hilum); grade II (moderately dilated veins filling the hilum, the normal echogenic hilum is absent, the lymph node is spontaneously recognizable); and grade III (markedly dilated veins with abnormal morphology of the lymph node; nodal features apparent only after the compression maneuver and emptying of the varices).

Statistical Analysis

Statistical analysis was conducted with SPSS (IBM SPSS Statistics 29.0). The Kolmogorov–Smirnov and Shapiro-Wilk tests were used to evaluate the normality of data. Normally distributed quantitative data were presented as means ± standard deviation (SD). Non-normal distributed data were presented as median and range. The rank-biserial correlation coefficient was used to assess the relationship between a dichotomous categorical variable and ordinal variables. Spearman's rank-order correlation was used to measure the strength and direction of the monotonic relationship between two ranked nonparametric variables. Phi and Cramer's V tests were used to represent the correlation between categorical dichotomous variables. An ordinal regression analysis was conducted for the CVD stages by the presence of intranodal varices. A p-value under 0.05 was considered statistically significant.

Results

The selection of the study subjects is shown in figure 1.

A total of 183 subjects were included in the study (116 women and 67 men; median 55 years for the entire group, 54 years for men, 55.5 for women, age range 16-80 years). The main demographic characteristics are summarised in Table I.

Table I. Descriptive data of the subjects

Variable	N = 183
Chronic venous disease stage	
C0	53 (29.0)
C1	25 (13.7)
C2+C3	41 (22.4)
C4a	23 (12.6)
C4b	24 (13.1)
C5	9 (4.9)
C6	8 (4.4)
Great saphenous vein reflux (present)	90 (49.2)
Signs of chronic deep venous thrombosis (present)	
Proximal	29 (15.8)
Distal	26 (14.2)
Chronic superficial venous thrombosis (present)	22 (12.0)
Variceal thrombosis (present)	24 (13.1)
Intranodal varices	
Grade I	25 (13.7)
Grade II	30 (16.4)
Grade III	12 (6.6)

The results are expressed as number (%). N = total number of subjects

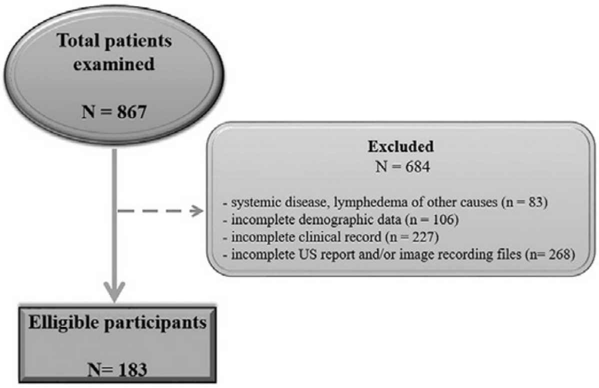

Fig 1. The flowchart showing patient selection.

The demographic characteristics divided by age groups are illustrated in Table II. As the great majority of the patients with varicose veins (C2) also had edema (C3) in variable degrees, the two stages were grouped in a single category.

Figure 2 exemplifies the original classification of intranodal varices, described accordingly.

The correlations between intranodal varices and signs of CVD are detailed in Table III. There was a statistically significant association, between the presence of intranodal varices and the presence of the following features:

Table II. Descriptive statistics by age

Variable	Age (years)						
	Total (N = 183)	**16–30 (N = 9)**	**31–40 (N = 33)**	**41–50 (N = 25)**	**51–60 (N = 53)**	**61–70 (N = 49)**	**71–80 (N = 14)**
Chronic venous disease stage							
C0	53 (29.0)	3 (33.3)	18 (54.5)	12 (48.0)	14 (26.4)	5 (10.2)	1 (7.1)
C1	25 (13.7)	3 (33.3)	2 (6.1)	3 (12.0)	8 (15.1)	8 (16.3)	1 (7.1)
C2+C3	41 (22.4)	1 (11.1)	3 (9.1)	5 (20.0)	12 (22.6)	17 (34.7)	3 (21.4)
C4a	23 (12.6)	1 (11.1)	8 (24.2)	3 (12.0)	10 (18.9)	1 (2.0)	0 (0.0)
C4b	24 (13.1)	0 (0.0)	2 (6.1)	1 (4.0)	3 (5.7)	14 (28.6)	4 (28.6)
C5	9 (4.9)	1 (11.1)	0 (0.0)	1 (4.0)	4 (7.5)	1 (2.0)	2 (14.3)
C6	8 (4.4)	0 (0.0)	0 (0.0)	0 (0.0)	2 (3.8)	3 (6.1)	3 (21.4)
GSV reflux (prestent)	90 (49.2)	5 (55.6)	13 (39.4)	11 (44.0)	27 (50.9)	25 (51.0)	9 (64.3)
Signs of chronic deep venous thrombosis (present)							
Proximal	29 (15.8)	2 (22.2)	3 (9.1)	2 (8.0)	10 (18.9)	9 (18.4)	3 (21.4)
Distal	26 (14.2)	2 (22.2)	3 (9.1)	1 (4.0)	7 (13.2)	9 (18.4)	4 (28.6)
Signs of chronic SVT (present)	22 (12.0)	1 (11.1)	0 (0.0)	4 (16.0)	8 (15.1)	7 (14.3)	2 (14.3)
VT (present)	24 (13.1)	1 (11.1)	4 (12.1)	1 (4.0)	10 (18.9)	5 (10.2)	3 (21.4)
Intranodal varices							
Grade I	25 (13.7)	0 (0.0)	3 (9.1)	1 (4.0)	6 (11.3)	10 (20.4)	5 (35.7)
Grade II	30 (16.4)	1 (11.1)	4 (12.1)	3 (12.0)	9 (17.0)	10 (20.4)	3 (21.4)
Grade III	12 (6.6)	1 (11.1)	0 (0.0)	1 (4.0)	6 (11.3)	4 (8.2)	0 (0.0)

The results are expressed as number (%). N = number of subjects; GSV = Great saphenous vein; SVT = superficial venous thrombosis; VT = Variceal thrombosis

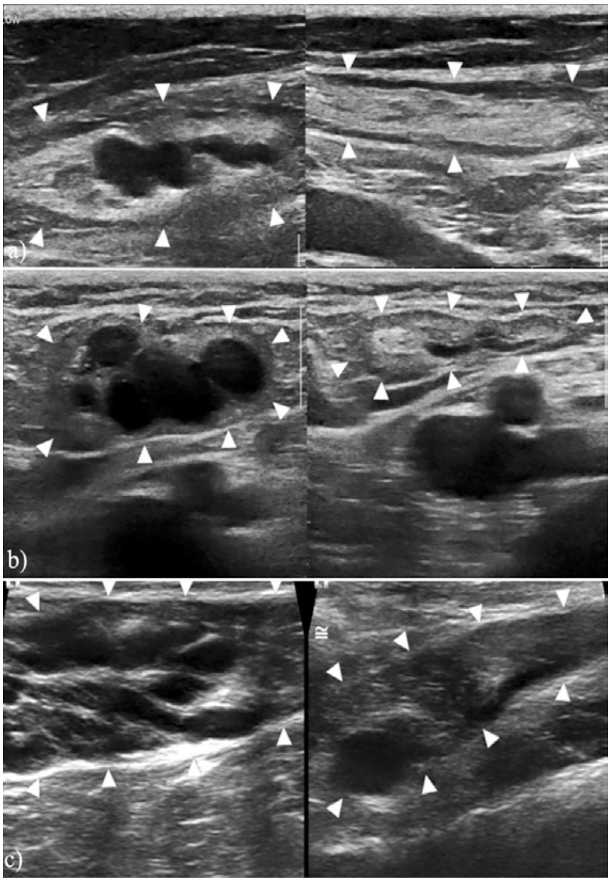

Fig 2. Ultrasound aspect of the infrainguinal lymph node varicose veins, without (left) and with transducer compression (right): a) Lymph node with a mildly dilated hilar vein, with visible echogenic hilum (grade I); b) Lymph node with moderately dilated veins filling the hilum, absent echogenic hilum (grade II); c) Lymph node with markedly dilated veins, with abnormal morphology, spontaneously unrecognizable lymph node and incomplete emptying of the varices with transducer compression (grade III). The white arrowheads point to the lymph nodes in each case.

GSV reflux (φ=0.341, p=0.000), variceal thrombosis (φ=0.209, p=0.005), signs of chronic deep venous thrombosis (φ=0.236, p=0.004).

A Spearman's rank-order correlation was run to assess the relationship between chronic venous insufficiency stages and the grade of intranodal varices, but there was no statistically significant correlation between the variables (rs=0.043, p=0.730).

There was a moderate-to-high positive correlation between intranodal varices and the chronic venous disease stage (rrb=0.457, p=0.000). The Pearson coefficient (r=0.249, p=0.042) indicates a moderate, positive, correlation between the variables, with evidence of statistically significant bivariate association.

An ordinal logistic regression was performed to assess the correlation of intranodal varices with higher stages of CVD. The final model statistically significantly predicted the dependent variable over and above the intercept-only model ($\chi^2(1)$=37.071, p=0.000). However, the Pearson goodness-of-fit indicated that the model was not a good fit for the observed data ($\chi^2(5)$=36.593, p=0.000). The pseudo-R-square values indicate that the presence of intranodal varices explains just a small proportion of the variation between CVD stages. A model containing only intranodal varices would be a poor predictor for a particular stage of CVD. The probability of having nodal varicose veins is estimated to rise by 1.708 with each stage of CVD, 95% CI [1.128,2.287]. The odds ratio of being in a higher stage of CVD of the patients with intranodal varices versus patients without, is 5.518, a statistically significant effect (p=0.000).

Discussion

The literature referring to LNVN is relatively sparse. To the best of our knowledge, this is the first study on the

Table III. Associations between variables

Method	**Variables**		**Coefficient**	**Significance**
Rank biserial correlation	Chronic venous disease stage	Presence of intranodal varices	0.457	**0.000**
Spearman's rank-order correlation	Chronic venous disease stage	Grade of intranodal varices	0.043	0.730
Phi and Cramer's V	Presence of intranodal varices	Presence of variceal thrombosis	0.209	**0.005**
Phi and Cramer's V	Presence of intranodal varices	Presence of great saphenous vein reflux	0.341	**0.000**
Phi and Cramer's V	Presence of intranodal varices	Signs of chronic proximal deep venous thrombosis	0.167	**0.024**
Phi and Cramer's V	Presence of intranodal varices	Signs of chronic distal deep venous thrombosis	0.211	**0.004**
Phi and Cramer's V	Presence of intranodal varices	Signs of chronic deep venous thrombosis	0.236	**0.001**
Phi and Cramer's V	Presence of intranodal varices	Signs of chronic superficial venous thrombosis	0.138	0.063
Rank biserial correlation	Grade of intranodal varices	Signs of chronic proximal deep venous thrombosis	0.249	**0.042**
Rank biserial correlation	Grade of intranodal varices	Signs of chronic distal deep venous thrombosis	0.151	0.221

association of CVD with the morphological changes of infrainguinal lymph nodes.

In our study, we found a statistically significant and moderately-strong association between the presence of intranodal varices and GSV reflux. Lower associations were found between the presence of intranodal varices and variceal thrombosis or with signs of chronic deep venous thrombosis. Our research demonstrated a positive correlation between intranodal varices and the chronic venous disease stage; patients in a more advanced stage of CVD had a higher chance of presenting intranodal varices.

We also assessed the correlation between CVD stages and intranodal varices severity. The relationship was monotonic, but not statistically significant. The analysis should be repeated in a larger overall patient group.

The great majority of the patients with advanced stages of CVD were in the 50-70 age range, and the same age groups presented the greatest proportion of intranodal varices (79.1%). This data distribution follows the natural progression of the disease, explained by a decrease in the production of collagen, which causes the veins to dilate and the valves more likely to become incompetent [12].

The first studies published on this subject [7-9] are case reports, therefore strictly descriptive, and do not analyze a possible relationship between lymph node varicose veins and typical aspects of venous insufficiency such as GSV reflux or venous thrombosis. More recent studies [8,10,13] are based on a morphological and anatomical exploration of the LNVN. For this reason, we did not have a comparison term for the results obtained in our study.

Lemasle et al [8,13] describe the LNVN as tortuous veins in connection with a lymph node, raising the theory that these veins could develop a connection with the superficial tributaries or with the saphenous stump and, in time, enlarge and exhibit reflux. In a series of 100 patients who had undergone surgery for GSV reflux, Lemasle et al [8] found that LNVN was the main cause of reflux in 6% of the cases. Uhl et al. describe in a larger study [10], the anatomy of the infrainguinal veno-lymphatic network, investigated by US, contrast-enhanced computer tomography, and anatomical dissection of 400 limbs from 200 cadavers post latex injection. The LNVN was found both in subjects with and without chronic venous pathology. Since the diameter of the LNVN is approximately 1 mm or less, in normal subjects it is frequently missed by Duplex US. Dilated LNVN was depicted in 15% of the cadavers with known CVD. According to the Union International de Phlébologie (UIP) consensus in 2011 [14], neovascularization was defined as the presence of newly visualized veins, in post-operative US, located at the site of the suppressed saphenous-femoral junction. In the absence of clear histological evidence, Uhl et al. suggest several hypotheses for the pathogenesis of lymph node varicose veins: lymphatic dystrophic changes that occur as a result of local inflammatory processes, the release of angiogenic factors, pre-existing intranodal venous channels that dilate; all these could lead to an increase in the volume of the lymph node, with fibrosis of the medullary sinuses and consequently, functional incompetence.

The anatomy and topography of the groin area were of interest to authors [15,16] who described lymphatic collectors clustered around the GSV and the AASV, explaining the connection between impaired lymphatic function and chronic venous hypertension. De Maeseneer et al [14,17] also advise a careful evaluation of the groin area, looking for LNVN reflux and connections with the CFV, the pelvic veins, or the GSV and AASV. Their observation points especially to patients with varix recurrency.

The existence of spontaneous lympho-venous shunts was proven in several anatomical studies [10,18]. Moreover, the experimental evidence published by Koltowska et al [18] described the development of lymphatic vessels from venous blood vasculature in vertebrates.

The pressure gradient between the two systems is unidirectional, ensuring the lymph drainage into the venous system at definite sites. Could intranodal varices appear as a consequence of high venous pressure in these preexistent lympho-venous shunts? We consider it to be a reasonable theory. In our classification, in grade III intranodal varix, we found small caliber, transfixing veins passing through the lymph node cortex, an abnormal feature. The hilum contains the vein and the artery, no veins pass through the cortex [19]. Afferent lymphatic vessels cross through the cortex and exit as efferent lymphatics in the hilum. Inside the lymph node, a natural lympho-venous anastomosis was described as connecting the intermediate sinus and the high endothelial venule, keeping a unidirectional flow (from the lymphatic channel to the venule) [19-21].

Could the flow direction invert, leading to a transformation of the lymphatic channel into a venous one? Pathological lympho-venous anastomoses were described in lymphedema and primary or secondary malignancies [19-21], but only recently in CVI [22-24]. Patients with CVD grades C3-C6 present with edema, thus the high pressure in the lymphatic system could explain the dilation of these anastomoses and a greater frequency of intranodal varix in patients with advanced stages. Another theory is that chronic inflammation acts as a trigger for lymphangiogenesis. Rasmussen et al [23] demonstrated that lymphatic anatomy and function degradation (such as vessel dilation, segmentation, interstitial and dermal backflow) tends to be progressive, connected to the more advanced stages of CVD (C2-C4). Miranda Garces et al [21] mentions a similar theory, that venous obstruction could stimulate neovascularisation, with lymphatic endothelial cells of the lymph node sinuses transforming into vascular endothelial cells.

All of these theories may be valid explanations for the pathogenesis of lymph node varicose veins, at this stage, however, they remain hypotheses.

In the matter of impact on patient care and treatment strategies, the recognition and description of intranodal varix in the preoperative Doppler US report may be useful to the surgeon. The LNVN reflux can supply an incompetent GSV through communicating veins, in the presence of a normal terminal GSV valve. Would the removal of these lymph nodes cause or worsen lymphoedema? Or would it reduce venous hypertension? Several authors [6,10,16] advise against surgical intervention in this area (in particular around the saphenous opening, GSV stripping), instead recommending foam sclerotherapy. In light of these aspects, we believe that LNVN identification could have a considerable impact on clinical decision-making and treatment choices.

We acknowledge that our study has limitations. Firstly, being an observational research, our study only analyzes data collected at one single point in time across a predefined subset of the population, patients clinically diagnosed with CVD. Secondly, the study did not assess the status of patients at the time of the examination, i.e. whether they were at a first diagnosis or had relapsed after surgery. Another limitation is the sample size, a rather small size for a study that aims to assess correlation and infer that morphological alterations in infrainguinal lymph nodes could become a source of primary CVD. Some other limitations of our study consist of not considering confounding factors: patients' comorbidities (risk factors such as female gender, history of multiple pregnancies, obesity, lifestyle, occupational hazard) or previous surgical intervention for CVD. However, these go beyond the scope of our study. We acknowledge that a more elaborated, comprehensive approach represents a challenge and a topic for further studies.

Conclusion

Our study demonstrated that patients with higher stages of CVD were more likely to have intranodal varices. We also found associations, to varying degrees, between the presence of intranodal varices and saphenous vein reflux, variceal thrombosis, and signs of chronic deep vein thrombosis. Identifying LNVN could have significant clinical and treatment implications.

Conflict of interest: none

References

1. Lurie F, Passman M, Meisner M, et al. The 2020 update of the CEAP classification system and reporting standards. J Vasc Surg Venous Lymphat Disord 2020;8:342-352.
2. Eklof B, Perrin M, Delis KT, et al. Updated terminology of chronic venous disorders: the VEIN-TERM transatlantic interdisciplinary consensus document. J Vasc Surg 2009;49:498-501.
3. Salim S, Machin M, Patterson BO, Onida S, Davies AH. Global epidemiology of chronic venous disease: a systematic review with pooled prevalence analysis. Ann Surg 2021;274:971-976.
4. De Maeseneer MG, Kakkos SK, Aherne T, et al. Editor's Choice - European Society for Vascular Surgery (ESVS) 2022 Clinical Practice Guidelines on the Management of Chronic Venous Disease of the Lower Limbs. Eur J Vasc Endovasc Surg 2022;63:184-267.
5. De Maeseneer MG, Kakkos SK, Aherne T, et al. Corrigendum to "European Society for Vascular Surgery (ESVS) 2022 Clinical Practice Guidelines on the Management of Chronic Venous Disease of the Lower Limbs. [Eur J Vasc Endovasc Surg (2022) 63, 184-267]". Eur J Vasc Endovasc Surg 2022;64:284-285.
6. Romualdo AP, Bastos RM, Cappucci A, et al. Lymph node veins: a little-known cause of varicose veins J Vasc Bras 2008;7:364-369.
7. Kohler A, Dirschs O, Brunner U. Veno-lymphatic angiodysplasia as the cause of recurrent inguinal varicose veins. Vasa 1997;26:52-54.
8. Lemasle P, Uhl J, Lefebre-Vilardebo, Baud J, Gillot C, Perrin M. Veines lympho-ganglionnaires inguinales: Aspects anatomiques et échographiques conséquences sur la définition de la néogenèse conséquences thérapeutiques. Discussion. Phlébologie 1999;52:263-269.
9. Leu HJ. A rare case of angiodysplasia: penetration of inguinal lymph nodes by large superficial leg veins. Report of five cases. Virchows Archiv A Pathol Anat Histopathol 1990;417:185-186.
10. Uhl JF, Vuolo ML, Labropoulos N. Anatomy of the lymph node venous networks of the groin and their investigation by ultrasonography. Phlebology 2016;31:334-343.
11. Dudea SM, Botar-Jid C, Ciuce C. Varices within groin lymph nodes in patients with surgically treated varicose disease: ultrasonographic appearance and relation to lower limb edema. Giornale Italiano di Ecografia 2006; 9(3).
12. Molnár AÁ, Nádasy GL, Dörnyei G, et al. The aging venous system: from varicosities to vascular cognitive impairment. Geroscience 2021;43:2761-2784.
13. Lemasle Ph, Lefebvre-Vilardebo M, Uhl JF, Vin F, Baud JM. Recidive variqueuse postoperatoire: et si la neo-vasculari-

sation inguinale post-chirurgicale n'etait que le developement d'un reseau pre-existant? Phlebologie 2009;62:42-48.

14. De Maeseneer M, Pichot O, Cavezzi A, et al; Union Internationale de Phlebologie. Duplex ultrasound investigation of the veins of the lower limbs after treatment for varicose veins - UIP consensus document. Eur J Vasc Endovasc Surg 2011;42:89-102.
15. Schacht V, Luedemann W, Abels C, Berens von Rautenfeld D. Anatomy of the subcutaneous lymph vascular network of the human leg in relation to the great saphenous vein. Anat Rec (Hoboken) 2009;292:87-93.
16. Kubik S, Manestar M. Topographic relationship of the ventromedial lymphatic bundle and the superficial inguinal nodes to the subcutaneous veins. Clin Anat 1995;8:25-28.
17. Maeseneer MD. Cavezzi A. Etiology and pathophysiology of varicose vein recurrence at the saphenofemoral or sapheno-popliteal junction: an update. Veins and Lymphatics 2012;1(1). Available at: https://doi.org/10.4081/vl.2012.e4.
18. Koltowska K, Betterman KL, Harvey NL, Hogan BM. Getting out and about: the emergence and morphogenesis of the vertebrate lymphatic vasculature. Development 2013;140:1857-1870.
19. Tucker AB, Krishnan P, Agarwal S. Lymphovenous shunts: from development to clinical applications. Microcirculation 2021;28:e12682.
20. Cheng MH, Huang JJ, Wu CW, et al. The mechanism of vascularized lymph node transfer for lymphedema: natural lymphaticovenous drainage. Plast Reconstr Surg 2014;133:192e-198e.
21. Miranda Garcés M, Mirapeix R, Pons G, Sadri A, Masià J. A comprehensive review of the natural lymphaticovenous communications and their role in lymphedema surgery. J Surg Oncol 2016;113:374-380.
22. Schacht V, Luedemann W, Abels C, Berens von Rautenfeld D. Anatomy of the subcutaneous lymph vascular network of the human leg in relation to the great saphenous vein. Anat Rec (Hoboken) 2009;292:87-93.
23. Rasmussen JC, Zhu B, Morrow JR, et al. Degradation of lymphatic anatomy and function in early venous insufficiency. J Vasc Surg Venous Lymphat Disord 2021;9:720-730.
24. Cigna E, Pierazzi DM, Sereni S, Marcasciano M, Losco L, Bolletta A. Lymphatico-venous anastomosis in chronic ulcer with venous insufficiency: A case report. Microsurgery 2021;41:574-578.

cancers

IMPACT FACTOR 4.5

Indexed in: PubMed

CITESCORE 8.0

Article

The Role of an MRI-Based Radiomic Signature in Predicting Malignancy of Parotid Gland Tumors

Delia Doris Muntean, Sorin Marian Dudea, Mihaela Băciuţ, Cristian Dinu, Sebastian Stoia, Carolina Solomon, Csutak Csaba, Georgeta Mihaela Rusu and Lavinia Manuela Lenghel

Special Issue
Recent Updates on Salivary Gland Tumors

Edited by
Prof. Dr. Stephan Lang and Dr. Moritz Meyer

MDPI

https://doi.org/10.3390/cancers15133319

cancers

Article

The Role of an MRI-Based Radiomic Signature in Predicting Malignancy of Parotid Gland Tumors

Delia Doris Muntean [1], Sorin Marian Dudea [1], Mihaela Băciuț [2], Cristian Dinu [2], Sebastian Stoia [2], Carolina Solomon [1,*], Csutak Csaba [1], Georgeta Mihaela Rusu [1] and Lavinia Manuela Lenghel [1]

[1] Department of Radiology, Faculty of Medicine, "Iuliu Hațieganu" University of Medicine and Pharmacy, 400012 Cluj-Napoca, Romania; muntean.delia.doris@elearn.umfcluj.ro (D.D.M.); sdudea@umfcluj.ro (S.M.D.); csutakcsaba@elearn.umfcluj.ro (C.C.); mihageorgeta@elearn.umfcluj.ro (G.M.R.); pop.lavinia@umfcluj.ro (L.M.L.)

[2] Department of Maxillofacial Surgery and Implantology, Faculty of Dentistry, "Iuliu Hațieganu" University of Medicine and Pharmacy, 400012 Cluj-Napoca, Romania; mbaciut@umfcluj.ro (M.B.); cristian.dinu@umfcluj.ro (C.D.); sebastian.stoia@umfcluj.ro (S.S.)

* Correspondence: cbotar@umfcluj.ro

Simple Summary: Differentiating between benign and malignant parotid gland tumors is of paramount importance as it impacts therapeutical management. MRI represents the best imaging technique in diagnosing and characterizing parotid gland tumors, offering a high soft tissue contrast resolution. However, there are still overlapping radiological features between tumoral types; thus, accurate malignancy detection remains a challenge. Recently, radiomics has gained recognition as a promising new non-invasive approach in oncological imaging, especially related to tumor classification, and has the potential to become an additional diagnostic tool that might offer support in the clinical decision-making scenario.

Abstract: The aim of this study was to assess the ability of MRI radiomic features to differentiate between benign parotid gland tumors (BPGT) and malignant parotid gland tumors (MPGT). This retrospective study included 93 patients who underwent MRI examinations of the head and neck region (78 patients presenting unique PGT, while 15 patients presented double PGT). A total of 108 PGT with histological confirmation were eligible for the radiomic analysis and were assigned to a training group ($n = 83$; 58 BPGT; 25 MPGT) and a testing group ($n = 25$; 16 BPGT; 9 MPGT). The radiomic features were extracted from 3D segmentations of the PGT on the T2-weighted and fat-saturated, contrast-enhanced T1-weighted images. Following feature reduction techniques, including LASSO regression analysis, a radiomic signature (RS) was built with five radiomic features. The RS presented a good diagnostic performance in differentiating between PGT, achieving an area under the curve (AUC) of 0.852 ($p < 0.001$) in the training set and 0.786 ($p = 0.017$) in the testing set. In both datasets, the RS proved to have lower values in the BPGT group as compared to MPGT group ($p < 0.001$ and $p = 0.023$, respectively). The multivariate analysis revealed that RS was independently associated with PGT malignancy, together with the ill-defined margin pattern ($p = 0.031$, $p = 0.001$, respectively). The complex model, using clinical data, MRI features and the RS, presented a higher diagnostic performance (AUC of 0.976) in comparison to the RS alone. MRI-based radiomic features could be considered potential additional imaging biomarkers able to discriminate between benign and malignant parotid gland tumors.

Keywords: radiomics; textural analysis; parotid gland tumors; differential diagnosis; MRI

Citation: Muntean, D.D.; Dudea, S.M.; Băciuț, M.; Dinu, C.; Stoia, S.; Solomon, C.; Csaba, C.; Rusu, G.M.; Lenghel, L.M. The Role of an MRI-Based Radiomic Signature in Predicting Malignancy of Parotid Gland Tumors. *Cancers* **2023**, *15*, 3319. https://doi.org/10.3390/cancers15133319

Academic Editors: Stephan Lang and Moritz Meyer

Received: 24 April 2023
Revised: 11 June 2023
Accepted: 21 June 2023
Published: 23 June 2023

1. Introduction

Parotid gland tumors (PGT) are rare, accounting for approximately 3% of all tumors in the cervical region and 80–85% of salivary gland tumors [1]. Approximately 80% of PGT are benign, the most common being pleomorphic adenomas and Warthin's tumors, while the remaining 20% of PGT are malignant [2,3].

The gold standard treatment for PGT is surgery, and the protocol is determined by the histopathological type of tumor: for benign lesions, local excision or partial parotidectomy may be sufficient, whereas for malignant lesions total parotidectomy and neck dissection is recommended [4].

For assessing PGT, the imaging method of choice is magnetic resonance imaging (MRI), which offers valuable information regarding morphology, disease extension, and deep surrounding structures imaging [1,5]. The main advantages of MRI over other imaging methods include the absence of ionizing radiation and an improved tissue contrast resolution which is particularly important in detecting tumoral local spread including perineural disease [6].

Multiparametric MRI allows morphological and signal pattern analysis of PGT using standard sequences (T1-WI, T2-WI, STIR). Moreover, MRI also allows for a functional assessment of PGT by using diffusion-weighted imaging with the corresponding ADC maps, and dynamic contrast-enhanced imaging, respectively [1,3]. Several algorithms have been proposed to determine the histopathological type of parotid tumors, but there is still no general validation of them as there are several overlapping MRI features between lesions [7]. An accurate differential diagnosis is mandatory to implement a clinically and surgically appropriate strategy for PGT patients.

In oncological imaging, radiomics has recently emerged as a promising novel non-invasive tool, particularly useful in areas such as tumor classification, prognosis prediction, or therapeutical response assessment [8,9]. Radiomic analysis refers to the extraction of numerous quantitative imaging features from specific regions of interest in medical images. The most discriminative radiomic features can further be combined into radiomic signatures, which can be used to differentiate between various tumors [10,11].

Although MRI-derived radiomic signatures have shown potential in distinguishing between different types of salivary gland tumors [12,13], a consistent generally validated signature has not yet been established in the literature.

The purpose of this study is to assess whether textural analysis biomarkers are able to predict malignancy in PGT using standard MRI sequences and to evaluate the diagnostic performance of the resulting predictive radiomic model. A second aim is to assess the radiomic analysis added benefit to clinical–radiological models in the differentiation between benign parotid gland tumors (BPGT) and malignant parotid gland tumors (MPGT).

2. Materials and Methods

This study adhered to the Declaration of Helsinki guidelines and was granted approval by the Ethical Committee of the "Iuliu Hațieganu" University of Medicine and Pharmacy Cluj-Napoca (registration number: 43; date: 11 February 2022). Owing to the retrospective nature of the research, informed consent was waived for all participants.

2.1. Study Population

A retrospective analysis was performed in the electronic clinical and radiological database for patients who underwent an MRI evaluation of the head and neck region during January 2018 and January 2023 to assess parotid gland lesions.

The following inclusion criteria were used: (1) patients with PG-related symptoms or masses; (2) histological confirmation of the PGT from biopsy or surgical specimen; (3) available MRI examinations with corresponding technical parameters mentioned in the "Image Acquisition" Section 2.2.

The exclusion criteria were as follows: (1) tumors with a maximum diameter <5 mm; and (2) the existence of imaging artifacts making the images unsatisfactory for radiomic analysis. The exclusion criterion for a maximum tumor diameter of 5 mm was set to reduce the potential impact of partial volume effects that could alter the genuine tissue-specific image texture [14].

A final cohort of 93 consecutive patients was formed, following the application of the inclusion and exclusion criteria. A total of 78 patients presented unique PGT, while 15 patients presented double PGT (8 patients with double Warthin tumors, 4 patients with double malignant tumors, and 3 patients with double pleomorphic adenoma).

This study included a final number of 108 PGT which were eligible for radiomic analysis. Using the "one-third" criteria proposed in radiomic studies [15], the samples were randomly divided into a training group (83 PGT; 58 benign, 25 malignant) and a testing group (25 PGT; 16 benign, 9 malignant).

2.2. Image Acquisition

The MRI examinations were performed in a single center, using a 1.5 Tesla MRI scanner (SIGNA™ Explorer, General Electric, Milwaukee, WI, USA) using a dedicated, 16-channel, high-resolution head coil. The acquisition protocol was constructed an of axial fast spin-eco (FSE) T1-WI; an axial FSE T2-WI using the PROPELLER (Periodically Rotated Overlapping ParallEL Lines with Enhanced Reconstruction) technique; a coronal STIR PROPELLER; an axial diffusion-weighted imaging (DWI) using echo-planar imaging sequences at multiple b-values with the corresponding ADC maps; an axial perfusion-weighted imaging; and an axial FSE fat-saturated contrast-enhanced T1-WI using intravenous contrast medium 0.1 mL/kg Gadobudrol, (Gadovist; Bayer HealthCare, Berlin, Germany).

For the textural analysis, the following sequences were used: axial FSE T2-WI PROPELLER (T2-WI) and axial fat-saturated contrast-enhanced T1-WI (fsCE-T1-WI). The corresponding MRI specifications are presented in Table 1.

Table 1. MRI sequences specifications.

MRI Parameter	T2-WI	fsCE-T1-WI
TE (ms) *	75 [62–92]	12 [8.9–15.6]
TR (ms) *	5450 [3540–8290]	680 [610–750]
Matrix (mm)	384 × 384	300 × 300
Flip angle	160	160
Slice thickness (mm)	3	3
Slice gap (mm)	3	3

* median (interquartile range).

2.3. Preprocessing, Segmentation, and Feature Extraction

Each examination was reviewed on a dedicated workstation (General Electric, Advantage workstation, 4.7 edition) by one radiologist specialized in head and neck imaging with more than 15 years-experience in MRI, who reviewed the images for possible artifacts and protocol errors. All examinations underwent anonymization, and the selected sequences were retrieved in DICOM format and imported into an open-source texture analysis software, Slicer version 4.11 (available online at: http://www.slicer.org/ accessed on 1 February 2023).

Within the 3D Slicer program, before segmentation and feature extraction, all MR images went through several preprocessing stages. Firstly, all images were normalized by division through standard deviation and the gray values were discretized using a fixed-bin width of 25. To maintain consistency in scaling and orientation while extracting 3D features, all images were resampled with a voxel size of $1 \times 1 \times 1$ mm^3 using a B-Spline interpolator. Isotropic resampling was preferred over anisotropic resampling as it is more suitable for computing 3D textural features [16]. The widely used "$\mu \pm 3\sigma$" algorithm was also utilized for image intensity normalization and for diminishing the fluctuation impact of the acquired scanning parameters of the MRI examination [17]. Therefore, image intensity outliers (which differed > 3 sigma from the mean) were identified and removed.

After the preprocessing steps, one radiology resident (DDM), blinded to the histopathological results, manually outlined each parotid lesion on sequential images; therefore, a 3D segmentation was performed, excluding vessels or areas with necrosis.

The contouring procedure aimed to cover the tumor's maximum area without exceeding the lesion's margin. Figure 1 shows an example of benign and malignant PGT 3D segmentation.

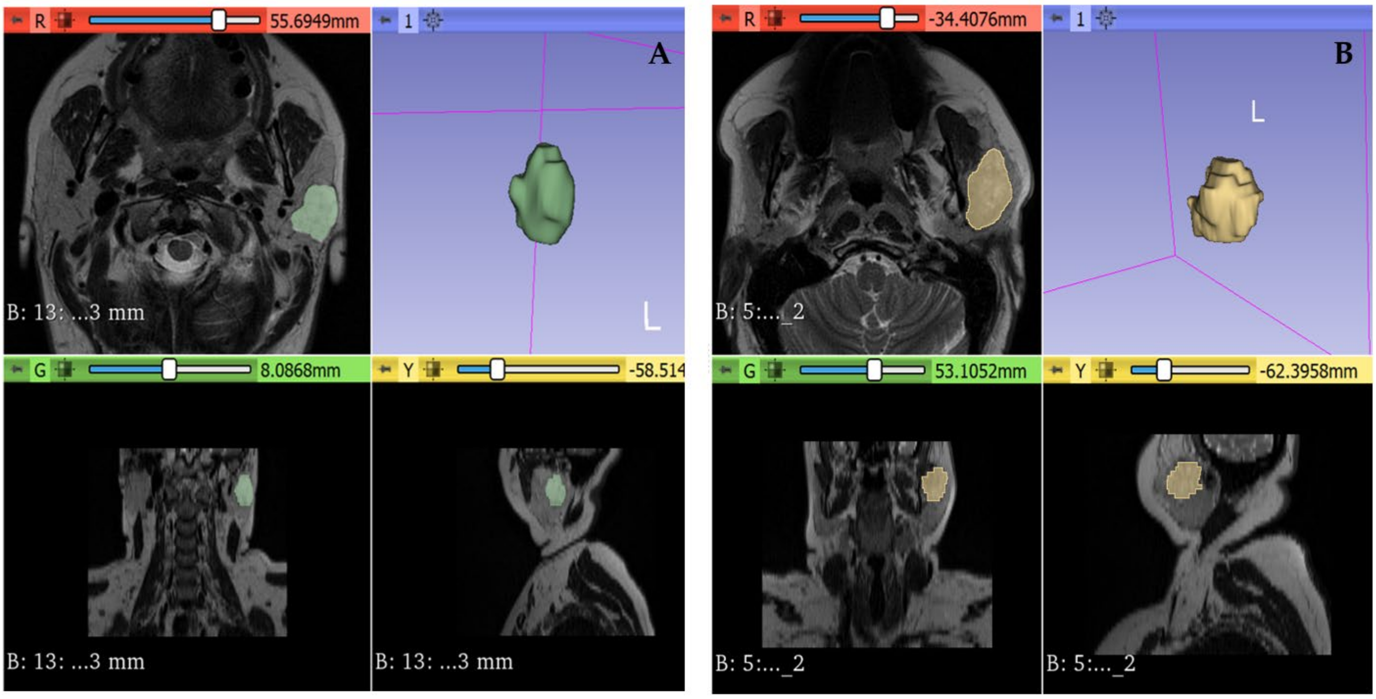

Figure 1. (**A**) 3D segmentation of a benign parotid tumor (confirmed as pleomorphic adenoma). (**B**) 3D segmentation of a malignant parotid tumor (confirmed as adenoid cystic carcinoma).

For the radiomic features extraction, the open source PyRadiomics package (version 3.0.1) was used. From each MRI sequence, 1037 quantitative radiomic features were extracted from the 3D segmentation of the PGT, using both original and filtered images.

The preprocessing filters were Laplacian of Gaussian (LoG), using fine and coarse patterns (sigma 3.0 and 5.0 mm) and wavelet filters.

The extracted radiomic features belonged to the following groups: first-order, gray-level co-occurrence matrix (GLCM), gray-level run length matrix (GLRLM), gray-level size zone matrix (GLSZM), gray-level dependence matrix (GLDM), neighboring gray-tone difference matrix (NGTDM), and shape.

2.4. Feature Selection and Statistical Analysis

The first step in the feature selection process was to assess feature stability between two segmentations. Therefore, 50 randomly selected PGT were resegmented by the same radiologist (DDM), two months after the initial segmentation. The intraobserver agreement was assessed by calculating the intraclass correlation coefficient (ICC). Features with an ICC ≤ 0.75 were excluded from further analysis.

All radiomic features underwent Z-score normalization.

To control data overfitting in this radiomic study, the following feature selection steps were conducted.

Firstly, to identify the statistically significant radiomic features able to differentiate between BPGT and MPGT, a univariate test was applied (Mann–Whitney U), using the Benjamini–Hochberg correction as an adjustment for multiple testing (corrected p-values < 0.05).

Secondly, to eliminate redundant features, the Spearman correlation was performed between any two features. When highly correlated features were encountered (Spearman's coefficient >0.9/<−0.9), only the feature with the lowest p-value in univariate analysis was retained.

The last step of feature reduction represented the multivariate logistic regression analysis using the least absolute shrinkage and selection operator (LASSO) with a ten -fold cross-validation.

Finally, five radiomic features were selected and combined into a Radiomic Signature, which was computed by taking a linear combination of the chosen features and weighting them based on their respective LASSO coefficients.

This three-step reduction technique was also performed in previous radiomic studies with favorable classification outcomes [18,19].

The diagnostic performance of the radiomic signature in both training and testing datasets was assessed by the Receiver operating characteristic (ROC) curve analysis.

The comparison between different areas under the ROC curve was performed using the DeLong test.

To analyze quantitative clinical and biological features, the independent-sample T or the Mann–Whitney U tests were employed, while for the assessment of categorical features, the exact Fisher test was utilized.

To identify independently associated features able to predict the malignancy of PGT, a binary logistic regression was performed using the enter method. The statistical significance value was set for $p < 0.05$.

The statistical analysis was conducted using the following software: SPSS Statistics for Windows, version 18.0 (SPSS Inc., Chicago, IL, USA), MedCalc version 14.8.1 (MedCalc Software, Mariakerke, Belgium), and R software version 3.6.3 (with the “glmnet” package).

An overview of the radiomic workflow used in this study is offered in Figure 2.

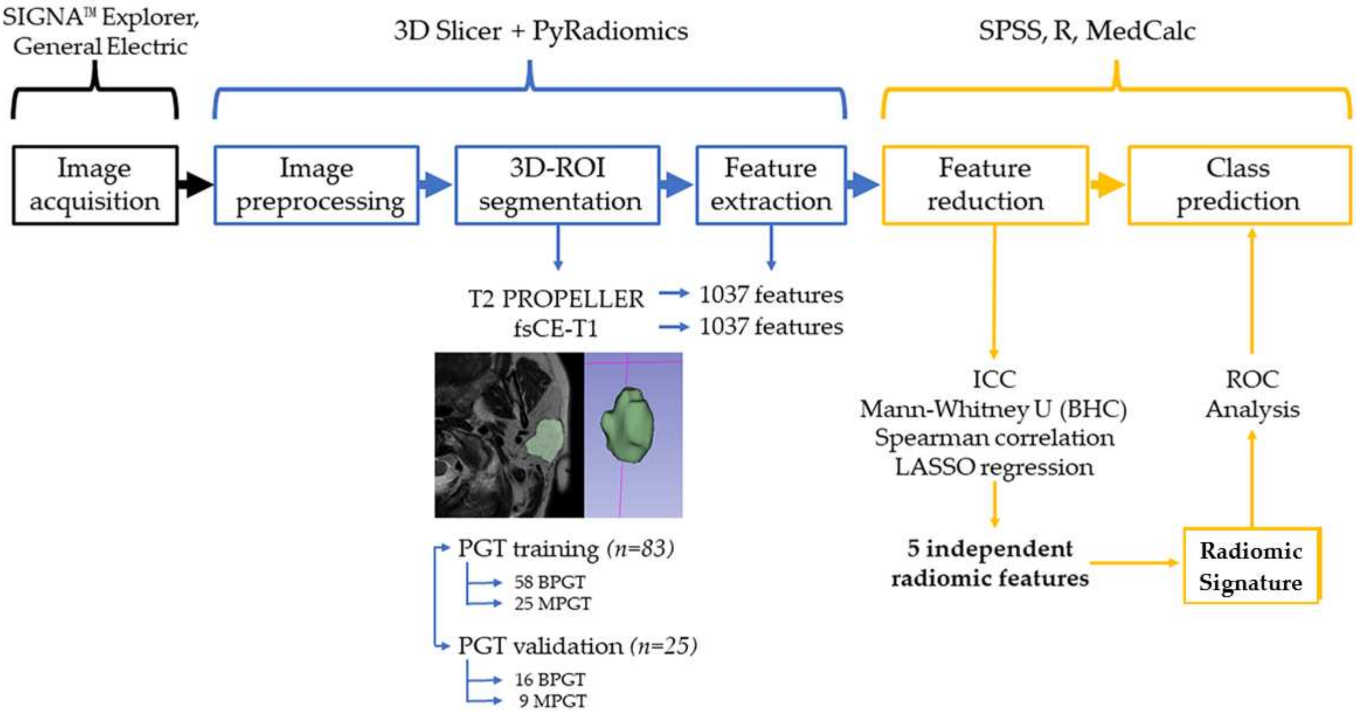

Figure 2. Radiomics workflow diagram. ROI = region of interest; PROPELLER = periodically rotated overlapping parallel lines with enhanced reconstruction; fsCE = fat-saturated contrast-enhanced; PGT = parotid gland tumors; BPGT = benign parotid gland tumor; MPGT = malignant parotid gland tumor; ICC = Intraclass Correlation Coefficient; BHC = Benjamini–Hochberg Correction; LASSO = Least Absolute Shrinkage and Selection Operator; ROC = Receiver-Operating Characteristic.

3. Results

In this radiomic study, a total of 108 PGT were analyzed, which were divided into a training set (83 PGT: 58 benign, 25 malignant) and a testing set (25 PGT: 16 benign, 9 malignant). Tumor characteristics are summarized in Table 2 and the histopathological distribution is presented in Table 3.

Table 2. Clinical and radiological characteristics of the benign and malignant PGT in the training and testing sets.

Feature		Training Set (n = 83)		p	Testing Set (n = 25)		p
		Benign PGT (n = 58)	**Malignant PGT (n = 25)**		**Benign PGT (n = 16)**	**Malignant PGT (n = 9)**	
Age (years)		49.6 ± 14.7	58.1 ± 13.4	0.014	54.2 ± 12.12	63.22 ± 14.87	0.115
Sex	Male	25 (43.1)	10 (40)	0.794	8 (50)	4 (44.4)	0.793
	Female	33 (56.9)	15 (60)		8 (50)	5 (55.6)	
Maximum size (mm)		26 [19, 32]	35 [25.7, 48.2]	0.011	19.5 [13, 24.5]	31 [21.5, 39]	0.046
Location	Superficial	35 (60.3)	10 (40)	0.14	13 (81.2)	8 (88.9)	0.513
	Deep	6 (10.3)	2 (8)		1 (6.3)	1 (11.1)	
	Both	17 (29.3)	13 (52)		2 (12.5)	0 (0)	
Side	Left	30 (51.7)	13 (52)	0.8	8 (50)	2 (22.2)	0.182
	Right	28 (48.3)	12 (48)		8 (50)	7 (77.8)	
Margin	Smooth	56 (96.6)	7 (28)	<0.001	14 (87.5)	2 (22.2)	0.001
	Ill-defined	2 (3.4)	18 (72)		2 (12.5)	7 (77.8)	
Cystic/necrotic areas	Present	36 (62.1)	16 (64)	0.755	12 (75)	5 (55.6)	0.327
	Absent	22 (37.9)	9 (36)		4 (24)	4 (44.4)	
T1-WI hyperintense spots	Present	14 (24.1)	2 (8)	0.089	8 (50)	7 (77.8)	0.228
	Absent	44 (75.9)	23 (92)		8 (50)	2 (22.2)	
T2-WI signal (vs. parotid)	Hypointense	16 (29.6)	17 (68)	<0.001	6 (37.5)	6 (66.7)	0.169
	Hyperintense	42 (72.4)	8 (32)		10 (62.5)	3 (33.3)	
T1-WI signal (vs. muscle)	Hypointense	49 (84.5)	24 (96)	0.141	14 (87.5)	9 (100)	0.278
	Hyperintense	9 (15.5)	1 (4)		2 (12.5)	0 (0)	
CE pattern	Homogenous	19 (32.7)	5 (20)	0.752	3 (18.7)	4 (44.4)	0.244
	Heterogenous	39 (67.2)	20 (80)		13 (81.3)	5 (55.6)	
T2-WI SI Ratio *		3.96 [2.46, 6.09]	2.85 [2.36, 3.66]	0.039	3.82 [2.51, 5.36]	2.56 [2.13, 2.88]	0.047
T1-WI SI Ratio *		1.14 [1, 1.27]	1.17 [1.08, 1.30]	0.605	1.23 [1.08, 1.39]	1.26 [1.10, 1.74]	0.428
fsCE-T1-WI SI Ratio *		1.61 [1.40, 2.18]	1.50 [1.40, 1.91]	0.461	1.33 [1.16, 1.95]	1.15 [1.11, 1.39]	0.212
ADC $(10^{-3}\ \mathrm{mm}^2/\mathrm{s})$		1.205	0.855	0.001	1.176	0.875	0.019
		[0.910, 1.800]	[0.728, 1.185]		[0.865, 1.459]	[0.670, 0.908]	

CE = contrast enhancement; SI = signal intensity; fs = fat-saturated; ADC = apparent diffusion coefficient; PGT = parotid gland tumor; p = statistical significance level. The results are presented as mean ± standard deviation, median and [interquartile range], or percentage (%). * Parotid gland tumor signal intensity/Masseter muscle signal intensity.

Table 3. Histopathology of parotid gland tumors.

	Training Set		Testing Set	
	Benign (n = 58)	**Malignant (n = 25)**	**Benign (n = 16)**	**Malignant (n = 9)**
Tumor histology	Pleomorphic adenoma 28 Warthin tumor 24 Basal cell adenoma 3 Parotid gland cyst 2 Reactive lymph node 1	Mucoepidermoid cc 3 Salivary duct cc 3 Adenoid cystic cc 3 Acinic cell cc 2 Lymphoma 7 Metastatic cc 3 Basal cell cc 2 Squamous cell cc 1 Undifferentiated sarcoma 1	Pleomorphic adenoma 6 Warthin tumor 8 Basal cell adenoma 1 Oncocytoma 1	Acinic cell cc 2 Salivary duct cc 2 Metastatic cc 2 Lymphoma 3

In the training group, the patient's age, maximum tumor size, tumor margin, T2-WI signal intensity compared to the parotid gland parenchyma, T2-WI signal intensity ratio (PGT signal intensity, divided by the masseter muscle signal intensity), and ADC value were significantly different between benign and malignant PGT.

MPGT appeared in older patients and presented greater dimensions than BPGT, predominant ill-defined margins, and hypointense signal on T2-WI. Furthermore, the T2-WI signal intensity ratio and the ADC values were lower for the MPGT in comparison to BPGT (2.85 vs. 3.96, $p = 0.039$; 0.855 vs. 1.205, $p = 0.001$, respectively).

Besides the age and the T2-WI intensity of PGT, all the parameters that proved to be statistically significant between the two study groups in the training set were also confirmed in the testing group.

3.1. Feature Selection and Radiomic Signature Construction in the Training Set

From each 3D segmentation of the PGT included in the training set, a total of 1037 radiomic features were extracted from T2-WI and another 1037 radiomic features from the fsCE-T1-WI, respectively. The intrareader agreement was tested and features with an ICC < 0.75 were excluded from further statistical analysis. Therefore, the features were reduced to 859 T2-WI features and 834 fsCE-T1-WI features.

To develop the radiomic signature, firstly, a univariate analysis was performed, and 67 T2-WI features and 50 fsCE-T1-WI features were found to be statistically significant between the two studied groups (with an adjusted p-value < 0.05 after Benjamini–Hochberg correction). Secondly, after performing Spearman's correlation analysis, 28 non-redundant features were retained for further analysis (Supplementary File: Table S1, Figure S1). The final parameter reduction technique was the ten-fold cross-validated LASSO (least absolute shrinkage and selection operator) regression which revealed five final radiomic features (Figure 3). By linearly combining these five radiomic features using their corresponding LASSO coefficients (Table 4), the following radiomic signature formula was generated:

$$\textbf{Radiomic Signature} = \sum_{\mathbf{x=0}}^{\mathbf{5}} \mathbf{C}_x * \mathbf{R}_x + \mathbf{I}, \tag{1}$$

where Cx is the coefficient of the xth radiomic feature, Rx the xth radiomic feature, and I the intercept.

3.2. The Performance of the Radiomic Signature in the Training Set

There was a significant difference in the radiomic signature value between BPGT and MPGT, −1.11 [−1.31, −0.71] versus −0.34 [−0.70, −0.15], $p < 0.001$.

In the training set, the radiomic signature predicted malignancy of PGT with an area under the curve (AUC) of 0.852, resulting in a sensitivity of 72% and a specificity of 87.7% for the cut-off value of >−0.614 (Figure 4).

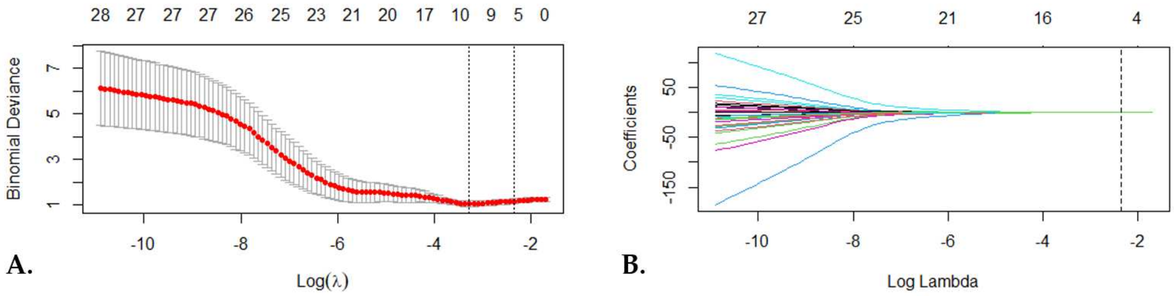

Figure 3. LASSO (least absolute shrinkage and selection operator) regression model. (**A**) Tuning parameter lambda (λ) selection using ten-fold cross-validation. The most favorable λ value was 0.045 and log (λ) = −3.08. The most favorable λ value according to the minimum criteria and 1 standard error of the minimum criteria are depicted with the dotted vertical lines. (**B**) The LASSO regression coefficients of the final 28 radiomics features and the most favorable λ (dotted vertical line).

Table 4. Radiomic feature selection results after LASSO regression.

MRI Sequence	Radiomic Feature	Radiomic Group	Associated Filter	Coefficient
fsCE-T1-WI	SizeZoneNonUniformityNormalized	Texture (glszm)	original	−0.865
fsCE-T1-WI	Skewness	First order	LoG filter (5 mm)	0.09
T2-WI	RootMeanSquared	First order	wavelet-HLL	0.136
T2-WI	Imc2	Texture (glcm)	wavelet-LLH	−0.167
T2-WI	Correlation	Texture (glcm)	wavelet-LHL	−0.296
	Intercept			−0.865

fsCE = fat-saturated with contrast enhancement; glszm = gray-level size zone matrix; glcm = gray-level co-occurrence matrix; LoG = Laplacian of Gaussian.

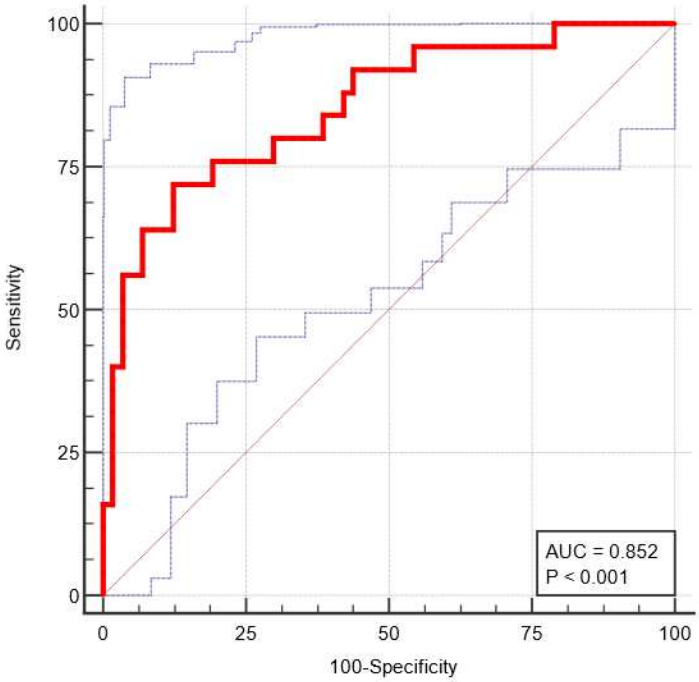

Figure 4. Receiver operating characteristic (ROC) curve of the radiomic signature for differentiating between BPGT and MPGT-training set (red line—ROC curve; thin dotted blue lines—ROC Confidence Interval).

The individual diagnostic performance of the five radiomic features was also assessed (Table 5). The AUC values varied between 0.668 and 0.747 and were lower than the one reached by the radiomic signature.

A clinical–radiological model was developed using a multivariate regression (Table 6) which included statistically significant features between BPGT and MPGT in the training group (age, maximum tumor size, margin, T2-WI signal intensity, T2-WI ratio, and ADC value). By adding the radiomic signature to the clinical–radiological model, a complex model was developed (Table 7). In the complex model, the radiomic signature and the ill-defined margin pattern were independently associated with malignancy of the PGT.

Table 5. Individual diagnostic performance of the final selected radiomic features.

Radiomic Feature	AUC (95% CI)	Cut-Off	Se (95% CI)	Sp (95% CI)	+LR (95% CI)	−LR (95% CI)	*p*
SizeZoneNonUniformityNormalized	0.668 (0.555–0.768)	≤−0.509	60 (38.7–78.9)	73.68 (60.3–84.5)	2.28 (1.33–3.91)	0.54 (0.33–0.90)	0.01
Skewness	0.695 (0.584–0.792)	>0.135	80 (59.3–93.2)	63.16 (49.3–75.6)	2.17 (1.47–3.21)	0.32 (0.14–0.71)	0.001
RootMeanSquared	0.678 (0.566–0.777)	>0.329	48 (27.8–68.7)	82.46 (70.1–91.3)	2.74 (1.37–5.48)	0.63 (0.42–0.94)	0.006
Imc2	0.74 (0.631–0.830)	≤−0.361	72 (50.6–87.9)	70.18 (56.6–81.6)	2.41 (1.51–3.85)	0.4 (0.21–0.77)	<0.001
Correlation	0.747 (0.639–0.836)	≤−0.211	76 (54.9–90.6)	70.18 (56.6–81.6)	2.55 (1.62–4.02)	0.34 (0.17–0.70)	<0.001

The 95% confidence interval (CI) values are shown in parentheses. AUC = area under curve; Se = sensitivity; Sp = specificity; +LR = positive likelihood ratio; −LR = negative likelihood ratio; *p* = statistical significance level.

Table 6. Multivariate logistic regression analysis for the PGT malignancy prediction—clinical–radiological model.

Variable	Coefficient	Std. Error	*p*	Odds Ratio
Patient's age	0.083	0.047	0.076	1.087
Maximum diameter	−0.016	0.047	0.736	0.984
Margin = "ill-defined"	5.649	1.488	<0.001	28.923
T2-WI = "hypointense"	2.520	1.491	0.091	12.435
T2-WI Ratio	0.030	0.387	0.937	1.030
ADC	−0.527	1.285	0.681	0.590
Constant	−7.558	4.341	0.081	

Std. Error = standard error; *p* = statistical significance level.

Table 7. Multivariate logistic regression analysis for the PGT malignancy prediction—complex model.

Variable	Coefficient	Std. Error	*p*	Odds Ratio
Patient's age	0.087	0.046	0.059	1.09
Maximum diameter	−0.029	0.052	0.582	0.97
Margin = "ill-defined"	7.277	2.332	0.001	29.21
T2-WI = "hypointense"	1.501	1.544	0.330	4.48
T2-WI Ratio	−0.146	0.468	0.753	0.86
ADC	−1.159	1.822	0.524	0.31
Radiomic Signature	5.307	2.467	0.031	22.43
Constant	−2.410	4.318	0.576	

Std. Error = standard error; *p* = statistical significance level.

Adding the radiomic signature to the first model slightly improved its performance for the differentiation between BPGT and MPGT: AUC = 0.943 (95% CI, 0.869 to 0.982) vs. AUC = 0.976 (95% CI, 0.916 to 0.997), $p = 0.064$, standard error = 0.02 (Figure 5).

A statistically significant difference between the AUC obtained by the radiomic signature and the one reached by the complex model was found: the difference between areas = 0.123; standard error = 0.04; 95% confidence interval, 0.0306 to 0.212, $p = 0.008$ (Figure 6).

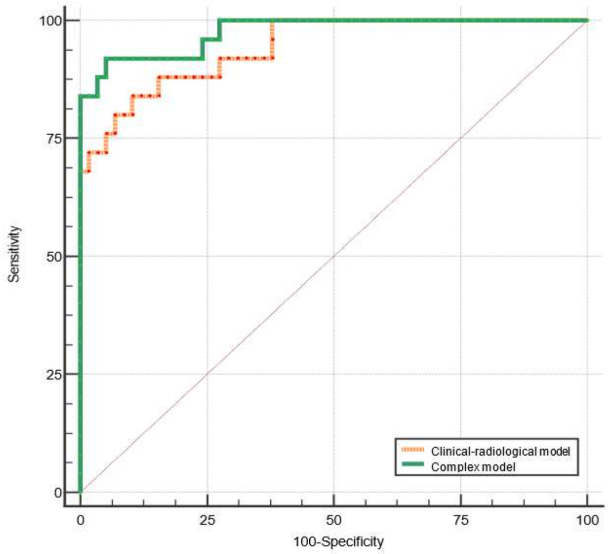

Figure 5. ROC curves of the clinical–radiological and complex models for differentiating between BPGT and MPGT.

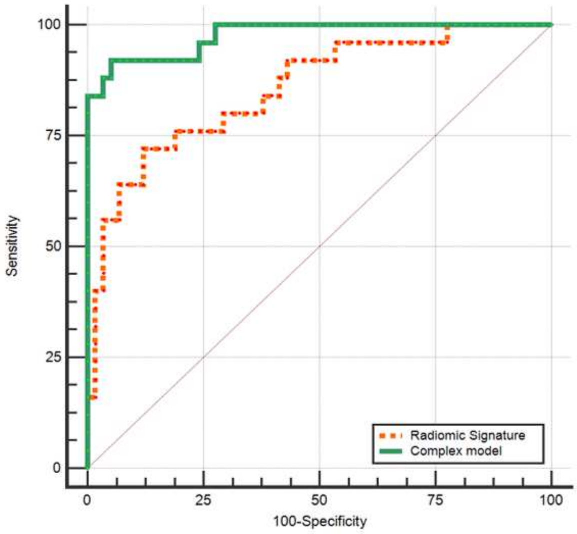

Figure 6. Comparison between ROC curves of the radiomic signature and the complex model for differentiating between BPGT and MPGT.

3.3. The Validation of the Radiomic Signature in the Testing Group

The radiomic signature of BPGT was significantly lower than MPGT (−0.859 vs. −0.527, $p < 0.05$) in the testing set as well (Table 8).

Table 8. Radiomic signature values of benign and malignant parotid gland tumors in the training and testing datasets.

Radiomic Signature	Median	Q1	Q3	*p*
Training set				
Benign	−1.11	−1.31	−0.71	<0.001
Malignant	−0.34	−0.7	−0.15	
Testing set				
Benign	−0.859	−1.435	−0.785	0.023
Malignant	−0.527	−0.787	−0.36	

Q1 = first quartile; Q3 = third quartile; *p* = statistical significance level.

The overall diagnostic performance of the radiomic signature in differentiating between BPGT and MPGT was attested in the testing group, reaching an AUC of 0.786, when the optimal cut-off value was chosen according to the Jouden index analysis (Figure 7 and Table 9).

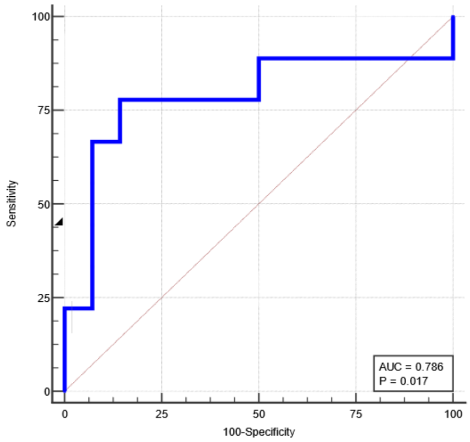

Figure 7. Receiver operating characteristic (ROC) curve (blue line) of the radiomic signature for differentiating between BPGT and MPGT in the testing set.

Table 9. Diagnostic performance of the radiomic signature in the training and testing datasets.

Radiomic Signature	**AUC (95% CI)**	**Cut-Off**	**Se (95% CI)**	**Sp (95% CI)**	**+LR (95% CI)**	**−LR (95% CI)**	***p***
Training set	0.852 0.756–0.921	>−0.614	72 50.6–87.9	87.72 76.3–94.9	5.86 2.81–12.23	0.32 0.17–0.60	<0.0001
Testing set	0.786 0.566–0.927	>−0.774	77.78 40.0–97.2	85.71 57.2–98.2	5.44 1.44–20.58	0.26 0.075–0.90	0.017

The 95% confidence interval (CI) values are shown in parentheses. AUC = area under curve; Se = sensitivity; Sp = specificity; +LR = positive likelihood ratio; −LR = negative likelihood ratio; *p* = statistical significance level.

For the previous cut-off value of >−0.614 (established in the training group), in the validation group, there 66.7% sensitivity and 81.3% specificity were recorded.

4. Discussion

The current study assessed the performance of MRI-based radiomic features to discriminate between benign and malignant PGT using a 3D segmentation approach on T2-WI and fsCE-T1-WI sequences.

Radiomics represents a non-invasive postprocessing imaging technique that implies extracting numerous quantitative features from digital images, thereby converting them into mineable high-dimensional data which could predict changes at a cellular, metabolic, or genetic level [11,20]. Recently, there has been an increasing interest in the radiomics of salivary gland imaging, mainly addressing the following three topics: differentiating between different PGT types, predicting xerostomia after radiation therapy in the head-neck region, or assessing PG parenchymal changes in diffuse inflammatory diseases, such as primary Sjogren's Syndrome [21].

The constructed radiomic signature in this study includes first-order radiomic features derived from the histogram, and second-order radiomic features from the gray-level co-occurrence matrix (GLCM) and gray-level size zone matrix (GLSZM). First-order features provide information about the voxels' intensity distribution inside a region or volume of interest, regardless of any spatial relationships between each other, while second-order features are computed from various matrices to describe the spatial arrangement and interaction between voxels [22]. GLCM assesses the spatial relationships between individual voxels with different gray-level values, while GLSZM considers the size and frequency of connected regions of voxels with the same intensity value within a given region/volume of interest in a medical image [23,24].

The feature extraction process was performed from both unfiltered and filtered images. As a pre-processing step, to all images, we applied Laplacian of Gaussian filters, which highlight regions of rapid change (for instance, edge detection) and wavelet filters, which separate information with high and low spatial frequency [25]. The majority of the radiomic features included in the final radiomic signature were extracted from images with wavelet filters, which proved to be especially useful in imaging denoising [26].

Regarding the PGT segmentation, a volume of interest was delineated in the three-dimensional (3D) approach, as we considered it would provide representative information more reliable for entire tumor characterization and heterogeneity assessment in comparison to a 2D segmentation.

The chosen MRI sequences for segmentation were T2-WI acquired with the PROPELLER technique and fsCE-T1-WI. By using PROPELLER, the image quality increases, and any potential motion artifacts are diminished [27]. Contrast-enhanced imaging is often used in radiomic studies as it provides information regarding tumor vascularity and heterogeneity that would not be discernible without the use of contrast material [15].

The results obtained in this study demonstrate that the proposed MRI-based radiomic signature, obtained from the combination of five radiomic features extracted from two standard sequences, achieved a promising performance in differentiating benign from malignant PGT. The AUC of the radiomic signature in the training group was 0.852, higher than the AUC of each radiomic feature individually, which ranged between 0.668–0.747. In the testing dataset, the radiomic signature maintained a good diagnostic performance, with an AUC of 0.786.

There are several studies performed so far that assessed the ability of MRI radiomic features to differentiate MPGT from BPGT using either features extracted from one sequence alone or multiple sequences combined. The reported diagnostic performances of the obtained radiomic models are variable.

The best radiomic model proposed by Zheng et al. was built using a combination of T1-WI-logarithm and fsT2-WI-exponential features and reached an average AUC of 0.846 for differentiating benign from malignant SGT. This study, however, included not only PGT, as in our study, but also tumors of the submandibular and sublingual glands [28]. By combining radiomic features extracted from manual segmentations of PGT on T1- and T2-WI, Vernuccio et al. obtained a radiomic model that presented an AUC of 0.927, with high specificity (93.4%), albeit at a cost of low sensitivity (57.2%) in the diagnosis of PGT malignancy [29].

Another study used Linear Discriminant Analysis (LDA) and Support Vector Machine (SVM) classifiers to discriminate between BPGT and MPGT on T2-WI, ADC map, and DCE-MRI, and the reported AUC for each sequence was 93.3%, 100%, 99.2% for LDA, and 100%, 100%, 100% for SMV, respectively. When the classifiers were trained using features from all three sequences combined, the AUC reached 100% for both LDA and SMV [30].

Using only the conventional T2-WI, SVM classifier training was performed using five non-redundant discriminative features between BPGT and MPGT, and all feature subsets were tested as well. The radiomic signature resulting after combining the gray-level mean, skewness, and autocorrelation values performed the best in classifying PGT, yielding a high specificity (88.5%), but low sensitivity and accuracy (29.4%, 0.594, respectively) [31].

One study proposed a mixed model that combined four parameters: the 25th percentile extracted from the ADC map, the 10th percentile extracted from T2-WI, and the type of contrast enhancement and margins. The model's accuracy in differentiating BPGT from MPGT was 80.4% in the training cohort and 89.2% in the validation cohort [32].

A multisequence combined radiomic model presented a higher differentiation performance (BPGT vs MPGT, AUC = 0.863) than the single- or double-sequence radiomic models (AUC between 0.792–0.855), while the radiomic nomogram reached the highest

AUC of 0.907 [33]. Liu et al. also proved that adding 2D and/or 3D radiomic features extracted from T1- and T2-WI to clinical and radiological data improved the diagnostic performance in differentiating BPGT from MPGT (0.85 AUC for the complex model versus 0.72 AUC for the clinical reference model) [34].

Similarly, to provide a more holistic model, we have also performed a multivariate analysis using clinical data, MRI features, and the radiomic signature. This integrated approach improved the diagnostic performance in differentiating BPGT from MPGT, in comparison to the radiomic signature alone.

Radiomic imaging is under constant development and recent studies aim to propose new and improved classification algorithms and radiomic signatures. However, there is still a need to prove how radiomic features can systematically outperform other competitors, ideally across multiple datasets.

Using multiparametric MRI in assessing PGT has already demonstrated promising results, currently representing the first-line imaging method in assessing this pathology. According to Zeng et al., using conventional MRI and DWI combined reached 91% diagnostic accuracy in differentiating between MPGT and BPGT (82% sensitivity and 94% specificity), while adding DCE MRI to the assessment boosted the accuracy to 96% [35]. This was confirmed in another study which showed that assessing the tumor shape and capsule presence on conventional MRI sequences in conjunction with functional MRI features (such as ADC and TIC patterns) demonstrated great performance: 91.2% accuracy in diagnosing parotid gland lesions, i.e., higher than the individual diagnostic performance of each MRI sequence [36].

Our proposed radiomic signature reached a sensitivity of 72% and a specificity of 87.7% in differentiating between BPGT and MPGT and the AUC was 0.852. When clinical–radiological data were added and a complex model was built, the AUC increased to 0.976. This supports the idea that radiomics present great diagnostic potential when used in addition to other imaging features and not just as an individual diagnostic tool [21].

However, the current study presents several limitations. Firstly, there was a relatively low number of observations, particularly in the MPGT group. This is due mainly to a generally higher incidence of benign PGT (approximately 80%) [3]. Secondly, although we were able to split the acquired observations into a training and testing dataset, the obtained radiomic signature lacks external validation on a new data set from a different institution, which would have increased the signature's generalizability. The logistic regressions were only performed on the training dataset and were not assessed in the testing dataset due to the low number of cases assigned in the latter, which would not have allowed a fair regression analysis with statistical significance.

MR images are known to be subject to increased variations in signal intensity between examinations, which is a main problem in radiomics that requires special consideration [37,38]. As this study was monocentric, all patients were examined in the radiology department using a standardized MRI head-neck protocol. However, there were still some variations in the acquisition parameters (TE, TR) and consequently, before PGT segmentation and feature extraction, all MR images underwent several pre-processing techniques to obtain a homogenous set of images.

Another important aspect is related to the ability of many texture analysis programs to extract a high number of radiomic features, which often exceeds the number of samples and therefore increases the risk of overfitting [11,39]. To counteract this aspect, we have performed several feature reduction techniques to exclude redundant features. We have also performed corrections for multiple testing, and p-values were adjusted using a false discovery rate method such as the Benjamini–Hochberg correction [40].

Some authors report an interobserver variability regarding the segmentation of the PG, which might impact the value of the extracted radiomic feature [41]. Unfortunately, this confounder effect was not assessed in the current study, and only the intraobserver variability was tested.

Finally, the current study only assessed radiomic features extracted from two conventional anatomical MRI sequences and did not assess other sequences such as diffusion or perfusion-weighted imaging.

5. Conclusions

The current study proved that radiomic features extracted from MR images and the proposed radiomic signature are able to discriminate between benign and malignant parotid gland tumors. An integrated approach using clinical, radiological, and radiomic features achieved a better diagnostic performance than the radiomic signature alone, suggesting the current adjuvant role of radiomics as a diagnostic tool. Nevertheless, the validation of the proposed radiomic model in larger, multicentric studies, is warranted.

Supplementary Materials: The following supporting information can be downloaded at: https://www.mdpi.com/article/10.3390/cancers15133319/s1, Table S1: List of the selected radiomic features able to discriminate between benign and malignant PGT, that were included in the LASSO regression analysis. Figure S1: Correlogram of the final selected radiomic features (n = 28) using the Spearman's correlation.

Author Contributions: Conceptualization, D.D.M., S.M.D. and L.M.L.; methodology, D.D.M., M.B., C.D., S.S., C.S.; software, D.D.M., C.C., L.M.L.; validation, M.B., C.D., S.S., L.M.L.; formal analysis, D.D.M., C.C., G.M.R.; investigation, C.S., C.D., S.S.; data curation, S.M.D., C.S., G.M.R.; writing—original draft preparation, D.D.M.; writing—review and editing D.D.M., S.M.D.; visualization, D.D.M., C.S.; L.M.L.; supervision, S.M.D., L.M.L.; project administration, S.M.D., C.D., L.M.L. All authors have read and agreed to the published version of the manuscript.

Funding: This work was granted by project PDI-PFE-CDI 2021, entitled Increasing the Performance of Scientific Research, Supporting Excellence in Medical Research and Innovation, PROGRES, no. 40PFE/30.12.2021.

Institutional Review Board Statement: The study was conducted in accordance with the Declaration of Helsinki and was approved by the Ethics Committee of "Iuliu Hațieganu" University of Medicine and Pharmacy Cluj-Napoca (DEP43/11 February 2022).

Informed Consent Statement: Informed consent was waived, given the study's retrospective nature.

Data Availability Statement: The data are available only by request.

Conflicts of Interest: The authors declare no conflict of interest.

References

1. Abdel Razek, A.A.K.; Mukherji, S.K. State-of-the-Art Imaging of Salivary Gland Tumors. *Neuroimaging Clin. N. Am.* **2018**, *28*, 303–317. [CrossRef]
2. Kennedy, R.A. WHO is in and WHO is out of the mouth, salivary glands, and jaws sections of the 4th edition of the WHO classification of head and neck tumours. *Br. J. Oral Maxillofac. Surg.* **2018**, *56*, 90–95. [CrossRef]
3. Lobo, R.; Hawk, J.; Srinivasan, A. A Review of Salivary Gland Malignancies: Common Histologic Types, Anatomic Considerations, and Imaging Strategies. *Neuroimaging Clin. N. Am.* **2018**, *28*, 171–182. [CrossRef]
4. Sood, S.; McGurk, M.; Vaz, F. Management of Salivary Gland Tumours: United Kingdom National Multidisciplinary Guidelines. *J. Laryngol. Otol.* **2016**, *130* (Suppl. S2), S142–S149. [CrossRef]
5. Stoia, S.; Lenghel, M.; Dinu, C.; Tamaș, T.; Bran, S.; Băciuț, M.; Boțan, E.; Leucuța, D.; Armencea, G.; Onișor, F.; et al. The Value of Multiparametric Magnetic Resonance Imaging in the Preoperative Differential Diagnosis of Parotid Gland Tumors. *Cancers* **2023**, *15*, 1325. [CrossRef]
6. Afzelius, P.; Nielsen, M.Y.; Ewertsen, C.; Bloch, K.P. Imaging of the major salivary glands. *Clin. Physiol. Funct. Imaging* **2016**, *36*, 1–10. [CrossRef]
7. Espinoza, S.; Felter, A.; Malinvaud, D.; Badoual, C.; Chatellier, G.; Siauve, N.; Halimi, P. Warthin's tumor of parotid gland: Surgery or follow-up? Diagnostic value of a decisional algorithm with functional MRI. *Diagn. Interv. Imaging* **2016**, *97*, 37–43. [CrossRef]
8. Caruso, D.; Polici, M.; Zerunian, M.; Pucciarelli, F.; Guido, G.; Polidori, T.; Landolfi, F.; Nicolai, M.; Lucertini, E.; Tarallo, M.; et al. Radiomics in Oncology, Part 1: Technical Principles and Gastrointestinal Application in CT and MRI. *Cancers* **2021**, *13*, 2522. [CrossRef]

9. Caruso, D.; Polici, M.; Zerunian, M.; Pucciarelli, F.; Guido, G.; Polidori, T.; Landolfi, F.; Nicolai, M.; Lucertini, E.; Tarallo, M.; et al. Radiomics in Oncology, Part 2: Thoracic, Genito-Urinary, Breast, Neurological, Hematologic and Musculoskeletal Applications. *Cancers* **2021**, *13*, 2681. [CrossRef]
10. Liu, Z.; Wang, S.; Dong, D.; Wei, J.; Fang, C.; Zhou, X.; Sun, K.; Li, L.; Li, B.; Wang, M.; et al. The Applications of Radiomics in Precision Diagnosis and Treatment of Oncology: Opportunities and Challenges. *Theranostics* **2019**, *9*, 1303–1322. [CrossRef]
11. Lambin, P.; Leijenaar, R.T.H.; Deist, T.M.; Peerlings, J.; de Jong, E.E.C.; van Timmeren, J.; Sanduleanu, S.; Larue, R.T.H.M.; Even, A.J.G.; Jochems, A.; et al. Radiomics: The bridge between medical imaging and personalized medicine. *Nat. Rev. Clin. Oncol.* **2017**, *14*, 749–762. [CrossRef]
12. Zheng, Y.M.; Li, J.; Liu, S.; Cui, J.F.; Zhan, J.F.; Pang, J.; Zhou, R.Z.; Li, X.L.; Dong, C. MRI-Based radiomics nomogram for differentiation of benign and malignant lesions of the parotid gland. *Eur. Radiol.* **2021**, *31*, 4042–4052. [CrossRef]
13. He, Z.; Mao, Y.; Lu, S.; Tan, L.; Xiao, J.; Tan, P.; Zhang, H.; Li, G.; Yan, H.; Tan, J.; et al. Machine learning-based radiomics for histological classification of parotid tumors using morphological MRI: A comparative study. *Eur. Radiol.* **2022**, *32*, 8099–8110. [CrossRef]
14. Fruehwald-Pallamar, J.; Czerny, C.; Holzer-Fruehwald, L.; Nemec, S.F.; Mueller-Mang, C.; Weber, M.; Mayerhoefer, M.E. Texture-based and diffusion-weighted discrimination of parotid gland lesions on MR images at 3.0 Tesla. *NMR Biomed.* **2013**, *26*, 1372–1379. [CrossRef]
15. Shur, J.D.; Doran, S.J.; Kumar, S.; Ap Dafydd, D.; Downey, K.; O'Connor, J.P.B.; Papanikolaou, N.; Messiou, C.; Koh, D.M.; Orton, M.R. Radiomics in Oncology: A Practical Guide. *Radiographics* **2021**, *41*, 1717–1732. [CrossRef]
16. Zwanenburg, A.; Vallières, M.; Abdalah, M.A.; Aerts, H.J.W.L.; Andrearczyk, V.; Apte, A.; Ashrafinia, S.; Bakas, S.; Beukinga, R.J.; Boellaard, R.; et al. The Image Biomarker Standardization Initiative: Standardized Quantitative Radiomics for High-Throughput Image-based Phenotyping. *Radiology* **2020**, *295*, 328–338. [CrossRef]
17. Collewet, G.; Strzelecki, M.; Mariette, F. Influence of MRI acquisition protocols and image intensity normalization methods on texture classification. *Magn. Reson. Imaging* **2004**, *22*, 81–91. [CrossRef]
18. Petresc, B.; Lebovici, A.; Caraiani, C.; Feier, D.S.; Graur, F.; Buruian, M.M. Pre-Treatment T2-WI Based Radiomics Features for Prediction of Locally Advanced Rectal Cancer Non-Response to Neoadjuvant Chemoradiotherapy: A Preliminary Study. *Cancers* **2020**, *12*, 1894. [CrossRef]
19. Moldovanu, C.G.; Boca, B.; Lebovici, A.; Tamas-Szora, A.; Feier, D.S.; Crisan, N.; Andras, I.; Buruian, M.M. Preoperative Predicting the WHO/ISUP Nuclear Grade of Clear Cell Renal Cell Carcinoma by Computed Tomography-Based Radiomics Features. *J. Pers. Med.* **2020**, *11*, 8. [CrossRef]
20. Gillies, R.J.; Kinahan, P.E.; Hricak, H. Radiomics: Images Are More than Pictures, They Are Data. *Radiology* **2016**, *278*, 563–577. [CrossRef]
21. Aringhieri, G.; Fanni, S.C.; Febi, M.; Colligiani, L.; Cioni, D.; Neri, E. The Role of Radiomics in Salivary Gland Imaging: A Systematic Review and Radiomics Quality Assessment. *Diagnostics* **2022**, *12*, 3002. [CrossRef]
22. Lubner, M.G.; Smith, A.D.; Sandrasegaran, K.; Sahani, D.V.; Pickhardt, P.J. CT Texture Analysis: Definitions, Applications, Biologic Correlates, and Challenges. *Radiographics* **2017**, *37*, 1483–1503. [CrossRef]
23. Haralick, R.M.; Shanmugam, K. Textural features for image classification. *IEEE Trans. Syst. Man Cybern.* **1973**, *3*, 610–621. [CrossRef]
24. Thibault, G.; Angulo, J.; Meyer, F. Advanced statistical matrices for texture characterization: Application to cell classification. *IEEE Trans. Biomed. Eng.* **2014**, *61*, 630–637. [CrossRef]
25. Ganeshan, B.; Miles, K.A. Quantifying tumour heterogeneity with CT. *Cancer Imaging* **2013**, *13*, 140–149. [CrossRef]
26. Bnou, K.; Raghay, S.; Hakim, A. A wavelet denoising approach based on unsupervised learning model. *EURASIP J. Adv. Signal Process.* **2020**, *1*, 1–26. [CrossRef]
27. Shimamoto, H.; Tsujimoto, T.; Kakimoto, N.; Majima, M.; Iwamoto, Y.; Senda, Y.; Murakami, S. Effectiveness of the periodically rotated overlapping parallel lines with enhanced reconstruction (PROPELLER) technique for reducing motion artifacts caused by mandibular movements on fat-suppressed T2-weighted magnetic resonance (MR) images. *Magn. Reson. Imaging* **2018**, *54*, 1–7. [CrossRef]
28. Zhang, R.; Ai, Q.Y.H.; Wong, L.M.; Green, C.; Qamar, S.; So, T.Y.; Vlantis, A.C.; King, A.D. Radiomics for Discriminating Benign and Malignant Salivary Gland Tumors; Which Radiomic Feature Categories and MRI Sequences Should Be Used? *Cancers* **2022**, *14*, 5804. [CrossRef]
29. Vernuccio, F.; Arnone, F.; Cannella, R.; Verro, B.; Comelli, A.; Agnello, F.; Stefano, A.; Gargano, R.; Rodolico, V.; Salvaggio, G.; et al. Diagnostic performance of qualitative and radiomics approach to parotid gland tumors: Which is the added benefit of texture analysis? *Br. J. Radiol.* **2021**, *94*, 20210340. [CrossRef]
30. Fathi Kazerooni, A.; Nabil, M.; Alviri, M.; Koopaei, S.; Salahshour, F.; Assili, S.; Saligheh Rad, H.; Aghaghazvini, L. Radiomic Analysis of Multi-parametric MR Images (MRI) for Classification of Parotid Tumors. *J. Biomed. Phys. Eng.* **2022**, *12*, 599–610. [CrossRef]
31. Gabelloni, M.; Faggioni, L.; Attanasio, S.; Vani, V.; Goddi, A.; Colantonio, S.; Germanese, D.; Caudai, C.; Bruschini, L.; Scarano, M.; et al. Can Magnetic Resonance Radiomics Analysis Discriminate Parotid Gland Tumors? A Pilot Study. *Diagnostics* **2020**, *10*, 900. [CrossRef]

32. Piludu, F.; Marzi, S.; Ravanelli, M.; Pellini, R.; Covello, R.; Terrenato, I.; Farina, D.; Campora, R.; Ferrazzoli, V.; Vidiri, A. MRI-Based Radiomics to Differentiate between Benign and Malignant Parotid Tumors With External Validation. *Front. Oncol.* **2021**, *11*, 656918. [CrossRef]
33. Qi, J.; Gao, A.; Ma, X.; Song, Y.; Zhao, G.; Bai, J.; Gao, E.; Zhao, K.; Wen, B.; Zhang, Y.; et al. Differentiation of Benign From Malignant Parotid Gland Tumors Using Conventional MRI Based on Radiomics Nomogram. *Front. Oncol.* **2022**, *12*, 937050. [CrossRef]
34. Liu, Y.; Zheng, J.; Zhao, J.; Yu, L.; Lu, X.; Zhu, Z.; Guo, C.; Zhang, T. Magnetic resonance image biomarkers improve differentiation of benign and malignant parotid tumors through diagnostic model analysis. *Oral Radiol.* **2021**, *37*, 658–668. [CrossRef]
35. Zheng, N.; Li, R.; Liu, W.; Shao, S.; Jiang, S. The diagnostic value of combining conventional, diffusion-weighted imaging and dynamic contrast-enhanced MRI for salivary gland tumors. *Br. J. Radiol.* **2018**, *91*, 20170707. [CrossRef]
36. Tao, X.; Yang, G.; Wang, P.; Wu, Y.; Zhu, W.; Shi, H.; Gong, X.; Gao, W.; Yu, Q. The value of combining conventional, diffusion-weighted and dynamic contrast-enhanced MR imaging for the diagnosis of parotid gland tumours. *Dento Maxillo Facial Radiol.* **2017**, *46*, 20160434. [CrossRef]
37. Buch, K.; Kuno, H.; Qureshi, M.M.; Li, B.; Sakai, O. Quantitative variations in texture analysis features dependent on MRI scanning parameters: A phantom model. *J. Appl. Clin. Med. Phys.* **2018**, *19*, 253–264. [CrossRef]
38. Cattell, R.; Chen, S.; Huang, C. Robustness of radiomic features in magnetic resonance imaging: Review and a phantom study. *Vis. Comput. Ind. Biomed. Art* **2019**, *2*, 19. [CrossRef]
39. Van Timmeren, J.E.; Cester, D.; Tanadini-Lang, S.; Alkadhi, H.; Baessler, B. Radiomics in medical imaging-"how-to" guide and critical reflection. *Insights Imaging* **2020**, *11*, 91. [CrossRef]
40. Benjamini, Y.; Hochberg, Y. Controlling the False Discovery Rate: A Practical and Powerful Approach to Multiple Testing. *J. R. Stat. Soc. Ser. B* **1995**, *57*, 289–300. [CrossRef]
41. Forde, E.; Leech, M.; Robert, C.; Herron, E.; Marignol, L. Influence of inter-observer delineation variability on radiomic features of the parotid gland. *Phys. Med.* **2021**, *82*, 240–248. [CrossRef]

diagnostics

IMPACT FACTOR 3.0

Indexed in: PubMed

CITESCORE 4.7

Article

Viscosity Plane-Wave UltraSound (Vi PLUS) in the Evaluation of Thyroid Gland in Healthy Volunteers—A Preliminary Study

Diana-Raluca Petea-Balea, Carolina Solomon, Delia Doris Muntean, Ioana-Teofana Dulgheriu, Cristina Alina Silaghi and Sorin Marian Dudea

MDPI

https://doi.org/10.3390/diagnostics12102474

diagnostics

Article

Viscosity Plane-Wave UltraSound (Vi PLUS) in the Evaluation of Thyroid Gland in Healthy Volunteers—A Preliminary Study

Diana-Raluca Petea-Balea [1], Carolina Solomon [1,*], Delia Doris Muntean [1], Ioana-Teofana Dulgheriu [1], Cristina Alina Silaghi [2] and Sorin Marian Dudea [1]

[1] Department of Radiology, "Iuliu Hațieganu" University of Medicine and Pharmacy, 400012 Cluj-Napoca, Romania
[2] Department of Endocrinology, "Iuliu Hațieganu" University of Medicine and Pharmacy Cluj-Napoca, 8 Victor Babes Street, 400012 Cluj-Napoca, Romania
* Correspondence: carolinasolomon12@gmail.com

Abstract: Viscosity and elasticity represent biomechanical properties of soft tissues that suffer changes during the pathophysiological alterations of the tissue in various conditions. This study aimed to determine average viscosity values for the thyroid gland and to evaluate the potential influences of age, gender and body mass index (BMI), using a recent technique Viscosity Plane-wave UltraSound (Vi PLUS). A total of 85 healthy Caucasian volunteers (56 women and 29 men, median age of 29 years, range 17–81 years) were included in this prospective monocentric study conducted between January 2022 and March 2022. Thyroid viscosity was measured using the SuperSonic MACH 30® Ultrasound system (Aixplorer, SuperSonic Imagine, Aix-en-Provence, France), equipped with a curvilinear C6-IX transducer that allows simultaneous quantification of the viscosity and stiffness. The mean thyroid viscosity measurement value was 2.63 ± 0.47 Pa.s. No statistically significant differences were detected between the left and the right lobes of the thyroid gland. A significant positive correlation was found between thyroid viscosity and elasticity (r = 0.685, $p < 0.0001$). There was no statistically significant correlation between body mass index (BMI) and thyroid gland viscosity and elasticity values (r = 0.215, $p = 0.053$; r = 0.106, $p = 0.333$). No correlation between viscosity and gender was established ($p > 0.05$). Vi PLUS represents a new and promising ultrasonographic technique that can provide helpful information for evaluating the thyroid parenchyma, similar to elastography. The effect of the potential confounding factors on thyroid viscosity was negligible, except for BMI.

Keywords: viscosity; shear wave elastography; thyroid gland; healthy subjects

Citation: Petea-Balea, D.-R.; Solomon, C.; Muntean, D.D.; Dulgheriu, I.-T.; Silaghi, C.A.; Dudea, S.M. Viscosity Plane-Wave UltraSound (Vi PLUS) in the Evaluation of Thyroid Gland in Healthy Volunteers—A Preliminary Study. *Diagnostics* **2022**, *12*, 2474. https://doi.org/10.3390/diagnostics12102474

Academic Editor: Po-Hsiang Tsui

Received: 7 August 2022
Accepted: 10 October 2022
Published: 13 October 2022

1. Introduction

Various ultrasound methods for evaluating the mechanical proprieties of biological tissues have been widely studied and integrated into daily medical practice throughout the last decades [1]. Among these methods, shear wave elastography (SWE) has proved to be a reliable, non-invasive imaging method that allows for the quantitative evaluation of tissue stiffness [2,3].

Similar to other ultrasonic techniques based on acoustic radiation impulses, SWE considered that biological tissues are purely elastic, neglecting viscosity [1]. Nevertheless, biological tissues demonstrate both elastic and viscous proprieties [1,4]. Previous studies, focused mostly on liver pathologies, have shown that ignoring tissue viscosity leads to errors in elasticity measurements and may bias information crucial for diagnostics [1,5,6]. Since dispersion links to the frequency dependence of the speed of shear waves (SW) and the attenuation of SWs, evaluation of the dispersion proprieties of SWs can be used as an indirect method for measuring viscosity [5,7,8].

The foundation of elastography imaging modalities is that pathological conditions like inflammation and tumors alter tissue elasticity and viscosity. These changes are reflected in alterations in the mechanical viscoelastic properties of soft tissues [5].

Viscosity Plane-wave UltraSound (Vi PLUS) 2D imaging performed via the new Aixplorer MACH 30 system (SuperSonic Imagine, Aix-en-Provence, France) represents a 2D imaging mode that provides visualization and quantification of tissue viscosity. The result is a local measurement of the tissue viscosity at each point of interest in an organ, expressed in pascal second (Pa.s) [6,9].

Thyroid stiffness has been extensively studied using elastography methods, including SWE and strain elastography, and has become a commonly used parameter in evaluating thyroid parenchyma in focal and diffuse pathologies [2,3,10,11]. So far, no general reference values for thyroid viscosity have been established. Therefore, the goal of this study was to determine normal reference viscosity and elasticity values for the thyroid gland and to evaluate the influences of age, gender, and body mass index (BMI). A second objective was to establish a correlation between the viscosity values and the values obtained using 2D Shear-Wave Elastography PLUS (2D-SWE.PLUS).

2. Materials and Methods

2.1. Study Population

A total of 85 healthy Caucasian volunteers (56 women and 29 men, median age of 29 years, range 17–81 years) were included in this prospective monocentric study conducted between January 2022 and March 2022 at the Radiology Department, Emergency County Hospital, Cluj-Napoca, Romania. The subjects were selected from patients referred for neck ultrasound for non-thyroid pathologies (sialadenitis, lymphadenopathy, temporomandibular joint disorders, etc.). All the healthy volunteers had normal clinical findings, and normal ultrasound B mode, and color Doppler findings regarding the thyroid gland. Patients with a history of thyroid disorders (autoimmune, inflammatory, or thyroid nodules), thyroid hemiagenesis, or previous exposure to radioiodine therapy were excluded.

This study was approved by the Local Ethics Committee and complied with the World Medical Association Declaration of Helsinki, revised in 2000, Edinburgh. Written consent was obtained from all the subjects before study entry.

2.2. Viscosity and Shear-Wave Ultrasound Technique

Viscosity and stiffness measurements of the thyroid parenchyma were performed via the new SuperSonic MACH® 30 Ultrasound system (Aixplorer, SuperSonic Imagine, Aix-en-Provence, France). This study involved a single researcher with five years of experience in sonography.

Vi PLUS mode analyzes the shear wave propagation speed at various frequencies to provide information about shear wave dispersion within tissues. Acquisitions of viscosity measurements were done concurrently with the stiffness measurements and utilizing the same methodology since the Vi PLUS mode is coupled with the SWE mode and cannot be applied independently.

The subjects were examined in a supine position with the neck extended, facilitated by the position of a small pillow under the shoulders. No patient preparation was needed. An initial assessment of the thyroid parenchyma was performed using a high-frequency linear transducer (SuperLinearTM SL10-2) to evaluate thyroid volume and exclude unknown pathologies.

Thyroid viscosity and stiffness measurements were performed using the curvilinear transducer (C6-1X) in the sagittal plane for each thyroid lobe to avoid motion artifacts produced by the carotid arteries and trachea. First, we obtained an ultrasound B-mode image with the best gain setting. The probe was placed perpendicularly on the skin surface, and an abundant amount of gel was used to avoid precompression. The measurements were taken while the patient was holding his breath, avoiding deep inspiration or the Valsalva maneuver, which can impact the stiffness of the thyroid parenchyma.

The Vi PLUS mode was activated, and a region of interest was placed at about 1.5–2 cm beneath the skin, with the Vi PLUS box positioned over an area of homogeneous parenchyma, free of large vessels or other structures that might interfere with the measurements. A 5 mm diameter Q-Box placed in the center of the Vi PLUS box was used to obtain the measurements after the image had stabilized for 3 s. The quality control standard for image acquisition was represented by the stability index (SI). If the SI was greater than 90% and the standard deviation was less than 10% of the determined mean viscosity value, the measurement was deemed valid (Figure 1). The acquisition was performed for each thyroid lobe three times to obtain three valid viscosity measurements. The three measures were averaged, resulting in a single value used in subsequent analyses.

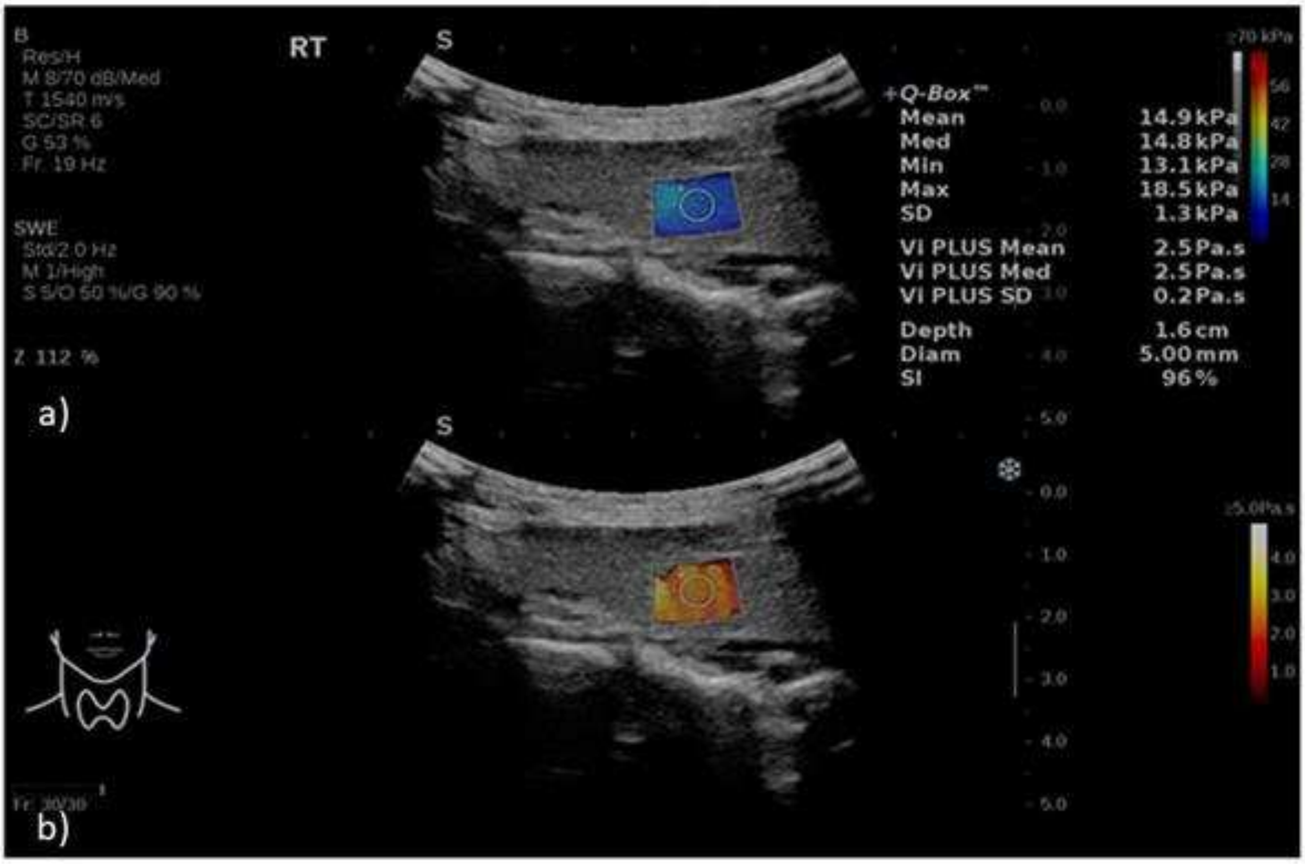

Figure 1. 2D-SWE.PLUS (**a**) and Vi PLUS (**b**) measurements obtained in the right thyroid lobe of a healthy volunteer. Vi PLUS box represents a duplicate of the SWE box and for each parameter, a color scale map is displayed. For the SWE mode (range 0 to 70 kPa), low elasticity is coded in blue and high elasticity is coded in red. On Vi PLUS mode (range 0 to 5 Pa.s), low viscosity is color-coded in red, while high viscosity is depicted in white-yellow colors. Simultaneously, quantitative assessment is displayed on the right side of the image for Vi PLUS (expressed in Pa.s) and for SWE (expressed in kPa).

2.3. Statistical Analysis

The statistical analysis was performed with a dedicated software: MedCalc Version 20 (MedCalc Software 127 Corp., Brunswick, ME, USA). Descriptive statistics were computed—for normally distributed quantitative variables (means and standard deviation) and for non-normal distributed variables (median values and range). Categorical variables were presented as percentages and numbers. One-way analysis of variance (ANOVA) was used to assess the difference between the means of several subgroups. For all the tests, the statistical significance was defined as $p < 0.05$.

3. Results

Demographic statistics for the 85 healthy volunteers included in our study are summarized in Table 1.

Table 1. Demographic characteristics of the study group.

Descriptor	N (%)/Median (Range)
Total no subjects	85
Female	56 (65.9%)
Male	29 (34.1%)
Age (years)	29 (17–81)
BMI groups	
Normal weight range (18.5–24.9)	51
Overweight range (> 25)	33

N = number of subjects; BMI = body mass index.

No significant differences were found between viscosity and stiffness values of the right and left lobes of the thyroid gland in healthy volunteers (p = 0.524; p = 0.910) (Table 2). Consequently, the mean measurements of the right and left thyroid lobes were included in the analysis for each healthy volunteer.

Table 2. Mean viscosity and stiffness values of the right and left thyroid lobes.

		Right Lobe	Left Lobe	
Viscosity (Pa.s)	Mean	2.73	2.64	**p = 0.525**
	SD	1.12	0.54	
	95% CI	2.48–2.97	2.52–2.76	
SWE (kPa)	Mean	**15.88**	**15.80**	**p = 0.911**
	SD	4.24	5.40	
	95% CI	14.95–16.80	14.61–16.98	

SD = Standard deviation, CI = Confidence interval.

The mean viscosity value of normal thyroid parenchyma was 2.63 ± 0.47 Pa.s, and the mean stiffness value was 15.89 ± 4.25 kPa (Table 3).

Table 3. Mean viscosity and stiffness values of thyroid parenchyma in healthy volunteers.

	Viscosity (Pa.s)	SWE (kPa)
Mean± SD	2.63 ± 0.47	15.89 ± 4.25
95% CI	2.52–2.73	14.98–16.81
Min	1.53	6.7
Max	3.95	33.65

SD = Standard deviation, CI = Confidence interval, Min = Minimum, Max = Maximum.

There was no statistically significant difference between mean values of viscosity and stiffness regarding gender groups (p = 0.501; p = 0.655, respectively), (Table 4). No statistically significant difference was found regarding viscosity between age groups (p = 0.958). In the age group between 30–50 years, the SWE values were slightly higher (17.22 ± 5.96) in comparison with the age groups between 17–29 years (15.56 ± 3.84), respectively 51–81 years (15.72 ± 3.73), but did not reach statistical significance as the p value was 0.413 (Table 5).

Table 4. Mean viscosity and stiffness values of the thyroid parenchyma in the healthy volunteers group according to gender.

		Male	Female	
Viscosity (Pa.s)	Mean SD 95% CI	**2.67** 0.59 2.50–2.85	**2.60** 0.39 2.48–2.73	***p* = 0.501**
SWE (kPa)	Mean SD 95% CI	**15.60** 4.23 14.03–17.18	**16.04** 4.29 14.91–17.18	***p* = 0.655**

SD = standard deviation.

Table 5. Mean viscosity and stiffness values of the thyroid parenchyma in healthy volunteers group based on the age distribution.

		Age Group (17–29)	Age Group (30–50)	Age Group (51–81)	
Viscosity (Pa.s)	**Mean** **SD** **95% CI**	**2.63** 0.48 2.49–2.76	**2.65** 0.50 2.41–2.90	**2.60** 0.43 2.40–2.81	***p*= 0.958**
SWE (kPa)	**Mean** **SD** **95% CI**	**15.56** 3.84 14.35–16.77	**17.22** 5.96 15.03–19.41	**15.72** 3.73 13.87–17.57	***p*= 0.413**

SD = Standard deviation, CI = Confidence interval.

There was no statistically significant correlation between BMI and thyroid gland viscosity and stiffness values (r = 0.215, $p = 0.053$; r = 0.106, $p = 0.333$).

The thyroid gland viscosity and stiffness values were significantly lower in the normal weighted volunteers in comparison with overweighted volunteers (2.52 ± 0.44 Pa.s versus 2.79 ± 0.47 Pa.s, $p = 0.009$; 15.12 ± 3.90 kPa versus 17.11 ± 4.55 kPa, $p = 0.035$) (Figure 2, Table 6).

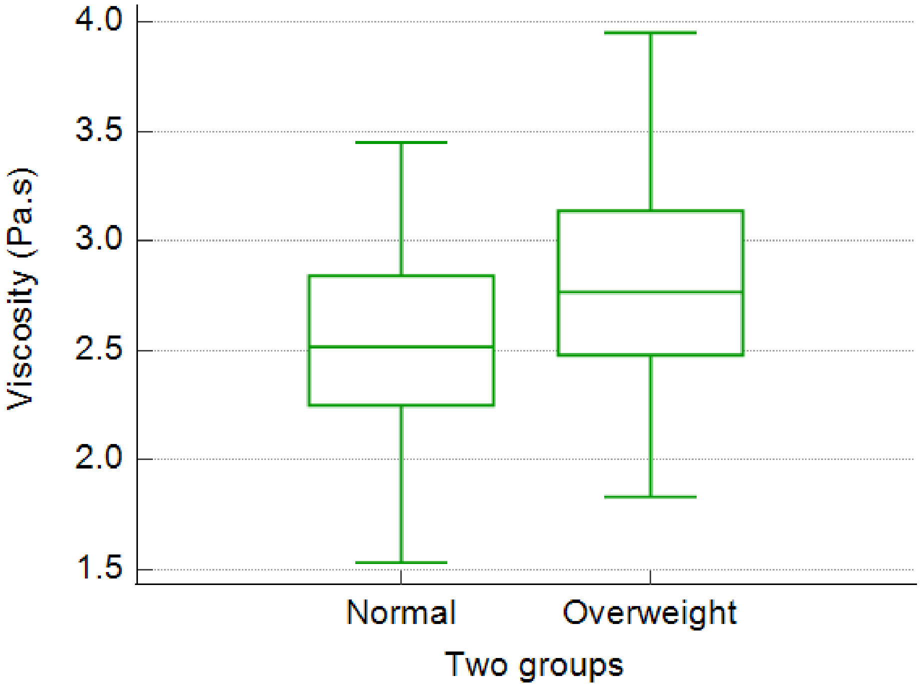

Figure 2. Boxplot diagrams illustrating the differences in mean normal viscosity values of thyroid parenchyma between normal weighted and overweighted groups.

Table 6. Mean viscosity and stiffness values of the thyroid parenchyma in the healthy volunteers group according to BMI.

		Normal Weighted (BMI = 18.5–24.9)	Overweighted (BMI > 25)	
Viscosity (Pa.s)	**Mean**	**2.52**	**2.79**	p **= 0.009**
	SD	0.44	0.47	
	95% CI	2.40–2.65	2.63–2.95	
SWE (kPa)	**Mean**	**15.12**	**17.11**	p **= 0.035**
	SD	3.90	4.55	
	95% CI	13.97–16.27	15.67–18.55	

SD = Standard deviation, CI = Confidence interval, Min = Minimum, Max = Maximum.

A significant positive correlation was found between viscosity values and stiffness values for thyroid parenchyma (r = 0.685; $p < 0.0001$) (Figure 3).

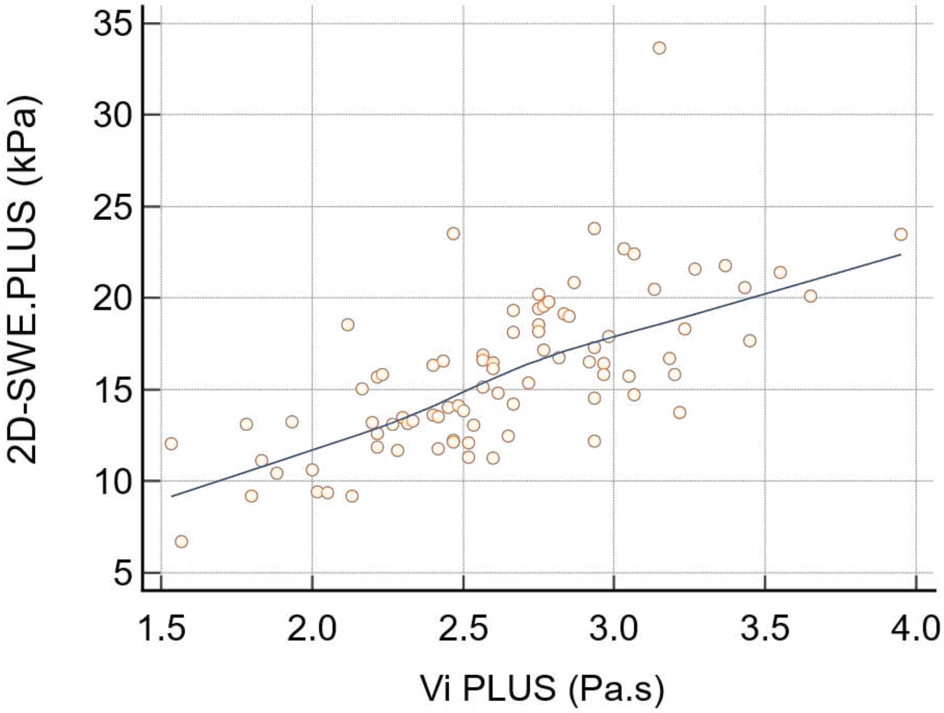

Figure 3. Correlation between the mean viscosity values and stiffness values of thyroid parenchyma in healthy volunteers (blue line—trend line).

4. Discussion

Ultrasound SWE has proved to be a helpful diagnostic tool in differentiating between benign and malignant thyroid nodules, especially when combined with Thyroid Imaging Reporting Data System (TIRADS) and has a significant role in identifying the thyroid nodules that can be followed with imaging techniques, reducing the number of fine needle aspiration (FNA) [3,11–13]. Additionally, previous studies have shown that SWE has the potential to detect changes in patients with diffuse thyroid diseases, such as autoimmune thyroiditis, acute thyroiditis and Riedel thyroiditis [2,10,14]. A study by Fukuhara et al. showed that SWE measurements were significantly higher in patients with chronic autoimmune thyroiditis in comparison with healthy volunteers [15]. However, SWE techniques were focused mostly on evaluating the differences between benign and malignant thyroid nodules, omitting the viscous component of the parenchyma [12].

Vi PLUS is a recent ultrasound technique that allows the quantification of information regarding shear wave dispersion within a tissue [5]. The principles of wave propagation, where the dispersion is characterized as a compound expression of the poroelastic and microstructural media proprieties controlled by the complex fibrous multiscale microstructure of the stroma, give rise to one of the main characteristics of viscoelastic tissues [16]. The viscosity of the environment seems to play an important role, affecting wave phase velocity, which is dependent on frequency, and wave amplitude which is conditioned by geometric factors. These changes are described in a highly viscous environment. Neglecting viscosity leads to bias for the estimation of stiffness, since the effect of wave dispersion is ignored [16].

In a study by Sugimoto et al. [5], alterations in tissue viscosity correlated to the degree of inflammation in patients with liver fibrosis. Thus, dispersion slope, which reflects viscosity, may provide additional pathophysiological insight into diffuse or focal changes in thyroid parenchyma, especially in the differential diagnosis between focal areas of acute inflammation and focal areas of chronic inflammation. Rianna et al. [17] evaluated thyroid viscoelastic proprieties only on experimental models, showing that malignant thyroid cells tend to be constant regarding viscosity and elasticity proprieties, regardless of substrate stiffness. In comparison, normal thyroid cells become more rigid as the substrate stiffness rises, and the dynamic viscosity exhibits a similar pattern.

In light of the existing studies on the liver parenchyma, it seems that the best use of viscosity lies in determining tissue inflammation and not tumors [5,6,18,19]. Therefore, the usefulness of viscosity in the evaluation of the thyroid gland as well might be directed more towards thyroid acute inflammation and not detect or characterize tumors.

To date, only a few studies have evaluated the potential of this recent ultrasound technique. Muntean et al. [9,20] prospectively evaluated the capability of Vi PLUS in establishing reference values for the parotid and submandibular glands in healthy subjects and also evaluated the functional changes in major salivary glands in healthy subjects. Popa et al. [5] studied the role of viscosity using Vi PLUS mode in patients with liver steatosis, fibrosis, and inflammation in patients with non-alcoholic fatty liver disease (NAFLD) and concluded there is an independent association between viscosity values and liver stiffness values.

To the best of our knowledge, no research has been done to ascertain healthy individuals' thyroid gland viscosity measurements so far. Establishing the reference viscosity value of thyroid parenchyma is the first step in verifying this novel approach and it also may facilitate early detection of thyroid abnormalities, especially in diffuse inflammatory pathologies.

In our study, we performed three measurements for each thyroid lobe, similar to the procedure followed by Muntean et al. [9].

No considerable differences were found regarding viscosity and stiffness between the left and the right thyroid lobes, therefore the mean viscosity and stiffness values for thyroid parenchyma in healthy volunteers were considered to be 2.63 ± 0.47 Pa.s, respectively 15.89 ± 4.25 kPa. The mean values for thyroid stiffness were higher in our study compared to the values reported in previous studies [21,22]. Arda et al. [21] found in a prospective study that stiffness values of thyroid range between 1–24 kPa, with a mean stiffness of 10.97 ± 3.1 kPa. One study evaluated thyroid stiffness in the pediatric population and showed that the SWE values are lower (10.9 ± 1.78) in comparison with the adult population [13].

Variability regarding the elasticity of the thyroid parenchyma has been previously reported. It may be related to various technical factors such as vendor-specific implementations of SWE mode and increased compression of the thyroid parenchyma, also known as preload [23]. Another possible explanation could be the fact that we used the curvilinear transducer instead of the linear transducer for measuring the elasticity values, at the time of the study the Vi PLUS mode and SWE mode were available only on this type of transducer.

In our study, viscosity and stiffness were not significantly affected by gender. This is in accordance with previous studies that failed to confirm a correlation between gender and thyroid gland stiffness [21,24].

The age group between 30–50 years included in our study presented a mean thyroid elasticity value slightly higher compared with the younger and older age groups but did not reach statistical significance. This incidental finding might be related to the small number of subjects included in this age group.

The thyroid gland viscosity and stiffness values were higher for the patients with an abnormal body mass index. Herman et al. [24] assessed the stiffness of the neck anatomical structures in a normal population using SWE and found that BMI and weight had no significant influence on thyroid stiffness.

A significant positive correlation was found between viscosity values and SWE values for thyroid parenchyma.

Although the diagnostic capabilities of viscosity in identifying acute inflammatory changes have been proved in previous studies on liver, breast and prostate [16], from the clinical point of view the utility of this new parameter is still questionable due to the risk of overdiagnosis.

Combining viscosity with elasticity could result in a more robust imaging approach that provides a complementary understanding of thyroid alterations, especially in diffuse inflammatory conditions.

There were several limitations in this study. First, we did not assess intra- and interobserver reproducibility, all measurements being performed by a single observer. However, recent studies published by our group [20,25] have shown good intra- and interobserver reproducibility of applying Vi PLUS method in calculating viscosity to other soft tissues with similar depth to thyroid parenchyma. Second, no blood tests were performed to confirm normal thyroid function for the healthy volunteers. Third, this study had a relatively small number of subjects. However, we tried to include patients from all age groups, but there was an imbalance in gender distribution with a predominance of female subjects. Fourth, we used the curvilinear transducer to perform all the measurements, given the fact that the Vi PLUS mode was only available on this type of transducer. Although higher frequency transducers are required to determine parenchymal structural changes, this preliminary study's main goal was to collect quantitative data regarding thyroid viscosity. We used the stability index (SI) greater than 90% to make sure that the image acquisition process was correctly done.

To determine the diagnostic role of this novel technique, further studies with larger series of subjects should be performed to compare the viscosity values of normal and pathologic thyroid tissue.

5. Conclusions

In this preliminary study, we used Vi PLUS mode and SWE mode embedded in the new ultrasound machine to determine the mean viscosity and stiffness values of thyroid parenchyma in healthy volunteers. Vi PLUS could represent an important tool that can provide relevant information in respect of the viscous proprieties of biological tissues and open the gates for a new revolutionary field in ultrasound imaging.

Author Contributions: Conceptualization, D.-R.P.-B. and C.S.; Formal analysis, C.S. and S.M.D.; Investigation, C.S., D.D.M., I.-T.D. and C.A.S.; Methodology, D.-R.P.-B., C.S., D.D.M., I.-T.D., C.A.S. and S.M.D.; Writing—original draft, D.-R.P.-B. and D.D.M.; Writing—review and editing, C.S. and S.M.D. All authors have read and agreed to the published version of the manuscript.

Funding: This research received no external funding.

Institutional Review Board Statement: The study was conducted according to the guidelines of the Declaration of Helsinki, and approved by the Ethics Committee of "Iuliu Hatieganu" University of Medicine and Pharmacy (registration number 106; 3 May 2022).

Informed Consent Statement: Informed consent was obtained from all subjects involved in the study.

Data Availability Statement: The data is available only by request.

Conflicts of Interest: The authors declare no conflict of interest.

References

1. Hossain, M.M.; Gallippi, C.M. Viscoelastic Response Ultrasound Derived Relative Elasticity and Relative Viscosity Reflect True Elasticity and Viscosity: In Silico and Experimental Demonstration. *IEEE Trans. Ultrason. Ferroelectr. Freq. Control* **2020**, *67*, 1102–1117. [CrossRef] [PubMed]
2. Bakırtaş Palabıyık, F.; İnci, E.; Papatya Çakır, E.D.; Hocaoğlu, E. Evaluation of Normal Thyroid Tissue and Autoimmune Thyroiditis in Children Using Shear Wave Elastography. *J. Clin. Res. Pediatr. Endocrinol.* **2019**, *11*, 132–139. [CrossRef] [PubMed]
3. Petersen, M.; Schenke, S.A.; Firla, J.; Croner, R.S.; Kreissl, M.C. Shear Wave Elastography and Thyroid Imaging Reporting and Data System (TIRADS) for the Risk Stratification of Thyroid Nodules-Results of a Prospective Study. *Diagnostics* **2022**, *12*, 109. [CrossRef]
4. Bamber, J.; Cosgrove, D.; Dietrich, C.F.; Fromageau, J.; Bojunga, J.; Calliada, F.; Cantisani, V.; Correas, J.M.; D'Onofrio, M.; Drakonaki, E.E.; et al. EFSUMB guidelines and recommendations on the clinical use of ultrasound elastography. Part 1: Basic principles and technology. *Ultraschall Med.* **2013**, *34*, 169–184. [CrossRef]
5. Sugimoto, K.; Moriyasu, F.; Oshiro, H.; Takeuchi, H.; Yoshimasu, Y.; Kasai, Y.; Furuichi, Y.; Itoi, T. Viscoelasticity Measurement in Rat Livers Using Shear-Wave US Elastography. *Ultrasound Med. Biol.* **2018**, *44*, 2018–2024. [CrossRef] [PubMed]
6. Popa, A.; Bende, F.; Șirli, R.; Popescu, A.; Bâldea, V.; Lupușoru, R.; Cotrău, R.; Fofiu, R.; Foncea, C.; Sporea, I. Quantification of Liver Fibrosis, Steatosis, and Viscosity Using Multiparametric Ultrasound in Patients with Non-Alcoholic Liver Disease: A "Real-Life" Cohort Study. *Diagnostics* **2021**, *11*, 783. [CrossRef] [PubMed]
7. Chen, X.; Wang, Y.; Lu, J.; Li, P. Simultaneous viscosity and elasticity measurement using laser speckle contrast imaging. *Opt. Lett.* **2018**, *43*, 1582–1585. [CrossRef]
8. Zhu, Y.; Dong, C.; Yin, Y.; Chen, X.; Guo, Y.; Zheng, Y.; Shen, Y.; Wang, T.; Zhang, X.; Chen, S. The role of viscosity estimation for oil-in-gelatin phantom in shear wave based ultrasound elastography. *Ultrasound Med. Biol.* **2015**, *41*, 601–609. [CrossRef]
9. Muntean, D.; Lenghel, M.; Ciurea, A.; Dudea, S. Viscosity Plane-wave UltraSound (ViPLUS) in the assessment of parotid and submandibular glands in healthy subjects—Preliminary results. *Med. Ultrason.* **2022**, *24*, 300–304. [CrossRef]
10. Kara, T.; Ateş, F.; Durmaz, M.S.; Akyürek, N.; Durmaz, F.G.; Özbakır, B.; Öztürk, M. Assessment of thyroid gland elasticity with shear-wave elastography in Hashimoto's thyroiditis patients. *J. Ultrasound* **2020**, *23*, 543–551. [CrossRef]
11. Liu, Z.; Jing, H.; Han, X.; Shao, H.; Sun, Y.X.; Wang, Q.C.; Cheng, W. Shear wave elastography combined with the thyroid imaging reporting and data system for malignancy risk stratification in thyroid nodules. *Oncotarget* **2017**, *8*, 43406–43416. [CrossRef]
12. Săftoiu, A.; Gilja, O.H.; Sidhu, P.S.; Dietrich, C.F.; Cantisani, V.; Amy, D.; Bachmann-Nielsen, M.; Bob, F.; Bojunga, J.; Brock, M.; et al. The EFSUMB Guidelines and Recommendations for the Clinical Practice of Elastography in Non-Hepatic Applications: Update 2018. *Ultraschall Med.* **2019**, *40*, 425–453. [CrossRef]
13. Hazem, M.; Al Jabr, I.K.; AlYahya, A.A.; Hassanein, A.G.; Algahlan, H.A.E. Reliability of shear wave elastography in the evaluation of diffuse thyroid diseases in children and adolescents. *Eur. J. Radiol.* **2021**, *143*, 109942. [CrossRef]
14. Zhao, C.K.; Xu, H.X. Ultrasound elastography of the thyroid: Principles and current status. *Ultrasonography* **2019**, *38*, 106–124. [CrossRef]
15. Fukuhara, T.; Matsuda, E.; Izawa, S.; Fujiwara, K.; Kitano, H. Utility of Shear Wave Elastography for Diagnosing Chronic Autoimmune Thyroiditis. *J. Thyroid Res.* **2015**, *2015*, 164548. [CrossRef]
16. Rus, G.; Faris, I.H.; Torres, J.; Callejas, A.; Melchor, J. Why Are Viscosity and Nonlinearity Bound to Make an Impact in Clinical Elastographic Diagnosis? *Sensors* **2020**, *20*, 2379. [CrossRef]
17. Rianna, C.; Radmacher, M. Comparison of viscoelastic properties of cancer and normal thyroid cells on different stiffness substrates. *Eur. Biophys. J.* **2017**, *46*, 309–324. [CrossRef]
18. Sugimoto, K.; Moriyasu, F.; Oshiro, H.; Takeuchi, H.; Yoshimasu, Y.; Kasai, Y.; Itoi, T. Clinical utilization of shear wave dispersion imaging in diffuse liver disease. *Ultrasonography* **2020**, *39*, 3–10. [CrossRef]
19. Deffieux, T.; Gennisson, J.L.; Bousquet, L.; Corouge, M.; Cosconea, S.; Amroun, D.; Tripon, S.; Terris, B.; Mallet, V.; Sogni, P.; et al. Investigating liver stiffness and viscosity for fibrosis, steatosis and activity staging using shear wave elastography. *J. Hepatol.* **2015**, *62*, 317–324. [CrossRef]
20. Muntean, D.D.; Lenghel, M.L.; Petea-Balea, D.R.; Ciurea, A.I.; Solomon, C.; Dudea, S.M. Functional Evaluation of Major Salivary Glands Using Viscosity PLUS and 2D Shear-Wave PLUS Elastography Techniques in Healthy Subjects-A Pilot Study. *Diagnostics* **2022**, *12*, 1963. [CrossRef]
21. Arda, K.; Ciledag, N.; Aktas, E.; Aribas, B.K.; Köse, K. Quantitative assessment of normal soft-tissue elasticity using shear-wave ultrasound elastography. *AJR Am. J. Roentgenol.* **2011**, *197*, 532–536. [CrossRef]
22. Ferraioli, G.; Barr, R.G.; Farrokh, A.; Radzina, M.; Cui, X.W.; Dong, Y.; Rocher, L.; Cantisani, V.; Polito, E.; D'Onofrio, M.; et al. How to perform shear wave elastography. Part I. *Med. Ultrason.* **2022**, *24*, 95–106. [CrossRef]
23. Ozturk, A.; Zubajlo, R.E.; Dhyani, M.; Grajo, J.R.; Mercaldo, N.; Anthony, B.W.; Samir, A.E. Variation of Shear Wave Elastography with Preload in the Thyroid: Quantitative Validation. *J. Ultrasound Med.* **2021**, *40*, 779–786. [CrossRef]
24. Herman, J.; Sedlackova, Z.; Vachutka, J.; Furst, T.; Salzman, R.; Vomacka, J. Shear wave elastography parameters of normal soft tissues of the neck. *Biomed. Pap. Med. Fac. Univ. Palacky Olomouc Czech Repub.* **2017**, *161*, 320–325. [CrossRef]
25. Dulgheriu, I.T.; Solomon, C.; Muntean, D.D.; Petea-Balea, R.; Lenghel, M.; Ciurea, A.I.; Dudea, S.M. Shear-Wave Elastography and Viscosity PLUS for the Assessment of Peripheric Muscles in Healthy Subjects: A Pre- and Post-Contraction Study. *Diagnostics* **2022**, *12*, 2138. [CrossRef]

diagnostics

IMPACT FACTOR 3.0
Indexed in: PubMed
CITESCORE 4.7

Article

Shear-Wave Elastography and Viscosity PLUS for the Assessment of Peripheric Muscles in Healthy Subjects: A Pre- and Post-Contraction Study

Ioana-Teofana Dulgheriu, Carolina Solomon, Delia Doris Muntean, Raluca Petea-Balea,
Manuela Lenghel, Anca Ileana Ciurea and Sorin Marian Dudea

MDPI

https://doi.org/10.3390/diagnostics12092138

diagnostics

MDPI

Article

Shear-Wave Elastography and Viscosity PLUS for the Assessment of Peripheric Muscles in Healthy Subjects: A Pre- and Post-Contraction Study

Ioana-Teofana Dulgheriu , Carolina Solomon *, Delia Doris Muntean, Raluca Petea-Balea, Manuela Lenghel, Anca Ileana Ciurea and Sorin Marian Dudea

Department of Radiology, "Iuliu Hatieganu" University of Medicine and Pharmacy,
400012 Cluj-Napoca, Romania
* Correspondence: carolinasolomon12@gmail.com

Abstract: Viscosity is a novel parameter, recently introduced in the use of elastographic techniques, correlating to shear-wave dispersion. The purpose of this study was to provide normal reference viscosity values for the peripheral muscles in healthy volunteers. This prospective study included 38 subjects who underwent US examinations between November 2021 and January 2022. Measurements were taken on the calf and the deltoid muscles in both pre- and post-contraction states. The age range was 21–29 years, with a median of 26 years. The SWE and ViPLUS values in the deltoid muscles were significantly higher than in the soleus muscles in both pre- and post-contraction sets ($p = 0.002$). There were statistically significant differences between the pre- and post-contraction values for both the SWE and ViPLUS values in the subgroup analysis. The ICC estimates and the 95% confidence intervals were based on a mean rating ($k = 2$), an absolute agreement, and a two-way random-effects model, demonstrating excellent agreement between the measurements taken by the two examiners.

Keywords: musculoskeletal ultrasound; elastography; viscoelasticity; ViPLUS; novel techniques

check for updates

Citation: Dulgheriu, I.-T.; Solomon, C.; Muntean, D.D.; Petea-Balea, R.; Lenghel, M.; Ciurea, A.I.; Dudea, S.M. Shear-Wave Elastography and Viscosity PLUS for the Assessment of Peripheric Muscles in Healthy Subjects: A Pre- and Post-Contraction Study. *Diagnostics* **2022**, *12*, 2138. https://doi.org/10.3390/diagnostics12092138

Academic Editor: Giorgio Treglia

Received: 22 July 2022
Accepted: 30 August 2022
Published: 2 September 2022

1. Introduction

Elastography is a novel, non-invasive ultrasound application used to assess tissue stiffness. The values obtained can be qualitative or quantitative, differing in the underlying physical mechanism and further dividing the method into the following two categories: strain elastography and shear-wave elastography (SWE). Shear-wave velocities are measured after the propagation of high-frequency acoustic pulses in a transverse direction from the transducer [1]. The general principle is that shear waves move faster through more rigid tissues. The tissue rigidity is expressed in absolute values, meters per second (m/s), or calculated using the Young's modulus in kilopascals (kPa). In order to calculate Young's modulus, the machine assumes that the tissue density is linear, constant, and isotropic [2]. However, soft tissues are nonlinear, heterogeneous, anisotropic, and viscoelastic. Viscosity is an ignored parameter in the current use of elastographic techniques. Viscosity correlates to the shear-wave dispersion [3]. Various methods have been developed to assess the tissue viscoelastic properties by measuring the shear-wave dispersion and attenuation, especially in dedicated phantom models or in the liver [4–9].

Anisotropy is a well-known property of skeletal muscles that depends on the angle of insonation of the incident ultrasound beam. Additionally, the skeletal muscle tissue is a viscous material, and this feature has an effect on the mechanics of passive muscle extensions. The behavior of viscoelastic materials under uniaxial loading has been long represented by different conceptual models, known as rheological or mechanical models, such as the Maxwell model or the Voigt model [10]. Adding viscosity to the medium will also affect the tissue stiffness measured as an effect of dispersion. Isotropy and homogeneity assumptions can also be broken at tissue interfaces, where wave reflection can cause erroneous measurements. As Van Loocke et al. [11] and Wheatley et al. [12] showed in their proposed constitutive models, the viscoelastic component plays an important role in muscle mechanics. The elastic behavior of muscles is nonlinear and transversely isotropic, with the stiffest direction in the fiber direction [11]. Chen et al. [13] presented a model to measure viscosity using ultrasound radiation force to generate cylindrical shear waves of certain frequencies in dedicated phantoms. As Romano et al. [14] correctly observed, there are numerous protocols and general factors that prevent the standardization of the muscle SWE measurements.

Many manufacturers have developed elastography techniques for their machines, but no consensus concerning the measurements and cut-offs exists. A great range of normal SWE values are reported but without clear reference values.

Studies on muscle elastography suggest that this technique can provide important information on the mechanical properties of muscles and detect particular changes in different pathologies [15–17]. Elastography can quantify alterations related to inflammation, degeneration, injury, healing, and treatment response [1,18].

The EFSUMB Guidelines and Recommendations mention an increase in the number of studies using musculoskeletal elastography and recommend it as an alternative to electromyography in neurologic disorders or as a complementary method in the diagnosis and surveillance of inflammatory myopathies [19]. There are also studies that show statistically significant differences in the values of contracted muscles compared to their relaxed state [16]. A few studies exist on the viscoelastic properties of muscles [20–22].

The purpose of this study was to provide normal reference viscosity values for the peripheral muscles in healthy volunteers. The primary objective was to assess the existence of different viscosity values in muscles in pre- and post-contraction states. The secondary objective was to compare the SWE and the Viscosity Plane-Wave Ultrasound (ViPLUS) values in order to evaluate the correlation between the two methods and to analyze the inter-observer variability of the values on the same machine. To the best of our knowledge, the present study is the first to attempt to provide normal muscle reference viscosity values.

2. Materials and Methods

A prospective, monocentric study was performed between November 2021 and January 2022. The study comprised 38 healthy and young volunteers, with no known muscular pathologies. Subjects with neuromuscular diseases or musculoskeletal injuries were excluded. The images were obtained on an Aixplorer MACH® ultrasound machine (Supersonic Imagine, Aix-en-Provence, France) with a curvilinear transducer model C6-1X using a B-mode ultrasound, SWE elastography, and ViPLUS. The imaging parameters were as follows: maximum transducer frequency available; optimization, resolution; persistence, medium; color box, minimum dimensions available; ROI diameter, 5 mm; depth, 2 cm. The transducer used was the only one with a ViPLUS mode available.

2.1. Image Acquisition

Two examiners with five and four years of experience in ultrasound, respectively, performed the measurements for each subject on the same day with a 15-min pause between the measurement sets. The subjects were instructed to refrain from performing physical activity for 24 h prior to the examination. Before the examination, the subjects were asked to rest for 30 min and adjust to the room temperature. Measurements were made on the right calf (soleus) and the right deltoid muscles of each volunteer. For the deltoid muscle, a relaxing position was defined as a flexed elbow and the arm resting on a pillow. For the calf measurements, the subjects were laid in a prone position with their knees fully extended. Firstly, the transducer was oriented parallel to the longitudinal axis of the muscle fibers and an optimal B-mode image was obtained. Then, the SWE and ViPLUS modes were activated with minimum compression used, avoiding vessels and interfascial planes. The locations that achieved less than a 90% stability index (SI) or more than a 10% standard deviation were rejected. The acquisition depths were set at 2 to 2.5 cm from the skin surface for the deltoid and at 3–4 cm from the skin in the midportion of the muscle belly for the soleus muscles. The elastographic color box was adjusted to the minimum dimensions available and placed in the center of the image with the regions of interest (ROIs) in the center. Following the stabilization of the hand, the probe, and the image for 3–5 s, the values were measured as follows: three measurements in a neutral position with relaxed muscles and three measurements after 30 s of sustained continuous contractions. To obtain a homogenous, reproducible contraction in all subjects, the contraction was obtained by holding a 3-kg dumbbell weight in a 90-degree horizontal position for the deltoid muscle (as shown in Figure 1) and by pointing the toes forward whilst resisting an elastic band and holding the tension, for the calf muscles (Figure 2). The SWE measurements were expressed in kilopascals (kPa) as a mean and standard deviation (SD). The ViPLUS mode provides a color-coded map and a quantitative expression of the values in pascal-seconds (Pa.s) as a mean, median, minimum, maximum, and SD. Underneath these values, the depth of the Qbox, the ROI diameter, and the SI are shown. The mean values of the consecutive measurements obtained were used to assess the muscle rigidity and viscosity.

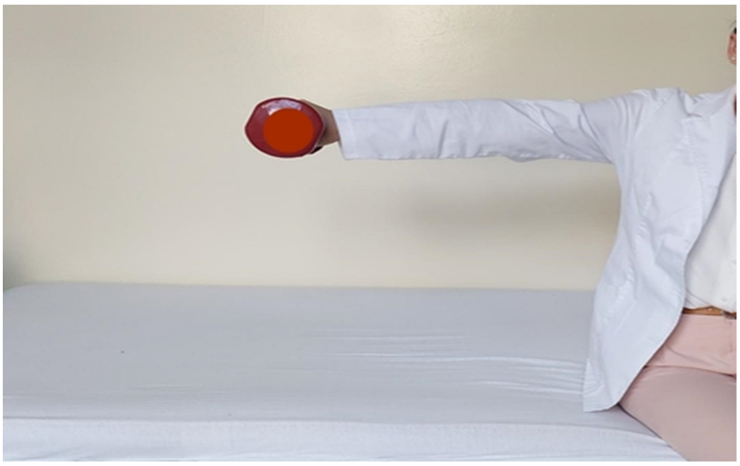

Figure 1. Sustained (30-s) deltoid contraction obtained by holding a 3-kg dumbbell weight.

Figure 2. Sustained (30-s) calf muscle contraction obtained by pointing the toes forward, resisting the elastic band, and holding the tension.

2.2. Statistical Analysis

The statistical analysis was conducted with the MedCalc Statistical Software version 20 (MedCalc Software Corp., Brunswick, ME, USA) and the GraphPad Prism v. 8.0.1 for Windows (GraphPad Software, San Diego, CA, USA) at a significance level of 5%.

The Kolmogorov–Smirnov and Shapiro–Wilk tests were used to evaluate the normality of the data. The normally distributed quantitative data were presented as a mean ± standard deviation (SD). The non-normally distributed data were presented as a median and range. A paired t-test was used to assess for differences in the means between the subgroups. The Wilcoxon matched-pairs signed-rank test was used for the non-normally distributed data. The relationship between the SWE data and the ViPLUS was investigated using the Pearson's correlation coefficient, and the Spearman rank correlation was used for the non-normal distribution. The size of the correlation was interpreted as very low (<0.19), low (0.2–0.39), moderate (0.4–0.59), high (0.6–0.79), and very high (0.8–1.0). A one-way analysis of variance (ANOVA) was performed to compare the effects of sex or body mass index (BMI) on the SWE and ViPLUS measurements.

The reproducibility was assessed by determining the ICCs (Intraclass Correlation Coefficients) as follows: a low level of agreement is close to 0, and a high level of agreement tends to be 1. ICC values of $\geq$0.9 indicate excellent reliability; values between 0.75 and 0.9 indicate good reliability; values between 0.5 and 0.75 indicate moderate reliability; values less than 0.5 are indicative of poor reliability.

3. Results

Thirty-eight healthy subjects were studied (30 women and 8 men; age range = 21–29 years; median = 26 years). The median BMI was 20.98 (ranging from 17.85 to 34.88). The main demographic characteristics are presented in Table 1. A one-way ANOVA revealed that there were no statistically significant differences in the SWE and ViPLUS measurements related to gender (p = 0.518). Figures 3 and 4 show examples of the measurements in different subjects with all of the parameters described accordingly.

Table 1. Descriptive statistics of subjects' demographics.

Variables	All Samples (n = 38) Median Range (Min–Max)	Male (n = 8) Median Range (Min–Max)	Female (n = 30) Median Range (Min–Max)
Age (years)	26 (21–29)	24 (21–28)	27 (21–29)
BMI (kg/m^2)	20.98 (17.85–34.88)	25.78 (19.5–34.88)	20.5 (17.8–27.5)

Abbreviations: BMI, body mass index; n, total number of subjects; median range expressed as minimum–maximum values.

Table 2 provides the muscle measurements in both the pre- and post-contraction sets. The SWE and ViPLUS values in the deltoid muscles were significantly higher than in the soleus muscles in both the pre- and post-contraction sets (p = 0.002). The same trend was observed for the ViPLUS values, as shown in Figure 5.

Table 2. Descriptive statistics of muscle mechanical properties.

Variables	Deltoid (Precontraction) Mean ± SD 95% CI of Mean	Deltoid (Postcontraction) Mean ± SD 95% CI of Mean	Soleus (Precontraction) Mean ± SD 95% CI of Mean	Soleus (Postcontraction) Mean ± SD Median (Range) 95% CI of Mean 25–75% Percentile
SWE (kPa/s)	22.2 ± 4.4 [21.2–23.2]	24.9 ± 5.3 [23.6–26.1]	13.1 ± 4.7 [12–14.1]	14.2 (4.2–31.7) [25% 11.3–75% 18.5]
ViPLUS (Pa.s)	2.9 ± 0.5 [2.8–3]	3.1 ± 0.5 [3–3.2]	2.1 ± 0.5 [1.9–2.2]	2.4 ± 0.6 [2.3–2.6]

Abbreviations: SWE, Shear-Wave Elastography; kPa/s, kiloPascal/second; ViPLUS, Viscosity Plane-Wave Ultrasound; Pa.s, Pascal.second; SD, Standard Deviation, CI, Confidence Interval.

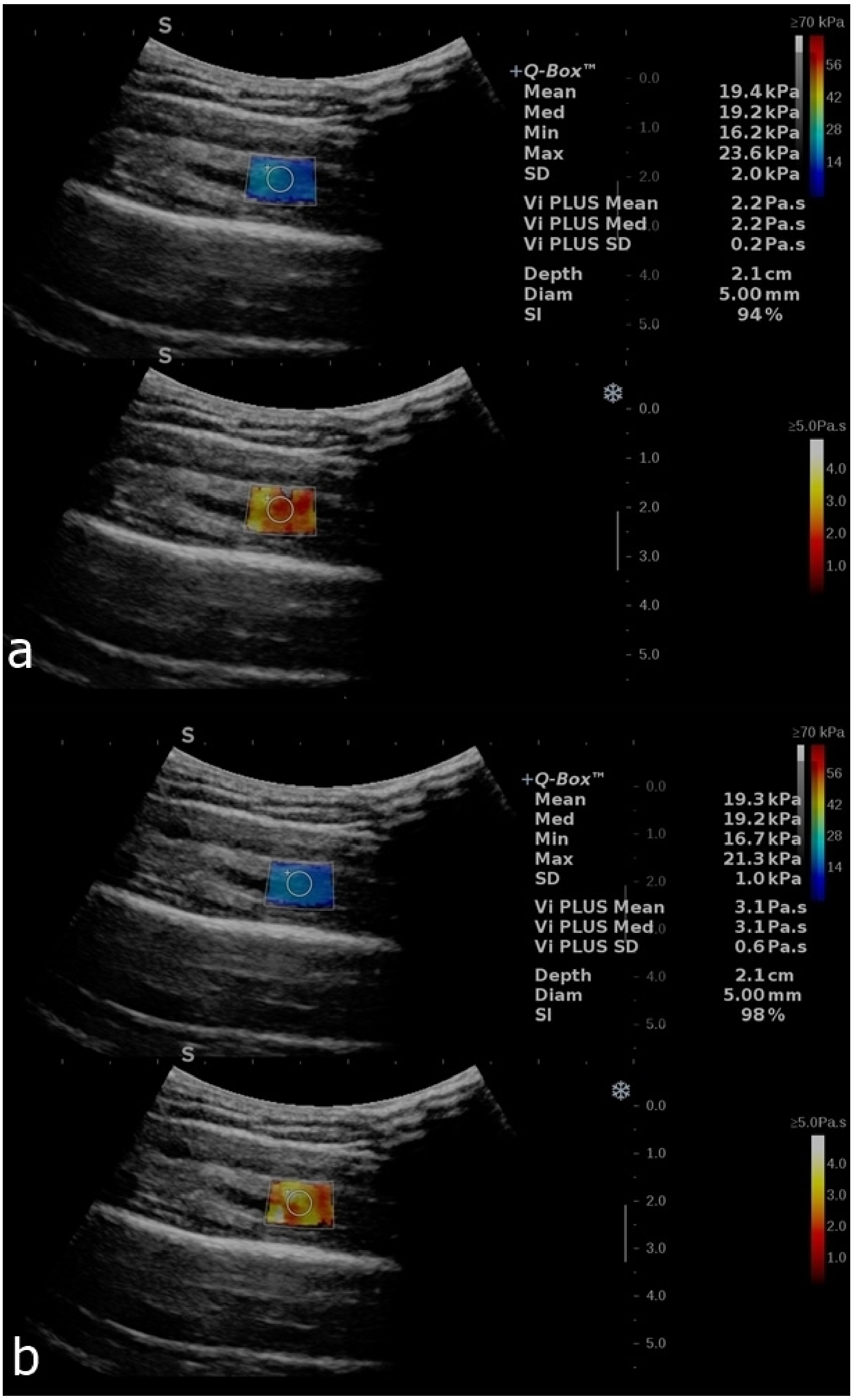

Figure 3. B-mode image with an elastogram of the deltoid muscle in a healthy volunteer. Longitudinal plans of the deltoid muscle as follows: relaxed (**a**) and after contraction (**b**). The regions of interest (ROIs) were placed in the box when the homogenous coloring of the box was obtained with a stability index of over 90%. The top image in each set reflects the SWE mode, and the bottom image reflects the ViPLUS application. ROI values are expressed in kPa for SWE and Pa.s for ViPLUS.

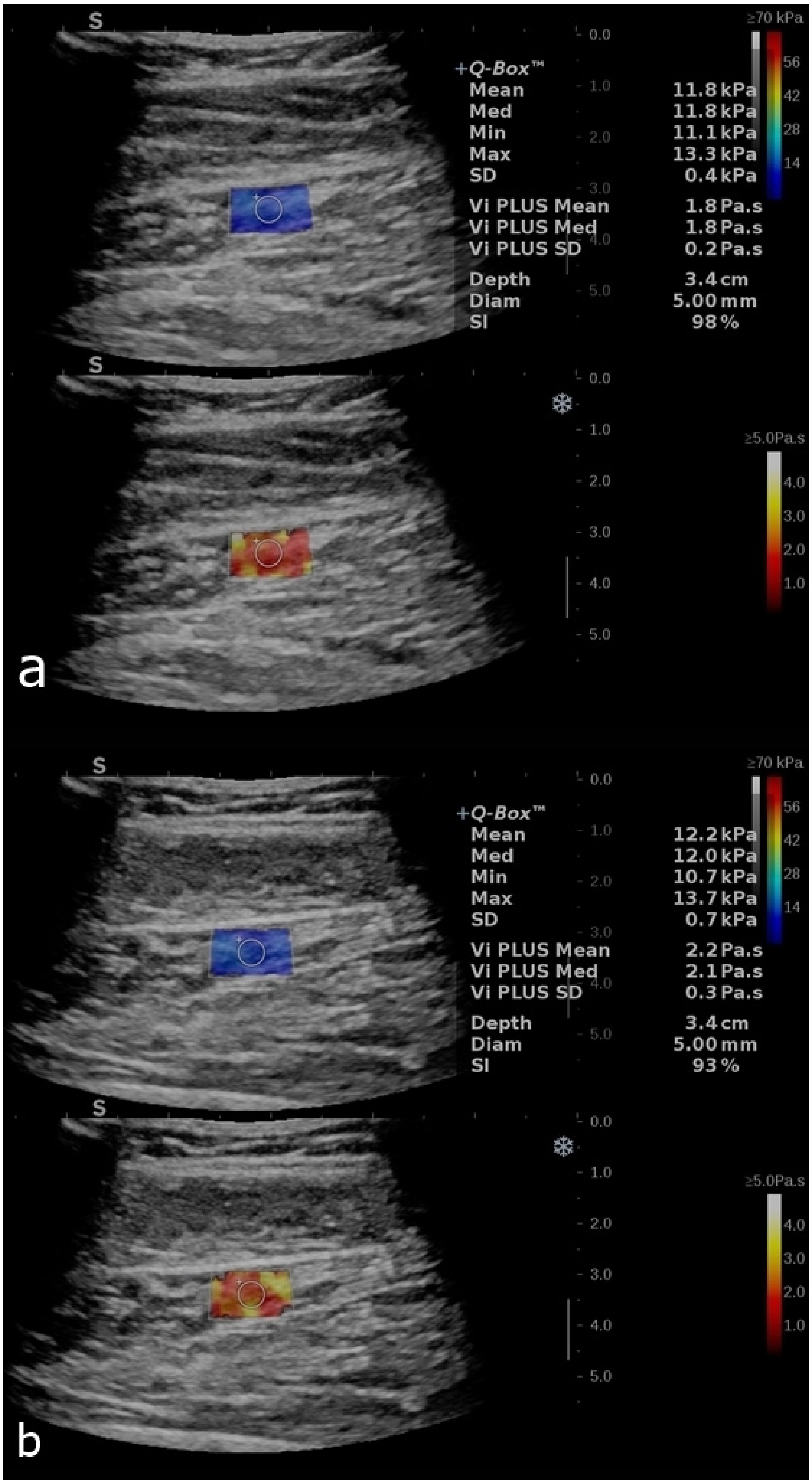

+Q-Box™
Mean 11.8 kPa
Med 11.8 kPa
Min 11.1 kPa
Max 13.3 kPa
SD 0.4 kPa
Vi PLUS Mean 1.8 Pa.s
Vi PLUS Med 1.8 Pa.s
Vi PLUS SD 0.2 Pa.s
Depth 3.4 cm
Diam 5.00 mm
SI 98 %

+Q-Box™
Mean 12.2 kPa
Med 12.0 kPa
Min 10.7 kPa
Max 13.7 kPa
SD 0.7 kPa
Vi PLUS Mean 2.2 Pa.s
Vi PLUS Med 2.1 Pa.s
Vi PLUS SD 0.3 Pa.s
Depth 3.4 cm
Diam 5.00 mm
SI 93 %

Figure 4. B-mode image with an elastogram of the calf muscle in a healthy volunteer. Longitudinal plans of the calf muscles as follows: relaxed (**a**) and after contraction (**b**). The regions of interest (ROIs) were placed in the box when the homogenous coloring of the box was obtained with a stability index of over 90%. The top image reflects the SWE mode, and the bottom image reflects the ViPLUS application. ROI values are expressed in kPa for SWE and Pa.s for ViPLUS.

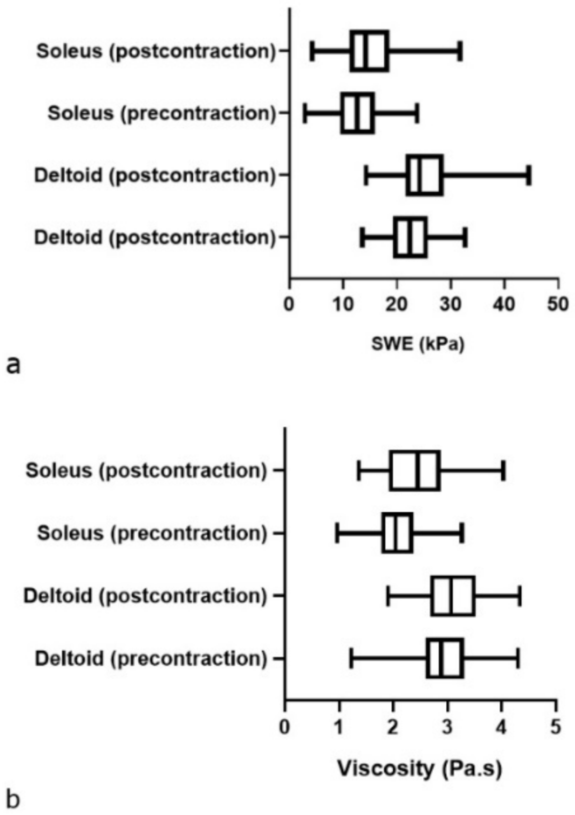

Figure 5. Boxplot showing the tissue elasticity (**a**) and viscosity (**b**) of the deltoid and soleus muscles measured in the longitudinal plane before and after contraction. $p < 0.05$, a significant difference between the two sets of measurements.

There were statistically significant differences between the pre- and post-contraction values in both the SWE and ViPLUS in the subgroup analysis, shown in Table 3.

Table 3. Paired group comparisons of elastographic and viscosity values between the pre- and post-contraction.

Variables	**Deltoid SWE Comparison Pre/Post Contraction Paired *t*-Test**	**Deltoid ViPLUS Comparison Pre/Post Contraction PAIRED *t*-Test**	**Soleus SWE Comparison Pre/Post Contraction Wilcoxon Matched-Pairs Signed-Rank Test**	**Soleus ViPLUS Comparison Pre/Post Contraction Paired *t*-Test**
t,df	4.72, 75	2.56, 75		4.48, 75
* *p* value (two-tailed)	**<0.0001**	**0.0124**	**0.0003**	**<0.0001**
r (correlation coefficient), *p* value (one tailed)	0.5, <0.0001	0.4, 0.0006	0.6, <0.0001	0.3, 0.0147

Abbreviations: SWE, Shear-Wave Elastography; ViPLUS, Viscosity Plane-Wave Ultrasound; *t*, *t*-value of the paired *t*-test; df, degrees of freedom. * *p* value is significant at <0.05 level.

There was a moderate to high correlation between the SWE and ViPLUS values in all subgroups, shown in Table 4 and Figure 6.

Table 4. Multiple correlations between the elastography and viscosity values.

Correlation Coefficient [95% Confidence Interval] Significance Level *p* * (Two-Tailed)	**Deltoid ViPLUS Precontraction**	**Deltoid ViPLUS Postcontraction**	**Soleus ViPLUS Precontraction**	**Soleus ViPLUS Post-Contraction**
Deltoid SWE precontraction	Pearson r = 0.48 [95% CI 0.28–0.63] $p < 0.0001$			
Deltoid SWE postcontraction		Pearson r = 0.57 [95% CI 0.4–0.7] $p < 0.0001$		
Soleus SWE precontraction			Pearson r = 0.63 [95% 0.48 = 0.75], $p < 0.0001$	
Soleus SWE postcontraction				Spearman r = 0.75 [95% 0.63–0.83], $p < 0.0001$

Abbreviations: SWE, Shear-Wave Elastography; ViPLUS, Viscosity Plane-Wave Ultrasound; CI, Confidence Interval; r, Pearson/Spearman correlation coefficient; * *p* value is significant at <0.05 level.

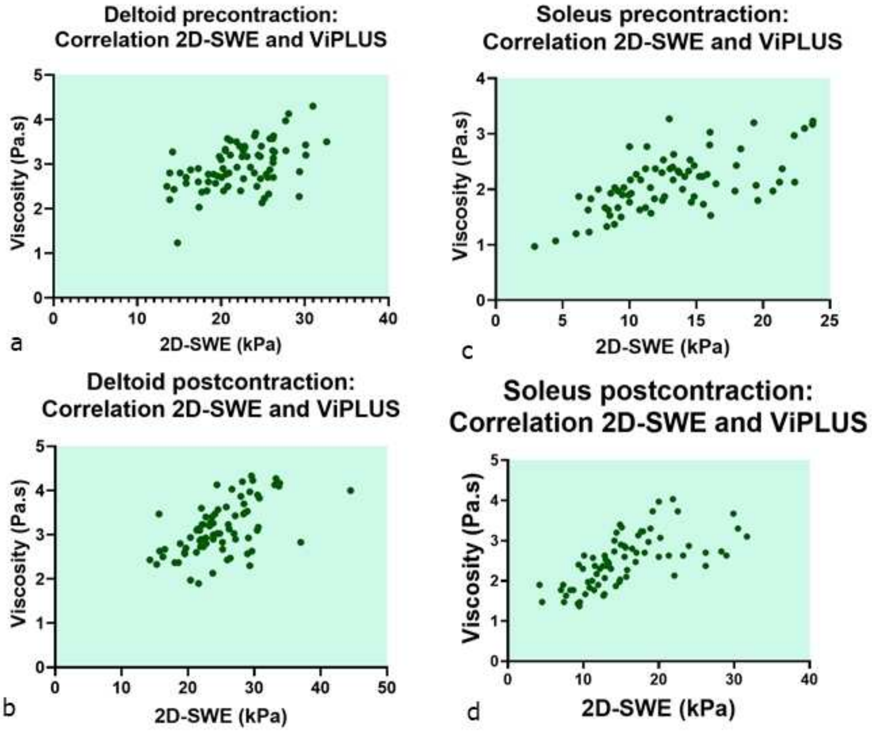

Figure 6. Scatter plot observing the relationship between the elastographic and viscosity data in both muscle groups in pre- (**a**,**c**) and post-contraction (**b**,**d**), showing a moderate to high positive correlation.

The ICC estimates and the 95% confidence intervals were based on a mean rating (k = 2), an absolute agreement, and a two-way random-effects model, as shown in Table 5, demonstrating excellent agreement between the measurements taken by the two examiners.

Table 5. Results of the ICC calculations using a mean of two raters, an absolute agreement, and a two-way random-effects model [23].

Intraclass Correlation Coefficient							
	Intraclass Correlation [b]	95% Confidence Interval		F Test with True Value 0			
		Lower Bound	Upper Bound	Value	df1	df2	Sig
Single Measures	0.912 [a]	0.891	0.929	21.671	303	303	0.000
Average Measures	0.954	0.942	0.963	21.671	303	303	0.000

Abbreviations: df, degrees of freedom; Sig, significance. A two-way random-effects model where both the people and the measured effects are random. [a]. The estimator is the same, whether the interaction effect is present or not. [b]. Type A intraclass correlation coefficients using an absolute agreement definition.

4. Discussion

The purpose of the present study was to provide normal reference viscosity values for two different muscle groups in a relaxed and post-contraction status (Table 2). We also measured the normal SWE values, which are close to the values obtained in the literature. For example, for the relaxed soleus muscles, our mean value was 13.1 ± 4.7 kPa. Akkoc et al. [24] obtained a value of 13.4 ± 3.5 kPa and Ferraioli et al. [25] obtained a value of 14.5 kPa.

Our primary objective was met; we found statistically significant differences in the subgroup analysis between the pre- and post-contraction sets. We also found higher values in the deltoid muscle compared to the soleus muscle in both the ViPLUS and the SWE values (Table 3; Figure 5). The boxplot in Figure 5 provides a visual summary of the data, easily identifying the mean values, the dispersion of the sets, and the occasional skewness. In the viscosity boxplot for the soleus group, the median line in the post-contraction group lies outside of the pre-contraction box, showing a likely difference between the two groups. In all of the other boxes, the median line does not lie outside of the comparison box but corresponds to a statistically significant different value in each case. The box lengths (the interquartile ranges) tend to vary more in the viscosity boxplot, suggesting more dispersed data.

Muscle stretching could be an explanation for the increase in muscle stiffness. Our results support other published observations in the literature, which show an increase in stiffness in post-exercise values compared with the pre-exercise values [16]. Nakamura et al. [26] observed that stretching for more than 2 min decreases muscle stiffness. In our study, the second set of measurements was taken immediately after a 30-s contraction. Gennisson et al. [20] assessed the anisotropic nature of the muscles by using SWE during muscle contractions, as well as in a passive extension. Chen et al. [13] presented a model to measure viscosity using an ultrasound radiation force but observed that tissue inhomogeneity can cause a reflection of the shear waves and, consequently, imprecise measurements. Studies [27] performed on the active stretching of the muscles have shown a linear increase between the SWE measurements and the progressive contractions. The same principle was observed in our study, with statistically significant greater values in both the SWE and ViPLUS modes. The reliability appears to be higher for superficial muscles in comparison to deeper muscles as the attenuation of the acoustic pulses and tracking waves increases at greater depths [14].

The ViPLUS modulus provided by the Aixplorer MACH 30 system analyzes the shear-wave propagation speed in order to give information concerning shear-wave dispersion in the tissues. Concerning our secondary objective, the relationship between the elastographic and viscosity data showed a positive moderate to high correlation (Figure 6).

Previous studies have indicated that the shear-wave velocity is sensitive to the probe position with respect to the direction of the fascicle plane. In a study of reproducibility of

SWE values on the gastrocnemius medialis and tibialis anterior, Cortez et al. [28] demonstrated a fair-to-excellent interoperator reliability for measurements in the longitudinal plane, but a poor one for the transverse ones. The shear modulus in the longitudinal direction has been shown to be linearly related to passive and active muscle forces [29]. Romano et al. [14] described two protocols, one in a routine clinical setting and a dedicated protocol aiming for low muscle extension with statically significant lower variability, indicating the importance of precise member positioning in relaxed states. Similar to Romano et al., Lacourpaille et al. [30] described a protocol with various subject positioning using alternate degrees of muscle extension and reported good intra- and inter-observer reliability. Chino et al. [31] also obtained higher stability images in the longitudinal plane with a lower coefficient of variance (CV), showing better repeatability in the longitudinal measurements. This was the reason why we only took the measurements in a single location, in the longitudinal plane, avoiding vessels and fascia. In our study, for the deltoid muscle, patients were placed supine, with their elbow resting on a pillow and their arm bent at 90 degrees, a position that avoided passive stretching. However, for the soleus muscle, the prone position with knees fully extended presents a greater chance of passive stretching. We can hypothesize that as the overall stress–strain behavior of the muscle depends on fiber orientation and distribution, the viscoelasticity being an intrinsic parameter may generate anisotropy from a structural perspective, as both the elasticity and viscosity increase with contraction. The results from Looke et al. [11] suggest that the influence of the viscoelastic component is greater in the direction of the muscle fiber, as the fluid component moves easier along the fibers than across them. However, studying the relationship between viscosity and anisotropy is beyond the scope of this study; further studies are needed to give an answer to this inquiry.

An important limitation of our study is the rather small size of the sample (38 subjects). Ultrasound elastography, in general, is considered to be an operator-dependent technique. The development of various systems and the imaging methods available make homogenization difficult. However, the ICC showed excellent reproducibility between the measurements taken by the two sonographers, suggesting a very reproducible technique. There are other factors to consider, such as the reproducibility of the protocol; caution is needed when evaluating the same patients multiple times as reference values have to be clearly defined for a specific technical setup (the same machine, the same transducer, and, preferably, the same sonographer).

Dominance effects were not considered in our study, all the measurements were performed on the right arm and the right calf of the subjects.

Another limitation is using the curvilinear probe, as it was the only one available for the ViPLUS examination. High-frequency shear waves travel faster, so the measured viscosity of the muscle can also vary with frequency [1]. A possible technical limitation is reading the values in kilopascals, as they are susceptible to tissue heterogeneity and less precise compared to meters per second [32]. Further studies with linear transducers are mandatory to confirm these reference viscosity values and to assess the structural alterations in patients with musculoskeletal pathology.

5. Conclusions

The lack of standardization in muscle SWE measuring techniques still poses difficulty in using it as a reliable diagnostic method. Nowadays, a definitive diagnosis for neuromuscular diseases is based on muscle biopsy and genetic testing. However, for an experienced sonographer with a rigorously planned protocol, SWE and the novel ultrasound technique ViPLUS have great potential in monitoring the effectiveness of treatments, diagnosing muscle inflammatory disease. By quantifying the changes in the mechanical properties of the muscles, SWE and ViPLUS may become a reliable non-invasive biomarker.

Author Contributions: Conceptualization, C.S. and S.M.D.; data curation, I.-T.D. and D.D.M.; formal analysis, I.-T.D., D.D.M. and R.P.-B.; methodology, S.M.D.; project administration, C.S. and R.P.-B.; resources, A.I.C.; supervision, C.S., M.L., A.I.C. and S.M.D.; visualization, I.-T.D. and M.L.; writing—original draft, I.-T.D.; writing—review and editing, I.-T.D., C.S. and S.M.D. All authors have read and agreed to the published version of the manuscript.

Funding: This research received no external funding.

Institutional Review Board Statement: The study was conducted in accordance with the Declaration of Helsinki, and approved by the Ethics Committee of "Iuliu Hatieganu" University of Medicine and Pharmacy (protocol code, DEP130/28.04.2022).

Informed Consent Statement: Informed consent was obtained from all subjects involved in the study.

Data Availability Statement: The data presented in this study are available on request from the corresponding author.

Conflicts of Interest: The authors declare no conflict of interest.

References

1. Ryu, J.; Jeong, W.K. Current status of musculoskeletal application of shear wave elastography. *Ultrasonography* **2017**, *36*, 185–197. [CrossRef]
2. Cosgrove, D.; Piscaglia, F.; Bamber, J.; Bojunga, J.; Correas, J.M.; Gilja, O.A.; Dietrich, C.F. EFSUMB guidelines and recommendations on the clinical use of ultrasound elastography. Part 1: Basic principles and technology. *Ultraschall. Med.* **2013**, *34*, 169–184.
3. Hossain, M.M.; Gallippi, C.M. Viscoelastic Response Ultrasound Derived Relative Elasticity and Relative Viscosity Reflect True Elasticity and Viscosity: In Silico and Experimental Demonstration. *IEEE Trans. Ultrason. Ferroelectr. Freq. Control* **2020**, *67*, 1102–1117. [CrossRef] [PubMed]
4. Van Sloun, R.J.; Wildeboer, R.R.; Wijkstra, H.; Mischi, M. Viscoelasticity Mapping by Identification of Local Shear Wave Dynamics. *IEEE Trans. Ultrason. Ferroelectr. Freq. Control* **2017**, *64*, 1666–1673. [CrossRef] [PubMed]
5. Kazemirad, S.; Bernard, S.; Hybois, S.; Tang, A.; Cloutier, G. Ultrasound Shear Wave Viscoelastography: Model-Independent Quantification of the Complex Shear Modulus. *IEEE Trans. Ultrason. Ferroelectr. Freq. Control* **2016**, *63*, 1399–1408. [CrossRef] [PubMed]
6. Sugimoto, K.; Moriyasu, F.; Oshiro, H.; Takeuchi, H.; Yoshimasu, Y.; Kasai, Y.; Itoi, T. Viscoelasticity Measurement in Rat Livers Using Shear-Wave US Elastography. *Ultrasound Med. Biol.* **2018**, *44*, 2018–2024. [CrossRef]
7. Chen, S.; Sanchez, W.; Callstrom, M.R.; Gorman, B.; Lewis, J.T.; Sanderson, S.O.; Metz, S. Assessment of liver viscoelasticity by using shear waves induced by ultrasound radiation force. *Radiology* **2013**, *266*, 964–970. [CrossRef]
8. Sugimoto, K.; Moriyasu, F.; Oshiro, H.; Takeuchi, H.; Yoshimasu, Y.; Kasai, Y.; Itoi, T. Clinical utilization of shear wave dispersion imaging in diffuse liver disease. *Ultrasonography* **2020**, *39*, 3–10. [CrossRef]
9. Rus, G.; Faris, I.H.; Torres, J.; Callejas, A.; Melchor, J. Why Are Viscosity and Nonlinearity Bound to Make an Impact in Clinical Elastographic Diagnosis? *Sensors* **2020**, *20*, 2379. [CrossRef]
10. Zhou, B.; Zhang, X. Comparison of five viscoelastic models for estimating viscoelastic parameters using ultrasound shear wave elastography. *J. Mech. Behav. Biomed. Mater.* **2018**, *85*, 109–116. [CrossRef]
11. Van Loocke, M.; Lyons, C.G.; Simms, C.K. Viscoelastic properties of passive skeletal muscle in compression: Stress-relaxation behaviour and constitutive modelling. *J. Biomech.* **2008**, *41*, 1555–1566. [CrossRef] [PubMed]
12. Wheatley, B.B.; Pietsch, R.B.; Haut Donahue, T.L.; Williams, L.N. Fully non-linear hyper-viscoelastic modeling of skeletal muscle in compression. *Comput. Methods Biomech. Biomed. Eng.* **2016**, *19*, 1181–1189. [CrossRef] [PubMed]
13. Chen, S.; Fatemi, M.; Greenleaf, J.F. Quantifying elasticity and viscosity from measurement of shear wave speed dispersion. *J. Acoust. Soc. Am.* **2004**, *115*, 2781–2785. [CrossRef] [PubMed]
14. Romano, A.; Staber, D.; Grimm, A.; Kronlage, C.; Marquetand, J. Limitations of Muscle Ultrasound Shear Wave Elastography for Clinical Routine-Positioning and Muscle Selection. *Sensors* **2021**, *21*, 8490. [CrossRef]
15. Creze, M.; Nordez, A.; Soubeyrand, M.; Rocher, L.; Maître, X.; Bellin, M.F. Shear wave sonoelastography of skeletal muscle: Basic principles, biomechanical concepts, clinical applications, and future perspectives. *Skeletal Radiol.* **2018**, *47*, 457–471. [CrossRef]
16. Snoj, Ž.; Wu, C.H.; Taljanovic, M.S.; Dumić-Čule, I.; Drakonaki, E.E.; Klauser, A.S. Ultrasound Elastography in Musculoskeletal Radiology: Past, Present, and Future. *Semin. Musculoskelet Radiol.* **2020**, *24*, 156–166. [CrossRef]
17. Yanagisawa, O.; Niitsu, M.; Kurihara, T.; Fukubayashi, T. Evaluation of human muscle hardness after dynamic exercise with ultrasound real-time tissue elastography: A feasibility study. *Clin. Radiol.* **2011**, *66*, 815–819. [CrossRef]
18. Botar Jid, C.; Vasilescu, D.; Damian, L.; Dumitriu, D.; Ciurea, A.; Dudea, S.M. Musculoskeletal sonoelastography—Pictorial essay. *Med. Ultrasound* **2012**, *14*, 239–245.

19. Săftoiu, A.; Gilja, O.H.; Sidhu, P.S.; Dietrich, C.F.; Cantisani, V.; Amy, D.; Vilmann, P. The EFSUMB Guidelines and Recommendations for the Clinical Practice of Elastography in Non-Hepatic Applications: Update 2018. *Ultraschall. Med.* **2019**, *40*, 425–453. [CrossRef]
20. Gennisson, J.L.; Deffieux, T.; Macé, E.; Montaldo, G.; Fink, M.; Tanter, M. Viscoelastic and anisotropic mechanical properties of in vivo muscle tissue assessed by supersonic shear imaging. *Ultrason. Med. Biol.* **2010**, *36*, 789–801. [CrossRef]
21. Hoyt, K.; Kneezel, T.; Castaneda, B.; Parker, K.J. Quantitative sonoelastography for the in vivo assessment of skeletal muscle viscoelasticity. *Phys. Med. Biol.* **2008**, *53*, 4063–4080. [CrossRef] [PubMed]
22. Moore, C.J.; Caughey, M.C.; Meyer, D.O.; Emmett, R.; Jacobs, C.; Chopra, M.; Gallippi, C.M. In Vivo Viscoelastic Response (VisR) Ultrasound for Characterizing Mechanical Anisotropy in Lower-Limb Skeletal Muscles of Boys with and without Duchenne Muscular Dystrophy. *Ultrasound Med. Biol.* **2018**, *44*, 2519–2530. [CrossRef] [PubMed]
23. Koo, T.K.; Li, M.Y. A guideline of selecting and reporting intraclass correlation coefficients for reliability research. *J. Chiropr. Med.* **2016**, *15*, 155–163, Erratum in *J. Chiropr. Med.* **2017**, *16*, 346. [CrossRef] [PubMed]
24. Akkoc, O.; Caliskan, E.; Bayramoglu, Z. Effects of passive muscle stiffness measured by Shear Wave Elastography, muscle thickness, and body mass index on athletic performance in adolescent female basketball players. *Med. Ultrason.* **2018**, *2*, 170–176. [CrossRef]
25. Ferraioli, G.; Barr, R.G.; Farrokh, A.; Radzina, M.; Cui, X.W.; Dong, Y.; Dietrich, C.F. How to perform shear wave elastography. Part II. *Med. Ultrason.* **2022**, *24*, 196–210. [CrossRef]
26. Nakamura, M.; Ikezoe, T.; Kobayashi, T.; Umegaki, H.; Takeno, Y.; Nishishita, S.; Ichihashi, N. Acute effects of static stretching on muscle hardness of the medial gastrocnemius muscle belly in humans: An ultrasonic shear-wave elastography study. *Ultrasound Med. Biol.* **2014**, *40*, 1991–1997. [CrossRef]
27. Davis, L.C.; Baumer, T.G.; Bey, M.J.; Van Holsbeeck, M. Clinical utilization of shear wave elastography in the musculoskeletal system. *Ultrasonography* **2019**, *38*, 2–12. [CrossRef]
28. Cortez, C.D.; Hermitte, L.; Ramain, A.; Mesmann, C.; Lefort, T.; Pialat, J.B. Ultrasound shear wave velocity in skeletal muscle: A reproducibility study. *Diagn. Interv. Imaging* **2016**, *97*, 71–79. [CrossRef]
29. Eby, S.F.; Song, P.; Chen, S.; Chen, Q.; Greenleaf, J.F.; An, K.-N. Validation of Shear Wave Elastography in Skeletal Muscle. *J. Biomech.* **2013**, *46*, 2381–2387. [CrossRef]
30. Lacourpaille, L.; Hug, F.; Bouillard, K.; Hogrel, J.-Y.; Nordez, A. Supersonic shear imaging provides a reliable measurement of resting muscle shear elastic modulus. *Physiol. Meas.* **2012**, *33*, N19–N28. [CrossRef]
31. Chino, K.; Kawakami, Y.; Takahashi, H. Tissue elasticity of in vivo skeletal muscles measured in the transverse and longitudinal planes using shear wave elastography. *Clin. Physiol. Funct. Imaging* **2017**, *37*, 394–399. [CrossRef] [PubMed]
32. Alfuraih, A.M.; O'Connor, P.; Hensor, E.; Tan, A.L.; Emery, P.; Wakefield, R.J. The effect of unit, depth, and probe load on the reliability of muscle shear wave elastography: Variables affecting reliability of SWE. *J. Clin. Ultrasound* **2018**, *46*, 108–115. [CrossRef] [PubMed]

diagnostics

IMPACT FACTOR 3.0

Indexed in: PubMed

CITESCORE 4.7

Case Report

Primary Pericardial Synovial Sarcoma: A Case Report and Literature Review

Simona Manole, Roxana Pintican, Emanuel Palade, Maria Magdalena Duma, Alexandra Dadarlat-Pop, Calin Schiau, Ioana Bene, Raluca Rancea, Diana Miclea, Viorel Manole et al.

MDPI

https://doi.org/10.3390/diagnostics12010158

diagnostics

Case Report

Primary Pericardial Synovial Sarcoma: A Case Report and Literature Review

Simona Manole [1,2], Roxana Pintican [2,*], Emanuel Palade [3,4], Maria Magdalena Duma [5], Alexandra Dadarlat-Pop [6,7], Calin Schiau [2], Ioana Bene [2], Raluca Rancea [6], Diana Miclea [8], Viorel Manole [9], Adrian Molnar [3,9] and Carolina Solomon [2,*]

[1] Department of Radiology, "Niculae Stancioiu" Heart Institute, 400001 Cluj-Napoca, Romania; simona.manole@gmail.com
[2] Department of Radiology, "Iuliu Hatieganu" University of Medicine and Pharmacy, 400012 Cluj-Napoca, Romania; calin.schiau@yahoo.com (C.S.); ioanaboca90@yahoo.com (I.B.)
[3] Department of Cardiovascular and Thoracic Surgery, "Iuliu Hatieganu" University of Medicine and Pharmacy, 400012 Cluj-Napoca, Romania; paladeemanuel1@gmail.com (E.P.); adimolnar45@yahoo.com (A.M.)
[4] Department of Thoracic Surgery, Leon Daniello" Pneumophtysiology Hospital Cluj-Napoca, 400332 Cluj-Napoca, Romania
[5] Medimages Breast Center, 400458 Cluj-Napoca, Romania; magdaduma@gmail.com
[6] Cardiology Department, Heart Institute "N. Stăncioiu", 400001 Cluj-Napoca, Romania; dadarlat.alexandra@yahoo.ro (A.D.-P.); raluca_rancea@yahoo.com (R.R.)
[7] Department of Internal Medicine, Faculty of Medicine, "Iuliu Hatieganu" University of Medicine and Pharmacy, 400012 Cluj-Napoca, Romania
[8] Department of Medical Genetics, "Iuliu Hatieganu" University of Medicine and Pharmacy, 400012 Cluj-Napoca, Romania; bolca12diana@yahoo.com
[9] Department of Cardiovascular Surgery, Heart Institute "N. Stăncioiu", 400001 Cluj-Napoca, Romania; v_manole@yahoo.com
* Correspondence: roxana.pintican@gmail.com (R.P.); carolinasolomon12@gmail.com (C.S.)

Abstract: We report a case of a 52-year-old woman who was referred to our institution with a superior vena cava syndrome and was investigated through echocardiography, CT and MRI revealing a well-defined, encapsulated pericardial mass. The pathology, correlated with the immunohistochemical analysis, concluded it was an extremely rare primary pericardial synovial sarcoma. The patient underwent surgery and chemotherapy with a 16-month disease-free survival and passed away after a contralateral aggressive relapse. Moreover, we discuss the role of each imaging modality together with their pericardial synovial sarcoma reported features.

Keywords: synovial sarcoma; pericardium; intrapericardial mass; superior vena cava syndrome; cardiac tamponade

Citation: Manole, S.; Pintican, R.; Palade, E.; Duma, M.M.; Dadarlat-Pop, A.; Schiau, C.; Bene, I.; Rancea, R.; Miclea, D.; Manole, V.; et al. Primary Pericardial Synovial Sarcoma: A Case Report and Literature Review. *Diagnostics* **2022**, *12*, 158. https://doi.org/10.3390/diagnostics12010158

Academic Editor: Ernesto Di Cesare

Received: 9 December 2021
Accepted: 3 January 2022
Published: 10 January 2022

1. Introduction

Primary pericardial tumor is an uncommon, extremely rare disorder. Pleuro-pericardial cyst and lipomas are by far the most common benign pericardial masses, while mesothelioma is the most frequently encountered malignant tumor.

Primary pericardial sarcomas are a group of extremely rare malignancies which include in order of frequency: angiosarcomas, undifferentiated sarcomas, leiomyosarcomas and, exceptionally, synovial sarcomas.

To the best of our knowledge, there are less than 15 published cases of primary pericardial synovial sarcomas in the last decade [1,2].

Synovial sarcoma (SS) accounts for up to 10% of all soft tissue sarcomas and usually affects older children and young adults. It arises commonly around the knee and the ankle, while the neck, abdomen, pleura and lungs are less common locations [3].

Even if substantial advances were made in terms of SS natural history and behavior, its prognosis is still scarce [4]. SS is considered a high-grade sarcoma with an overall survival rate of 50.8% at 10 years.

2. Case Report

We report a case of a 52-year-old woman who was referred to our institution with a superior vena cava syndrome (dyspnea, jugular vein distension, facial, neck and left upper limb edema). An echocardiography was performed and showed a large intrapericardial mass surrounded by a substantial amount of fluid. Furthermore, cardiac CT and MRI highlighted the mass location and mass effect related with the surrounding mediastinal structures. The large mass was situated anterior to the right side of the heart, close to the superior right pulmonary vein, compressing the superior vena cava, right atrium and right ventricle. A heterogeneous solid mass with late, heterogeneous enhancement was noted on both CT and MRI exams (Figure 1). The tumor seemed to be located within the pericardium, with no coronary artery or cardiac cavity invasion.

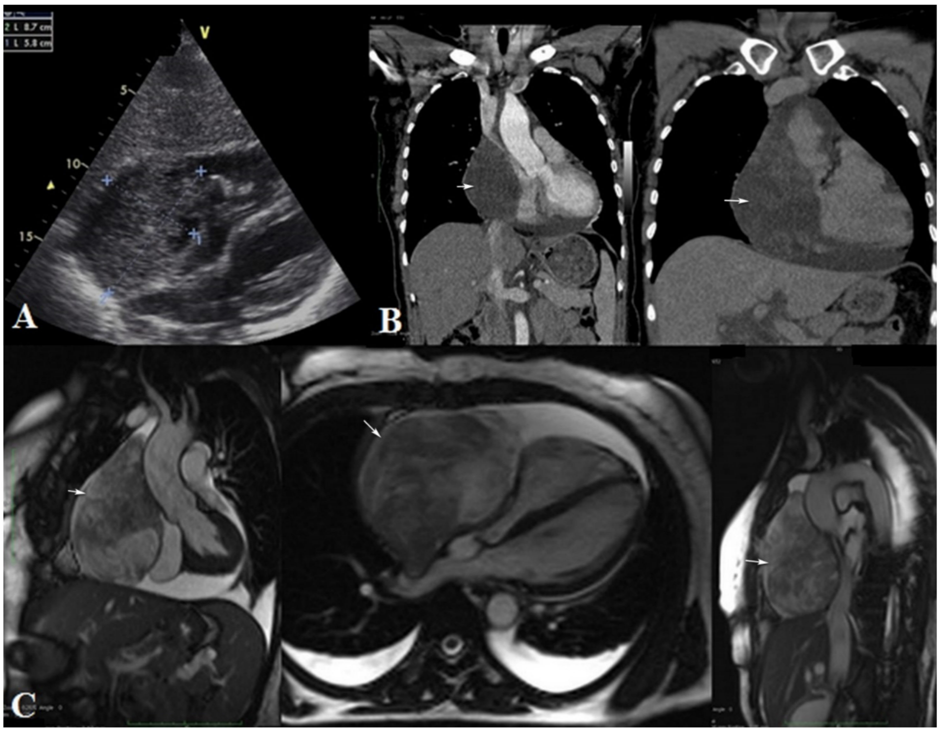

Figure 1. (**A**): Echocardiography; (**B**): computer tomography with contrast enhancement—coronal plane; (**C**): MRI—coronal, axial and sagittal T2 WI; There is a large, inhomogeneous, enhancing intrapericardial mass, surrounded by fluid, with marked compressive effect on the superior vena cava and right heart cavities (arrows). No intracavitary or endoluminal invasive aspects are present.

On echocardiography and dynamic sequence MRI (cine sequences), the interventricular septum displayed a paradoxical motion with the right atrium and ventricle being collapsed and dyskinetic. All the above-mentioned characteristics represented indirect signs of cardiac tamponade.

The cardiovascular surgeons opted for an immediate surgical excision without prior biopsy. The surgical approach included a longitudinal pericardiotomy which revealed an encapsulated stiff mass (Figure 2). The tumor appeared to arise at the level of the right pulmonary vein pericardial recess and extended throughout the entire anterior aspect of the right heart. Total tumor resection was possible without intra- or postoperative complications. The excised tissue weighed 300 g and measured 10/8/5 cm.

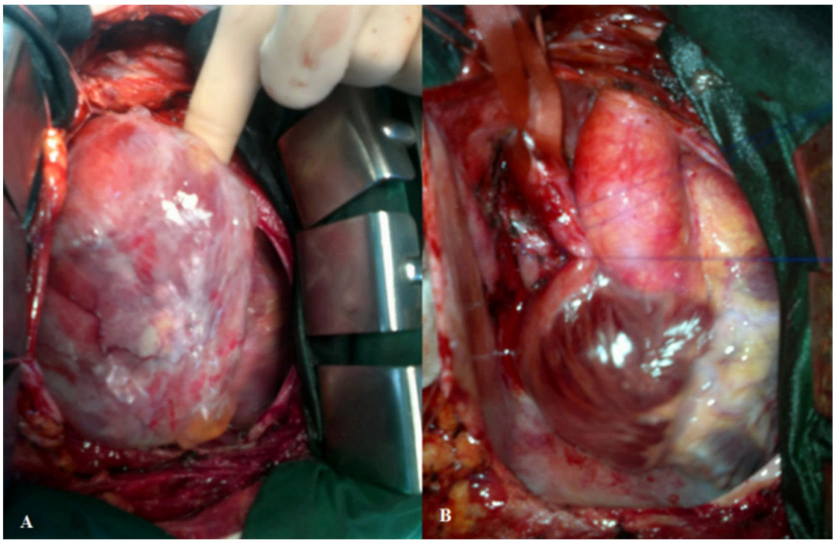

Figure 2. Intraoperative findings: a large, encapsulated mass developed along the entire right aspect of the heart. (**A**): Preoperative image; (**B**): Postoperative image: the SVC can be identified by the blue thread around it.

The pathology report (Figures 3 and 4) described interlacing fascicles of spindle cells with myxoid changes. Tumoral cells displayed a monotonous, uniform pattern with the predominance of rounded, large nuclei. Less than 50% of examined tissue presented necrotic or hemorrhagic areas. Immunohistochemistry revealed a high mitosis index (Ki67 intensely positive) and positive reactivity for the following markers: cytokeratin AE1/3, cytokeratin 7, epithelial membrane antigen (EMA), vimentin, S100, CD99 and Bcl2. Staining for desmin and CD34 was negative. The FISH test for the t (X; 18) (p11.2; q11.2) genetic change proved negative and was used to accurately exclude other differentials.

Figure 3. Surgical specimen of the first tumor—gross macroscopic appearance.

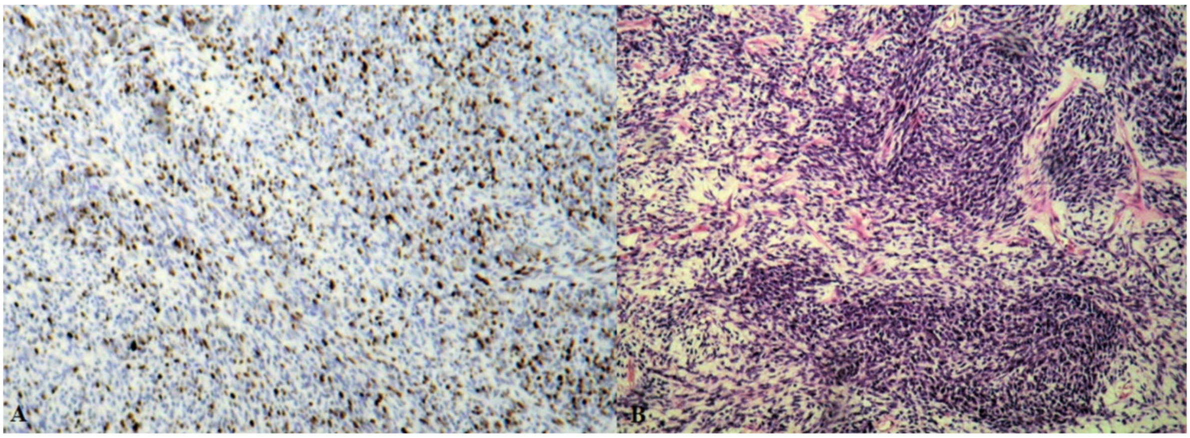

Figure 4. Histopathological findings of the surgical specimen: (**A**): Ki67 immunoreactivity highlights a high-grade sarcoma; (**B**): high-magnification view of the synovial sarcoma; H&E.

The final report concluded that the tumor was a grade 3 monophasic poorly differentiated synovial sarcoma.

After surgery, the patient was submitted to six cycles of chemotherapy following the MAID protocol (MESNA doxorubicine, ifosfamide, dacarbazine) with acceptable tolerance.

There were 14 months disease-free with negative follow-up imaging (Figure 5). Four months later, the patient complained of fatigue, chest pain and exertional and at rest dyspnea. She was referred to our department where echocardiography, CT and MRI examinations showed tumoral relapse (Figure 6). The tumor was located adjacent to the left atrium and ventricle, and pulmonary artery trunk, and was extending inferiorly between the right and left pulmonary veins and superiorly towards the inferior surface of the aortic arch (Figure 5). A partial thrombosis of the superior lobar branch of the right pulmonary artery was depicted. The pulmonary veins appeared compressed but permeable. The tumor covered the left circumflex and the anterior interventricular coronary artery. There were no signs of recurrence on the site where the primary tumor was located. Debulking surgery was performed, with incomplete removal of the tumor mass, due to the myocardium and coronary arteries' involvement. Pathology analysis described the second tumor as a grade 3, poorly differentiated monophasic synovial sarcoma; this time categorized as high-grade with S100 negative and calretinin positive markers, in many more areas than before. The FISH test was again negative for the t(X; 18) (p11.2; q11.2) but positive for *BCL*-2 genetic change. The patient was discharged 10 days after surgery with no notable complications, but unfortunately, she passed over two months later.

Figure 5. At 14 months, follow-up axial coronal and axial CT images postcontrast enhancement revealed no local relapse.

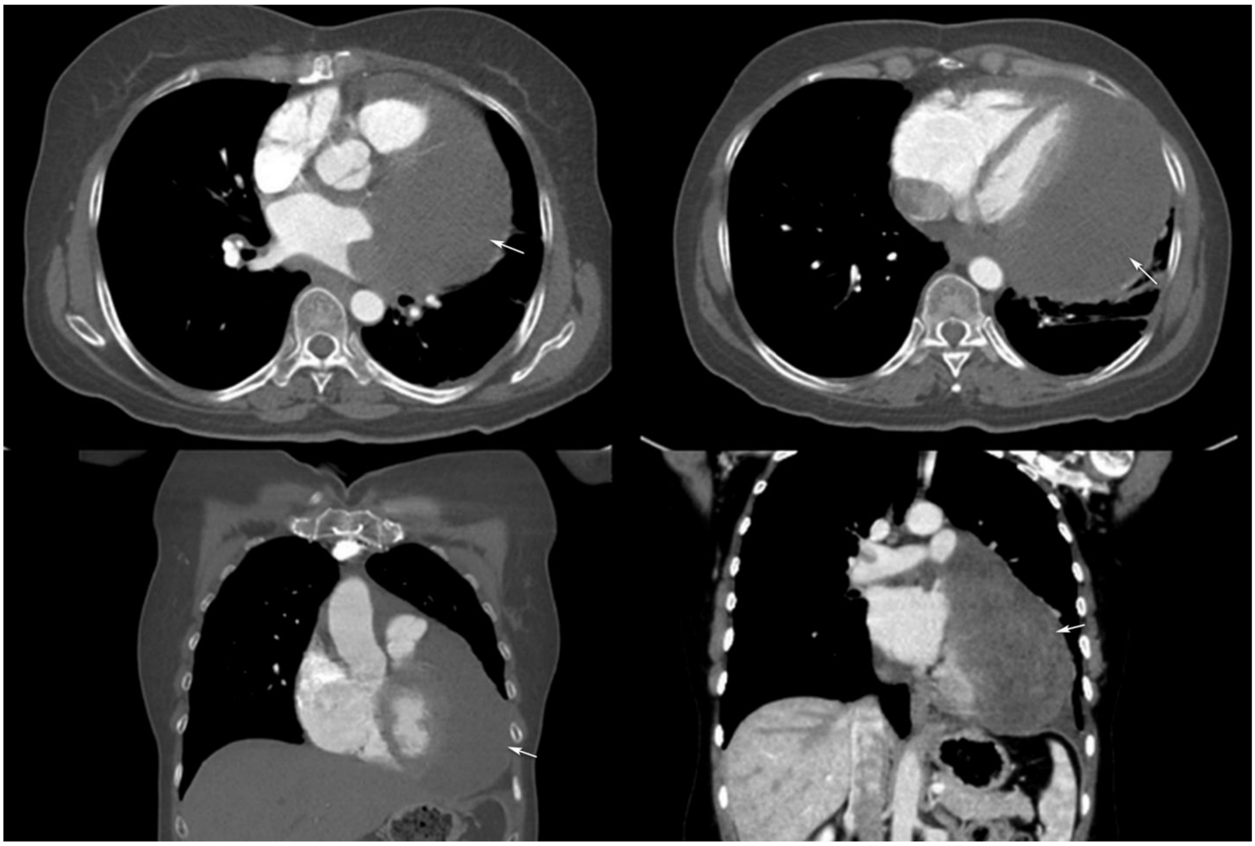

Figure 6. At 18 months, a follow-up CT with contrast enhancement—axial (upper images) and coronal (lower images) plane reveals a homogeneous tumor relapse near the left heart border (arrows), invading the left atrium, right superior pulmonary vein and periaortic root.

3. Discussion

Monophasic synovial sarcoma of the pericardium is an extremely rare malignant tumor with challenging diagnosis and an unpredictable outcome.

One vital differential diagnosis is represented by sarcomatoid mesothelioma, especially in older patients. Distinguishing between the two entities is of utmost importance since the clinical management is completely different [4]. The chromosomal translocation (X; 18) (p11.2; q11.2) is found in almost all (>90%) SS [5] while *BCL*-2 immunohistochemical analysis is found in 0–8% of sarcomatous mesothelioma and a much higher percentage of SS [6,7]. Our patient had two negative FISH tests for the chromosomal translocation t(X; 18) (p11.2; q11.2) but a positive immunohistochemical *BCL*-2 analysis. Pathologists considered that there was enough material examined and the immune-morphologic features were conclusive for a complete diagnosis.

Recent data report histology and grading as important prognostic factors for synovial sarcoma patients. Furthermore, a worse prognosis was observed for monophasic patients and grade 3 tumors (all $p < 0.05$) [8], as in the case of our patient.

Another important aspect for appropriate surgical management is represented by an accurate report of the tumor boundaries, location and relation with surrounding structures. In the few cases reported in the literature, echocardiography was used as the first-line imaging tool, showing in most of the cases only pericardial effusion. CT and MRI are second-line imaging modalities used to provide more accurate tumor characterization, thus, being able to guide the surgical procedures.

While the echocardiography usually highlights pericardial effusion and a solid, well-defined mass, the imaging characteristic on CT and MRI are variable. Authors reported masses with ill-defined margins, invading the surrounding structures, with homogeneous or heterogeneous aspect on postcontrast enhancement sequences. On MRI, a mass with slightly hyper-T2 signal intensity was observed and reported by two papers, including our case.

The role of PET CT in stratifying soft tissue sarcoma patients is still controversial. The latest data report significant differences in SUV uptake among the different subtypes of sarcoma. Synovial and myxoid sarcoma of the extremities seem to have low SUV uptake (<10.3) on PET CT, questioning its role in follow-up, relapsing or recurrent disease [9]. For the pericardial location, the results are contradictory, with max SUV reported between 3–13, ranging from mild to high uptake [10,11]. Thus, the role of PET-CT in the follow-up of patients with pericardial synovial sarcoma, still remains debatable Table 1.

Table 1. Pericardial synovial sarcoma—reported imaging features.

Author/Year	**General Aspect**	**Size (cm)**	**US ***	**CT/CT Angiography**	**MRI**	**PET CT**
Gerry Van der Mieren et al./2004	Recurrent mediastinal mass Ill-defined mass	2.4/2.3	N/A	Mediastinal mass Pleural metastasis	Ill-defined mass Slightly hyper T2 SI	N/A
Gayatri Ravikumar et al./2011	Heterogeneous, invading mass	9/9/2	N/A	Heterogeneous, invading mass	N/A	N/A
Yufan Cheng et al./2012	Heterogeneous, invading mediastinal mass	8/8/2	N/A	Heterogeneous mediastinal mass	N/A	N/A
Prajakta Phatak et al./2014	Heterogeneous pericardial mass	N/A	Pericardial effusion Right atrium collapse	Heterogeneous mass within pericardial cavity	N/A	N/A
Hyo Chul Youn et al./2016	Thickened pericardium	6.3/10.1	Pericardial effusion	Pericardial effusion with thickened pericardium	N/A	N/A
Jose Duran-Moreno et al./2019	Heterogeneous, pericardial, invading mass	8.1/5.6	Pericardial effusion + mass	Mass adherent from the pericardium	Inhomogeneous, mass with cardiac involvement	Mild FDG uptake SUV Max 3.1
Kirsten Y Wong et al./2020	Homogeneous, invading mass	11/10/8	N/A	Homogeneous mass invading coronaries	Myocardium invasion	FDG avid mass SUV max13
Ammar Farook Chapra et al./2021	Heterogeneous, invading pericardial mass	13.5/5	Pericardial effusion	Heterogenous mediastinal mass abutting aorta and heart	Pericardial mass invading pleura and diaphragm	FDG avid mass SUV N/A
Manole Simona et al./2021	Heterogeneous, well-defined, pericardial mass Homogeneous relapse mass	10/8/5	Pericardial mass Pericardial effusion	Heterogeneous, encapsulated mass	Well-defined pericardial mass with iso- and hyper T2 SI	N/A

* US = echocardiography; SI = signal intensity; N/A = not reported; References [6,8,12–17].

There are a few distinct features in our case when compared to the literature review: first, the lack of invasive aspects—in spite of an aggressive histological subtype of the primary tumor, the mass appeared well defined, encapsulated and occupying only the pericardium, sparing cardiac cavities and blood vessels; second, despite the fact that the primary tumor was very large, the patient survived three times the mean survival length of 6 months compared with the literature reports [13]; third, the pericardial mass was depicted also on echocardiography and last, this is the first reported contralateral aggressive relapse.

Particularly, the margins reported on imaging play an important role in the surgical management of all sarcomas. From a macroscopic point-of-view, MRI is the imaging modality of choice in assessing the tumor irregular surface and invasion in the surrounding structures. Regarding the microscopic evaluation of margins, a “free margin” of <2 cm in width is a practical recommendation for all soft tissue sarcomas [18], but virtually impossible to reach in cases with primary pericardial location.

Our patient presented with well-defined, circumscribed margins on all imaging modality assessed, including MRI; but the peculiar location within the thin pericardium did not allow the pathologist to report any "free-margins", even if the tumor did not invade the extra-pericardial structures.

4. Conclusions

This case report emphasizes the importance of prompt clinical suspicion, accurate histopathological diagnosis and the use of appropriate immunohistochemistry markers in the diagnosis of this rare tumor with an unusual location. Pericardial synovial sarcoma may present with various imaging characteristics on echocardiography, CT and MRI and should be included in the differential diagnosis of well-defined pericardial masses.

Author Contributions: Conceptualization, S.M. and R.P.; methodology, S.M., R.P., C.S. (Carolina Solomon); validation, S.M., R.P., C.S. (Calin Schiau), M.M.D., E.P., R.R., D.M., A.D.-P., V.M., A.M., C.S. (Carolina Solomon) and I.B.; formal analysis, S.M., R.P., C.S. (Carolina Solomon); investigation, S.M.; resources, S.M., R.P., E.P., R.R., D.M., A.D.-P., V.M., A.M., C.S. (Calin Schiau) and I.B.; data curation, S.M., R.P., C.S. (Calin Schiau), E.P., R.R., D.M., A.D.-P., V.M., A.M., C.S. (Carolina Solomon) and I.B.; writing—original draft preparation, S.M. and R.P.; writing—review and editing, S.M., R.P., C.S. (Calin Schiau), E.P., R.R., D.M., A.D.-P., V.M., A.M., C.S. (Carolina Solomon) and I.B.; visualization, S.M., R.P., C.S. (Carolina Solomon); supervision, S.M., R.P., C.S. (Carolina Solomon); project administration, S.M., R.P., C.S. (Carolina Solomon) All authors have read and agreed to the published version of the manuscript.

Funding: No funding was received for this study.

Institutional Review Board Statement: The study was conducted in accordance with the Declaration of Helsinki, and approved by the Ethics Committee of "Niculae Stancioiu" Heart Institute, Cluj Napoca, Romania.

Informed Consent Statement: Written informed consent has been obtained from the patient to publish this paper.

Conflicts of Interest: The authors declare no conflict of interest.

References

1. Fletcher, C.H. *Diagnostic Histopathology of Tumors*; Churchill Livingstone Elsevier: Philadelphia, PA, USA, 2007; Volume 2, pp. 1576–1578.
2. Weiss, S.W.; Goldblum, R.J. *Enzinger and Weiss's Soft Tissue Tumors*, 5th ed.; Mosby Elsevier: Maryland Heights, MO, USA, 2008; pp. 1161–1181.
3. Silver, M.; Gotlieb, A.; Schoen, F. *Cardiovascular Pathology*; Churchill Livingstone Elsevier: Philadelphia, PA, USA, 2001; pp. 596–600.
4. Fiore, M.; Sambri, A.; Spinnato, P.; Zucchini, R.; Giannini, C.; Caldari, E.; Pirini, M.G.; De Paolis, M. The Biology of Synovial Sarcoma: State-of-the-Art and Future Perspectives. *Curr. Treat Options Oncol.* **2021**, *22*, 109. [CrossRef] [PubMed]
5. Burke, A.; Virmani, R. *Tumors of the Heart and Great Vessels*; Armed Forces Institute of Pathology: Bethesda, MD, USA, 1996; pp. 158–161.
6. Cheng, Y.; Sheng, W.; Zhou, X.; Wang, J. Pericardial Synovial Sarcoma, a potential for Misdiagnosis. *Am. J. Clin. Pathol.* **2012**, *137*, 142–149. [CrossRef] [PubMed]
7. Nicholson, A.G.; Goldstraw, P.; Fisher, C. Synovial sarcoma of the pleura and its differentiation from other primary pleural tumors: A clinicopathological and immunohistochemical review of three cases. *Histopathology* **1998**, *33*, 508–513. [CrossRef] [PubMed]
8. Yoshino, M.; Sekine, Y.; Koh, E.; Kume, Y.; Saito, H.; Kimura, S.; Hamada, H.; Wu, D.; Hiroshima, K. Pericardial synovial sarcoma: A case report and review of the literature. *Surg. Today* **2013**, *44*, 2167–2173. [CrossRef] [PubMed]
9. Bianchi, G.; Sambri, A.; Righi, A.; Dei Tos, A.P.; Picci, P.; Donati, D. Histology and grading are important prognostic factors in synovial sarcoma. *Eur. J. Surg. Oncol.* **2017**, *43*, 1733–1739. [CrossRef] [PubMed]
10. Sambri, A.; Bianchi, G.; Longhi, A.; Righi, A.; Donati, D.M.; Nanni, C.; Fanti, S.; Errani, C. The role of 18F-FDG PET/CT in soft tissue sarcoma. *Nucl. Med. Commun.* **2019**, *40*, 626–631. [CrossRef] [PubMed]
11. Al-Rajhi, N.; Husain, S.; Coupland, R.; McNamee, C.; Jha, N. Primary pericardial synovial sarcoma: A case report and literature review. *J. Surg. Oncol.* **1999**, *70*, 194–198. [CrossRef]

12. Duran-Moreno, J.; Kampoli, K.; Kapetanakis, E.I.; Mademli, M.; Koufopoulos, N.; Foukas, P.G.; Kostopanagiotou, K.; Tomos, P.; Koumarianou, A. Pericardial Synovial Sarcoma: Case Report, Literature Review and Pooled Analysis. *In Vivo* **2019**, *33*, 1531–1538. [CrossRef] [PubMed]
13. Wong, K.Y.; Hong, E.; Fong, C.M.; Wong, P.S. Pericardial synovial sarcoma presenting with unstable angina. *Asian Cardiovasc. Thorac. Ann.* **2020**, *28*, 59–61. [CrossRef] [PubMed]
14. Van der Mieren, G.; Willems, S.; Sciot, R.; Dumez, H.; Van Oosterom, A.; Flameng, W.; Herijgers, P. Pericardial synovial sarcoma: 14-year survival with multimodality therapy. *Ann. Thorac. Surg.* **2004**, *78*, e41–e42. [CrossRef] [PubMed]
15. Ravikumar, G.; Mullick, S.; Ananthamurthy, A.; Correa, M. Primary synovial sarcoma of the mediastinum: A case report. *Case Rep Surg.* **2011**, *2011*, 602853. [CrossRef] [PubMed]
16. Phatak, P.; Khanagavi, J.; Aronow, W.S.; Puri, S.; Yusuf, Y.; Puccio, C. Pericardial synovial sarcoma: Challenges in diagnosis and management. *F1000Research* **2014**, *3*, 15. [CrossRef] [PubMed]
17. Chapra, A.F.; Maliyakkal, A.M.; Naushad, V.A.; Valiyakath, H.S.; Ahmed, M.S. Primary Pericardial Synovial Sarcoma: An Extremely Rare Cardiac Neoplasm. *Cureus* **2021**, *13*, e14583. [CrossRef] [PubMed]
18. Sambri, A.; Caldari, E.; Fiore, M.; Zucchini, R.; Giannini, C.; Pirini, M.G.; Spinnato, P.; Cappelli, A.; Donati, D.M.; De Paolis, M. Margin Assessment in Soft Tissue Sarcomas: Review of the Literature. *Cancers* **2021**, *13*, 1687. [CrossRef] [PubMed]

The EFSUMB Guidelines and Recommendations for the Clinical Practice of Elastography in Non-Hepatic Applications: Update 2018

Die EFSUMB-Leitlinien und Empfehlungen für die klinische Praxis der Elastografie bei nichthepatischen Anwendungen: Update 2018

Authors

Adrian Săftoiu[1], Odd Helge Gilja[2], Paul S. Sidhu[3], Christoph F. Dietrich[4], Vito Cantisani[5], Dominique Amy[6], Michael Bachmann-Nielsen[7], Flaviu Bob[8], Jörg Bojunga[9], Marko Brock[10], Fabrizio Calliada[11], Dirk André Clevert[12], Jean-Michel Correas[13], Mirko D'Onofrio[14], Caroline Ewertsen[7], André Farrokh[15], Daniela Fodor[16], Pietro Fusaroli[17], Roald Flesland Havre[2], Michael Hocke[18], André Ignee[4], Christian Jenssen[19], Andrea Sabine Klauser[20], Christian Kollmann[21], Maija Radzina[22], Kumar V. Ramnarine[23], Luca Maria Sconfienza[24], Carolina Solomon[25], Ioan Sporea[26], Horia Ştefănescu[27], Mickael Tanter[28], Peter Vilmann[29]

Affiliations

1 Research Center of Gastroenterology and Hepatology Craiova, University of Medicine and Pharmacy Craiova, Romania
2 National Centre for Ultrasound in Gastroenterology, Haukeland University Hospital, Bergen, and Department of Clinical Medicine, University of Bergen, Norway
3 Department of Radiology, King's College London, King's College Hospital, United Kingdom of Great Britain and Northern Ireland
4 Medizinische Klinik 2, Caritas-Krankenhaus, Bad Mergentheim, Germany
5 Radiological, Pathological and Oncological Sciences Department, University Sapienza, Rome, Italy
6 Radiology Department, Breast Center, Aix-en-Provence, France
7 Department of Radiology, Copenhagen-University-Hospital, Rigshospitalet, Copenhagen OE, Denmark
8 Nephrology Department, University of Medicine and Pharmacy "Victor Babeș" Timișoara, Romania
9 Med. Klinik I, Department of Endocrinology Universitätsklinikum, Frankfurt am Main, Germany
10 Department of Urology, Marien Hospital Herne, Ruhr-University Bochum, Germany
11 Department of Radiology, Policlinico San Matteo, University of Pavia, Pavia, Italy
12 Department of Clinical Radiology, University of Munich-Grosshadern Campus, Munich, Germany
13 Service de Radiologie adultes, Hôpital Necker, Université Paris Descartes, Paris, France
14 Department of Radiology, G.B. Rossi University Hospital, University of Verona, Verona, Italy
15 Department of Breast Imaging and Interventions, University Hospital Schleswig-Holstein Campus Kiel, Germany
16 2nd Medical Clinic, "Iuliu Hațieganu" University of Medicine and Pharmacy Cluj-Napoca, Romania
17 Gastroenterology Unit, Department of Medical and Surgical Sciences, University of Bologna/Hospital of Imola, Italy
18 Internal Medicine II, Klinikum Meiningen, Germany
19 Klinik für Innere Medizin, Krankenhaus Märkisch Oderland Strausberg/Wriezen, Germany
20 Universitätsklinik für Radiologie/Medizinische Universität Innsbruck, Austria
21 Center for Medical Physics & Biomedical Engineering, Medical University of Vienna, Austria
22 Radiology Research Laboratory, Riga Stradins University, Medical faculty, University of Latvia, Diagnostic Radiology Institute, Paula Stradina Clinical University Hospital, Riga, Latvia
23 Medical Physics Department, Guy's and St Thomas' NHS Foundation Trust, London, and University of Leicester, Leicester, United Kingdom of Great Britain and Northern Ireland
24 IRCCS Istituto Ortopedico Galeazzi, Milano Italy and Department of Biomedical Sciences for Health, University of Milano, Italy
25 Radiology Department, "Iuliu Hațieganu" University of Medicine and Pharmacy Cluj-Napoca, Emergency Clinical County Hospital, Cluj-Napoca, Romania
26 Department of Gastroenterology and Hepatology, University of Medicine and Pharmacy "Victor Babeș" Timișoara, Romania
27 Hepatology Unit, Regional Institute of Gastroenterology and Hepatology, Cluj-Napoca, Romania

---

All authors contributed equally to the manuscript.

28 Physics for Medicine Paris Institute, INSERM, CNRS, ESPCI Paris, France
29 Endoscopy Department, Copenhagen University Hospital Herlev, Denmark

Key words
ultrasound elastography, guideline, EFSUMB

received 22.08.2018
accepted 10.03.2019

Bibliography
DOI https://doi.org/10.1055/a-0838-9937

Ultraschall in Med 2019; 40: 425–453

ISSN 0172-4614

Correspondence
Prof. Adrian Saftoiu
Research Center in Gastroenterology and Hepatology, University of Medicine and Pharmacy Craiova, Macinului 1, 200640 Craiova, Romania
Tel.: ++ 40/7 44 82 33 55
Fax: ++ 40/2 51/31 02 87
adrian.saftoiu@umfcv.ro

ABSTRACT

This manuscript describes the use of ultrasound elastography, with the exception of liver applications, and represents an update of the 2013 EFSUMB (European Federation of Societies for Ultrasound in Medicine and Biology) Guidelines and Recommendations on the clinical use of elastography.

ZUSAMMENFASSUNG

Diese Arbeit beschreibt den Einsatz der Ultraschall-Elastografie mit Ausnahme der Leberanwendungen und ist eine Aktualisierung der Leitlinien und Empfehlungen der EFSUMB (European Federation of Societies for Ultrasound in Medicine and Biology) von 2013 zum klinischen Einsatz der Elastografie.

ABBREVIATIONS

SE	strain elastography
SWE	shear wave elastography
pSWE	point shear wave elastography
TE	transient elastography
IQR	interquartile range
IQR/M	interquartile range/median
ARFI	acoustic radiation force impulse
BIRADS	Breast Imaging Reporting and Data System
TIRADS	Thyroid Imaging Reporting and Data System
TI	thermal index
MI	mechanical index
SR	strain ratio
SH	strain histogram
EFSUMB	European Federation of Societies for Ultrasound in Medicine and Biology
ECMUS	European Committee of Medical Ultrasound Safety
WFUMB	World Federation for Ultrasound in Medicine and Biology
LoE	levels of evidence
GoR	grades of recommendation

1. Introduction

This manuscript describes the use of ultrasound elastography, with the exception of liver applications, and represents an update of the 2013 EFSUMB (European Federation of Societies for Ultrasound in Medicine and Biology) Guidelines and Recommendations on the clinical use of elastography. A taskforce comprising 32 EFSUMB members was established in 2017 to draft a manuscript derived and updated from the previous EFSUMB guidelines on elastography: part 1 (Basic Principles and Technology) and part 2 (Clinical Applications) [1, 2]. For each recommendation levels of evidence (LoE) and grades of recommendation (GoR) were also included to show the clinical role and value of elastography in various non-liver applications. These were assigned according to the Oxford Centre for Evidence-based Medicine criteria (http://www.cebm.net/oxford-centre-evidencebased-medicine-levels-evidence-march-2009/). A consensus opinion was established by vote as follows: strong consensus (> 95 %), broad consensus (> 80 %), with approval, disapproval or abstaining from each participant. The manuscript was prepared initially by e-mail communication and was discussed in a consensus meeting in Frankfurt am Main, Germany, during February 2018.

2. Training

EFSUMB maintains a policy to attain high quality in all aspects of ultrasound education and to promote excellent professional standards in the practice of elastography. EFSUMB has defined three levels of competence, defined in the document on minimal training requirements [3], and these training levels also apply to the application of elastography. To ensure high-quality scanning and the lowest possible intra-operator variability, EFSUMB recommends that ultrasound elastography should be performed by operators that have passed competence Level 1. This is particularly relevant to the evaluation of focal lesions present in various organs as these lesions must be first assessed by B-mode and Doppler ultrasound [4]. However, it is possible to train dedicated personnel to selectively perform elastography, e. g. for the thyroid gland [5]. Nevertheless, there has to be an appreciation of the difference between acquisition and interpretation of elastography, as the latter also requires knowledge of the patient's clinical history, hematological and biochemical parameters, and other comparative imaging findings. Furthermore, experience in ultrasonography is important as this influences the ability to perform shear wave measurements, particularly in obese patients [6]. For all ultrasound operators it is important to follow international guidelines, obtain adequate knowledge and training, and to perform elastography in accordance with national medico-legal regulations.

RECOMMENDATION 1

The operator should obtain adequate knowledge and training in ultrasonography and elastographic methods and perform the examination within the medico-legal framework of the specific country (LoE 5, GoR C) (For 20, Abstain 0, Against 0).

3. Terminology

Terminology of ultrasound elastography has been widely accepted [1, 7]. In the following, we briefly refer to the distinction between strain elastography (SE) and shear wave elastography (SWE), which includes acoustic radiation force impulse (ARFI) based techniques and transient elastography (TE). All available ultrasound elastography methods employ ultrasound to measure the internal tissue shear deformations resulting from an applied force but the type of force is important. If the force varies slowly relative to the shear propagation time to the depth of interest, as is the case for transducer palpation or physiological motion, it is considered quasi-static. The signal processing within the scanner for all current commercial ultrasound elastography methods begins with the measurement of tissue displacement as a function of spatial position and time, which is performed using cross-correlation tracking, Doppler, or other signal processing. The various elastography methods differ importantly according to what they do with these displacement data, to create an elastogram or elasticity measurement.

According to the EFSUMB guidelines, there are two options for the property displayed [8, 9]:

- Display tissue strain or strain rate, calculated from the spatial gradient of displacement or velocity respectively, as in SE. SE is a type of quasistatic elastography, because the applied force varies slowly, while the acquired images are qualitative for tissue properties.
- Display shear wave speed, calculated by using the time varying displacement data to measure the arrival time of a shear wave at various locations. There are a number of such methods, which are grouped under the heading SWE, and include transient elastography (TE), point shear wave elastography (pSWE) and multidimensional SWE (2D-SWE and 3D-SWE). These are based on either a transient shear deformation induced by a controlled applied force (TE) or by quantification of tissue displacement induced by acoustic radiation force impulse (ARFI) [8, 9].

Most SE ultrasound systems do have an indicator (quality index) displayed in real time, indicating that the degree of compressions/decompressions is appropriate to generate repeatable and reproducible SE images [7 – 11]. The pressure and direction of compressions can be changed by the examiner, especially for external ultrasound procedures, with the compressions/decompressions needed by most systems being less than 2 %. Quality factors for the shear wave speed estimate are available also for the 2D-SWE techniques. For ARFI-based techniques, an approach similar to that of TE has been employed to assess the quality of the measurement, including the interquartile range (IQR) values (i. e. the difference between the 75th and 25th percentile) and IQR/median. Assessment is considered reliable when the IQR is less than 30 % of the median [8, 9]. The values obtained for SWE vary between different machines and are not interchangeable.

For more terminology and quality assurance details, refer to the EFSUMB and WFUMB guidelines on the use of elastography [1, 2, 7 – 11].

4. Safety

Elastography needs a "push" to the organ of interest that can be produced either mechanically or acoustically and may be quasistatic or dynamic. Different techniques are commercially available for the measurement of elastic values for an increasingly wide range of clinical applications. It is essential to know the principle of each of the techniques and how it is applied to understand the implications for patient safety [1 – 3]. A possible risk depends on the technology or type of elastography used and its anatomical application.

4.1 Methods

Techniques which utilize a mechanically induced force to generate SE, strain rate imaging, TE and time harmonic elastography (which uses external vibrations at multiple frequencies to create compound shear wave speed maps) share the same output issues as conventional B-mode ultrasound examination [1]. Therefore, applications of TE measuring quantitative stiffness data were demonstrated to be feasible for children to assess not only liver stiffness data [12, 13] but also spleen stiffness measurement [14] with no increased risk. Also, there is new evidence that patients with cardiac pacemakers or implantable cardioverter defibrillators, have a low potential to be harmed by TE applications [15, 16].

Acoustically induced techniques which require push pulses (known as ARFI imaging, ARFI quantification, pSWE, SWE [2]) on the other hand operate with higher output (higher TI and MI values) [17, 18]. The safety profile is comparable with pulse-wave Doppler mode and the acoustic output will depend on the applied sequence and repetition of pushing and tracking pulses.

A certain amount of energy is required to displace the tissue, even a few microns, using acoustic radiation force to generate shear waves within the tissue (longer pulses of up to 1000 µs are needed, as compared to short pulses up to 2 µs for diagnostic ultrasound) [8, 9]. The number of push pulses and repetitions during the measurement determine the amount of energy deposited in the tissue. Simulations have revealed a possible temperature rise of about 5 degrees Celsius if bone is present or sensitive tissues such as the eye and a fetus are involved with the temperature maximum at the focus [19 – 21]. Also, tracking beams, repeated with high frequencies, use pulse pressures close to the upper Food and Drug Administration limit (MI ≤ 1.9) to ensure a sufficient signal-to-noise ratio for reliable detection [22]. During ARFI imaging, the displayed indices (MI and TI) may be underestimated.

RECOMMENDATION 2

To comply with safety, the ALARA (as low as reasonably achievable) principle should be applied when using ultrasound elastography (LoE 2b, GoR B) (For 18, Abstain 2, Against 0).

RECOMMENDATION 3

Caution is recommended for shear wave elastography using long pulse sequences, particularly when exposing sensitive tissues (LoE 2b, GoR B) (For 19, Abstain 1, Against 0).

5. Breast

5.1 Background

Breast elastography is used for differentiating benign focal lesions from suspicious focal lesions – benign lesions have low stiffness, while malignant lesions have high stiffness. Both strain and shear wave methods have been evaluated for improving the generally high sensitivity and specificity of the Breast Imaging Reporting and Data System (BIRADS) and it is recommended that they are used as add-ons to the regular B-mode examination.

5.2 Methods

5.2.1 Strain elastography

SE images in breast ultrasound may be evaluated visually using the Tsukuba score (also known as the Itoh or Ueno score) [23], semi-quantitatively using strain ratio (SR) or strain histograms (SH) [24] or by the lesion size on elastography divided by the lesion size on B-mode ultrasound (E/B ratio) [25]. An optimal elastogram includes the glandular tissue, the surrounding fat, and the lesion [11].

The Tsukuba score is a five-point visual scale, where the lesion is scored according to the extent of stiff tissue. A lesion not stiffer than the surrounding tissue is designated as 1, a value of 2 or 3 is assigned to lesions with increasing proportions of stiff tissue, a value of 4 is assigned to a lesion that is stiffer throughout, and 5 indicates that the stiffness extends beyond the margins of the mass seen on B-mode. The best cut-off point for discriminating benign from suspicious masses has been shown to be a score between 3 and 4 [26 – 28]. It has been shown that SE, in addition to B-mode ultrasound, increases the specificity of the examination (up to 97 %) and helps to avoid unnecessary biopsies [29].

Anechoic lesions with liquid content show a typical three-layered echo-pattern in SE, called the Blue Green Red (BGR) sign.

5.2.2 Shear wave elastography

For SWE, findings are measured in m/s but may also be reported in kPa depending on the system used. As for SE the optimal image should include the lesion, fat and the glandular tissue. Malignant tumors tend to be more heterogeneous and stiffer than benign tumors. Often the stiffness seems to be most marked at the periphery of the mass and may demonstrate such high values that the system is unable to record a measurement.

5.3 Clinical Applications

5.3.1 Evaluation of breast masses

An early study using SR in 99 nonpalpable benign and malignant breast masses established an optimal cut-off of 2.24 and stated that the higher the SR, the higher the risk of malignancy [30]. The cut-off for SR has since been evaluated in several studies with different systems and is incomparable between different vendors, as seen in other organ applications. In a recent meta-analysis [31], the accuracy of SR was evaluated based on 9 studies (2087 tumors) with a sensitivity of 0.88 and a specificity of 0.83. The E/B ratio (ratio of the lesion size with SE to the lesion size with B-mode ultrasound) increases with increasing tumor grading, with low grade tumors having a ratio close to 1 [11].

In the BE1 multicenter study SWE results were studied retrospectively and several parameters were examined. One finding of the study was that the addition of SWE resulted in some BIRADS 3 lesions appearing stiffer and potentially allowed for an upgrade to a 4a mass, requiring a biopsy. If SWE had been included and used in this way, the overall sensitivity and specificity would have increased to 98.6 % and 78.5 % versus 97.2 % and 61.1 % for B-mode ultrasound alone [32]. Increasing stiffness has also been shown to correlate with increasing tumor grading [33 – 36].

In cysts with pure liquid, no signals are obtained from the shear waves and the lesion is seen as black. However, in cysts with a higher viscosity shear wave signals may be obtained depicting the cyst as having a low stiffness.

5.3.2 Evaluation of axillary lymph nodes

Both SWE and SE have been used in the evaluation of axillary lymph nodes, with one study reporting a sensitivity and specificity of 82.8 % and 69.6 %, respectively, using SWE to distinguish between benign and malignant lymph nodes using a cut-off of 1.44 m/s [37]. Using SE, the sensitivity was 60 % and the specificity was 79.6 % for the diagnosis of malignancy [38]. Another study compared the AUROC for elastography with the AUROC for conventional B-mode ultrasound. The values were 62 % and 92 %, respectively, and no significant improvement was shown when elastography was added to B-mode ultrasound (AUC: 93 %) [39].

5.3.3 Prognosis

The key factors for prognostic information are provided by histological and pathological analysis, based on cancer sub-typing and also immuno-histochemical analysis. Univariate analysis has demonstrated a significant correlation between stiffness of a breast cancer and prognostic factors. For SWE, studies reported an increased stiffness for cancer grading of more malignant tumors, larger lesion size, tumor and lympho-vascular invasion in invasive breast cancer. Triple-negative carcinomas (testing negative for oestrogen, progesterone and HER2 receptors), which are often evaluated with BIRADS 3 on B-mode ultrasound, are quite difficult to assess in clinical practice. SWE is reported to show increased stiffness in these cases and can lead to the correct assessment [33 – 35, 40].

A study reporting the analysis of 396 breast cancers showed that SWE is an independent predictor of lymph node metastasis when using E-mean (mean elasticity values for a defined region of interest) as a descriptor. When the breast cancer had E-mean < 50 kPa, only 7 % of the lymph nodes were metastatic, whereas 41 % of the lymph nodes were positive when E-mean was higher than 150 kPa [41].

5.3.4 Efficacy of neoadjuvant therapy

The tumor response to neoadjuvant chemotherapy may be evaluated with different imaging modalities. In a study with a small sample size of 15 patients, the possibility of predicting response to neoadjuvant chemotherapy with SE was reported [42]. However, larger studies for SE using commercially available systems are not available. A significant correlation between response to treatment and the decrease in heterogeneity and tumor stiffness has been reported [43, 44]. Currently, imaging methods other than elastography should be used in the evaluation of tumor response to neoadjuvant chemotherapy.

5.4 Limitations and artifacts

Pre-compression with the transducer should be avoided as this increases the stiffness of all tissues. Normal fatty tissue has E-mean values ranging from 5 – 10 kPa (using SWE) if the scale is from 0 – 180, although the color scale may be changed. If the color changes according to these values, the pre-compression should be adjusted [45].

RECOMMENDATION 4

Ultrasound elastography could be used to increase diagnostic confidence in the characterization of a breast lesion (LoE 2a, GoR B) (For 20, Abstain 0, Against 0).

RECOMMENDATION 5

A BIRADS 3 lesion appearing stiffer on breast ultrasound elastography should be considered for biopsy (LoE 2a, GoR b) (For 20, Abstain 0, Against 0).

6. Prostate

6.1 Background

The screening standard for prostate abnormalities has been the combination of digital rectal examination and the serum prostate specific antigen (PSA) level. However, PSA screening leads to a substantial number of unnecessary biopsies in patients with no or indolent cancer who do not need immediate treatment [46] and has a high false-negative rate (17 – 21 %) [47]. Saturation biopsy (up to 40 cores) can rule out prostate cancer, but has many limitations, including cost and morbidity, and over-diagnosis of microscopic tumor foci [48]. SE and SWE assessment and identification of stiff prostatic tissue with a transrectal ultrasound approach can be useful as described in previous elastography guidelines [1].

6.2 Methods

6.2.1 Strain elastography

Hypoechoic stiff lesions of the prostate are suspicious for malignancy [49]. Slight compressions are induced using the transrectal transducer. The use of an inflatable balloon has been suggested to improve the standardization of compressions. The elastography box should cover the entire gland and the surrounding tissues, but avoid the bladder. Semi-quantitative information can be derived by measuring the SR between two regions of interest.

Using stepwise scanning of the prostate from base to apex, SE allows detection of stiff regions and provides stiffness comparisons between lesions and the adjacent prostatic tissue. Most studies report a significant improvement in prostate cancer identification with SE, including guidance for targeted biopsies [50 – 53]. However, there are still controversies and one recent study reported the inability to differentiate prostate cancer from chronic prostatitis [54]. The sensitivity, specificity, negative predictive value, positive predictive value, and accuracy for identifying cancer index lesions for focal therapy were 58.8 %, 43.3 %, 54.1 %, 48.1 %, and 51.6 %, respectively [55]. Though improvement in biopsy guidance is reported in many studies [53, 56, 57], others did not confirm this result [58].

6.2.2 Shear wave elastography

Unlike SE, SWE requires no compression on the rectal wall [59]. Optimized settings include maximizing penetration and setting up an appropriate scale. The image can cover the entire gland in the transverse section when the prostate is not markedly enlarged. Otherwise, each side of the prostate is imaged separately from base to apex for review and measurements of elastography values. For each plane, the transducer is maintained in a steady position until the image stabilizes. Hypoechoic stiff lesions are suspicious for malignancy. The ratio between the mean elasticity values of two regions can be calculated.

In young healthy subjects the entire prostate exhibits a uniform low stiffness appearance with low elasticity values [60, 61]. In benign prostate hyperplasia, the peripheral zone remains homogeneous with low stiffness, while the central and transition zones become heterogeneous and stiff, particularly when there are calcifications. Typical benign peripheral lesions have a similar stiffness as the surrounding normal parenchyma, while cancers are stiff [60, 61]. The best cut-off stiffness value to maximize the negative predictive value for malignant lesions was found to be 35 and 37 kPa in two studies with 2D-SWE [57, 58] with a sensitivity, specificity, PPV and NPV of 63 %, 91 %, 69.4 %, and 91 %, respectively. The SWE ratio provided additional information as it considers the increased stiffness of the peripheral zone from calcification and chronic prostatitis. The ratio showing the best accuracy to differentiate between the nodule and the adjacent peripheral gland for benign and malignant lesions was 1.5 ± 0.9 and 4.0 ± 1.9, respectively ($p < 0.002$) [61].

6.3 Clinical applications

Several studies indicate that elastography provides useful additional information to conventional transrectal ultrasound for prostate cancer detection. Applications that have been more extensively investigated include the characterization of abnormal areas, the detection of lesions not seen with any previous imaging technique and biopsy targeting. Additionally, elastography could be combined with other imaging techniques in the same examination to address the heterogeneous growth pattern of prostate cancer. Improvement in detection and prediction of cancer was seen during multiparametric ultrasound when elastography is used as a triage test followed by contrast-enhanced ultrasound or as an adjunct during image fusion of magnetic resonance imaging and transrectal ultrasound [62 – 65].

6.4 Limitations and artifacts

Both techniques suffer from intrinsic limitations: not all cancers are stiff and not all stiff lesions are cancers (particularly in the presence of calcifications and fibrosis). The transrectal technique carries an intrinsic risk of inadvertently applying excess pre-compression because of the end fire arrangement of the transducer.

Limitations of SE include the non-uniform force over the gland and intra- and inter-operator dependency. 2D-SWE has additional limitations such as a slower frame rate and the small elasticity box which only allows examination of half the gland at a time.

RECOMMENDATION 6

Transrectal ultrasound elastography of the prostate could be used to identify suspicious target regions for biopsy in order to increase the diagnostic yield of biopsy (LoE 2b, GoR b) (For 20, Abstain 0, Against 0).

7. Thyroid

7.1 Background

Chronic thyroiditis and malignant tumors increase diffuse or focal thyroid stiffness [66]. Elastography is emerging as a potential indicator for these abnormalities and may provide additional information to support clinical decision-making.

7.2 Classification systems – TIRADS

Accurate estimation of the malignancy risk by ultrasound could help to select thyroid nodules with a high risk of cancer for fine needle aspiration and biopsy (FNAB). More recently, an assessment concept called “grading system” or “reporting system” termed “Thyroid Imaging Reporting and Data System” or TIRADS has emerged, allowing thyroid nodules to be classified into categories related to their ultrasound patterns [66 – 74].

7.3 Methods

SE is the initial method which has been implemented on most commercially available ultrasound systems, thus evidence is quite consolidated on this topic, with a number of studies and meta-analyses being published [75 – 81]. More recently, SWE has become available for thyroid evaluation with multiple studies reported [82 – 85].

7.4 Clinical applications

7.4.1 Strain elastography

Two different methods of assessing SE outcome have been reported, namely semi-quantitative scoring systems involving five, four, or two color patterns respectively [86 – 88] and SR, which compares the strain values of the nodule to those of the surrounding thyroid parenchyma (parenchyma-to-nodule ratio) or the surrounding muscles (muscle-to-nodule ratio) [4, 89]. Although no consensus has been reached about the cut-off values to use for SR (as low as 1.5 for benign nodules and as high as 5 for malignant nodules have been suggested), it has been shown that the SR has a lower interobserver variability and is more easily learned than simple color patterns [4]. Importantly, most studies on SE were performed in selected populations with a high prevalence of malignant nodules. It has been shown that SE has a lower sensitivity and specificity in a low-risk population [4, 90]. Furthermore, tumors other than papillary carcinomas may have an unexpectedly low stiffness [4, 91, 92]. In patients with coexistent diffuse thyroid disease, the role of SE in detecting malignant nodules has still not been validated [4]. The most recent meta-analysis [81] included 13 studies on SE performed from 2007 to 2016, with sensitivities ranging from 48 % [93] to 97 % [94] and specificities ranging from 64 % [95] to 100 % [94]. The pooled sensitivity and specificity of the meta-analysis was 84 % (95 % CI, 76 % – 90 %) and 90 % (95 % CI, 85 % – 94 %), respectively, with pooled accuracy of 94 % (95 % CI, 91 % – 96 %).

7.4.2 SWE

The mean SW elasticity for malignant thyroid nodules is 19.60 – 52.18 kPa with a reported cut-off value of 26.6 – 65 kPa [96 –

104]. For benign nodules the mean elasticity is lower at 15.3 – 28 kPa [96 – 104]. Studies included nodules from 2 – 71 mm and most were papillary carcinomas. Therefore, cut-off values have a wide range and a single threshold cannot be established [82, 83, 85]. The sensitivity for SWE has been reported as 63.8 – 93.8 %, and the specificity as 50 – 88.2 % [96, 97, 100, 102, 104 – 106]. The most recent meta-analysis [82] included 14 studies and 2851 thyroid nodules with cut-off values ranging from 26.6 to 85.2 kPa. It concluded that 2D-SWE has a fairly good diagnostic accuracy although the sensitivity and specificity are average. Studies using ARFI indicated that it enables the evaluation of tissue stiffness and the mean SWE velocity for malignant nodules is 3.13 – 3.9 m/s [96, 107 – 111] with a cut-off value 2.15 – 3.77 m/s [96, 107 – 111]. Interestingly, a recent meta-analysis [81] showed that SE and SWE are not significantly different in terms of sensitivity (SWE pooled sensitivity = 79 % [95 % CI, 73 % – 84 %]) but SE is superior to SWE in terms of specificity (SWE pooled specificity = 87 % [95 % CI, 79 % – 92 %]) and accuracy (SWE pooled accuracy = 83 % [95 % CI, 80 % – 86 %]).

7.5 Limitations and artifacts

The thyroid is among the most extensively investigated non-liver application after the breast. Nevertheless, the relevance in the malignant/benign differential diagnosis remains unclear. Recent American Thyroid Association and Korean guidelines do not consider stiffness as an indicator of malignancy. However, elastography was recently mentioned by both the French TIRADS and the EU-TIRADS as a complementary imaging tool [70, 112]. Thus, elastography should not replace B-mode US assessment but should be used as a complementary tool for assessing nodules for fine-needle aspiration, especially due to its high negative predictive value (only 3 % false-positive results) [70].

RECOMMENDATION 7

Ultrasound elastography of the thyroid could be used as part of nodule characterization, particularly with use of semi-quantitative methods (LoE 2A, GoR A) (For 17, Abstain 3, Against 0).

8. Pancreas

8.1 Background

Elastographic properties of the pancreas may be studied with a transabdominal approach, as well as with an endoscopic or intraoperative ultrasound approach. Pancreatic transabdominal ultrasound elastography requires clear visualization of the gland (which is not always possible with external ultrasound), whereas endoscopic ultrasound (EUS) is a minimally invasive technique that provides high-resolution images of the pancreas, with the close vicinity of the transducer and the pancreas avoiding artifacts (fat, gas, etc.).

8.2 Methods

For the elastographic assessment of the pancreatic parenchyma and focal pancreatic lesions, SWE [7, 113 – 133] as well as SE [7, 119, 120, 123, 124, 131, 134 – 177] may be used. Transabdominal elastography can be performed both by using SE with qualitative and semiquantitative information, and SWE with qualitative and quantitative data. EUS can be performed currently only with SE techniques with qualitative and semi-quantitative evaluation [178]. For the semi-quantitative approach, both SR and SH can be used in order to obtain an estimate of the elasticity [153].

The normal pancreas has a uniform intermediate stiffness throughout the head, body, and tail [123, 124, 129, 130, 132]. Embryologically, the pancreas develops from two primordia, a dorsal and a ventral part. With SE, elasticity properties seem to be almost similar in the two parts of a healthy pancreas with a homogeneous low stiffness appearance [158]. Studies in normal volunteers affirmed that the mean wave velocity value obtained in a healthy pancreas with the ARFI technique is approximately 1.40 m/s [114].

8.3 Clinical applications

8.3.1 Effect of aging, gender, anatomical segment, and other variables

With advancing age, pancreatic elasticity may decrease as has been shown consistently for SE [134] and SWE [121, 129, 131]. Data on the influence of gender, body mass index (BMI), and pancreatic echogenicity are not consistent, with most studies demonstrating no significant influence of these variables on shear wave velocity [113, 116, 121, 129, 131]. One study using SE with SH analysis showed lower mean strain values in patients with a hyperechoic pancreas and higher BMI [134]. In another study shear wave velocity was significantly lower in men compared to women [129].

8.3.2 Acute pancreatitis

The consistency of the pancreatic parenchyma usually becomes stiffer in acute pancreatitis as compared to the healthy pancreas, which is identifiable with SE and SWE, including ARFI [116]. Necrosis is identified as a low stiffness area. However, studies using elastographic techniques in patients with acute pancreatitis are conflicting [116, 130, 179, 180]. One prospective study failed to find significant differences in pancreatic shear wave velocities between patients with acute pancreatitis and healthy volunteers [130]. Three other studies showed significantly higher pancreatic shear wave velocities in patients with acute pancreatitis compared to persons with a normal pancreas [116, 179, 180]. In one of these studies, shear wave velocities of patients with acute pancreatitis were higher than in chronic pancreatitis patients [179]. Another prospective study compared transabdominal ARFI imaging with B-mode ultrasound and computed tomography (CT) at hospital admission for the diagnosis of acute pancreatitis. SWE was more accurate (100 %) for the diagnosis of acute pancreatitis than CT (76 %) and B-mode ultrasound (53.4 %). The authors were able to identify segmental involvement of the pancreas as well as parenchymal necrosis [180].

8.3.3 Chronic pancreatitis

Qualitative SE displays the pancreatic parenchyma in chronic pancreatitis with a heterogeneous colored (honeycombed) pattern, with predominantly stiffer strands. Nevertheless, differential diagnosis between chronic pancreatitis and pancreatic tumor can be challenging during elastography because both diseases have a similar stiffness. Therefore, elastography alone is not able to distinguish chronic pancreatitis from malignant tumors [164].

Both SWE and SE may be used to assess pancreatic fibrosis and chronic pancreatitis and in particular to grade the severity of fibrosis (based on simple scoring systems with 4 grades) and chronic pancreatitis [115 – 117, 122 – 124, 127, 131, 136, 138, 142, 146, 151, 164, 167, 169, 170, 179, 181 – 185]. In patients with chronic pancreatitis, pancreatic shear wave velocities [116, 124, 127, 131, 186], SR [148] and SH [146] are significantly higher than in healthy volunteers or patients with a normal pancreatic parenchyma. Several studies have shown a significant correlation between SWE [117, 123, 184] and semi-quantitative SE [138, 167, 169, 185] and histological pancreatic fibrosis stage. Moreover, SWE [122, 124, 169] and SR [141] are significantly correlated with stages of chronic pancreatitis derived from EUS-based criteria for the diagnosis of chronic pancreatitis. Another recent study showed significantly higher pancreatic SWE velocities in patients with clinical markers of severe disease (disease duration > 10 years, chronic analgesic treatment, lower body weight) [127]. A direct relationship between the SR of pancreatic parenchyma and low stiffness peripancreatic tissue and the probability of pancreatic exocrine insufficiency was shown in a study using EUS-SE [136]. Another study reported an inverse correlation between preoperative SW velocity and postoperative exocrine function in patients undergoing pancreatic resection [117].

EUS elastography might be helpful in identifying patients with autoimmune pancreatitis, due to the unique appearance of diffuse stiff tissue with an elastographic pattern visible both in the mass lesion and in the adjacent pancreatic parenchyma, with mainly stiff color signals that were evenly spread over the head and the body of the pancreas [161, 187].

8.3.4 Preoperative indications

Recently, elastography has been used prior to pancreatic surgery to examine the gland stiffness in order to assess the risk of surgical complications. Evaluation of pancreatic stiffness might be an objective index to estimate pancreatic fibrosis and predict the risk of postoperative pancreatic fistula. Data from several studies suggest that SWE [115, 117, 184, 188] and SE [138, 170, 185] may be used for this purpose. In particular, a pancreatic parenchyma with a low stiffness as determined by semi-quantitative SE [138, 170] or SWE [117] proved to be an independent predictor of postoperative pancreatic fistula.

8.3.5 Pancreatic ductal adenocarcinoma and other solid pancreatic neoplasms

In pancreatic ductal adenocarcinoma (PDAC), shear wave velocities are significantly higher than in normal pancreatic parenchyma obtained in healthy subjects [116, 125, 133] as well as in pancreatic parenchyma surrounding the tumor [125]. Shear wave velocities measured in PDAC usually exceed 3 m/s [116, 125, 126, 133]. However, there is a significant overlap of SWE velocities between malignant solid lesions, benign solid lesions, and chronic pancreatitis [116, 126]. One study demonstrated a significantly higher difference between the SWE velocities of malignant lesions and surrounding pancreatic parenchyma compared to the difference values between benign lesions and surrounding parenchyma [126]. No large prospective comparative studies evaluating the accuracy of SWE for the characterization of solid pancreatic lesions are available.

More evidence is available on the clinical value of EUS-SE for the differential diagnosis of solid pancreatic lesions [172, 189 – 192]. An early study described EUS elastography patterns in healthy subjects, in diffuse chronic pancreatitis and in focal pancreatic lesions [139]. All malignant pancreatic tumors and serous cystadenomas showed a honeycomb pattern of medium stiffness, and were well delineated against healthy parenchyma. However, this pattern was also observed in half of the chronic pancreatitis patients, so that the specificity of the method was reported at only about 60 %, attributed to fibrotic structures producing similar mechanical properties in cancer and chronic pancreatitis [139, 164]. Therefore, elastography is not sufficient to contribute to the early diagnosis of pancreatic carcinoma in chronic pancreatitis [139, 164].

Qualitative [137, 139, 163, 164, 193 – 195] and semi-quantitative SE approaches (SR, SH analysis) [135, 142 – 144, 149, 150, 152 – 156, 175, 177, 196 – 199] have been used for the differential diagnosis of benign and malignant focal pancreatic masses, with both showing high overall accuracy. Computer-aided diagnosis techniques might improve the accuracy for the differential diagnosis of focal pancreatic masses, with artificial neural networks being used most often [154, 156]. Several multicenter studies [155, 156, 194] and other prospective studies [135, 149, 150, 152, 177, 197, 198] consistently showed a very high sensitivity (over 90 %), but considerably lower specificity and negative predictive values for the diagnosis of benign versus malignant focal pancreatic masses. These findings have been summarized in meta-analyses, affirming the very high sensitivity (95 % – 99 %) and negative predictive value of EUS-SE, but limited specificity (64 % – 76 %) and positive predictive value to diagnose pancreatic malignancy [172, 189 – 192]. Significant differences in favor of qualitative or semi-quantitative assessment techniques have not been observed in meta-analyses. Therefore, there is expert consensus that SE cannot replace a cytopathological diagnosis of focal pancreatic disease [162, 200, 201]. Combining several EUS-based advanced tools of tissue characterization may provide the best results in differential diagnosis of focal pancreatic lesions [135, 143, 144, 149, 202 – 205]. Nevertheless, when EUS-guided sampling is negative or inconclusive, suspicious findings with elastography and contrast-enhanced techniques will influence further clinical decisions by indicating repeat sampling or direct referral to surgery. On the other hand, the finding of a solid pancreatic lesion with elastographic properties of low stiffness and without hypo-enhancement in contrast-enhanced EUS is nearly always predictive for the benign nature of the lesion. Since the negative predictive value of EUS-FNA for the diagnosis of a malignant solid pancreatic lesion is only 72 % [203 – 207], such a finding may prevent potentially nondiagnostic or risky procedures [195, 207].

8.3.6 Cystic pancreatic tumors

Elastography can have a role in pancreatic cystic lesions, both with SE and with SWE, in particular with ARFI. SWE has been shown to be accurate for the differentiation between serous and mucinous cystic pancreatic lesions [133, 208 – 212]. Serous cystadenomas are filled with serous fluid exhibiting similar physical properties as water, while numerous and dense septa together with a fibrous scar can be present in a mucinous cystadenoma. Therefore, the microcystic serous cystadenoma appears as a very stiff lesion with EUS-SE [139, 164, 196]. With ARFI, shear wave velocity in serous cystadenoma is infinitely high and numerical values cannot be obtained. Due to the more complex fluid content, shear wave velocities in mucinous cystic lesions are very high, but numerical values may be obtained in most cases [133, 208 – 212].

8.4 Limitations and artifacts

EUS-elastography suffers from technical limitations and artifacts. Some issues are common with transabdominal ultrasound, such as the need to obtain a close proximity to the target and to avoid anatomical planes allowing slip movements anterior to or within the imaged region [1]. In particular, large vessels in the imaged area represent the main reason for shear stress damping. Issues peculiar to EUS are essentially caused by the small size of the transducer providing a limited stress source to image the region of interest. In addition, it is very difficult to standardize the pressure exerted by the echoendoscope tip to the gastrointestinal wall, resulting in variability of the color mapping. Lastly, respiration and heartbeat-induced movements of the target lesion may cause a complete lack of color signal within the region of interest. As far as the color mapping of EUS elastography is concerned, disadvantages include subjective differences in color vision and image categories that may not correspond well to pathology [194]. The selection of frames for the SR or SH measurements is user-dependent. In addition, unrepresentative elastograms or reference tissues with a different distance to the stress source may result in method bias [213]. For these reasons, finding an optimal cut-off for differentiating pancreatic tumors from benign disease has been challenging.

RECOMMENDATION 8

Transabdominal and endoscopic ultrasound elastography may be used as additional imaging tools for the diagnosis and grading of chronic pancreatitis (LoE 2b, GoR B) (For 20, Abstain 0, Against 0).

RECOMMENDATION 9

Endoscopic ultrasound elastography could be used as a complementary imaging tool for the characterization of solid pancreatic lesions. However, it cannot decisively differentiate focal pancreatitis from pancreatic carcinoma (LoE 2a, GoR B) (For 20, Abstain 0, Against 0).

RECOMMENDATION 10

When a combination of endoscopic ultrasound elastography with contrast studies suggests pancreatic cancer despite a negative or inconclusive biopsy, repeated sampling or surgery should be considered (LoE 2b, GoR B) (For 12, Abstain 7, Against 1).

9. GastroIntestinal Tract

9.1 Background

The gastrointestinal tract wall may be visualized by ultrasound as a layered structure consisting of typically 5 layers [214, 215]. When examining the intestine, it is preferable to use frequencies above 7.5 MHz to enable optimal visualization of wall layers, thickened bowel wall and focal lesions. This also applies for SE and SWE.

9.2 Methods

SE and SWE are the methods used for elasticity imaging and measurements in bowel examinations. Studies investigating elastography of bowel wall lesions are predominantly based on SE.

9.2.1 Image interpretation and evaluation

Pathological lesions that increase wall thickness are most relevant for SE and SWE. This is because the bowel wall is a thin structure on ultrasound imaging that has natural peristalsis and allows considerable movement on both the serosa and the luminal sides. This tends to add artifacts to strain imaging and makes a targeted SWE or SE measurement more difficult and user-dependent. The bowel wall may become thickened in both neoplastic and inflammatory disease, predominantly in Crohn's disease (CD). In particular, SE has been applied in order to clinically distinguish fibrotic from inflammatory lesions in CD and to distinguish rectal adenoma from adenocarcinoma.

9.3 Clinical applications

9.3.1 Distinction between fibrous and inflammatory strictures in Crohn's disease

Several studies on CD in animal models and human specimens conclude that stiffness is associated with the presence of fibrotic strictures. Some studies indicate that SE and SWE elastography can differentiate fibrosis from inflammatory lesions [216 – 218]. A study compared SE in terminal ileum stenosis in CD reporting a higher visual score of tissue stiffness in fibrosis using magnetic resonance (MR) enterography as a reference [219]. Another ex-vivo study on bowel specimens from CD and neoplastic lesions also showed that higher stiffness was present in both CD lesions and in adenocarcinoma, but not in adenomas [220].

The results from seven small series were included in a systematic review of 154 CD lesions in 129 patients [221], suggesting that stiffness was significantly higher in fibrotic stenosis. Nevertheless, the systematic review mentions “inhomogeneous and scarcely comparable” endpoints, as authors used either absolute strain values or a strain ratio with various anatomic structures for comparison (mesenteric fat surrounding the bowel wall or abdominal wall muscles). In a study of ten patients, SE using the mean strain in the bowel wall of affected and unaffected bowel segments pre-, intra- and postoperatively found significant differences in strain values in affected and unaffected segments which correlated well with the histological distribution of connective tissue and collagen content [222]. Also, the strain measurements had an acceptable intraclass correlation coefficient (ICC) in the three examinations. A study of 23 consecutive patients undergoing surgery for CD [223] found excellent differentiation of patients with severe ileal fibrosis by histology but also by using SR (including an excellent inter-rater agreement). Conflicting findings are reported in a prospective study on SE in 26 patients undergoing surgery for stricturing CD. On preoperative ultrasound, the SR did not correlate with histological scoring of fibrosis or inflammation [224]. Strain imaging of bowel lesions in CD may predict the response to anti-inflammatory treatment. In a prospective study of 30 patients with CD, the five patients who needed surgery had significantly higher SR measurements at baseline and there was a significant negative correlation between the SR at baseline and wall thickness following 52 weeks of anti-tumor necrosis factor (TNF) therapy [225]. SWE should not be used as a method to distinguish fibrotic from inflammatory lesions in CD based on current evidence.

9.3.2 Characterization and staging of rectal tumors

The differentiation and staging of rectal tumors can be performed using SE as an add-on to B-mode endoscopic rectal ultrasound (ERUS). Thus, SE may improve the staging of rectal cancer and differentiate adenoma from adenocarcinoma, when compared to ERUS alone and with MR imaging (with high interobserver agreement of recorded videos and images) [226 – 228]. Another group found good correlation between diffusion-weighted MR imaging which is associated with fibrosis, and SWE of malignant rectal tumors [229]. Another study assessed the performance of ERUS for rectal tumors using SWE using an 8 MHz endorectal transducer, finding that the tumor stiffness measurements corresponded accurately to the pathological tumor T-stage and diagnostic accuracy of tumor staging improved from 76.7 % to 93.3 % [230].

RECOMMENDATION 11

Ultrasound strain elastography can be used to characterize bowel wall lesions in Crohn’s disease (LoE 3b, GoRC) (For 19, Abstain 1, Against 0).

RECOMMENDATION 12

Ultrasound elastography may improve the staging of rectal cancer when used as an add-on to endoscopic rectal ultrasound and magnetic resonance imaging (LoE 2b, GoRC) (For 17, Abstain 3, Against 0).

10. Spleen

10.1 Background

Spleen stiffness measurement is an elastography technique used to assess the severity of chronic liver disease, mainly in conjunction with liver stiffness measurements for the evaluation of liver fibrosis or portal hypertension-related complications. Various SWE techniques have been investigated to predict the presence of clinically significant portal hypertension, esophageal varices or to predict long-term prognosis.

10.2 Methodology

Spleen elastography should be performed after at least 3 hours of fasting and after at least 10 minutes of rest [231, 232], with the patient in dorsal decubitus and with the left arm in maximal adduction [233]. The transducer should be placed between the left intercostal spaces in an area with a good ultrasound window needed for TE [234], or at least 2 cm below the capsule for non-TE techniques [235, 236], with the measurement preferably being performed at the inferior pole [237].

10.3. Clinical applications

a) Assessment of liver fibrosis

Using spleen stiffness as a surrogate marker for staging liver fibrosis, two studies [238, 239] demonstrated a pooled sensitivity and specificity for detecting significant fibrosis (F2) and cirrhosis (F4) of 0.70 and 0.87 and 0.77 and 0.82, respectively with an AUROC of 0.88 and 0.85, respectively [22].

b) Assessment of clinically significant portal hypertension

Spleen stiffness correlates well with the hepatic vein portal gradient and has an excellent diagnostic accuracy (AUROC = 0.92) for clinically significant portal hypertension, irrespective of the technique used [240], with TE showing a better correlation with the hepatic vein portal gradient than measuring liver stiffness [234]. For values ≥ 46 kPa, the AUROC for clinically significant portal hypertension varies from 0.846 to 0.966, with good sensitivity (0.77 – 0.88) and specificity (0.79 – 0.91) [234, 241].

For pSWE, the overall correlation with the hepatic vein portal gradient is similar and better than for liver stiffness measurements [242], but for values > 10 mmHg, the association is weaker [242, 243]. However, for pSWE, the plotted sensitivity is higher than for other techniques (0.98 vs. 0.62 – 0.83), while the specificity is lower (0.78 vs. 0.89 – 0.93), thus raising the possibility of the heterogeneity and variability of this technique [240, 244].

As for 2D-SWE, the diagnostic accuracy varied significantly, as AUROC analysis shows: 0.63 (for a cut-off value of 34 kPa) [245], 0.725 [235] or 0.84 [237]. Despite the fact that the last two studies recommend different cut-off values to rule-in (≥ 40 or 35.6 kPa) or out (≤ 22.7 or 21.7 kPa) clinically significant portal hypertension, the diagnostic accuracy remains low for the study by Procopet et al. [235] (12/40 correctly classified), but satisfactory for the study by Jansen et al. [237] (66/111 patients correctly classified). However, if a combined approach is used (both spleen and liver stiffness measured), only 11/109 patients (89.9 % accuracy) are misclassified [237].

c) Assessment of oesophageal varices

TE of splenic stiffness has a good accuracy to detect the presence of oesophageal varices (80.4 %), but it is unable to differentiate the grade [233]. Values ≤ 40kPa were proposed to rule-out esophageal varices, while values ≥ 55kPa were suggested to rule them in [234]. In a meta-analysis, the pooled sensitivity and specificity to detect varices was satisfactory (0.76 and 0.78, respectively), while the sensitivity is better (0.86 vs. 0.69) for the detection of varices needing treatment [246]. A modified calculation algorithm for TE was proposed, so that values > 75 kPa could be measured, which proved to be the sole independent predictor of the need to treat [247]. Therefore, a dedicated transducer and calculation algorithm were developed, showing better performance compared with the original algorithm and with liver stiffness [248].

For pSWE, the sensitivity and specificity for detecting oesophageal varices varies from 0.31 and 0.79 [249] up to 0.95 and 0.92 [243]. However, the pooled performance for detecting the need to treat appears to be lower than for TE [246], although the analysis did not take into account a report which showed very good positive and negative predictive values: 0.97 and 0.89, respectively [243].

With 2D-SWE, [245] there is no discrimination between patients with and without varices needing treatment. In a much larger cohort, however, the AUROC for detecting oesophageal varices of any grade was 0.8, while the probability is only 10 % for patients with compensated cirrhosis if the spleen stiffness is lower than 25.6 kPa (10). If 2D-SWE SSM (</≥ 38 kPa) is used in a stepwise approach alongside liver stiffness (</≥ 19 kPa) and platelet count (≤/> 100x103), the oesophageal varices can be ruled-out with 83 % accuracy and 74 % of unnecessary endoscopies could be eliminated [248].

d) Assessment of prognosis and response to therapy

Spleen stiffness can also predict liver-related complications, as the only independent predictor of decompensation besides the MELD score (if higher than 54 kPa), in a cohort of compensated hepatitis C virus (HCV) cirrhosis, during a 2-year follow-up period [250]. No data is available regarding the role of spleen stiffness in monitoring the response to non-selective beta-blockers. Spleen stiffness (assessed by pSWE) seems to decrease after TIPS placement [251, 252], suggesting that spleen stiffness could be an additional tool to evaluate TIPS efficiency.

Small series also suggest that successful antiviral therapy of HCV cirrhosis induces a small reduction of spleen stiffness during follow-up, which is not always significant and it is not as important or as persistent as liver stiffness reduction [253, 254], reflecting more likely a reduction of hepatic inflammation.

e) Miscellaneous

Spleen stiffness was also used to assess patients with non-cirrhotic portal hypertension. In extrahepatic portal vein obstruction, spleen stiffness increases and is higher in patients with a history of bleeding [255]. In patients with idiopathic portal sinusoidal disease, spleen stiffness is markedly increased, in contrast to quasi-normal liver stiffness values [256, 257]. Furthermore, a combination could be used in children with biliary atresia before or after Kasai portoenterostomy to predict outcome or to monitor subsequent liver disease and portal hypertension [258, 259]. Spleen stiffness by TE was also positively correlated with the grade of bone-marrow fibrosis in patients with primary myelofibrosis, suggesting that this could be a simple noninvasive method to monitor disease progression [260].

10.4 Limitations and artifacts

TE can be performed in only 85 – 90 % of cases, mainly because of high BMI, presence of ascites, lung or colonic gas interposition, or transverse spleen diameter < 4 cm [233, 234, 247]. An additional 12 – 21 % of patients reach the maximum value (75 kPa) measured by the conventional machine [233, 247], hence the applicability of TE is approximately 70 %. The applicability of 2D-SWE is similar and appears to be related to a higher BMI and smaller spleen size [261]. As for pSWE, the applicability is higher (up to 97 %) [242], but the reproducibility is influenced by small spleen size and central obesity [244].

RECOMMENDATION 13

Ultrasound elastography of the spleen can be used as an additional noninvasive method to assess portal hypertension (LoE 2b, GoR B) (For 20, Abstain 0, Against 0).

11. Kidney

11.1 Background

Renal elastography has been used for the noninvasive assessment of chronic kidney disease (CKD), particularly for the early stages when renal function is not yet significantly affected, or for disease monitoring [262]. The hypothesis that the development of glomerular and interstitial fibrosis should lead to stiffness changes is supported by experimental findings in a rat model of CKD [263].

11.2 Methods & confounding factors

11.2.1 Strain elastography

SE can only be used for superficial kidneys, usually renal transplants, mainly a qualitative technique that supposes uniform deformation of the tissue of interest, with a limited role due to the depth of the organ, the difficulty to apply reproducible homogeneous external deformation and the inability to achieve absolute stiffness measurements [264].

11.2.2 Shear wave elastography

TE allows quantitative evaluation of the tissue stiffness and has been widely used for liver fibrosis estimation [2, 265], but the volume of tissue involved in the measurement is at a fixed depth and has a length of 40 mm, making this technique unsuitable for renal stiffness estimation.

The inter-operator agreement of pSWE used in transplanted kidneys obtained in different studies was fair or moderate with the ICC ranging between 0.31 [268] and 0.47 [269]. In studies performed in native kidneys, the reproducibility of the method was strong, with ICCs between 0.60 [270] and 0.71 [271]. The inter-operator agreement obtained in the elastographic assessment of the kidneys (native and transplant) was lower compared to studies of liver stiffness (ICCs are over 0.80), because of confounding factors. Currently, there are few studies available using 2D SWE techniques in the assessment of the kidneys [272, 273].

11.3 Clinical applications

11.3.1 Normal kidney stiffness

A limited number of studies (most of them using pSWE) report normal kidney stiffness, and are different depending on the type of pSWE device used. In adult native kidneys, normal cortical stiffness values range from 2.15 to 2.54 m/s with one system [114, 270, 271, 277 – 279] compared to 1.23 to 1.54 m/s with a different system [280]. In 9 – 16-year-old children, higher pSWE stiffness values were found, ranging from 3.00 to 3.33 m/sec (mean 3.13 ± 0.09 m/s, corresponding approximately to 29.4 kPa). In a study performed in healthy people aged 18 – 30, 31 – 50, 51 – 65, and above 65 years, pSWE was 2.94 ± 0.60, 2.26 ± 0.82, 2.48 ± 0.8 and 1.82 ± 0.63 m/s, respectively [277]. In the same study, a statistically significant difference was found between women and men. Surprisingly, normal kidney stiffness was found to exhibit an inverse, statistically significant relationship with patient age ($p = 0.0003$). Using pSWE, similar values were found in a small series of normal volunteers with superficial kidneys, with a cortical average stiffness of 15.4 ± 2.5 kPa [281]. The stiffness of the renal medulla was found to be lower than the cortical stiffness [272], except for in one study using pSWE [278].

11.3.2 Kidney stiffness for the assessment of renal pathology

In renal transplantation, serum creatinine levels and estimated Glomerular Filtration Rate (eGFR) are poor predictors of the severity of histological lesions. A noninvasive test that could provide diagnosis and/or prognosis early on to avoid repeated biopsies and to allow early targeted therapeutic intervention could improve patient management. Several studies report a correlation between renal stiffness and fibrosis or renal function. In experimental models of glomerulosclerosis, the cortical stiffness was correlated to the degree of renal dysfunction [263]. In humans, this correlation remains highly variable in both native and transplanted kidneys. Some authors reported a correlation between renal stiffness and fibrosis or renal function with several techniques [270, 278, 282 – 285].

In other studies, the correlation between CKD stages and kidney stiffness was negative, as shear wave velocity was found to decrease with increasing stages of CKD [270, 286] or decreasing eGFR [287, 288]. The cut-off values of renal stiffness proposed by different studies could only predict advanced stages of CKD. In the remaining studies, no correlation was found between renal stiffness and the degree of CKD or interstitial fibrosis and tubular atrophy, even in diabetic CKD [270, 272, 278, 288 – 294]. The renal perfusion changes might impact renal stiffness and explain some discrepancies between results [284], as intrarenal blood flow is decreased with the progression of fibrosis. Thus, renal blood flow decrease could be the cause of the decrease of stiffness with the progression of CKD, and could have a bigger influence on stiffness compared to renal fibrosis.

Additional preliminary applications include stiffness assessment in the case of reflux nephropathy and tumor. In a study of 28 children, CKD degree increased SWE values mainly in the kidney involved with vesicoureteral reflux (6.57 ± 0.96 m/s) but also in the contralateral kidney (4.09 ± 0.97 m/s) while the normal value in the pediatric population without renal disease was 3.13 ± 0.09 m/s [295]. The increased stiffness even in the contralateral kidney may result from increased glomerular filtration and minimal fibrosis. Renal elastography might also play a role in the detection and characterization of renal masses, improving the identification of ill-defined lesions and providing information about tumor stiffness [296].

11.4 Limitations and artifacts

Anatomical confounding factors include renal anisotropy, blood perfusion and hydronephrosis. The effect of anisotropy has been demonstrated in muscle and kidney elastography due to their spatial organization [275, 276]. When shear wave propagation is parallel to the renal tubules and interlobular arteries (and the ultrasound beam is perpendicular to these structures), the velocity of the shear waves is increased [262]. Elasticity measurements performed in the perpendicular direction to the long axis of the pyramids exhibit higher values for all renal compartments. Renal perfusion strongly affects renal elastography, with a drop in the medulla ranging from 44 % to 72.7 % in renal artery occlusion, and an increase over 500 % in renal vein thrombosis [276]. Hydronephrosis also results in a renal elasticity increase, with a correlation between urinary tract pressure and cortical stiffness varying from 119 % to 137 % between 5 and 40 mmHg [276]. Additional confounding factors include the type of technology and effect of transmit frequency, attenuation of transmit pulse (deteriorating signal-to-noise ratio). Using ARFI, the shear wave velocity was reduced by 27 % when the depth increased from 2 – 3 cm to 6 – 7 cm (2.95 ± 0.41 m/s and 2.16 ± 0.61 m/s, respectively) [277].

Measurement depth influences the reproducibility of the method, a lower reproducibility being found in patients with deep kidneys, either native kidneys at a depth more than 4 cm or transplanted kidneys.

RECOMMENDATION 14

No current recommendation can be given for the application of ultrasound elastography in native kidneys (LoE 2b, GoR B) (For 10, Abstain 0, Against 0).

RECOMMENDATION 15

Ultrasound renal elastography can be used as an additional tool for the diagnosis of chronic allograft nephropathy (LoE 2b, GoR B) (For 9, Abstain 1, Against 0).

12. Lymph nodes

12.1 Background

Noninvasive discrimination of malignant and benign lymph nodes is important for further diagnostic and clinical decision-making. Whereas contrast-enhanced ultrasound is not recommended for the assessment of lymph nodes [297], elastography has a better diagnostic performance [298], with evidence for the examination of superficial lymph nodes and mediastinal lymph nodes. Superficial lymph nodes have been investigated by percutaneous US using SE and SWE. Mediastinal lymph nodes have been investigated by endoscopic ultrasound using only SE.

12.2 Methods

SE is the method most frequently described, as the technique is more widely available on most commercial systems, with more consolidated evidence with a number of single research studies and two meta-analyses published. More recently, SWE has been evaluated with one meta-analysis published.

12.3 Clinical applications

12.3.1 Differential diagnosis of lymphadenopathy

Assessment of superficial lymph nodes using SE presents conflicting data. Two recent meta-analyses demonstrated a high accuracy in differentiating between benign and malignant lymph nodes. The first meta-analysis included 578 patients with 936 lymph nodes with a sensitivity of the scoring and SR measurements of 76 % and 83 %, respectively [299]. The second meta-analysis included 545 patients with 835 lymph nodes and indicated a sensitivity of the elasticity scoring and SR measurements of 74 % and 88 %, with a specificity of 88 % and 91 %, respectively [300].

A meta-analysis including 481 patients with 647 lymph nodes evaluated the role of SWE in superficial lymph nodes. SWE for the discrimination of malignant and benign lymph nodes achieved a sensitivity of 81 % and specificity of 85 % [301]. The latest meta-analysis regarding the value of EUS elastography for the differentiation of malignant and benign lymph nodes included 6 studies with 368 patients and 431 lymph node, with SE demonstrating a sensitivity of 88 %, and a specificity of 85 % [302]. Newer studies including patients investigated by endobronchial ultrasound (EBUS) had similar performance [303, 304].

12.3.2 Preoperative Assessment of Lymph Nodes in Patients with Known Primary Cancer

With preoperative lymph node assessment for metastatic involvement, no systematic review is available. Two studies investigated SWE in the prediction of metastatic involvement from thyroid cancer. A retrospective analysis [305] found that using the Mean Elastic Modulus with a cut-off set to 29 kPa led to 66.67 % sensitivity and 72.62 % specificity, 78 % PPV, 64.71 % NPV and 0.748 AUC, whereas the combination with B-mode ultrasound lead to 98.04 % sensitivity, 45.45 % specificity, 73.53 % PPV, 93.75 % NPV and 0.811 AUROC. Other authors found that the best SWE parameter for predicting metastatic involvement was the maximum value of elasticity with the cut-off set to 40 kPa, leading to 80 % sensitivity, 93.1 % specificity and 0.918 AUC [306].

12.4 Limitations and artifacts

Elastography is unlikely to be suitable for a differential diagnosis, but is more likely to be useful for targeting malignant lymph nodes for fine needle aspiration if multiple lymph nodes are present [307]. It cannot be assumed that the entire lymph node is involved in malignancy, but may range from a few undetectable cells to involvement of a small area. Only a limited number of studies with small sample sizes are available and invariably have a selection bias [308, 309]. Some malignant lymph nodes cannot be discriminated by tissue stiffness alone, as is the case with the lymph nodes of lymphoma [310]. There is no standardization of the technique particularly in SE, making study comparisons difficult [311]. Often with lymph node imaging in EUS, there is a relative depletion of surrounding tissue as a normal reference for SR calculation, including the gastrointestinal wall advocated as the standard comparison for tissue reference [309].

RECOMMENDATION 16

High-frequency transcutaneous and endoscopic ultrasound elastography can be used as additional tools for the differentiation between benign and malignant lymph nodes (LoE 2a GoR B) (For 20, Abstain 0, Against 0).

RECOMMENDATION 17

Ultrasound elastography can be used for identifying the most suspicious lymph nodes and/or suspicious areas within the lymph node to be targeted for sampling (LoE 5, GoR D) (For 19, Abstain 1, Against 0).

13. MusculoSkeletal

13.1 Background

In comparison with the previous guidelines, there has been an increase in studies regarding musculoskeletal (MSK) elastography [2].

13.2 Methods

Published data concerning the use of SE, ARFI imaging, and SWE for elastographic evaluation of the MSK structures, especially for tendons, muscles and nerves, are available.

13.3 Clinical applications

13.3.1 Tendons

In SE the healthy Achilles tendon is mostly rigid (86.7 – 93 % of the tendon has high stiffness) [312, 313] and there is an increase in stiffness with age [314]. Using SWE, different values of shear wave velocity or elastic modulus were obtained depending on the machine used, tendon position, or plane of imaging [113, 315, 316]. In Achilles tendinopathy the SR (comparing tendon with Kager's fat) is higher and the tendon becomes less stiff [317]. SE proved to be superior to B-mode ultrasound (sensitivity 99 %, specificity 78 %, accuracy 95 %) [318], underlining the ability of SE to detect pathology before the appearance of the B-mode ultrasound morphologic changes [319, 320]. No differences between athletes and controls nor between the dominant and non-dominant leg were found in SE evaluation of the patellar tendon [321]. With age, a significant decrease in shear wave velocity values was detected, with SWE having the capacity to detect aging tendons before morphologic abnormalities were observed on B-mode ultrasound [322, 323].

For lateral epicondylitis the addition of SE to B-mode ultrasound findings improves the sensitivity for detecting tendon pathology [324, 325]. Using B-mode ultrasound in combination with SE resulted in a better correlation with histologic results. In the rotator cuff, SE can detect small partial tears of the supraspinatus tendon [326]. In patients with tendinopathy, a significant decrease in the shear wave velocity of the supraspinatus muscle was observed [327]. Currently, no observations monitoring tendon healing are available in longitudinal studies.

13.3.2 Muscle

Using SE, the normal relaxed muscle appears as an inhomogeneous mosaic of intermediate or increased stiffness with scattered less stiff and stiffer areas, especially at the boundaries of the muscle [328, 329]. In SWE the normal relaxed muscle has a lower shear wave velocity (which increases during contraction) and the boundary fascia or aponeurosis show intermediate shear wave velocity [330].

Physiological factors (age, sex, muscle performance, fatigue, or training) and pathological changes (trauma, degeneration, or neuromuscular disease) influence muscle elasticity [331 – 337]. Normal and abnormal ranges of shear wave velocity of various muscles are available [327, 333, 336, 338] but the results are limited, without establishing any reference values.

SWE for the evaluation of muscle stiffness in various neurologic conditions (Parkinson disease, chronic stroke, cerebral palsy, multiple sclerosis or Duchenne dystrophy) is a reliable quantitative imaging technique for diagnosis, treatment decisions and follow-up and may be an alternative to electromyography [333, 338 – 342].

In inflammatory myopathies SE demonstrated that the involved muscles become stiffer, and significant correlations with histological findings were obtained [328, 343]. Acute muscle and fascial tears show a lower shear wave velocity [330], but no prospective studies have been published.

13.3.3 Ligaments and fascia

Using SWE in patients with adhesive capsulitis, the coracohumeral ligament proved to be stiffer in the symptomatic shoulder [344]. The increased stiffness of the transverse carpal ligament evaluated on SE may be one of the causes for carpal tunnel syndrome [345]. The plantar fascia becomes less stiff with age and in subjects with plantar fasciitis abnormality is seen when using ARFI imaging (pixel intensity), SE or SWE even in the absence of pathological findings on B-ode ultrasound examination [346 – 350], suggesting a role of elastography in the diagnosis of early stages of plantar fasciitis.

13.3.4 Nerves

Median nerve strain is significantly lower in patients with carpal tunnel syndrome than in controls [351], and the perineural area surrounding the median nerve is stiffer than in healthy volunteers [352]. The SE can be used to follow up the median nerve recovering after carpal tunnel release [353] or after local corticosteroid injection [354] but does not have the capability to categorize the severity. The combined use of B-mode ultrasound and SE has been suggested [355].

Using pSWE the shear wave velocity of the median nerve was 3.857 m/s in patients with carpal tunnel syndrome and 2.542 m/s in the control group ($p < 0.05$) [356]. Using 2D-SWE the mean shear modulus of the median nerve was 66.7 kPa in patients and 32.0 kPa in the control group ($p < 0.001$) [357]. Both methods have high sensitivity and specificity for carpal tunnel syndrome diagnosis and are highly reproducible. The increased stiffness was attributed to nerve fibrosis or edema.

The elasticity of the tibial nerve in diabetic patients is reduced compared with a control group and decreased further after developing diabetic peripheral neuropathy [358 – 360].

The joints and limb position and the patients' age should be taken into consideration during a nerve ultrasound examination [361].

13.4 Practical points

SE is an operator-dependent technique, with a recommendation to record several (at least 3) compression-relaxation cycles as cine-loops and then select the best elastograms for evaluation. The examination transducer should be perpendicular to the tissue to avoid anisotropy, as the B-mode ultrasound appearance influences the quality of the elastogram.

The use of standoff devices for SE of the superficial structures does not influence the elastogram (a minimum 3 mm distance between transducer and lesion being necessary) [362], but the inclusion of gel within the region of interest should be avoided (may mask minimal differences in tendon stiffness) [329].

The SWE examination of muscles and tendons should be performed with the lightest transducer pressure. The dimension of the region of interest does not influence the mean elastic modulus [363].

The transducer must be oriented longitudinally to the muscle fibers in order to achieve accurate and reliable SWE measurements. The shear waves propagate faster in contracted tendons and muscles and along the long axis of tendons [330]. The ligaments should be examined in the same position as the corresponding joints [344].

13.5 Limitations and artifacts

When a solid structure is delimited by an incompressible shell, SE analysis of the internal structure is limited (the eggshell effect) [364]. Cystic masses characteristically have a mosaic of all levels of stiffness. Low stiffness lines may appear at the interfaces between tissues (due to tissue shifting), around calcifications, behind bone or at the superficial edge of a homogeneous lesion. Fluctuant changes at the borders of the Achilles tendon in an axial elastogram can be seen due to varying contact with the skin [365].

A limitation of SWE is depth of penetration. Superficial structures may be better visualized by applying a 5 mm layer of coupling ultrasound gel as standoff. SWE examination is influenced by the transducer pressure and angle, and the shear modulus depends on the orientation of the transducer relative to the examined structures [330, 366].

RECOMMENDATION 18

Ultrasound elastography can be used as a supplementary tool to increase confidence in diagnosing tendinopathy, particularly for Achilles tendinopathy, for evaluating muscle stiffness and for plantar fasciitis (LoE 2b GoR B) (For 19, Abstain 1, Against 0).

RECOMMENDATION 19

Ultrasound elastography can be used for the diagnosis and follow-up of carpal tunnel syndrome and diabetic peripheral neuropathy (LoE 2b, GoR B) (For 19, Abstain 1, Against 0).

14. Testis

14.1 Background

Traditionally the presence of a focal lesion in the testis was addressed by removing the testis for histological examination, on the premise that nearly all of these lesions are malignant. However, access to modern ultrasound technology has rendered this approach obsolete, and as many as 80 % of incidentally discovered lesions are benign [367]. The use of newer contrast-enhanced ultrasound and elastography techniques [368], combined as multiparametric ultrasound [369], has resulted in a more cautious approach to incidental focal testicular lesions [370]. The use of elastography to assess the stiffness of abnormal areas of the testis to ascertain stiffness as a sign of underlying malignancy is an attractive proposition to add to the overall multiparametric assessment.

14.2 Methods

14.2.1 Strain elastography

SE has been the most employed technique for the assessment of testicular lesions [371 – 375]. Early studies, predominantly retrospective, have commented on the possibility of differentiating malignant from benign lesions with certainty using SE and SR. However, these findings have not been confirmed in recent studies, with specificities between 25.0 % and 37.5 % in differentiating benign from malignant lesions [375 – 377]. A number of case series detailing the use of SE and SR (some in combination with contrast-enhanced ultrasound) have described the findings in Leydig cell tumors [378], epidermoid cysts, hematoma, lymphoma, focal infarction, capillary hemangioma, adrenal rest cells [379 – 384] and in extra-testicular lesions [385], without comparison between the findings of these different lesions.

14.2.2 SWE

There is limited information regarding the use of SWE in the evaluation of testicular lesions. Investigation of the role of SWE in the overall assessment of background parenchyma has suggested that values may be elevated in the case of testicular microlithiasis [386], infertility [387], undescended testis [388]. It also has the potential to differentiate seminomas from non-seminomatous lesions [389] and has been evaluated in burnt-out tumors [390]. No prospective study reporting the differences in SWE in focal testicular lesions has been published.

14.3 Clinical applications

The use of all forms of elastography in the assessment of focal testicular lesions is promising, with tissue stiffness confirmed with both SE and SWE techniques, but with overlap in findings between benign and malignant neoplasms. The current status would allow elastography to be an adjunct to the overall ultrasound examination rather than a standalone technique.

14.4 Limitations and artifacts

For testicular lesions, the values obtained for SWE vary between different machines and are not interchangeable [391]. The problems associated with the areas of fibrosis adjacent to the tunica albuginea hamper the assessment of focal lesions adjacent to this region [392]. Measurements using SWE between the center and peripheral zones differ and the point of measurement requires standardization [393, 394].

RECOMMENDATION 20

Ultrasound elastography for the evaluation of focal testicular lesions can only be recommended in conjunction with other ultrasound techniques, as there is overlap between benign and malignant neoplasms (LoE 3A GoR B) (For 19, Abstain 1, Against 0).

15. Vascular

15.1 Background

It is well established that ageing and atherosclerotic disease increases arterial stiffness [395]. Elastography biomarkers are emerging as potential indicators for diseases such as stroke, hypertension, diabetes mellitus and cardiovascular disease, and may provide additional information to support clinical decision-making.

15.2 Methods

The majority of studies are based on SE. Early studies used intravascular ultrasound and more recent studies have focused on noninvasive techniques including SWE. These techniques have been compared with alternative imaging techniques, histology, clinical outcome measures and/or in experimental phantoms and simulations.

15.3 Clinical applications

15.3.1 Strain elastography

Plaque characterization is a challenging, clinically important application for which evidence of clinical benefit is growing [396]. Evidence from animal and human studies [397 – 403] typically associates vulnerable plaque with regions of high strain. The potential to detect and age thrombus has been demonstrated in animal models [404, 405]. A clinical application to differentiate acute from chronic deep vein thrombosis (DVT) has been demonstrated in humans [406 – 408], and a systematic review concluded that elastography imaging is a feasible adjunct to current first-line imaging for DVT [409]. However, at least one recent study was not able to differentiate acute DVT from subacute DVT [410]. Other potential vascular applications include cardiac, abdominal aorta and the use of elastography biomarkers for disease [411 – 414].

15.3.2 SWE

The feasibility of quantifying Young's modulus in arteries has been demonstrated in human [415], ex-vivo animal [416, 417] and phantom [418 – 420] studies. Identification of the vulnerable carotid plaque is emerging as a promising clinical application. Phantom studies have demonstrated the feasibility of Young's modulus estimates but highlight errors due to the requirement for a different wave propagation model than used by current commercial systems [418 – 421]. Nevertheless, human studies show good reproducibility and potential clinical benefit [422 – 426], with evidence that Young's modulus of carotid plaque correlates with qualitative (Gray-Weale scale) appearance [422, 425, 426] and quantitative (grayscale median) B-mode ultrasound measurements [422, 426], and helps to provide improved diagnostic performance of carotid plaque vulnerability [422, 426]. Studies found a lower mean Young's modulus for vulnerable plaque, although values differ (50 kPa vs. 79 kPa [426]; 62 kPa vs. 88 kPa [422]; 81 kPa vs. 115 kPa [425]). Evidence is limited for other vascular applications such as cardiac [427 – 429] and DVT [430, 431].

15.4 Limitations and artifacts

Vascular imaging is challenging due to the small heterogeneous tissue size, the dynamic environment resulting from pulsatile blood flow, thin vessel walls, non-linear tissue elasticity and shear wave propagation model assumptions which may not be valid due to the potential for Lamb wave propagation in vessel walls [415, 418]. Studies should report the shear wave velocity or calculation used to convert velocity to Young's modulus as future scanners may implement different models of wave propagation. Vascular applications are promising, especially for the assessment of carotid plaque, where larger, multicenter studies are required to validate initial findings, establish cut-off values and optimize methodologies.

RECOMMENDATION 21

Vascular ultrasound elastography is an area of active research. However, it cannot currently be recommended for clinical decision-making (LoE 5, GoR C) (For 20, Abstain 0, Against 0).

16. Intraoperative

16.1 Background

All surgical disciplines make use of preoperative imaging to visualize a pathology for improved surgical planning.

16.2 Methods

Improved ultrasound technology has resulted in high-frequency small transducers with better resolution including 3 D ultrasound, contrast-enhanced ultrasound and elastography.

16.3 Clinical applications

The utility of intraoperative ultrasound is less obvious. The advantages include intraoperative navigation without ionizing radiation exposure or relevant workflow interruption, assessment of the extent of resection, and organ shift monitoring and compensation (most important for the brain). Disadvantages for ultrasound elastography include organ deformity intraoperatively due to a number of factors including tumor resection sequelae and post-interventional swelling. The use of intraoperative elastography has been reported for the liver [8, 9, 432 – 435], brain [436 – 443], pancreas [115, 185], prostate [444], lung [445] and other organs [446].

RECOMMENDATION 22

Intraoperative ultrasound elastography is an area of active research. However, it cannot be currently recommended for clinical decision-making (LoE 5, GoR C) (For 20, Abstain 0, Against 0).

Conflict of interest

Odd Helge Gilja: Advisory Board/Consultant fee from: AbbVie, Bracco, GE Healthcare, Samsung, and Takeda
Paul S. Sidhu: Speaker honoraria, Bracco, Siemens, Samsung, Hiatchi, GE and Philips
Christoph F. Dietrich: Speaker honoraria, Bracco, Hitachi, GE, Mindray, Supersonic, Pentax, Olympus, Fuji, Boston Scientific, AbbVie, Falk Foundation, Novartis, Roche; Advisory, Board Member, Hitachi, Mindray, Siemens; Research grant, GE, Mindray, SuperSonic
Vito Cantisani: Speaker honoraria, Canon/Toshiba, Bracco, Samsung
Dominique Amy: Speaker honoraria, Hitachi, Supersonic, EpiSonica
Marco Brock: Speaker honoraria, Hitachi
Fabrizio Calliada: Speaker honoraria, Bracco, Hitachi, Shenshen Mindray
Dirk Andre Clevert: Speaker honoraria, Siemens, Samsung, GE, Bracco, Philips; Advisory Board, Siemens, Samsung, Bracco, Philips
Jean-Michel Correas: Speaker honoraria, Hitachi-Aloka, Canon/Toshiba, Philips, Supersonic, Bracco, Guerbet; Research collaboration, Bracco Sonocap, Guerbet NsSafe and Secure protocols
Mirko D'Onofrio: Speaker honoraria, Siemens, Bracco, Hitachi; Advisory Board Siemens, Bracco
Andre Farrokh: Speaker honoraria, Hitachi
Pietro Fusaroli: Speaker honoraria, Olympus
Roald Flesland Havre: Speaker honoraria, GE Healthcare, Conference participation support from Pharmacosmos, Ultrasound equipment from Samsung Medison
André Ignee: Speaker honoraria: Siemens, Canon/Toshiba, Hitachi, Boston Scientific, Bracco, Supersonic, Abbvie
Christian Jenssen: Speaker honoraria, Bracco, Hitachi, Canon/Toshiba, Falk Foundation, Covidien; Research grant, Novartis
Maija Radzina: Speaker honoraria, Bracco, Canon/Toshiba
Luca Sconfienza: Travel grants from Bracco Imaging Italia Srl, Esaote SPA, Abiogen SPA, Fidia Middle East. Speaker honoraria from Fidia Middle East
Ioan Sporea: Speaker honoraria, Philips, GE, Canon/Toshiba; Advisory Board Member, Siemens; Congress participation support, Siemens
Mickael Tanter: Speaker honoraria, Supersonic; Co Founder and shareholder, Supersonic; Research collaboration, Supersonic
Peter Vilmann: Speaker honoraria, Pentax, Norgine; Advisory Board, Boston Scientific; Consultancy MediGlobe
The following members declared no conflicts of interest: Adrian Săftoiu, Michael Bachmann Nielsen, Flaviu Bob, Jörg Bojunga, Caroline Ewertsen, Michael Hocke, Andrea Klauser, Christian Kollmann, Kumar V Ramnarine, Carolina Solomon, Daniela Fodor, Horia Ștefănescu

Acknowledgement

The authors thank the EFSUMB secretary Lynne Rudd for her never-ending support of the EFSUMB guidelines. We also thank the following companies for funding a consensus meeting of the authors held in Frankfurt in February 2018, at which we agreed the recommendations made in this paper: bk/Ultrasound, Echosens, Esaote SpA, GE Healthcare, Hitachi, Medical Systems, Philips Healthcare, Shenzhen Mindray Bio-medical Electronics Co., Ltd, Siemens Healthineers, SuperSonic and Canon/Toshiba Medical. Representatives of these companies were in attendance at this meeting, to assist with product technical information, but did not take part in forming the manuscript or the recommendations.

References

[1] Bamber J, Cosgrove D, Dietrich CF et al. EFSUMB Guidelines and Recommendations on the Clinical Use of Ultrasound Elastography. Part 1: Basic Principles and Technology. Ultraschall in Der Medizin 2013; 34: 169 – 184
[2] Cosgrove D, Piscaglia F, Bamber J et al. EFSUMB Guidelines and Recommendations on the Clinical Use of Ultrasound Elastography. Part 2: Clinical Applications. Ultraschall in Der Medizin 2013; 34: 238 – 253
[3] Education and Practical Standards Committee ErFoSfUiMaB. Minimum training recommendations for the practice of medical ultrasound. Ultraschall in Med 2006; 27: 79 – 105
[4] Cosgrove D, Barr R, Bojunga J et al. WFUMB Guidelines and Recommendations on the Clinical Use of Ultrasound Elastography: Part 4. Thyroid. Ultrasound Med Biol 2017; 43: 4 – 26
[5] Tatar IG, Kurt A, Yilmaz KB et al. The learning curve of real time elastosonography: a preliminary study conducted for the assessment of malignancy risk in thyroid nodules. Med Ultrason 2013; 15: 278 – 284
[6] Grădinaru-Taşcău O, Sporea I, Bota S et al. Does experience play a role in the ability to perform liver stiffness measurements by means of supersonic shear imaging (SSI)? Med Ultrason 2013; 15: 180 – 183
[7] Shiina T, Nightingale KR, Palmeri ML et al. WFUMB guidelines and recommendations for clinical use of ultrasound elastography: Part 1: basic principles and terminology. Ultrasound Med Biol 2015; 41: 1126 – 1147
[8] Dietrich CF, Bamber J, Berzigotti A et al. EFSUMB Guidelines and Recommendations on the Clinical Use of Liver Ultrasound Elastography, Update 2017 (Long Version). Ultraschall in Der Medizin 2017; 38: E16 – E47
[9] Dietrich CF, Bamber J, Berzigotti A et al. EFSUMB Guidelines and Recommendations on the Clinical Use of Liver Ultrasound Elastography, Update 2017 (Short Version). Ultraschall in Der Medizin 2017; 38: 377 – 394
[10] Ferraioli G, Filice C, Castera L et al. WFUMB guidelines and recommendations for clinical use of ultrasound elastography: Part 3: liver. Ultrasound Med Biol 2015; 41: 1161 – 1179
[11] Barr RG, Nakashima K, Amy D et al. WFUMB guidelines and recommendations for clinical use of ultrasound elastography: Part 2: breast. Ultrasound Med Biol 2015; 41: 1148 – 1160
[12] Stenzel M, Mentzel HJ. Ultrasound elastography and contrast-enhanced ultrasound in infants, children and adolescents. Eur J Radiol 2014; 83: 1560 – 1569
[13] Goldschmidt I, Streckenbach C, Dingemann C et al. Application and limitations of transient liver elastography in children. J Pediatr Gastroenterol Nutr 2013; 57: 109 – 113
[14] Goldschmidt I, Brauch C, Poynard T et al. Spleen stiffness measurement by transient elastography to diagnose portal hypertension in children. J Pediatr Gastroenterol Nutr 2014; 59: 197 – 203

[15] Peralta L, Molina FS, Melchor J et al. Transient Elastography to Assess the Cervical Ripening during Pregnancy: A Preliminary Study. Ultraschall in Med 2017; 38: 395 – 402

[16] Friedrich-Rust M, Schoelzel F, Linzbach S et al. Safety of transient elastography in patients with implanted cardiac rhythm devices. Dig Liver Dis 2017; 49: 314 – 316

[17] Tabaru M, Yoshikawa H, Azuma T et al. Experimental study on temperature rise of acoustic radiation force elastography. J Med Ultrason (2001) 2012; 39: 137 – 146

[18] Herman BA, Harris GR. Models and regulatory considerations for transient temperature rise during diagnostic ultrasound pulses. Ultrasound Med Biol 2002; 28: 1217 – 1224

[19] Liu Y, Herman BA, Soneson JE et al. Thermal safety simulations of transient temperature rise during acoustic radiation force-based ultrasound elastography. Ultrasound Med Biol 2014; 40: 1001 – 1014

[20] Palmeri ML, Nightingale KR. On the thermal effects associated with radiation force imaging of soft tissue. IEEE Trans Ultrason Ferroelectr Freq Control 2004; 51: 551 – 565

[21] Skurczynski MJ, Duck FA, Shipley JA et al. Evaluation of experimental methods for assessing safety for ultrasound radiation force elastography. Br J Radiol 2009; 82: 666 – 674

[22] Deng Y, Palmeri ML, Rouze NC et al. Evaluating the Benefit of Elevated Acoustic Output in Harmonic Motion Estimation in Ultrasonic Shear Wave Elasticity Imaging. Ultrasound Med Biol 2018; 44: 303 – 310

[23] Itoh A, Ueno E, Tohno E et al. Breast disease: clinical application of US elastography for diagnosis. Radiology 2006; 239: 341 – 350

[24] Carlsen JF, Ewertsen C, Sletting S et al. Strain histograms are equal to strain ratios in predicting malignancy in breast tumours. PLoS One 2017; 12: e0186230

[25] Grajo JR, Barr RG. Strain elastography for prediction of breast cancer tumour grades. J Ultrasound Med 2014; 33: 129 – 134

[26] Hatzung G, Grunwald S, Zygmunt M et al. Sonoelastography in the diagnosis of malignant and benign breast lesions: initial clinical experiences. Ultraschall in Med 2010; 31: 596 – 603

[27] Cho N, Jang M, Lyou CY et al. Distinguishing benign from malignant masses at breast US: combined US elastography and color doppler US-influence on radiologist accuracy. Radiology 2012; 262: 80 – 90

[28] Wojcinski S, Farrokh A, Weber S et al. Multicenter study of ultrasound real-time tissue elastography in 779 cases for the assessment of breast lesions: improved diagnostic performance by combining the BI-RADS®-US classification system with sonoelastography. Ultraschall in Med 2010; 31: 484 – 491

[29] Sadigh G, Carlos RC, Neal CH et al. Ultrasonographic differentiation of malignant from benign breast lesions: a meta-analytic comparison of elasticity and BIRADS scoring. Breast Cancer Res Treat 2012; 133: 23 – 35

[30] Cho N, Moon WK, Kim HY et al. Sonoelastographic strain index for differentiation of benign and malignant nonpalpable breast masses. J Ultrasound Med 2010; 29: 1 – 7

[31] Sadigh G, Carlos RC, Neal CH et al. Accuracy of quantitative ultrasound elastography for differentiation of malignant and benign breast abnormalities: a meta-analysis. Breast Cancer Res Treat 2012; 134: 923 – 931

[32] Berg WA, Cosgrove DO, Doré CJ et al. Shear-wave elastography improves the specificity of breast US: the BE1 multinational study of 939 masses. Radiology 2012; 262: 435 – 449

[33] Evans A, Whelehan P, Thomson K et al. Invasive breast cancer: relationship between shear-wave elastographic findings and histologic prognostic factors. Radiology 2012; 263: 673 – 677

[34] Chang JM, Park IA, Lee SH et al. Stiffness of tumours measured by shear-wave elastography correlated with subtypes of breast cancer. Eur Radiol 2013; 23: 2450 – 2458

[35] Choi WJ, Kim HH, Cha JH et al. Predicting prognostic factors of breast cancer using shear wave elastography. Ultrasound Med Biol 2014; 40: 269 – 274

[36] Berg WA, Mendelson EB, Cosgrove DO et al. Quantitative Maximum Shear-Wave Stiffness of Breast Masses as a Predictor of Histopathologic Severity. Am J Roentgenol 2015; 205: 448 – 455

[37] Tamaki K, Tamaki N, Kamada Y et al. Non-invasive evaluation of axillary lymph node status in breast cancer patients using shear wave elastography. Tohoku J Exp Med 2013; 231: 211 – 216

[38] Wojcinski S, Dupont J, Schmidt W et al. Real-time ultrasound elastography in 180 axillary lymph nodes: elasticity distribution in healthy lymph nodes and prediction of breast cancer metastases. BMC Med Imaging 2012; 12: 35

[39] Park YM, Fornage BD, Benveniste AP et al. Strain elastography of abnormal axillary nodes in breast cancer patients does not improve diagnostic accuracy compared with conventional ultrasound alone. Am J Roentgenol 2014; 203: 1371 – 1378

[40] Youk JH, Gweon HM, Son EJ et al. Shear-wave elastography of invasive breast cancer: correlation between quantitative mean elasticity value and immunohistochemical profile. Breast Cancer Res Treat 2013; 138: 119 – 126

[41] Evans A, Rauchhaus P, Whelehan P et al. Does shear wave ultrasound independently predict axillary lymph node metastasis in women with invasive breast cancer? Breast Cancer Res Treat 2014; 143: 153 – 157

[42] Falou O, Sadeghi-Naini A, Prematilake S et al. Evaluation of neoadjuvant chemotherapy response in women with locally advanced breast cancer using ultrasound elastography. Transl Oncol 2013; 6: 17 – 24

[43] Evans A, Armstrong S, Whelehan P et al. Can shear-wave elastography predict response to neoadjuvant chemotherapy in women with invasive breast cancer? Br J Cancer 2013; 109: 2798 – 2802

[44] Lee SH, Chang JM, Han W et al. Shear-Wave Elastography for the Detection of Residual Breast Cancer After Neoadjuvant Chemotherapy. Ann Surg Oncol 2015; 22 (Suppl. 3): S376 – S384

[45] Tanter M, Bercoff J, Athanasiou A et al. Quantitative assessment of breast lesion viscoelasticity: initial clinical results using supersonic shear imaging. Ultrasound Med Biol 2008; 34: 1373 – 1386

[46] Kelloff GJ, Choyke P, Coffey DS et al. Challenges in clinical prostate cancer: role of imaging. Am J Roentgenol 2009; 192: 1455 – 1470

[47] Singh H, Canto EI, Shariat SF et al. Predictors of prostate cancer after initial negative systematic 12 core biopsy. J Urol 2004; 171: 1850 – 1854

[48] Ashley RA, Inman BA, Routh JC et al. Reassessing the diagnostic yield of saturation biopsy of the prostate. Eur Urol 2008; 53: 976 – 981

[49] Onur R, Littrup PJ, Pontes JE et al. Contemporary impact of transrectal ultrasound lesions for prostate cancer detection. J Urol 2004; 172: 512 – 514

[50] Pallwein L, Mitterberger M, Struve P et al. Real-time elastography for detecting prostate cancer: preliminary experience. BJU Int 2007; 100: 42 – 46

[51] Salomon G, Köllerman J, Thederan I et al. Evaluation of prostate cancer detection with ultrasound real-time elastography: a comparison with step section pathological analysis after radical prostatectomy. Eur Urol 2008; 54: 1354 – 1362

[52] Brock M, von Bodman C, Sommerer F et al. Comparison of real-time elastography with grey-scale ultrasonography for detection of organ-confined prostate cancer and extra capsular extension: a prospective analysis using whole mount sections after radical prostatectomy. BJU Int 2011; 108: E217 – 222

[53] Brock M, von Bodman C, Palisaar RJ et al. The impact of real-time elastography guiding a systematic prostate biopsy to improve cancer detection rate: a prospective study of 353 patients. J Urol 2012; 187: 2039 – 2043

[54] Kapoor A, Mahajan G, Sidhu BS. Real-time elastography in the detection of prostate cancer in patients with raised PSA level. Ultrasound Med Biol 2011; 37: 1374 – 1381

[55] Walz J, Marcy M, Pianna JT et al. Identification of the prostate cancer index lesion by real-time elastography: considerations for focal therapy of prostate cancer. World J Urol 2011; 29: 589 – 594

[56] Aigner F, Pallwein L, Junker D et al. Value of real-time elastography targeted biopsy for prostate cancer detection in men with prostate specific antigen 1.25 ng/ml or greater and 4.00 ng/ml or less. J Urol 2010; 184: 913 – 917

[57] Aboumarzouk OM, Ogston S, Huang Z et al. Diagnostic accuracy of transrectal elastosonography (TRES) imaging for the diagnosis of prostate cancer: a systematic review and meta-analysis. BJU Int 2012; 110: 1414 – 1423; discussion 1423

[58] Kamoi K, Okihara K, Ochiai A et al. The utility of transrectal real-time elastography in the diagnosis of prostate cancer. Ultrasound Med Biol 2008; 34: 1025 – 1032

[59] Bercoff J, Tanter M, Muller M et al. The role of viscosity in the impulse diffraction field of elastic waves induced by the acoustic radiation force. IEEE Trans Ultrason Ferroelectr Freq Control 2004; 51: 1523 – 1536

[60] Barr RG, Memo R, Schaub CR. Shear wave ultrasound elastography of the prostate: initial results. Ultrasound Q 2012; 28: 13 – 20

[61] Correas JM, Tissier AM, Khairoune A et al. Ultrasound elastography of the prostate: state of the art. Diagn Interv Imaging 2013; 94: 551 – 560

[62] Aigner F, Schäfer G, Steiner E et al. Value of enhanced transrectal ultrasound targeted biopsy for prostate cancer diagnosis: a retrospective data analysis. World J Urol 2012; 30: 341 – 346

[63] Brock M, Eggert T, Löppenberg B et al. Value of real-time elastography to guide the systematic prostate biopsy in men with normal digital rectal exam. Aktuelle Urol 2013; 44: 40 – 44

[64] Brock M, Löppenberg B, Roghmann F et al. Impact of real-time elastography on magnetic resonance imaging/ultrasound fusion guided biopsy in patients with prior negative prostate biopsies. J Urol 2015; 193: 1191 – 1197

[65] Brock M, Roghmann F, Sonntag C et al. Fusion of Magnetic Resonance Imaging and Real-Time Elastography to Visualize Prostate Cancer: A Prospective Analysis using Whole Mount Sections after Radical Prostatectomy. Ultraschall in Med 2015; 36: 355 – 361

[66] Friedrich-Rust M, Meyer G, Dauth N et al. Interobserver agreement of Thyroid Imaging Reporting and Data System (TIRADS) and strain elastography for the assessment of thyroid nodules. PLoS One 2013; 8: e77927

[67] Ito Y, Amino N, Yokozawa T et al. Ultrasonographic evaluation of thyroid nodules in 900 patients: comparison among ultrasonographic, cytological, and histological findings. Thyroid 2007; 17: 1269 – 1276

[68] Tae HJ, Lim DJ, Baek KH et al. Diagnostic value of ultrasonography to distinguish between benign and malignant lesions in the management of thyroid nodules. Thyroid 2007; 17: 461 – 466

[69] Haugen BR, Alexander EK, Bible KC et al. 2015 American Thyroid Association Management Guidelines for Adult Patients with Thyroid Nodules and Differentiated Thyroid Cancer: The American Thyroid Association Guidelines Task Force on Thyroid Nodules and Differentiated Thyroid Cancer. Thyroid 2016; 26: 1 – 133

[70] Russ G, Bonnema SJ, Erdogan MF et al. European Thyroid Association Guidelines for Ultrasound Malignancy Risk Stratification of Thyroid Nodules in Adults: The EU-TIRADS. Eur Thyroid J 2017; 6: 225 – 237

[71] Kwak JY, Han KH, Yoon JH et al. Thyroid imaging reporting and data system for US features of nodules: a step in establishing better stratification of cancer risk. Radiology 2011; 260: 892 – 899

[72] Horvath E, Majlis S, Rossi R et al. An ultrasonogram reporting system for thyroid nodules stratifying cancer risk for clinical management. J Clin Endocrinol Metab 2009; 94: 1748 – 1751

[73] Park JY, Lee HJ, Jang HW et al. A proposal for a thyroid imaging reporting and data system for ultrasound features of thyroid carcinoma. Thyroid 2009; 19: 1257 – 1264

[74] Yoon JH, Lee HS, Kim EK et al. Malignancy Risk Stratification of Thyroid Nodules: Comparison between the Thyroid Imaging Reporting and Data System and the 2014 American Thyroid Association Management Guidelines. Radiology 2016; 278: 917 – 924

[75] Cantisani V, Grazhdani H, Drakonaki E et al. Strain US Elastography for the Characterization of Thyroid Nodules: Advantages and Limitation. Int J Endocrinol 2015; 2015: 908575

[76] Cantisani V, Maceroni P, D'Andrea V et al. Strain ratio ultrasound elastography increases the accuracy of colour-Doppler ultrasound in the evaluation of Thy-3 nodules. A bi-centre university experience. Eur Radiol 2016; 26: 1441 – 1449

[77] Cantisani V, Grazhdani H, Ricci P et al. Q-elastosonography of solid thyroid nodules: assessment of diagnostic efficacy and interobserver variability in a large patient cohort. Eur Radiol 2014; 24: 143 – 150

[78] Ghajarzadeh M, Sodagari F, Shakiba M. Diagnostic accuracy of sonoelastography in detecting malignant thyroid nodules: a systematic review and meta-analysis. Am J Roentgenol 2014; 202: W379 – W389

[79] Razavi SA, Hadduck TA, Sadigh G et al. Comparative effectiveness of elastographic and B-mode ultrasound criteria for diagnostic discrimination of thyroid nodules: a meta-analysis. Am J Roentgenol 2013; 200: 1317 – 1326

[80] Sun J, Cai J, Wang X. Real-time ultrasound elastography for differentiation of benign and malignant thyroid nodules: a meta-analysis. J Ultrasound Med 2014; 33: 495 – 502

[81] Hu X, Liu Y, Qian L. Diagnostic potential of real-time elastography (RTE) and shear wave elastography (SWE) to differentiate benign and malignant thyroid nodules: A systematic review and meta-analysis. Medicine (Baltimore) 2017; 96: e8282

[82] Nattabi HA, Sharif NM, Yahya N et al. Is Diagnostic Performance of Quantitative 2D-Shear Wave Elastography Optimal for Clinical Classification of Benign and Malignant Thyroid Nodules?: A Systematic Review and Meta-analysis. Acad Radiol 2017. (Epub ahead of print)

[83] Tian W, Hao S, Gao B et al. Comparing the Diagnostic Accuracy of RTE and SWE in Differentiating Malignant Thyroid Nodules from Benign Ones: a Meta-Analysis. Cell Physiol Biochem 2016; 39: 2451 – 2463

[84] Lin P, Chen M, Liu B et al. Diagnostic performance of shear wave elastography in the identification of malignant thyroid nodules: a meta-analysis. Eur Radiol 2014; 24: 2729 – 2738

[85] Zhan J, Jin JM, Diao XH et al. Acoustic radiation force impulse imaging (ARFI) for differentiation of benign and malignant thyroid nodules – A meta-analysis. Eur J Radiol 2015; 84: 2181 – 2186

[86] Rago T, Vitti P. Role of thyroid ultrasound in the diagnostic evaluation of thyroid nodules. Best Pract Res Clin Endocrinol Metab 2008; 22: 913 – 928

[87] Rago T, Vitti P. Potential value of elastosonography in the diagnosis of malignancy in thyroid nodules. Q J Nucl Med Mol Imaging 2009; 53: 455 – 464

[88] Rago T, Scutari M, Santini F et al. Real-time elastosonography: useful tool for refining the presurgical diagnosis in thyroid nodules with indeterminate or nondiagnostic cytology. J Clin Endocrinol Metab 2010; 95: 5274 – 5280

[89] Ciledag N, Arda K, Aribas BK et al. The utility of ultrasound elastography and MicroPure imaging in the differentiation of benign and malignant thyroid nodules. Am J Roentgenol 2012; 198: W244 – W249

[90] Vidal-Casariego A, López-González L, Jiménez-Pérez A et al. Accuracy of ultrasound elastography in the diagnosis of thyroid cancer in a low-risk population. Exp Clin Endocrinol Diabetes 2012; 120: 635 – 638

[91] Hong Y, Liu X, Li Z et al. Real-time ultrasound elastography in the differential diagnosis of benign and malignant thyroid nodules. J Ultrasound Med 2009; 28: 861 – 867

[92] Unlütürk U, Erdoğan MF, Demir O et al. Ultrasound elastography is not superior to grayscale ultrasound in predicting malignancy in thyroid nodules. Thyroid 2012; 22: 1031 – 1038

[93] Zhan J, Diao XH, Chai QL et al. Comparative study of acoustic radiation force impulse imaging with real-time elastography in differential diagnosis of thyroid nodules. Ultrasound Med Biol 2013; 39: 2217 – 2225

[94] Rago T, Santini F, Scutari M et al. Elastography: new developments in ultrasound for predicting malignancy in thyroid nodules. J Clin Endocrinol Metab 2007; 92: 2917 – 2922

[95] Kagoya R, Monobe H, Tojima H. Utility of elastography for differential diagnosis of benign and malignant thyroid nodules. Otolaryngol Head Neck Surg 2010; 143: 230 – 234

[96] He YP, Xu HX, Li XL et al. Comparison of Virtual Touch Tissue Imaging & Quantification (VTIQ) and Toshiba shear wave elastography (T-SWE) in diagnosis of thyroid nodules: Initial experience. Clin Hemorheol Microcirc 2017; 66: 15 – 26

[97] Wang F, Chang C, Gao Y et al. Does Shear Wave Elastography Provide Additional Value in the Evaluation of Thyroid Nodules That Are Suspicious for Malignancy? J Ultrasound Med 2016; 35: 2397 – 2404

[98] Swan KZ, Nielsen VE, Bibby BM et al. Is the reproducibility of shear wave elastography of thyroid nodules high enough for clinical use? A methodological study. Clin Endocrinol (Oxf) 2017; 86: 606 – 613

[99] Bardet S, Ciappuccini R, Pellot-Barakat C et al. Shear Wave Elastography in Thyroid Nodules with Indeterminate Cytology: Results of a Prospective Bicentric Study. Thyroid 2017; 27: 1441 – 1449

[100] Liu Z, Jing H, Han X et al. Shear wave elastography combined with the thyroid imaging reporting and data system for malignancy risk stratification in thyroid nodules. Oncotarget 2017; 8: 43406 – 43416

[101] Dobruch-Sobczak K, Gumińska A, Bakuła-Zalewska E et al. Shear wave elastography in medullary thyroid carcinoma diagnostics. J Ultrason 2015; 15: 358 – 367

[102] Dobruch-Sobczak K, Zalewska EB, Gumińska A et al. Diagnostic Performance of Shear Wave Elastography Parameters Alone and in Combination with Conventional B-Mode Ultrasound Parameters for the Characterization of Thyroid Nodules: A Prospective, Dual-Center Study. Ultrasound Med Biol 2016; 42: 2803 – 2811

[103] Wang D, He YP, Zhang YF et al. The diagnostic performance of shear wave speed (SWS) imaging for thyroid nodules with elasticity modulus and SWS measurement. Oncotarget 2017; 8: 13387 – 13399

[104] Duan SB, Yu J, Li X et al. Diagnostic value of two-dimensional shear wave elastography in papillary thyroid microcarcinoma. Onco Targets Ther 2016; 9: 1311 – 1317

[105] Liu MJ, Men YM, Zhang YL et al. Improvement of diagnostic efficiency in distinguishing the benign and malignant thyroid nodules via conventional ultrasound combined with ultrasound contrast and elastography. Oncol Lett 2017; 14: 867 – 871

[106] Wang F, Chang C, Chen M et al. Does Lesion Size Affect the Value of Shear Wave Elastography for Differentiating Between Benign and Malignant Thyroid Nodules? J Ultrasound Med 2018; 37: 601 – 609

[107] Liu BJ, Lu F, Xu HX et al. The diagnosis value of acoustic radiation force impulse (ARFI) elastography for thyroid malignancy without highly suspicious features on conventional ultrasound. Int J Clin Exp Med 2015; 8: 15362 – 15372

[108] Liu BJ, Zhao CK, Xu HX et al. Quality measurement on shear wave speed imaging: diagnostic value in differentiation of thyroid malignancy and the associated factors. Oncotarget 2017; 8: 4848 – 4959

[109] Zhou H, Yue WW, Du LY et al. A Modified Thyroid Imaging Reporting and Data System (mTI-RADS) For Thyroid Nodules in Coexisting Hashimoto's Thyroiditis. Sci Rep 2016; 6: 26410

[110] Pandey NN, Pradhan GS, Manchanda A et al. Diagnostic Value of Acoustic Radiation Force Impulse Quantification in the Differentiation of Benign and Malignant Thyroid Nodules. Ultrason Imaging 2017; 39: 326 – 336

[111] Liu BJ, Li DD, Xu HX et al. Quantitative Shear Wave Velocity Measurement on Acoustic Radiation Force Impulse Elastography for Differential Diagnosis between Benign and Malignant Thyroid Nodules: A Meta-analysis. Ultrasound Med Biol 2015; 41: 3035 – 3043

[112] Russ G. Risk stratification of thyroid nodules on ultrasonography with the French TI-RADS: description and reflections. Ultrasonography 2016; 35: 25 – 38

[113] Arda K, Ciledag N, Aktas E et al. Quantitative assessment of normal soft-tissue elasticity using shear-wave ultrasound elastography. Am J Roentgenol 2011; 197: 532 – 536

[114] Gallotti A, D'Onofrio M, Pozzi Mucelli R. Acoustic Radiation Force Impulse (ARFI) technique in ultrasound with Virtual Touch tissue quantification of the upper abdomen. Radiol Med 2010; 115: 889 – 897

[115] D'Onofrio M, Tremolada G, De Robertis R et al. Prevent Pancreatic Fistula after Pancreatoduodenectomy: Possible Role of Ultrasound Elastography. Dig Surg 2018; 35: 164 – 170

[116] Goertz RS, Schuderer J, Strobel D et al. Acoustic radiation force impulse shear wave elastography (ARFI) of acute and chronic pancreatitis and pancreatic tumour. Eur J Radiol 2016; 85: 2211 – 2216

[117] Harada N, Ishizawa T, Inoue Y et al. Acoustic radiation force impulse imaging of the pancreas for estimation of pathologic fibrosis and risk of postoperative pancreatic fistula. J Am Coll Surg 2014; 219: 887 – 894. e885

[118] He Y, Wang H, Li XP et al. Pancreatic Elastography From Acoustic Radiation Force Impulse Imaging for Evaluation of Diabetic Microangiopathy. Am J Roentgenol 2017; 209: 775 – 780

[119] Hirooka Y, Kuwahara T, Irisawa A et al. JSUM ultrasound elastography practice guidelines: pancreas. J Med Ultrason (2001) 2015; 42: 151 – 174

[120] Kawada N, Tanaka S. Elastography for the pancreas: Current status and future perspective. World J Gastroenterol 2016; 22: 3712 – 3724

[121] Kawada N, Tanaka S, Uehara H et al. Potential use of point shear wave elastography for the pancreas: a single center prospective study. Eur J Radiol 2014; 83: 620 – 624

[122] Kuwahara T, Hirooka Y, Kawashima H et al. Usefulness of shear wave elastography as a quantitative diagnosis of chronic pancreatitis. J Gastroenterol Hepatol 2018; 33: 756 – 761

[123] Kuwahara T, Hirooka Y, Kawashima H et al. Quantitative evaluation of pancreatic tumour fibrosis using shear wave elastography. Pancreatology 2016; 16: 1063 – 1068

[124] Llamoza-Torres CJ, Fuentes-Pardo M, Álvarez-Higueras FJ et al. Usefulness of percutaneous elastography by acoustic radiation force impulse for the non-invasive diagnosis of chronic pancreatitis. Rev Esp Enferm Dig 2016; 108: 450 – 456

[125] Onoyama T, Koda M, Fujise Y et al. Utility of virtual touch quantification in the diagnosis of pancreatic ductal adenocarcinoma. Clin Imaging 2017; 42: 64 – 67

[126] Park MK, Jo J, Kwon H et al. Usefulness of acoustic radiation force impulse elastography in the differential diagnosis of benign and malignant solid pancreatic lesions. Ultrasonography 2014; 33: 26 – 33

[127] Pozzi R, Parzanese I, Baccarin A et al. Point shear-wave elastography in chronic pancreatitis: A promising tool for staging disease severity. Pancreatology 2017; 17: 905 – 910

[128] Sağlam D, Bilgici MC, Kara C et al. Acoustic Radiation Force Impulse Elastography in Determining the Effects of Type 1 Diabetes on Pancreas and Kidney Elasticity in Children. Am J Roentgenol 2017; 209: 1143 – 1149

[129] Stumpf S, Jaeger H, Graeter T et al. Influence of age, sex, body mass index, alcohol, and smoking on shear wave velocity (p-SWE) of the pancreas. Abdom Radiol (NY) 2016; 41: 1310 – 1316

[130] Xie J, Zou L, Yao M et al. A Preliminary Investigation of Normal Pancreas and Acute Pancreatitis Elasticity Using Virtual Touch Tissue Quantification (VTQ) Imaging. Med Sci Monit 2015; 21: 1693 – 1699

[131] Yashima Y, Sasahira N, Isayama H et al. Acoustic radiation force impulse elastography for noninvasive assessment of chronic pancreatitis. J Gastroenterol 2012; 47: 427 – 432

[132] Zaro R, Lupsor-Platon M, Cheviet A et al. The pursuit of normal reference values of pancreas stiffness by using Acoustic Radiation Force Impulse (ARFI) elastography. Med Ultrason 2016; 18: 425 – 430

[133] D'Onofrio M, De Robertis R, Crosara S et al. Acoustic radiation force impulse with shear wave speed quantification of pancreatic masses: A prospective study. Pancreatology 2016; 16: 106 – 109

[134] Chantarojanasiri T, Hirooka Y, Kawashima H et al. Age-related changes in pancreatic elasticity: When should we be concerned about their effect on strain elastography? Ultrasonics 2016; 69: 90 – 96

[135] Chantarojanasiri T, Hirooka Y, Kawashima H et al. Endoscopic ultrasound in diagnosis of solid pancreatic lesions: Elastography or contrast-enhanced harmonic alone versus the combination. Endosc Int Open 2017; 5: E1136 – E1143

[136] Dominguez-Muñoz JE, Iglesias-Garcia J, Castiñeira Alvariño M et al. EUS elastography to predict pancreatic exocrine insufficiency in patients with chronic pancreatitis. Gastrointest Endosc 2015; 81: 136 – 142

[137] Dyrla P, Gil J, Florek M et al. Elastography in pancreatic solid tumours diagnoses. Prz Gastroenterol 2015; 10: 41 – 46

[138] Harada N, Yoshizumi T, Maeda T et al. Preoperative Pancreatic Stiffness by Real-time Tissue Elastography to Predict Pancreatic Fistula After Pancreaticoduodenectomy. Anticancer Res 2017; 37: 1909 – 1915

[139] Hirche TO, Ignee A, Barreiros AP et al. Indications and limitations of endoscopic ultrasound elastography for evaluation of focal pancreatic lesions. Endoscopy 2008; 40: 910 – 917

[140] Iglesias García JJ, Lariño Noia J, Alvarez Castro A et al. Second-generation endoscopic ultrasound elastography in the differential diagnosis of solid pancreatic masses. Pancreatic cancer vs. inflammatory mass in chronic pancreatitis. Rev Esp Enferm Dig 2009; 101: 723 – 730

[141] Iglesias-Garcia J, Domínguez-Muñoz JE, Castiñeira-Alvariño M et al. Quantitative elastography associated with endoscopic ultrasound for the diagnosis of chronic pancreatitis. Endoscopy 2013; 45: 781 – 788

[142] Iglesias-Garcia J, Larino-Noia J, Abdulkader I et al. Quantitative endoscopic ultrasound elastography: an accurate method for the differentiation of solid pancreatic masses. Gastroenterology 2010; 139: 1172 – 1180

[143] Iglesias-Garcia J, Lindkvist B, Lariño-Noia J et al. Differential diagnosis of solid pancreatic masses: contrast-enhanced harmonic (CEH-EUS), quantitative-elastography (QE-EUS), or both? United European Gastroenterol J 2017; 5: 236 – 246

[144] Iordache S, Costache MI, Popescu CF et al. Clinical impact of EUS elastography followed by contrast-enhanced EUS in patients with focal pancreatic masses and negative EUSguided FNA. Medical Ultrasonography 2016; 18: 18 – 24

[145] Itokawa F, Itoi T, Sofuni A et al. EUS elastography combined with the strain ratio of tissue elasticity for diagnosis of solid pancreatic masses. J Gastroenterol 2011; 46: 843 – 853

[146] Janssen J, Papavassiliou I. Effect of aging and diffuse chronic pancreatitis on pancreas elasticity evaluated using semiquantitative EUS elastography. Ultraschall in Med 2014; 35: 253 – 258

[147] Kawada N, Tanaka S, Uehara H et al. Alteration of strain ratio evaluated by transabdominal ultrasound elastography may predict the efficacy of preoperative chemoradiation performed for pancreatic ductal carcinoma: preliminary results. Hepatogastroenterology 2014; 61: 480 – 483

[148] Kim SY, Cho JH, Kim YJ et al. Diagnostic efficacy of quantitative endoscopic ultrasound elastography for differentiating pancreatic disease. J Gastroenterol Hepatol 2017; 32: 1115 – 1122

[149] Kongkam P, Lakananurak N, Navicharern P et al. Combination of EUS-FNA and elastography (strain ratio) to exclude malignant solid pancreatic lesions: A prospective single-blinded study. J Gastroenterol Hepatol 2015; 30: 1683 – 1689

[150] Opačić D, Rustemović N, Kalauz M et al. Endoscopic ultrasound elastography strain histograms in the evaluation of patients with pancreatic masses. World J Gastroenterol 2015; 21: 4014 – 4019

[151] Rana SS, Dambalkar A, Chhabra P et al. Is pancreatic exocrine insufficiency in celiac disease related to structural alterations in pancreatic parenchyma? Ann Gastroenterol 2016; 29: 363 – 366

[152] Rustemović N, Kalauz M, Grubelić Ravić K et al. Differentiation of Pancreatic Masses via Endoscopic Ultrasound Strain Ratio Elastography Using Adjacent Pancreatic Tissue as the Reference. Pancreas 2017; 46: 347 – 351

[153] Săftoiu A, Vilmann P. Differential diagnosis of focal pancreatic masses by semiquantitative EUS elastography: between strain ratios and strain histograms. Gastrointest Endosc 2013; 78: 188 – 189

[154] Săftoiu A, Vilmann P, Gorunescu F et al. Neural network analysis of dynamic sequences of EUS elastography used for the differential diagnosis of chronic pancreatitis and pancreatic cancer. Gastrointest Endosc 2008; 68: 1086 – 1094

[155] Săftoiu A, Vilmann P, Gorunescu F et al. Accuracy of endoscopic ultrasound elastography used for differential diagnosis of focal pancreatic masses: a multicenter study. Endoscopy 2011; 43: 596 – 603

[156] Saftoiu A, Vilmann P, Gorunescu F et al. Efficacy of an Artificial Neural Network- Based Approach to Endoscopic Ultrasound Elastography in Diagnosis of Focal Pancreatic Masses. Clinical Gastroenterology and Hepatology 2012; 10: U84 – U167

[157] Cui XW, Chang JM, Kan QC et al. Endoscopic ultrasound elastography: Current status and future perspectives. World J Gastroenterol 2015; 21: 13212 – 13224

[158] Dietrich CF. Elastography, the new dimension in ultrasonography. Praxis (Bern 1994) 2011; 100: 1533 – 1542

[159] Dietrich CF, Barr RG, Farrokh A et al. Strain Elastography – How To Do It? Ultrasound Int Open 2017; 3: E137 – E149

[160] Dietrich CF, Cantisani V. Current status and perspectives of elastography. Eur J Radiol 2014; 83: 403 – 404

[161] Dietrich CF, Hirche TO, Ott M et al. Real-time tissue elastography in the diagnosis of autoimmune pancreatitis. Endoscopy 2009; 41: 718 – 720

[162] Dietrich CF, Săftoiu A, Jenssen C. Real time elastography endoscopic ultrasound (RTE-EUS), a comprehensive review. Eur J Radiol 2014; 83: 405 – 414

[163] Hocke M, Ignee A, Dietrich CF. Advanced endosonographic diagnostic tools for discrimination of focal chronic pancreatitis and pancreatic carcinoma–elastography, contrast enhanced high mechanical index (CEHMI) and low mechanical index (CELMI) endosonography in direct comparison. Z Gastroenterol 2012; 50: 199 – 203

[164] Janssen J, Schlörer E, Greiner L. EUS elastography of the pancreas: feasibility and pattern description of the normal pancreas, chronic pancreatitis, and focal pancreatic lesions. Gastrointest Endosc 2007; 65: 971 – 978

[165] Azemoto N, Kumagi T, Koizumi M et al. Diagnostic Challenge in Pancreatic Sarcoidosis using Endoscopic Ultrasonography. Intern Med 2018; 57: 231 – 235

[166] Chantarojanasiri T, Hirooka Y, Kawashima H et al. Endoscopic ultrasound in the diagnosis of acinar cell carcinoma of the pancreas: contrast-enhanced endoscopic ultrasound, endoscopic ultrasound elastography, and pathological correlation. Endosc Int Open 2016; 4: E1223 – E1226

[167] Itoh Y, Itoh A, Kawashima H et al. Quantitative analysis of diagnosing pancreatic fibrosis using EUS-elastography (comparison with surgical specimens). J Gastroenterol 2014; 49: 1183 – 1192

[168] Jafri M, Sachdev AH, Khanna L et al. The Role of Real Time Endoscopic Ultrasound Guided Elastography for Targeting EUS-FNA of Suspicious Pancreatic Masses: A Review of the Literature and A Single Center Experience. JOP 2016; 17: 516 – 524

[169] Kuwahara T, Hirooka Y, Kawashima H et al. Quantitative diagnosis of chronic pancreatitis using EUS elastography. J Gastroenterol 2017; 52: 868 – 874

[170] Kuwahara T, Hirooka Y, Kawashima H et al. Usefulness of endoscopic ultrasonography-elastography as a predictive tool for the occurrence of pancreatic fistula after pancreatoduodenectomy. J Hepatobiliary Pancreat Sci 2017; 24: 649 – 656

[171] Lee TH, Cho YD, Cha SW et al. Endoscopic ultrasound elastography for the pancreas in Korea: a preliminary single center study. Clin Endosc 2013; 46: 172 – 177

[172] Pei Q, Zou X, Zhang X et al. Diagnostic value of EUS elastography in differentiation of benign and malignant solid pancreatic masses: a meta-analysis. Pancreatology 2012; 12: 402 – 408

[173] Popescu A, Ciocalteu AM, Gheonea DI et al. Utility of endoscopic ultrasound multimodal examination with fine needle aspiration for the diagnosis of pancreatic insulinoma – a case report. Current health sciences journal 2012; 38: 36 – 40

[174] Rana SS, Sharma R, Guleria S et al. Endoscopic ultrasound (EUS) elastography and contrast enhanced EUS in groove pancreatitis. Indian J Gastroenterol 2018; 37: 70 – 71

[175] Schrader H, Wiese M, Ellrichmann M et al. Diagnostic value of quantitative EUS elastography for malignant pancreatic tumours: relationship with pancreatic fibrosis. Ultraschall in Med 2012; 33: E196 – E201

[176] Soares JB, Iglesias-Garcia J, Goncalves B et al. Interobserver agreement of EUS elastography in the evaluation of solid pancreatic lesions. Endosc Ultrasound 2015; 4: 244 – 249

[177] Rustemovic N, Opacic D, Ostojic Z et al. Comparison of elastography methods in patients with pancreatic masses. Endosc Ultrasound 2014; 3: S4

[178] Saftoiu A, Vilman P. Endoscopic ultrasound elastography – a new imaging technique for the visualization of tissue elasticity distribution. J Gastrointestin Liver Dis 2006; 15: 161 – 165

[179] Mateen MA, Muheet KA, Mohan RJ et al. Evaluation of ultrasound based acoustic radiation force impulse (ARFI) and eSie touch sonoelastography for diagnosis of inflammatory pancreatic diseases. JOP 2012; 13: 36 – 44

[180] Goya C, Hamidi C, Hattapoglu S et al. Use of acoustic radiation force impulse elastography to diagnose acute pancreatitis at hospital admission: comparison with sonography and computed tomography. J Ultrasound Med 2014; 33: 1453 – 1460

[181] Domínguez-Muñoz JE. Predicting Pancreatic Exocrine Insufficiency With EUS Elastography. Gastroenterol Hepatol (N Y) 2016; 12: 511 – 512

[182] Uchida H, Hirooka Y, Itoh A et al. Feasibility of tissue elastography using transcutaneous ultrasonography for the diagnosis of pancreatic diseases. Pancreas 2009; 38: 17 – 22

[183] Friedrich-Rust M, Schlueter N, Smaczny C et al. Non-invasive measurement of liver and pancreas fibrosis in patients with cystic fibrosis. J Cyst Fibros 2013; 12: 431 – 439

[184] Sugimoto M, Takahashi S, Kojima M et al. What is the nature of pancreatic consistency? Assessment of the elastic modulus of the pancreas and comparison with tactile sensation, histology, and occurrence of postoperative pancreatic fistula after pancreaticoduodenectomy. Surgery 2014; 156: 1204 – 1211

[185] Hatano M, Watanabe J, Kushihata F et al. Quantification of pancreatic stiffness on intraoperative ultrasound elastography and evaluation of its relationship with postoperative pancreatic fistula. Int Surg 2015; 100: 497 – 502

[186] D’Onofrio M, Crosara S, De Robertis R et al. Elastography of the pancreas. Eur J Radiol 2014; 83: 415 – 419

[187] Dong Y, D’Onofrio M, Hocke M et al. Autoimmune pancreatitis: Imaging features. Endosc Ultrasound 2018; 7: 196 – 203

[188] Lee TK, Kang CM, Park MS et al. Prediction of postoperative pancreatic fistulas after pancreatectomy: assessment with acoustic radiation force impulse elastography. J Ultrasound Med 2014; 33: 781 – 786

[189] Hu DM, Gong TT, Zhu Q. Endoscopic ultrasound elastography for differential diagnosis of pancreatic masses: a meta-analysis. Dig Dis Sci 2013; 58: 1125 – 1131

[190] Mei M, Ni J, Liu D et al. EUS elastography for diagnosis of solid pancreatic masses: a meta-analysis. Gastrointest Endosc 2013; 77: 578 – 589

[191] Li X, Xu W, Shi J et al. Endoscopic ultrasound elastography for differentiating between pancreatic adenocarcinoma and inflammatory masses: a meta-analysis. World J Gastroenterol 2013; 19: 6284 – 6291

[192] Ying L, Lin X, Xie ZL et al. Clinical utility of endoscopic ultrasound elastography for identification of malignant pancreatic masses: a meta-analysis. J Gastroenterol Hepatol 2013; 28: 1434 – 1443

[193] Iglesias-Garcia J, Larino-Noia J, Abdulkader I et al. EUS elastography for the characterization of solid pancreatic masses. Gastrointest Endosc 2009; 70: 1101 – 1108

[194] Giovannini M, Thomas B, Erwan B et al. Endoscopic ultrasound elastography for evaluation of lymph nodes and pancreatic masses: A multicenter study. World Journal of Gastroenterology 2009; 15: 1587 – 1593

[195] Ignee A, Jenssen C, Hocke M et al. Contrast-enhanced (endoscopic) ultrasound and endoscopic ultrasound elastography in gastrointestinal stromal tumours. Endoscopic Ultrasound 2017; 6: 55 – 60

[196] Havre RF, Ødegaard S, Gilja OH et al. Characterization of solid focal pancreatic lesions using endoscopic ultrasonography with real-time elastography. Scand J Gastroenterol 2014; 49: 742 – 751

[197] Dawwas MF, Taha H, Leeds JS et al. Diagnostic accuracy of quantitative EUS elastography for discriminating malignant from benign solid pancreatic masses: a prospective, single-center study. Gastrointest Endosc 2012; 76: 953 – 961

[198] Mayerle J, Beyer G, Simon P et al. Prospective cohort study comparing transient EUS guided elastography to EUS-FNA for the diagnosis of solid pancreatic mass lesions. Pancreatology 2016; 16: 110 – 114

[199] Figueiredo FA, da Silva PM, Monges G et al. Yield of Contrast-Enhanced Power Doppler Endoscopic Ultrasonography and Strain Ratio Obtained by EUS-Elastography in the Diagnosis of Focal Pancreatic Solid Lesions. Endosc Ultrasound 2012; 1: 143 – 149

[200] Popescu A, Ciocalteu AM, Gheonea DI et al. Utility of endoscopic ultrasound multimodal examination with fine needle aspiration for the diagnosis of pancreatic insulinoma – a case report. Curr Health Sci J 2012; 38: 36 – 40

[201] Deprez PH. EUS elastography: is it replacing or supplementing tissue acquisition? Gastrointest Endosc 2013; 77: 590 – 592

[202] Săftoiu A, Iordache SA, Gheonea DI et al. Combined contrast-enhanced power Doppler and real-time sonoelastography performed during EUS, used in the differential diagnosis of focal pancreatic masses (with videos). Gastrointest Endosc 2010; 72: 739 – 747

[203] Dumonceau JM, Deprez PH, Jenssen C et al. Indications, results, and clinical impact of endoscopic ultrasound (EUS)-guided sampling in gastroenterology: European Society of Gastrointestinal Endoscopy (ESGE) Clinical Guideline – Updated January 2017. Endoscopy 2017; 49: 695 – 714

[204] Jenssen C, Hocke M, Fusaroli P et al. EFSUMB Guidelines on Interventional Ultrasound (INVUS), Part IV – EUS-guided interventions: General Aspects and EUS-guided Sampling (Short Version). Ultraschall in Med 2016; 37: 157 – 169

[205] Jenssen C, Hocke M, Fusaroli P et al. EFSUMB Guidelines on Interventional Ultrasound (INVUS), Part IV – EUS-guided Interventions: General

aspects and EUS-guided sampling (Long Version). Ultraschall in Med 2016; 37: E33 – E76

[206] Hewitt MJ, McPhail MJ, Possamai L et al. EUS-guided FNA for diagnosis of solid pancreatic neoplasms: a meta-analysis. Gastrointest Endosc 2012; 75: 319 – 331

[207] Dietrich C, Sahai A, D'Onofrio M et al. Differential diagnosis of small solid pancreatic lesions. Gastrointestinal Endoscopy 2016; 84: 933 – 940

[208] D'Onofrio M, Crosara S, Canestrini S et al. Virtual analysis of pancreatic cystic lesion fluid content by ultrasound acoustic radiation force impulse quantification. J Ultrasound Med 2013; 32: 647 – 651

[209] D'Onofrio M, Gallotti A, Falconi M et al. Acoustic radiation force impulse ultrasound imaging of pancreatic cystic lesions: preliminary results. Pancreas 2010; 39: 939 – 940

[210] D'Onofrio M, Gallotti A, Martone E et al. Solid appearance of pancreatic serous cystadenoma diagnosed as cystic at ultrasound acoustic radiation force impulse imaging. JOP 2009; 10: 543 – 546

[211] D'Onofrio M, Gallotti A, Mucelli RP. Pancreatic mucinous cystadenoma at ultrasound acoustic radiation force impulse (ARFI) imaging. Pancreas 2010; 39: 684 – 685

[212] D'Onofrio M, Gallotti A, Salvia R et al. Acoustic radiation force impulse (ARFI) ultrasound imaging of pancreatic cystic lesions. Eur J Radiol 2011; 80: 241 – 244

[213] Havre RF, Waage JR, Gilja OH et al. Real-Time Elastography: Strain Ratio Measurements Are Influenced by the Position of the Reference Area. Ultraschall in Med 2011. (Epub ahead of print)

[214] Nylund K, Ødegaard S, Hausken T et al. Sonography of the small intestine. World J Gastroenterol 2009; 15: 1319 – 1330

[215] Nylund K, Maconi G, Hollerweger A et al. EFSUMB Recommendations and Guidelines for Gastrointestinal Ultrasound Part 1: Examination Techniques and Normal Findings (Long version). Ultraschall in Der Medizin 2017; 38: E1 – E15

[216] Kim K, Johnson LA, Jia C et al. Noninvasive ultrasound elasticity imaging (UEI) of Crohn's disease: animal model. Ultrasound Med Biol 2008; 34: 902 – 912

[217] Stidham RW, Higgins PD. Imaging of intestinal fibrosis: current challenges and future methods. United European Gastroenterol J 2016; 4: 515 – 522

[218] Dillman JR, Stidham RW, Higgins PD et al. US elastography-derived shear wave velocity helps distinguish acutely inflamed from fibrotic bowel in a Crohn disease animal model. Radiology 2013; 267: 757 – 766

[219] Sconfienza LM, Cavallaro F, Colombi V et al. In-vivo Axial-strain Sonoelastography Helps Distinguish Acutely-inflamed from Fibrotic Terminal Ileum Strictures in Patients with Crohn's Disease: Preliminary Results. Ultrasound Med Biol 2016; 42: 855 – 863

[220] Havre RF, Leh S, Gilja OH et al. Strain assessment in surgically resected inflammatory and neoplastic bowel lesions. Ultraschall in Med 2014; 35: 149 – 158

[221] Pescatori LC, Mauri G, Savarino E et al. Bowel Sonoelastography in Patients with Crohn's Disease: A Systematic Review. Ultrasound Med Biol 2018; 44: 297 – 302

[222] Baumgart DC, Müller HP, Grittner U et al. US-based Real-time Elastography for the Detection of Fibrotic Gut Tissue in Patients with Stricturing Crohn Disease. Radiology 2015; 275: 889 – 899

[223] Fraquelli M, Branchi F, Cribiù FM et al. The Role of Ultrasound Elasticity Imaging in Predicting Ileal Fibrosis in Crohn's Disease Patients. Inflamm Bowel Dis 2015; 21: 2605 – 2612

[224] Serra C, Rizzello F, Pratico' C et al. Real-time elastography for the detection of fibrotic and inflammatory tissue in patients with stricturing Crohn's disease. J Ultrasound 2017; 20: 273 – 284

[225] Orlando S, Fraquelli M, Coletta M et al. Ultrasound Elasticity Imaging predicts therapeutic outcomes of patients with Crohn's disease treated with anti-tumour necrosis factor antibodies. J Crohns Colitis 2018; 12: 63 – 70

[226] Waage JE, Bach SP, Pfeffer F et al. Combined endorectal ultrasonography and strain elastography for the staging of early rectal cancer. Colorectal Dis 2015; 17: 50 – 56

[227] Waage JE, Leh S, Røsler C et al. Endorectal ultrasonography, strain elastography and MRI differentiation of rectal adenomas and adenocarcinomas. Colorectal Dis 2015; 17: 124 – 131

[228] Waage JE, Rafaelsen SR, Borley NR et al. Strain Elastography Evaluation of Rectal Tumours: Inter- and Intraobserver Reproducibility. Ultraschall in Med 2015; 36: 611 – 617

[229] Rafaelsen SR, Vagn-Hansen C, Sørensen T et al. Elastography and diffusion-weighted MRI in patients with rectal cancer. Br J Radiol 2015; 88: 20150294

[230] Chen LD, Wang W, Xu JB et al. Assessment of Rectal Tumours with Shear-Wave Elastography before Surgery: Comparison with Endorectal US. Radiology 2017; 285: 279 – 292

[231] Arena U, Lupsor Platon M, Stasi C et al. Liver stiffness is influenced by a standardized meal in patients with chronic hepatitis C virus at different stages of fibrotic evolution. Hepatology 2013; 58: 65 – 72

[232] Berzigotti A, De Gottardi A, Vukotic R et al. Effect of meal ingestion on liver stiffness in patients with cirrhosis and portal hypertension. PLoS One 2013; 8: e58742

[233] Ștefănescu H, Grigorescu M, Lupşor M et al. Spleen stiffness measurement using Fibroscan for the noninvasive assessment of esophageal varices in liver cirrhosis patients. J Gastroenterol Hepatol 2011; 26: 164 – 170

[234] Colecchia A, Montrone L, Scaioli E et al. Measurement of spleen stiffness to evaluate portal hypertension and the presence of esophageal varices in patients with HCV-related cirrhosis. Gastroenterology 2012; 143: 646 – 654

[235] Procopet B, Berzigotti A, Abraldes JG et al. Real-time shear-wave elastography: applicability, reliability and accuracy for clinically significant portal hypertension. J Hepatol 2015; 62: 1068 – 1075

[236] Karlas T, Lindner F, Tröltzsch M et al. Assessment of spleen stiffness using acoustic radiation force impulse imaging (ARFI): definition of examination standards and impact of breathing maneuvers. Ultraschall in Med 2014; 35: 38 – 43

[237] Jansen C, Bogs C, Verlinden W et al. Shear-wave elastography of the liver and spleen identifies clinically significant portal hypertension: A prospective multicentre study. Liver Int 2017; 37: 396 – 405

[238] Samir AE, Dhyani M, Vij A et al. Shear-wave elastography for the estimation of liver fibrosis in chronic liver disease: determining accuracy and ideal site for measurement. Radiology 2015; 274: 888 – 896

[239] Grgurevic I, Puljiz Z, Brnic D et al. Liver and spleen stiffness and their ratio assessed by real-time two dimensional-shear wave elastography in patients with liver fibrosis and cirrhosis due to chronic viral hepatitis. Eur Radiol 2015; 25: 3214 – 3221

[240] Song J, Huang J, Huang H et al. Performance of spleen stiffness measurement in prediction of clinical significant portal hypertension: A meta-analysis. Clin Res Hepatol Gastroenterol 2018; 42: 216 – 226

[241] Zykus R, Jonaitis L, Petrenkienė V et al. Liver and spleen transient elastography predicts portal hypertension in patients with chronic liver disease: a prospective cohort study. BMC Gastroenterol 2015; 15: 183

[242] Takuma Y, Nouso K, Morimoto Y et al. Portal Hypertension in Patients with Liver Cirrhosis: Diagnostic Accuracy of Spleen Stiffness. Radiology 2016; 279: 609 – 619

[243] Attia D, Schoenemeier B, Rodt T et al. Evaluation of Liver and Spleen Stiffness with Acoustic Radiation Force Impulse Quantification Elastography for Diagnosing Clinically Significant Portal Hypertension. Ultraschall in Med 2015; 36: 603 – 610

[244] Balakrishnan M, Souza F, Muñoz C et al. Liver and Spleen Stiffness Measurements by Point Shear Wave Elastography via Acoustic Radiation Force Impulse: Intraobserver and Interobserver Variability and Predictors of Variability in a US Population. J Ultrasound Med 2016; 35: 2373 – 2380

[245] Elkrief L, Rautou PE, Ronot M et al. Prospective comparison of spleen and liver stiffness by using shear-wave and transient elastography for detection of portal hypertension in cirrhosis. Radiology 2015; 275: 589 – 598

[246] Singh S, Eaton JE, Murad MH et al. Accuracy of spleen stiffness measurement in detection of esophageal varices in patients with chronic liver disease: systematic review and meta-analysis. Clin Gastroenterol Hepatol 2014; 12: 935 – 945.e934

[247] Calvaruso V, Bronte F, Conte E et al. Modified spleen stiffness measurement by transient elastography is associated with presence of large oesophageal varices in patients with compensated hepatitis C virus cirrhosis. J Viral Hepat 2013; 20: 867 – 874

[248] Stefanescu H, Allegretti G, Salvatore V et al. Bidimensional shear wave ultrasound elastography with supersonic imaging to predict presence of oesophageal varices in cirrhosis. Liver Int 2017; 37: 1405

[249] Bota S, Sporea I, Sirli R et al. Can ARFI elastography predict the presence of significant esophageal varices in newly diagnosed cirrhotic patients? Ann Hepatol 2012; 11: 519 – 525

[250] Colecchia A, Colli A, Casazza G et al. Spleen stiffness measurement can predict clinical complications in compensated HCV-related cirrhosis: a prospective study. J Hepatol 2014; 60: 1158 – 1164

[251] Gao J, Ran HT, Ye XP et al. The stiffness of the liver and spleen on ARFI Imaging pre and post TIPS placement: a preliminary observation. Clin Imaging 2012; 36: 135 – 141

[252] Novelli PM, Cho K, Rubin JM. Sonographic assessment of spleen stiffness before and after transjugular intrahepatic portosystemic shunt placement with or without concurrent embolization of portal systemic collateral veins in patients with cirrhosis and portal hypertension: a feasibility study. J Ultrasound Med 2015; 34: 443 – 449

[253] Verlinden W, Bourgeois S, Gigase P et al. Liver Fibrosis Evaluation Using Real-time Shear Wave Elastography in Hepatitis C-Monoinfected and Human Immunodeficiency Virus/Hepatitis C-Coinfected Patients. J Ultrasound Med 2016; 35: 1299 – 1308

[254] Pons M, Simón-Talero M, Millán L et al. Basal values and changes of liver stiffness predict the risk of disease progression in compensated advanced chronic liver disease. Dig Liver Dis 2016; 48: 1214 – 1219

[255] Sharma P, Mishra SR, Kumar M et al. Liver and spleen stiffness in patients with extrahepatic portal vein obstruction. Radiology 2012; 263: 893 – 899

[256] Furuichi Y, Moriyasu F, Taira J et al. Noninvasive diagnostic method for idiopathic portal hypertension based on measurements of liver and spleen stiffness by ARFI elastography. J Gastroenterol 2013; 48: 1061 – 1068

[257] Seijo S, Reverter E, Miquel R et al. Role of hepatic vein catheterisation and transient elastography in the diagnosis of idiopathic portal hypertension. Dig Liver Dis 2012; 44: 855 – 860

[258] Uchida H, Sakamoto S, Kobayashi M et al. The degree of spleen stiffness measured on acoustic radiation force impulse elastography predicts the severity of portal hypertension in patients with biliary atresia after portoenterostomy. J Pediatr Surg 2015; 50: 559 – 564

[259] Colecchia A, Marasco G, Festi D. Are Noninvasive Methods Clinically Useful in Advanced, Decompensated Liver Cirrhosis When “Les Jeux Sont Faits”? Radiology 2016; 278: 304 – 305

[260] Iurlo A, Cattaneo D, Giunta M et al. Transient elastography spleen stiffness measurements in primary myelofibrosis patients: a pilot study in a single centre. Br J Haematol 2015; 170: 890 – 892

[261] Cassinotto C, Charrie A, Mouries A et al. Liver and spleen elastography using supersonic shear imaging for the non-invasive diagnosis of cirrhosis severity and oesophageal varices. Dig Liver Dis 2015; 47: 695 – 701

[262] Correas JM, Anglicheau D, Joly D et al. Ultrasound-based imaging methods of the kidney-recent developments. Kidney Int 2016; 90: 1199 – 1210

[263] Derieppe M, Delmas Y, Gennisson JL et al. Detection of intrarenal microstructural changes with supersonic shear wave elastography in rats. Eur Radiol 2012; 22: 243 – 250

[264] Franchi-Abella S, Elie C, Correas JM. Ultrasound elastography: advantages, limitations and artefacts of the different techniques from a study on a phantom. Diagn Interv Imaging 2013; 94: 497 – 501

[265] Ferraioli G, Tinelli C, Malfitano A et al. Performance of real-time strain elastography, transient elastography, and aspartate-to-platelet ratio index in the assessment of fibrosis in chronic hepatitis C. Am J Roentgenol 2012; 199: 19 – 25

[266] Nightingale K, Bentley R, Trahey G. Observations of tissue response to acoustic radiation force: opportunities for imaging. Ultrason Imaging 2002; 24: 129 – 138

[267] Sarvazyan AP, Rudenko OV, Nyborg WL. Biomedical applications of radiation force of ultrasound: historical roots and physical basis. Ultrasound Med Biol 2010; 36: 1379 – 1394

[268] Syversveen T, Brabrand K, Midtvedt K et al. Assessment of renal allograft fibrosis by acoustic radiation force impulse quantification–a pilot study. Transpl Int 2011; 24: 100 – 105

[269] Ozkan F, Yavuz YC, Inci MF et al. Interobserver variability of ultrasound elastography in transplant kidneys: correlations with clinical-Doppler parameters. Ultrasound Med Biol 2013; 39: 4 – 9

[270] Guo LH, Xu HX, Fu HJ et al. Acoustic radiation force impulse imaging for noninvasive evaluation of renal parenchyma elasticity: preliminary findings. PLoS One 2013; 8: e68925

[271] Bob F, Bota S, Sporea I et al. Kidney shear wave speed values in subjects with and without renal pathology and inter-operator reproducibility of acoustic radiation force impulse elastography (ARFI)–preliminary results. PLoS One 2014; 9: e113761

[272] Grenier N, Poulain S, Lepreux S et al. Quantitative elastography of renal transplants using supersonic shear imaging: a pilot study. Eur Radiol 2012; 22: 2138 – 2146

[273] Samir AE, Allegretti AS, Zhu Q et al. Shear wave elastography in chronic kidney disease: a pilot experience in native kidneys. BMC Nephrol 2015; 16: 119

[274] Gennisson JL, Rénier M, Catheline S et al. Acoustoelasticity in soft solids: assessment of the nonlinear shear modulus with the acoustic radiation force. J Acoust Soc Am 2007; 122: 3211 – 3219

[275] Gennisson JL, Deffieux T, Macé E et al. Viscoelastic and anisotropic mechanical properties of in vivo muscle tissue assessed by supersonic shear imaging. Ultrasound Med Biol 2010; 36: 789 – 801

[276] Gennisson JL, Grenier N, Combe C et al. Supersonic shear wave elastography of in vivo pig kidney: influence of blood pressure, urinary pressure and tissue anisotropy. Ultrasound Med Biol 2012; 38: 1559 – 1567

[277] Bota S, Bob F, Sporea I et al. Factors that influence kidney shear wave speed assessed by acoustic radiation force impulse elastography in patients without kidney pathology. Ultrasound Med Biol 2015; 41: 1 – 6

[278] Asano K, Ogata A, Tanaka K et al. Acoustic radiation force impulse elastography of the kidneys: is shear wave velocity affected by tissue fibrosis or renal blood flow? J Ultrasound Med 2014; 33: 793 – 801

[279] Bob F, Bota S, Sporea I et al. Relationship between the estimated glomerular filtration rate and kidney shear wave speed values assessed by acoustic radiation force impulse elastography: a pilot study. J Ultrasound Med 2015; 34: 649 – 654

[280] Singh H, Panta OB, Khanal U et al. Renal Cortical Elastography: Normal Values and Variations. J Med Ultrasound 2017; 25: 215 – 220

[281] Grenier N, Gennisson JL, Cornelis F et al. Renal ultrasound elastography. Diagn Interv Imaging 2013; 94: 545 – 550

[282] Arndt R, Schmidt S, Loddenkemper C et al. Noninvasive evaluation of renal allograft fibrosis by transient elastography–a pilot study. Transpl Int 2010; 23: 871 – 877

[283] Stock KF, Klein BS, Cong MT et al. ARFI-based tissue elasticity quantification and kidney graft dysfunction: first clinical experiences. Clin Hemorheol Microcirc 2011; 49: 527 – 535

[284] Marticorena GarciaSR, Guo J, Dürr M et al. Comparison of ultrasound shear wave elastography with magnetic resonance elastography and renal microvascular flow in the assessment of chronic renal allograft dysfunction. Acta Radiol 2018; 59: 1139 – 1145

[285] Grass L, Szekely N, Alrajab A et al. Point shear wave elastography (pSWE) using Acoustic Radiation Force Impulse (ARFI) imaging: a feasibility study and norm values for renal parenchymal stiffness in healthy children and adolescents. Med Ultrason 2017; 19: 366 – 373

[286] Sasaki Y, Hirooka Y, Kawashima H et al. Measurements of renal shear wave velocities in chronic kidney disease patients. Acta Radiol 2018; 59: 884 – 890

[287] He WY, Jin YJ, Wang WP et al. Tissue elasticity quantification by acoustic radiation force impulse for the assessment of renal allograft function. Ultrasound Med Biol 2014; 40: 322 – 329

[288] Bob F, Grosu I, Sporea I et al. Ultrasound-Based Shear Wave Elastography in the Assessment of Patients with Diabetic Kidney Disease. Ultrasound Med Biol 2017; 43: 2159 – 2166

[289] Syversveen T, Midtvedt K, Berstad AE et al. Tissue elasticity estimated by acoustic radiation force impulse quantification depends on the applied transducer force: an experimental study in kidney transplant patients. Eur Radiol 2012; 22: 2130 – 2137

[290] Wang L, Xia P, Lv K et al. Assessment of renal tissue elasticity by acoustic radiation force impulse quantification with histopathological correlation: preliminary experience in chronic kidney disease. Eur Radiol 2014; 24: 1694 – 1699

[291] Lee J, Oh YT, Joo DJ et al. Acoustic Radiation Force Impulse Measurement in Renal Transplantation: A Prospective, Longitudinal Study With Protocol Biopsies. Medicine (Baltimore) 2015; 94: e1590

[292] Bob F, Grosu I, Sporea I et al. Is there a correlation between kidney shear wave velocity measured with VTQ and histological parameters in patients with chronic glomerulonephritis? A pilot study. Med Ultrason 2018; 1: 27 – 31

[293] Early HM, Cheang EC, Aguilera JM et al. Utility of Shear Wave Elastography for Assessing Allograft Fibrosis in Renal Transplant Recipients: A Pilot Study. J Ultrasound Med 2018; 37: 1455 – 1465

[294] Yoo MG, Jung DC, Oh YT et al. Usefulness of Multiparametric Ultrasound for Evaluating Structural Abnormality of Transplanted Kidney: Can We Predict Histologic Abnormality on Renal Biopsy in Advance? Am J Roentgenol 2017; 209: W139 – W144

[295] Bruno C, Caliari G, Zaffanello M et al. Acoustic radiation force impulse (ARFI) in the evaluation of the renal parenchymal stiffness in paediatric patients with vesicoureteral reflux: preliminary results. Eur Radiol 2013; 23: 3477 – 3484

[296] Clevert DA, Stock K, Klein B et al. Evaluation of Acoustic Radiation Force Impulse (ARFI) imaging and contrast-enhanced ultrasound in renal tumours of unknown etiology in comparison to histological findings. Clin Hemorheol Microcirc 2009; 43: 95 – 107

[297] Sidhu PS. Ultrasound Collaboration across Europe: An EFSUMB success story in politically troubled times? Ultraschall in Med 2016; 37: 451 – 452

[298] Tan S, Miao LY, Cui LG et al. Value of Shear Wave Elastography Versus Contrast-Enhanced Sonography for Differentiating Benign and Malignant Superficial Lymphadenopathy Unexplained by Conventional Sonography. J Ultrasound Med 2017; 36: 189 – 199

[299] Ghajarzadeh M, Mohammadifar M, Azarkhish K et al. Sono-elastography for Differentiating Benign and Malignant Cervical Lymph Nodes: A Systematic Review and Meta-Analysis. Int J Prev Med 2014; 5: 1521 – 1528

[300] Ying L, Hou Y, Zheng HM et al. Real-time elastography for the differentiation of benign and malignant superficial lymph nodes: a meta-analysis. Eur J Radiol 2012; 81: 2576 – 2584

[301] Suh CH, Choi YJ, Baek JH et al. The diagnostic performance of shear wave elastography for malignant cervical lymph nodes: A systematic review and meta-analysis. Eur Radiol 2017; 27: 222 – 230

[302] Xu W, Shi J, Zeng X et al. EUS elastography for the differentiation of benign and malignant lymph nodes: a meta-analysis. Gastrointest Endosc 2011; 74: 1001 – 1009; quiz 1115.e1001–1004

[303] Mao XW, Yang JY, Zheng XX et al. Comparison of two quantitative methods of endobronchial ultrasound real-time elastography for evaluating intrathoracic lymph nodes. Zhonghua Jie He He Hu Xi Za Zhi 2017; 40: 431 – 434

[304] Sun J, Zheng X, Mao X et al. Endobronchial Ultrasound Elastography for Evaluation of Intrathoracic Lymph Nodes: A Pilot Study. Respiration 2017; 93: 327 – 338

[305] Jung WS, Kim JA, Son EJ et al. Shear wave elastography in evaluation of cervical lymph node metastasis of papillary thyroid carcinoma: elasticity index as a prognostic implication. Ann Surg Oncol 2015; 22: 111 – 116

[306] You J, Chen J, Xiang F et al. The value of quantitative shear wave elastography in differentiating the cervical lymph nodes in patients with thyroid nodules. J Med Ultrason (2001) 2018; 45: 251 – 259

[307] Janssen J, Dietrich CF, Will U et al. Endosonographic elastography in the diagnosis of mediastinal lymph nodes. Endoscopy 2007; 39: 952 – 957

[308] Bhatia KS, Lee YY, Yuen EH et al. Ultrasound elastography in the head and neck. Part II. Accuracy for malignancy. Cancer Imaging 2013; 13: 260 – 276

[309] Larsen MH, Fristrup C, Hansen TP et al. Endoscopic ultrasound, endoscopic sonoelastography, and strain ratio evaluation of lymph nodes with histology as gold standard. Endoscopy 2012; 44: 759 – 766

[310] Łasecki M, Olchowy C, Sokołowska-Dąbek D et al. Modified sonoelastographic scale score for lymph node assessment in lymphoma – a preliminary report. J Ultrason 2015; 15: 45 – 55

[311] Dudea SM, Botar-Jid C, Dumitriu D et al. Differentiating benign from malignant superficial lymph nodes with sonoelastography. Med Ultrason 2013; 15: 132 – 139

[312] De Zordo T, Chhem R, Smekal V et al. Real-time sonoelastography: findings in patients with symptomatic achilles tendons and comparison to healthy volunteers. Ultraschall in Med 2010; 31: 394 – 400

[313] De Zordo T, Fink C, Feuchtner GM et al. Real-time sonoelastography findings in healthy Achilles tendons. Am J Roentgenol 2009; 193: W134 – W138

[314] Turan A, Teber MA, Yakut ZI et al. Sonoelastographıc assessment of the age-related changes of the Achilles tendon. Med Ultrason 2015; 17: 58 – 61

[315] Aubry S, Risson JR, Kastler A et al. Biomechanical properties of the calcaneal tendon in vivo assessed by transient shear wave elastography. Skeletal Radiol 2013; 42: 1143 – 1150

[316] Chen XM, Cui LG, He P et al. Shear wave elastographic characterization of normal and torn achilles tendons: a pilot study. J Ultrasound Med 2013; 32: 449 – 455

[317] Ooi CC, Schneider ME, Malliaras P et al. Diagnostic performance of axial-strain sonoelastography in confirming clinically diagnosed Achilles tendinopathy: comparison with B-mode ultrasound and color Doppler imaging. Ultrasound Med Biol 2015; 41: 15 – 25

[318] Klauser AS, Miyamoto H, Tamegger M et al. Achilles tendon assessed with sonoelastography: histologic agreement. Radiology 2013; 267: 837 – 842

[319] Balaban M, Idilman IS, Ipek A et al. Elastographic Findings of Achilles Tendons in Asymptomatic Professional Male Volleyball Players. J Ultrasound Med 2016; 35: 2623 – 2628

[320] Ooi CC, Schneider ME, Malliaras P et al. Prevalence of morphological and mechanical stiffness alterations of mid Achilles tendons in asymptomatic marathon runners before and after a competition. Skeletal Radiol 2015; 44: 1119 – 1127

[321] Ozcan AN, Tan S, Tangal NG et al. Real-time sonoelastography of the patellar and quadriceps tendons: pattern description in professional athletes and healthy volunteers. Med Ultrason 2016; 18: 299 – 304

[322] Klauser AS, Pamminger M, Halpern EJ et al. Extensor tendinopathy of the elbow assessed with sonoelastography: histologic correlation. Eur Radiol 2017; 27: 3460 – 3466

[323] De Zordo T, Lill SR, Fink C et al. Real-time sonoelastography of lateral epicondylitis: comparison of findings between patients and healthy volunteers. Am J Roentgenol 2009; 193: 180 – 185

[324] Lacourpaille L, Nordez A, Hug F et al. Time-course effect of exercise-induced muscle damage on localized muscle mechanical properties assessed using elastography. Acta Physiol (Oxf) 2014; 211: 135 – 146

[325] Klauser AS, Pamminger MJ, Halpern EJ et al. Sonoelastography of the Common Flexor Tendon of the Elbow with Histologic Agreement: A Cadaveric Study. Radiology 2017; 283: 486 – 491

[326] Tudisco C, Bisicchia S, Stefanini M et al. Tendon quality in small unilateral supraspinatus tendon tears. Real-time sonoelastography correlates with clinical findings. Knee Surg Sports Traumatol Arthrosc 2015; 23: 393 – 398

[327] Rosskopf AB, Ehrmann C, Buck FM et al. Quantitative Shear-Wave US Elastography of the Supraspinatus Muscle: Reliability of the Method and Relation to Tendon Integrity and Muscle Quality. Radiology 2016; 278: 465 – 474

[328] Botar-Jid C, Damian L, Dudea SM et al. The contribution of ultrasonography and sonoelastography in assessment of myositis. Med Ultrason 2010; 12: 120 – 126

[329] Drakonaki E. Ultrasound elastography for imaging tendons and muscles. J Ultrason 2012; 12: 214 – 225

[330] Taljanovic MS, Gimber LH, Becker GW et al. Shear-Wave Elastography: Basic Physics and Musculoskeletal Applications. Radiographics 2017; 37: 855 – 870

[331] Akagi R, Kusama S. Comparison Between Neck and Shoulder Stiffness Determined by Shear Wave Ultrasound Elastography and a Muscle Hardness Meter. Ultrasound Med Biol 2015; 41: 2266 – 2271

[332] Andonian P, Viallon M, Le Goff C et al. Shear-Wave Elastography Assessments of Quadriceps Stiffness Changes prior to, during and after Prolonged Exercise: A Longitudinal Study during an Extreme Mountain Ultra-Marathon. PLoS One 2016; 11: e0161855

[333] Brandenburg JE, Eby SF, Song P et al. Quantifying passive muscle stiffness in children with and without cerebral palsy using ultrasound shear wave elastography. Dev Med Child Neurol 2016; 58: 1288 – 1294

[334] Dubois G, Kheireddine W, Vergari C et al. Reliable protocol for shear wave elastography of lower limb muscles at rest and during passive stretching. Ultrasound Med Biol 2015; 41: 2284 – 2291

[335] Eby SF, Cloud BA, Brandenburg JE et al. Shear wave elastography of passive skeletal muscle stiffness: influences of sex and age throughout adulthood. Clin Biomech (Bristol, Avon) 2015; 30: 22 – 27

[336] Koo TK, Guo JY, Cohen JH et al. Quantifying the passive stretching response of human tibialis anterior muscle using shear wave elastography. Clin Biomech (Bristol, Avon) 2014; 29: 33 – 39

[337] Nakamura M, Hasegawa S, Umegaki H et al. The difference in passive tension applied to the muscles composing the hamstrings – Comparison among muscles using ultrasound shear wave elastography. Man Ther 2016; 24: 1 – 6

[338] Du LJ, He W, Cheng LG et al. Ultrasound shear wave elastography in assessment of muscle stiffness in patients with Parkinson's disease: a primary observation. Clin Imaging 2016; 40: 1075 – 1080

[339] Eby S, Zhao H, Song P et al. Quantitative Evaluation of Passive Muscle Stiffness in Chronic Stroke. Am J Phys Med Rehabil 2016; 95: 899 – 910

[340] Lee SS, Spear S, Rymer WZ. Quantifying changes in material properties of stroke-impaired muscle. Clin Biomech (Bristol, Avon) 2015; 30: 269 – 275

[341] Lacourpaille L, Hug F, Guével A et al. Non-invasive assessment of muscle stiffness in patients with Duchenne muscular dystrophy. Muscle Nerve 2015; 51: 284 – 286

[342] Illomei G, Spinicci G, Locci E et al. Muscle elastography: a new imaging technique for multiple sclerosis spasticity measurement. Neurol Sci 2017; 38: 433 – 439

[343] Song Y, Lee S, Yoo DH et al. Strain sonoelastography of inflammatory myopathies: comparison with clinical examination, magnetic resonance imaging and pathologic findings. Br J Radiol 2016; 89: 20160283

[344] Wu CH, Chen WS, Wang TG. Elasticity of the Coracohumeral Ligament in Patients with Adhesive Capsulitis of the Shoulder. Radiology 2016; 278: 458 – 464

[345] Miyamoto H, Miura T, Morizaki Y et al. Comparative study on the stiffness of transverse carpal ligament between normal subjects and carpal tunnel syndrome patients. Hand Surg 2013; 18: 209 – 214

[346] Lee SY, Park HJ, Kwag HJ et al. Ultrasound elastography in the early diagnosis of plantar fasciitis. Clin Imaging 2014; 38: 715 – 718

[347] Ríos-Díaz J, Martínez-Payá JJ, del Baño-Aledo ME et al. Sonoelastography of Plantar Fascia: Reproducibility and Pattern Description in Healthy Subjects and Symptomatic Subjects. Ultrasound Med Biol 2015; 41: 2605 – 2613

[348] Sconfienza LM, Silvestri E, Orlandi D et al. Real-time sonoelastography of the plantar fascia: comparison between patients with plantar fasciitis and healthy control subjects. Radiology 2013; 267: 195 – 200

[349] Wu CH, Chen WS, Wang TG. Plantar fascia softening in plantar fasciitis with normal B-mode sonography. Skeletal Radiol 2015; 44: 1603 – 1607

[350] Miyamoto H, Siedentopf C, Kastlunger M et al. Intracarpal tunnel contents: evaluation of the effects of corticosteroid injection with sonoelastography. Radiology 2014; 270: 809 – 815

[351] Yoshii Y, Tung WL, Ishii T. Measurement of Median Nerve Strain and Applied Pressure for the Diagnosis of Carpal Tunnel Syndrome. Ultrasound Med Biol 2017; 43: 1205 – 1209

[352] Klauser AS, Miyamoto H, Martinoli C et al. Sonoelastographic Findings of Carpal Tunnel Injection. Ultraschall in Med 2015; 36: 618 – 622

[353] Yoshii Y, Tung WL, Ishii T. Strain and Morphological Changes of Median Nerve After Carpal Tunnel Release. J Ultrasound Med 2017; 36: 1153 – 1159

[354] Miyamoto H, Halpern EJ, Kastlunger M et al. Carpal tunnel syndrome: diagnosis by means of median nerve elasticity–improved diagnostic accuracy of US with sonoelastography. Radiology 2014; 270: 481 – 486

[355] Tatar IG, Kurt A, Yavasoglu NG et al. Carpal tunnel syndrome: elastosonographic strain ratio and cross-sectional area evaluation for the diagnosis and disease severity. Med Ultrason 2016; 18: 305 – 311

[356] Zhang C, Li M, Jiang J et al. Diagnostic Value of Virtual Touch Tissue Imaging Quantification for Evaluating Median Nerve Stiffness in Carpal Tunnel Syndrome. J Ultrasound Med 2017; 36: 1783 – 1791

[357] Kantarci F, Ustabasioglu FE, Delil S et al. Median nerve stiffness measurement by shear wave elastography: a potential sonographic method in the diagnosis of carpal tunnel syndrome. Eur Radiol 2014; 24: 434 – 440

[358] Dikici AS, Ustabasioglu FE, Delil S et al. Evaluation of the Tibial Nerve with Shear-Wave Elastography: A Potential Sonographic Method for the

Diagnosis of Diabetic Peripheral Neuropathy. Radiology 2017; 282: 494 – 501

[359] Ishibashi F, Taniguchi M, Kojima R et al. Elasticity of the tibial nerve assessed by sonoelastography was reduced before the development of neuropathy and further deterioration associated with the severity of neuropathy in patients with type 2 diabetes. J Diabetes Investig 2016; 7: 404 – 412

[360] Klauser AS, Miyamoto H, Bellmann-Weiler R et al. Sonoelastography: musculoskeletal applications. Radiology 2014; 272: 622 – 633

[361] Greening J, Dilley A. Posture-induced changes in peripheral nerve stiffness measured by ultrasound shear-wave elastography. Muscle Nerve 2017; 55: 213 – 222

[362] Klauser AS, Faschingbauer R, Jaschke WR. Is sonoelastography of value in assessing tendons? Semin Musculoskelet Radiol 2010; 14: 323 – 333

[363] Kot BC, Zhang ZJ, Lee AW et al. Elastic modulus of muscle and tendon with shear wave ultrasound elastography: variations with different technical settings. PLoS One 2012; 7: e44348

[364] Domenichini R, Pialat JB, Podda A et al. Ultrasound elastography in tendon pathology: state of the art. Skeletal Radiol 2017; 46: 1643 – 1655

[365] Drakonaki EE, Allen GM, Wilson DJ. Ultrasound elastography for musculoskeletal applications. Br J Radiol 2012; 85: 1435 – 1445

[366] Alfuraih AM, O'Connor P, Hensor E et al. The effect of unit, depth, and probe load on the reliability of muscle shear wave elastography: Variables affecting reliability of SWE. J Clin Ultrasound 2018; 46: 108 – 115

[367] Carmignani L, Gadda F, Gazzano G et al. High incidence of benign testicular neoplasms diagnosed by ultrasound. J Urol 2003; 170: 1783 – 1786

[368] Shah A, Lung PF, Clarke JL et al. Re: New ultrasound techniques for imaging of the indeterminate testicular lesion may avoid surgery completely. Clin Radiol 2010; 65: 496 – 497

[369] Sidhu PS. Multiparametric Ultrasound (MPUS) Imaging: Terminology Describing the Many Aspects of Ultrasonography. Ultraschall in Med 2015; 36: 315 – 317

[370] Huang DY, Sidhu PS. Focal testicular lesions: colour Doppler ultrasound, contrast-enhanced ultrasound and tissue elastography as adjuvants to the diagnosis. Br J Radiol 2012; 85 Spec No 1: S41 – S53

[371] Pozza C, Gianfrilli D, Fattorini G et al. Diagnostic value of qualitative and strain ratio elastography in the differential diagnosis of non-palpable testicular lesions. Andrology 2016; 4: 1193 – 1203

[372] Goddi A, Sacchi A, Magistretti G et al. Real-time tissue elastography for testicular lesion assessment. Eur Radiol 2012; 22: 721 – 730

[373] Auer T, De Zordo T, Dejaco C et al. Value of Multiparametric US in the Assessment of Intratesticular Lesions. Radiology 2017; 285: 640 – 649

[374] Aigner F, De Zordo T, Pallwein-Prettner L et al. Real-time sonoelastography for the evaluation of testicular lesions. Radiology 2012; 263: 584 – 589

[375] Schröder C, Lock G, Schmidt C et al. Real-Time Elastography and Contrast-Enhanced Ultrasonography in the Evaluation of Testicular Masses: A Comparative Prospective Study. Ultrasound Med Biol 2016; 42: 1807 – 1815

[376] Marsaud A, Durand M, Raffaelli C et al. Elastography shows promise in testicular cancer detection. Prog Urol 2015; 25: 75 – 82

[377] Grasso M, Blanco S, Raber M et al. Elasto-sonography of the testis: preliminary experience. Arch Ital Urol Androl 2010; 82: 160 – 163

[378] Lock G, Schröder C, Schmidt C et al. Contrast-enhanced ultrasound and real-time elastography for the diagnosis of benign Leydig cell tumours of the testis – a single center report on 13 cases. Ultraschall in Med 2014; 35: 534 – 539

[379] Jedrzejewski G, Ben-Skowronek I, Wozniak MM et al. Testicular adrenal rest tumours in boys with congenital adrenal hyperplasia: 3D US and elastography–do we get more information for diagnosis and monitoring? J Pediatr Urol 2013; 9: 1032 – 1037

[380] Bernardo S, Konstantatou E, Huang DY et al. Multiparametric sonographic imaging of a capillary hemangioma of the testis: appearances on gray-scale, color Doppler, contrast-enhanced ultrasound and strain elastography. J Ultrasound 2016; 19: 35 – 39

[381] Patel K, Sellars ME, Clarke JL et al. Features of testicular epidermoid cysts on contrast-enhanced sonography and real-time tissue elastography. J Ultrasound Med 2012; 31: 115 – 122

[382] Patel KV, Huang DY, Sidhu PS. Metachronous bilateral segmental testicular infarction: multi-parametric ultrasound imaging with grey-scale ultrasound, Doppler ultrasound, contrast-enhanced ultrasound (CEUS) and real-time tissue elastography (RTE). J Ultrasound 2014; 17: 233 – 238

[383] Yusuf G, Konstantatou E, Sellars ME et al. Multiparametric Sonography of Testicular Hematomas: Features on Grayscale, Color Doppler, and Contrast-Enhanced Sonography and Strain Elastography. J Ultrasound Med 2015; 34: 1319 – 1328

[384] Fang C, Konstantatou E, Romanos O et al. Reproducibility of 2-Dimensional Shear Wave Elastography Assessment of the Liver: A Direct Comparison With Point Shear Wave Elastography in Healthy Volunteers. J Ultrasound Med 2017; 36: 1563 – 1569

[385] Rafailidis V, Robbie H, Konstantatou E et al. Sonographic imaging of extra-testicular focal lesions: comparison of grey-scale, colour Doppler and contrast-enhanced ultrasound. Ultrasound 2016; 24: 23 – 33

[386] Pedersen MR, Møller H, Osther PJS et al. Comparison of Tissue Stiffness Using Shear Wave Elastography in Men with Normal Testicular Tissue, Testicular Microlithiasis and Testicular Cancer. Ultrasound Int Open 2017; 3: E150 – E155

[387] Rocher L, Criton A, Gennisson JL et al. Testicular Shear Wave Elastography in Normal and Infertile Men: A Prospective Study on 601 Patients. Ultrasound Med Biol 2017; 43: 782 – 789

[388] Ucar AK, Alis D, Samanci C et al. A preliminary study of shear wave elastography for the evaluation of unilateral palpable undescended testes. Eur J Radiol 2017; 86: 248 – 251

[389] Dikici AS, Er ME, Alis D et al. Is There Any Difference Between Seminomas and Nonseminomatous Germ Cell Tumours on Shear Wave Elastography? A Preliminary Study. J Ultrasound Med 2016; 35: 2575 – 2580

[390] Rocher L, Glas L, Bellin MF et al. Burned-Out Testis Tumours in Asymptomatic Infertile Men: Multiparametric Sonography and MRI Findings. J Ultrasound Med 2017; 36: 821 – 831

[391] Trottmann M, Rübenthaler J, Marcon J et al. Differences of standard values of Supersonic shear imaging and ARFI technique – in vivo study of testicular tissue. Clin Hemorheol Microcirc 2016; 64: 729 – 733

[392] De Zordo T, Stronegger D, Pallwein-Prettner L et al. Multiparametric ultrasonography of the testicles. Nat Rev Urol 2013; 10: 135 – 148

[393] D'Anastasi M, Schneevoigt BS, Trottmann M et al. Acoustic radiation force impulse imaging of the testes: a preliminary experience. Clin Hemorheol Microcirc 2011; 49: 105 – 114

[394] Trottmann M, Marcon J, D'Anastasi M et al. Shear-wave elastography of the testis in the healthy man – determination of standard values. Clin Hemorheol Microcirc 2016; 62: 273 – 281

[395] Zieman SJ, Melenovsky V, Kass DA. Mechanisms, pathophysiology, and therapy of arterial stiffness. Arteriosclerosis, thrombosis, and vascular biology 2005; 25: 932 – 943

[396] Mahmood B, Ewertsen C, Carlsen J et al. Ultrasound Vascular Elastography as a Tool for Assessing Atherosclerotic Plaques – A Systematic Literature Review. Ultrasound international open 2016; 2: E106 – E112

[397] de Korte CL, Pasterkamp G, van der Steen AF et al. Characterization of plaque components with intravascular ultrasound elastography in human femoral and coronary arteries in vitro. Circulation 2000; 102: 617 – 623

[398] de Korte CL, van der Steen AF. Intravascular ultrasound elastography: an overview. Ultrasonics 2002; 40: 859 – 865

[399] Majdouline Y, Ohayon J, Keshavarz-Motamed Z et al. Endovascular shear strain elastography for the detection and characterization of the severity of atherosclerotic plaques: in vitro validation and in vivo evaluation. Ultrasound in medicine & biology 2014; 40: 890 – 903

[400] Schaar JA, De Korte CL, Mastik F et al. Characterizing vulnerable plaque features with intravascular elastography. Circulation 2003; 108: 2636 – 2641

[401] Dahl JJ, Dumont DM, Allen JD et al. Acoustic radiation force impulse imaging for noninvasive characterization of carotid artery atherosclerotic plaques: a feasibility study. Ultrasound in medicine & biology 2009; 35: 707 – 716

[402] Czernuszewicz TJ, Homeister JW, Caughey MC et al. Non-invasive in vivo characterization of human carotid plaques with acoustic radiation force impulse ultrasound: comparison with histology after endarterectomy. Ultrasound in medicine & biology 2015; 41: 685 – 697

[403] Meshram NH, Varghese T, Mitchell CC et al. Quantification of carotid artery plaque stability with multiple region of interest based ultrasound strain indices and relationship with cognition. Physics in medicine and biology 2017; 62: 6341 – 6360

[404] Emelianov SY, Chen X, O'Donnell M et al. Triplex ultrasound: elasticity imaging to age deep venous thrombosis. Ultrasound in medicine & biology 2002; 28: 757 – 767

[405] Xie H, Kim K, Aglyamov SR et al. Staging deep venous thrombosis using ultrasound elasticity imaging: animal model. Ultrasound in medicine & biology 2004; 30: 1385 – 1396

[406] Rubin JM, Xie H, Kim K et al. Sonographic elasticity imaging of acute and chronic deep venous thrombosis in humans. Journal of ultrasound in medicine: official journal of the American Institute of Ultrasound in Medicine 2006; 25: 1179 – 1186

[407] Takimura H, Hirano K, Muramatsu T et al. Vascular elastography: a novel method to characterize occluded lower limb arteries prior to endovascular therapy. Journal of endovascular therapy: an official journal of the International Society of Endovascular Specialists 2014; 21: 654 – 661

[408] Yi X, Wei X, Wang Y et al. Role of real-time elastography in assessing the stage of thrombus. International angiology: a journal of the International Union of Angiology 2017; 36: 59 – 63

[409] Dharmarajah B, Sounderajah V, Rowland SP et al. Aging techniques for deep vein thrombosis: a systematic review. Phlebology 2015; 30: 77 – 84

[410] Aslan A, Barutca H, Ayaz E et al. Is real-time elastography helpful to differentiate acute from subacute deep venous thrombosis? A preliminary study. Journal of clinical ultrasound: JCU 2018; 46: 116 – 121

[411] Su Y, Liu W, Wang D et al. Evaluation of abdominal aortic elasticity by strain rate imaging in patients with type 2 diabetes mellitus. Journal of clinical ultrasound: JCU 2014; 42: 475 – 480

[412] Zheng XZ, Yang B, Wu J. A comparison of the approaches to assess the abdominal aortic stiffness using M-mode ultrasonography, tissue tracking and strain rate imaging. JNMA: journal of the Nepal Medical Association 2013; 52: 500 – 504

[413] Korshunov VA, Wang H, Ahmed R et al. Model-based vascular elastography improves the detection of flow-induced carotid artery remodeling in mice. Scientific reports 2017; 7: 12081

[414] Ribbers H, Lopata RG, Holewijn S et al. Noninvasive two-dimensional strain imaging of arteries: validation in phantoms and preliminary experience in carotid arteries in vivo. Ultrasound in medicine & biology 2007; 33: 530 – 540

[415] Couade M, Pernot M, Prada C et al. Quantitative assessment of arterial wall biomechanical properties using shear wave imaging. Ultrasound in medicine & biology 2010; 36: 1662 – 1676

[416] Widman E, Maksuti E, Amador C et al. Shear Wave Elastography Quantifies Stiffness in Ex Vivo Porcine Artery with Stiffened Arterial Region. Ultrasound in medicine & biology 2016; 42: 2423 – 2435

[417] Guo Y, Wang Y, Chang EJ et al. Multidirectional Estimation of Arterial Stiffness Using Vascular Guided Wave Imaging with Geometry Correction. Ultrasound Med Biol 2018; 44: 884 – 896

[418] Maksuti E, Bini F, Fiorentini S et al. Influence of wall thickness and diameter on arterial shear wave elastography: a phantom and finite element study. Physics in medicine and biology 2017; 62: 2694 – 2718

[419] Maksuti E, Widman E, Larsson D et al. Arterial Stiffness Estimation by Shear Wave Elastography: Validation in Phantoms with Mechanical Testing. Ultrasound in medicine & biology 2016; 42: 308 – 321

[420] Widman E, Maksuti E, Larsson D et al. Shear wave elastography plaque characterization with mechanical testing validation: a phantom study. Physics in medicine and biology 2015; 60: 3151 – 3174

[421] Ramnarine KV, Garrard JW, Dexter K et al. Shear wave elastography assessment of carotid plaque stiffness: in vitro reproducibility study. Ultrasound in medicine & biology 2014; 40: 200 – 209

[422] Ramnarine KV, Garrard JW, Kanber B et al. Shear wave elastography imaging of carotid plaques: feasible, reproducible and of clinical potential. Cardiovascular ultrasound 2014; 12: 49

[423] Garrard JW, Ramnarine K. Shear-wave elastography in carotid plaques: comparison with grayscale median and histological assessment in an interesting case. Ultraschall in der Medizin 2014; 35: 1 – 3

[424] Lei Z, Qiang Y, Tianning P et al. Quantitative assessment of carotid atherosclerotic plaque: Initial clinical results using ShearWave™ Elastography. Int J Clin Exp Med 2016; 9: 9347 – 9355

[425] Lou Z, Yang J, Tang L et al. Shear Wave Elastography Imaging for the Features of Symptomatic Carotid Plaques: A Feasibility Study. Journal of ultrasound in medicine: official journal of the American Institute of Ultrasound in Medicine 2017; 36: 1213 – 1223

[426] Garrard JW, Ummur P, Nduwayo S et al. Shear Wave Elastography May Be Superior to Greyscale Median for the Identification of Carotid Plaque Vulnerability: A Comparison with Histology. Ultraschall in der Medizin 2015; 36: 386 – 390

[427] Couade M, Pernot M, Messas E et al. In vivo quantitative mapping of myocardial stiffening and transmural anisotropy during the cardiac cycle. IEEE transactions on medical imaging 2011; 30: 295 – 305

[428] Pernot M, Couade M, Mateo P et al. Real-time assessment of myocardial contractility using shear wave imaging. Journal of the American College of Cardiology 2011; 58: 65 – 72

[429] Strachinaru M, Bosch JG, van Dalen BM et al. Cardiac Shear Wave Elastography Using a Clinical Ultrasound System. Ultrasound in medicine & biology 2017; 43: 1596 – 1606

[430] Bernal M, Gennisson JL, Flaud P et al. Shear wave elastography quantification of blood elasticity during clotting. Ultrasound in medicine & biology 2012; 38: 2218 – 2228

[431] Mfoumou E, Tripette J, Blostein M et al. Time-dependent hardening of blood clots quantitatively measured in vivo with shear-wave ultrasound imaging in a rabbit model of venous thrombosis. Thrombosis research 2014; 133: 265 – 271

[432] Kobayashi Y, Omichi K, Kawaguchi Y et al. Intraoperative real-time tissue elastography during laparoscopic hepatectomy. HPB (Oxford) 2018; 20: 93 – 99

[433] Platz Batista da Silva N, Schauer M, Hornung M et al. Intrasurgical dignity assessment of hepatic tumours using semi-quantitative strain elastography and contrast-enhanced ultrasound for optimisation of liver tumour surgery. Clin Hemorheol Microcirc 2016; 64: 735 – 745

[434] Jung EM, Platz Batista da Silva N, Jung W et al. Is Strain Elastography (IO-SE) Sufficient for Characterization of Liver Lesions before Surgical Resection–Or Is Contrast Enhanced Ultrasound (CEUS) Necessary? PLoS One 2015; 10: e0123737

[435] Kawaguchi Y, Tanaka N, Nagai M et al. Usefulness of Intraoperative Real-Time Tissue Elastography During Laparoscopic Hepatectomy. J Am Coll Surg 2015; 221: e103 – e111

[436] Sastry R, Bi WL, Pieper S et al. Applications of Ultrasound in the Resection of Brain Tumours. J Neuroimaging 2017; 27: 5 – 15

[437] Chauvet D, Imbault M, Capelle L et al. In Vivo Measurement of Brain Tumour Elasticity Using Intraoperative Shear Wave Elastography. Ultraschall in Med 2016; 37: 584 – 590

[438] Chan HW, Pressler R, Uff C et al. A novel technique of detecting MRI-negative lesion in focal symptomatic epilepsy: intraoperative Shear-Wave elastography. Epilepsia 2014; 55: e30 – e33

[439] Selbekk T, Brekken R, Indergaard M et al. Comparison of contrast in brightness mode and strain ultrasonography of glial brain tumours. BMC Med Imaging 2012; 12: 11

[440] Ji S, Hartov A, Roberts D et al. Data assimilation using a gradient descent method for estimation of intraoperative brain deformation. Med Image Anal 2009; 13: 744 – 756

[441] Joldes GR, Wittek A, Couton M et al. Real-time prediction of brain shift using nonlinear finite element algorithms. Med Image Comput Comput Assist Interv 2009; 12: 300 – 307

[442] Carter TJ, Sermesant M, Cash DM et al. Application of soft tissue modelling to image-guided surgery. Med Eng Phys 2005; 27: 893 – 909

[443] Scholz M, Noack V, Pechlivanis I et al. Vibrography during tumour neurosurgery. J Ultrasound Med 2005; 24: 985 – 992

[444] Fleming IN, Kut C, Macura KJ et al. Ultrasound elastography as a tool for imaging guidance during prostatectomy: initial experience. Med Sci Monit 2012; 18: CR635 – CR642

[445] Uramoto H, Nakajima Y, Ohtaki K et al. Intraoperative ultrasound elastography has little diagnostic benefit for deeper tumours of the lung. Eur J Cardiothorac Surg 2016; 49: 1538 – 1539

[446] Parekattil S, Yeung LL, Su LM. Intraoperative tissue characterization and imaging. Urol Clin North Am 2009; 36: 213 – 221, ix

Original papers

Med Ultrason 2019, Vol. 21, no. 2, 117-124
DOI: 10.11152/mu-1775

Musculoskeletal ultrasound versus MRI of the hands in healthy subjects – a pilot study

Mihaela C. Micu[1], Sorana D. Bolboacă[2], Georgeta M. Rusu[3], Carmen B. Crivii[4], Carolina M. Solomon[5]

[1]Rheumatology Division, 2nd Rehabilitation Department, Rehabilitation Clinical Hospital, [2]Department of Medical Informatics and Biostatistics, "Iuliu Haţieganu" University of Medicine and Pharmacy, [3]Radiology Department, Emergency Clinical County Hopsital, [4]Morphology Department, "Iuliu Haţieganu" University of Medicine and Pharmacy,[5]Department of Radiology, „Iuliu Haţieganu" University of Medicine and Pharmacy Cluj-Napoca, Romania

Abstract

Aim: High resolution imaging methods detect a spectrum of inflammatory-like and structural modifications at joint and tendon level in healthy subjects. The knowledge of their extent and degree is important when subclinical disease activity (implying therapy reassessment) must be differentiated from normality. Musculoskeletal ultrasound (MSUS) evaluation may be challenging even for experts when borderline or low grade lesions are present. Our objective was to analyse the frequency of inflammatory-like lesions in hand joint and tendons in healthy young subjects and to evaluate the concordance between MSUS and magnetic resonance imaging (MRI) findings. **Material and methods:** Ten healthy young women (age range 24-32 years) clinically asymptomatic (joints and tendons) were selected to have bilateral hand MSUS and MRI evaluation. Based on current definitions, synovitis/tenosynovitis-like lesions, erosions, osteophytes and bone edema were quantified and concordance between the two imaging methods was calculated. **Results:** Overall, both imaging evaluation methods showed a low frequency of inflammatory-like and structural lesions. No joint presented power Doppler signal or erosions. No abnormalities suggestive for inflammatory or structural pathology were detected at the tendon compartments level. No erosions and no signs of osteitis were detected. The concordance between MSUS and MRI findings was high except for the wrist area. **Conclusion:** MSUS was demonstrated to be a very accurate imaging method, mostly for hand tendon evaluation. This would allow a better discrimination between normality and pathologic findings, adding supplementary information.

Keywords: musculoskeletal ultrasound; Magnetic Resonance Imaging (MRI); joints; tendons; healthy subjects

Introduction

The border between imaging spectrum of normality in joints and tendons and subclinical pathology in rheumatoid arthritis (RA) is still under debate. Treatment readjustment represents a big challenge for practitioners when subclinical mild inflammatory lesions are detected.

Clinical and imaging remission reflects a different dimension of normality, the dissociation between the two being highlighted in several studies [1-3]. Imaging studies on RA patients in clinical remission, overlapping or not with patients' opinion for RA remission, certify the presence of residual inflammatory findings in joints as well as in tendons [1-21]. Among high resolution imaging methods, musculoskeletal ultrasound (MSUS) was demonstrated to be more suitable for clinical practice and studies, allowing more data collection in terms of patient numbers, in comparison to magnetic resonance imaging (MRI). Indeed, it has been shown to be a very attractive imaging tool because of its accuracy and feasibility in early as well as in longstanding disease [22-24].

Several MSUS studies focusing on healthy subjects identified the presence of grey scale inflammatory pathol-

---

Received 28.10.2018 Accepted 17.01.2019
Med Ultrason
2019, Vol. 21, No 2, 117-124
Corresponding author: Carmen B. Crivii
Morphology Department, "Iuliu Haţieganu"
University of Medicine and Pharmacy
Cluj-Napoca, 3-5 Clinicilor street,
400006, Cluj-Napoca, Romania
E-mail: bianca.crivii@umfcluj.ro

ogy-like findings (mild, prevalent effusion), mostly in the wrists (dominant hand) and rare in metacarpophalangeal joints (MCPj) or proximal interphalangeal joints (PIPj). These modifications were correlated with biomechanical factors and age [25-31]. Instead, tenosynovitis/tenosynovitis-like modifications and Power Doppler signal (PDUS) at joint and tendon level were depicted very rarely in healthy populations [32-35]. Recently, a longitudinal study on healthy women focused attention especially on flexor tendons in the hands, MCPj and extensor carpi ulnaris tendon (ECU) that seem to have a very low frequency of modifications in the younger healthy population. These structures were found to show stability in time when exposed to different factors linked to pregnancy status/ postpartum period [36].

Hands MRI studies in healthy subjects identified a low prevalence of true low-grade synovitis or synovitis-like changes (minimal early synovial enhancement) in MCPj and wrists. Osteophytes, small bone erosions and bone marrow edema were occasionally found. In contrast, a common finding was tendon sheath effusion identified on MRI without contrast [29,31,32,34,37].

Only one study evaluating MCPj in RA patients included a low number of controls which were evaluated by both imaging methods - MSUS versus contrast MRI, showing no synovial membrane thickening on greyscale MSUS, no intra-articular power Doppler (PD) signal and no or only slight synovial enhancement on dynamic MR images [27]. By now, no comparative MSUS vs MRI study in healthy subjects focusing on hand tendons was performed.

Our objective was to analyse the frequency of inflammatory-like lesions in hand joint and tendons in healthy young subjects and to evaluate the concordance between MSUS and MRI findings. The main focus was addressed to the wrist area, MCPj 2-5, ECU and flexor tendons.

Material and methods

This was a prospective cross-sectional study performed in May 2018. Ten healthy young women, age >18 years, clinically asymptomatic, with low up to moderate level of physical effort were selected. Exclusion criteria were: age >35 years, diagnosis of a current acute/subacute or chronic inflammatory/autoimmune rheumatic disease, history of NSAIDs/painkiller administration in the last 6 weeks, history of trauma in the hands in the last 2 years, intense physical activity involving hands (hard work/sport). All participants signed the informed written consent prior enrolment and local Ethical Committee approval was obtained.

Following demographic data were collected: type of profession, type of physical work/sport involving hands, dominant hand, personal and family medical history, current medication other than specified in the exclusion criteria, smoking, body mass index (BMI). Clinical, MSUS and MRI evaluation of the hands was done in an interval of maximum 72 hours, by a senior doctor with >10 years of experience.

Clinical examination

Clinical examination (CE) was focused on the following anatomic regions and structures: wrist, MCPj 1-5, PIPj 1-5, bilateral hand extensor tendon compartments 1-6, flexor pollicis longus tendon (FPL) and superficial and profound flexors of the digits 2-5 (F2-5) of both hands. The absence of any pain in active/passive motion along with a normal range of motion qualified the subject for the study.

MSUS examination

MSUS evaluation of both hands was performed on the same day as CE, according to current guidelines [22], in the same regions as CE. If present, following elementary lesions were recorded: joint synovial hypertrophy/effusion (SH/E) by grey scale (GS), intra-articular PD signal, erosions, osteophytes, SH/E and intra-tendon sheath and/ or intra-tendon belly PD signal. The OMERACT definitions for synovitis, tenosynovitis, effusion, erosion and osteophytes were used [38,39]. Joint and tendon pathology was quantified with a semi-quantitative scoring system for small joints [40] and tendons [39]. For erosions and osteophytes, a dichotomous (normal or abnormal) scoring system was used. Dorsal and volar scoring of each MCPj and PIPj were merged into a single scoring/ joint. If dorsal and volar scoring of one joint were different (one was normal and other was abnormal) the abnormal finding for SH, E and PD was chosen to be recorded as a single elementary lesion. Tendon examination was performed in a multi-plane (at the level of the extensor retinaculum for C1-C6 to the distal insertion and from the level of the flexor retinaculum up to the distal insertion for FPL, F2-F5) and dynamic fashion, according to specific manoeuvres. Lateral sites of MCPj 2 and 5 were also evaluated for erosions.

A Samsung RS 85 machine equipped with a 3-16 MHz broadband multi-frequency linear transducer was used. GS settings were adjusted in a standardized manner for superficial anatomic regions. The settings for PD examination were low filter wall and pulse repetition frequency for small vessels with slow flow 500-750 Hz.

MRI evaluation

A General Electric Sigma Explorer scanner 16 channels, 1.5-T, with dedicated hand protocol was used.

The following MRI 2D, without gadolinium administration, sequences were acquired: STIR (Short Tau Inversion Recovery), T2 MERGE (Multiple Echo Re-combined Gradient Echo) and T1 FSE (Fast Spin Echo). STIR was performed in axial plane; slices perpendicular on the metacarpal and phalangeal bones, included the radio-ulnar joint and the distal phalangeal bone of 3rd finger. T2 MERGE and T1 FSE in coronal plane covered the whole region, from dorsal to the palmar aspect. Slices were obtained parallel to the metacarpal and phalangeal bones. The same joint/tendon set as in MSUS evaluation was assessed together with following bones: distal radius epiphysis, carpal bones, digit 1-5 metacarpal, proximal and distal phalanx bones. Acquisition parameters are shown in Table I.

All MR images were assessed by a trained musculoskeletal radiologist with more than 14 years of experience who was blinded to clinical details. The following parameters were assessed based on the Outcome Measures in Rheumatology Clinical Trials (OMERACT) Rheumatoid Arthritis MRI Scoring System (RAMRIS): joint synovitis, bone marrow edema, bone erosions [41]. According to the present MRI protocol, without contrast, only joint capsule distension was possible to be identified. Absence of fluid was evaluated with 0 and fluid-like capsule distension (mild, moderate and severe) with 1, 2, and 3.

The fluid-like signal inside the tendon sheaths was measured according to a previous MRI protocol described [42] at the point of maximal thickness, perpendicular to the tendon surface. Bone marrow edema and erosions were noted when present or absent. Intra-osseous cysts were defined as sharply demarcated hyper-intense lesions within the bone on any fluid-sensitive MRI sequences, visible on two planes, without destruction of the overlaying cortical bone. Cysts were quantified using a dichotomous score.

Statistical analysis

Data were summarized according to their type. The quantitative data were presented as a median and interquartile range (IQR = Q1–Q3, where Q1 = first quartile, Q3 = third quartile). Absolute frequencies expressed as the number of cases with a specific characteristic divided to the number of possibilities were used to summarize the presence of effusion (E), synovial hypertrophy (SH), erosion (ER), and respectively osteophyte (O). The concordance between MSUS and MRI findings was evaluated by dividing the number of agreements to the number of cases and the percentages were reported associated with the 95% confidence interval [43].

Results

Ten healthy volunteers, all women, age between 24 and 32 years (median 29, IQR [26.00–31.25]) were included. All participants were right handed, half of them showing history of moderate physical effort. One participant had Hashimoto thyroiditis. Family history of RA was present in two participants and skin psoriasis and morfea in two other participants.

Most participants had normal body mass index (8/10), while two of them were obese (BMI range from 18 kg/m^2 to 28 kg/m^2, median of 19 kg/m^2 and IQR (19 to 22). Four out of 10 participants were smokers (≤8 cigarettes/day).

Overall, a low frequency of inflammatory-like and structural lesions were identified. MSUS evaluation identified SH in 7/20 (35%, 95%CI [15.25 to 59.75]) wrist joints, with distribution in both hands (4 of grade 1 and 3 of grade 2), grade 1 effusion in 6/80 (7.5%, 95%CI [2.52 to 14.98]) MCPj 2-5, one joint having in addition SH grade 1 (1.25%). Osteophytes were detected in 2/80 (2.5%, 95%CI [0.02 to 8.73]) MCPj 2-5 and in 40/100 (40%, 95%CI [30.01 to 49.99]) of the PIPj 1-5. No joint presented PD signal or erosions. In one subject, a nutritive vessel at the level of the 3rd metacarpal head was detected. No abnormalities were detected at the tendon compartments level. Dynamic tendon evaluation was asymptomatic and showed a smooth gliding of the tendons along with a normal joints range of motion. A small amount of fluid/fluid-like material, grade 1 (<1.5 mm, range 0.3-1.2 mm, mostly concentric) was detected inside the flexor tendon sheaths in several locations, in all participants, with the highest amount detection at MCPj level.

MRI evaluation identified very small quantities of effusion (grade 1) at the level of the MCPj 1 in 2/20 (10%, 95%CI [1.00 to 59.00]), MCPj 2-5 in 5/80 (6.25%, 95%CI [2.52 to 13.73]), osteophytes in the 1/80 (1.25%, 95%CI [0.02 to 6.23]) MCPj 2-5 and 16/100 (16%, 95%CI [9.01 to 24.99]) in the PIPj 2-5. No inflammatory-like pathol-

Table I. MRI acquisition parameters used

Plane and acquisition sequence	TR (ms)	TE (ms)	TI (ms)	FA (degrees)	FOV (cm)	Slice thickness (mm)	Interslice gap (mm)	Matrix (freq/phase)	Pixel size (mm)
Axial STIR	5400-5500	42-44	120	160	15	3	0.3	288/192	0.5x0.8
Coronal T2 MERGE	450-520	15		20	21	2	0.2	256/224	0.8x0.9
Coronal T1 FSE	500-600	13-15		160	21	2	0.2	412/224	0.5x0.9

TR - Repetition Time, TE - Echo Time, TI - Inversion Time, FA - Flip Angle, FOV - Field of View

Table II. Summary and distribution of grey scale ultrasound (US) findings vs. magnetic resonance imaging (MRI) findings

	US no/n				**MRI no/n**			
	E	SH	ER	O	E	SH	ER	O
Joints								
Wrist	0/20	7/20		0/20	0/20	0/20		0/20
MCP 1	0/20	0/20		0/20	2/20	0/20		1/20
MCP 2−5	6/80	1/80	0/40	2/80	5/80	0/80	0/40	1/80
PIP 1−5	0/100	0/100		40/100	3/100	0/100		16/100
Tendons								
C1−C5	0/100	0/100			0/100	0/100		
F1−F5	0/100	0/100			0/100	0/100		
ECU	0/20	0/20			0/20	0/20		

MCP - metacarpophalangeal, PIP - proximal interphalangeal, C1-C5 - extensor tendon compartments 1-5, F1-F5 - flexor tendons of the digits 1-5, ECU - extensor carpi ulnaris tendon, E - effusion, SH - synovial hypertrophy, ER - erosion, O - osteophyte, no - number of findings, n - number of areas.

ogy was detected at wrist level. No erosions and no signs of osteitis were detected. Several subchondral cysts were detected at carpal bones and metacarpal heads level (11 - lunate, 3 - trapezium, 3 - trapezoid, 8 - capitate bone, 1 - hamate, 3 - triquetrum, 4 - pisiform, 1 - MC1, 4 - MC2, 4 - MC3, 1 - MC4). Effusion inside the tendon sheath (grade 0, mean of 0.8±0.34 mm) was detected in 8 (8%, 95%CI [3.01 to 14.99]) tendon units- flexor tendons (4 F2, 1 F3, 3 F4) and one (1%) C2, in 5 out of 10 subjects, mostly unilateral. Table II presents the summary and distribution of the grey scale lesions MSUS vs MRI.

The overall concordance between US findings and MRI findings was evaluated whenever the results presented in Table II were discordant. Results are presented in Table III.

The lowest concordance between MSUS and MRI was found in wrist (65%) and PIP for osteophytes (72%). MRI detected a number of 5 MCPj 2-5 with effusion versus 6 effusions detected on MSUS, showing high concordance among the methods. Flexor tendon evaluation and ECU showed 100% concordance MSUS vs MRI.

Table III. Details of concordance between US findings and MRI findings

Area	**Concordance**	
	no/n	**% [95%CI]**
Wrist SH	13/20	65.00 [40.25 to 84.75]
MCP 1 E	18/20	90.00 [70.25 to 99.75]
MCP 1 O	19/20	95.00 [75.25 to 99.75]
MCP 2-5 SH	79/80	98.75 [91.27 to 99.98]
MCP 2-5 E	69/80*	86.25 [76.27 to 92.48]
MCP 2-5 O	77/80*	96.25 [90.02 to 98.73]
PIP O	72/100**	72.00 [62.01to 80.99]
PIP E	97/100	97.00 [92.01 to 98.99]

SH - synovial hypertrophy, E - effusion, O - osteophyte, MCP - metacarpophalangeal, PIP - proximal interphalangeal, no - the number of concordances, n - total number of the evaluated structure, * none of the effusion identified by MSUS was identified by MRI and none of the effusion identified by MRI was identified by MSUS, ** in 14 cases the osteophytes were identified by both MSUS and MRI

In figure 1 there are some findings encountered during MSUS and MRI examinations.

Discussions

Our study is the first to compare MSUS with MR findings in healthy subjects at the hand level. The concordance calculation between the two methods raised several issues to be clarified at the wrist, MCPj and tendon level.

Concordance for tendon findings was 100%, confirming that multi-plane and dynamic USMS evaluation identifies with high accuracy the normal aspect of these structures. In addition, we confirmed with both methods that young healthy subjects, performing moderate daily hand effort, present no grey scale or Doppler pathology at tendon level. Our focus was especially oriented on flexor tendon since a previous MSUS study performed in pregnant versus non-pregnant healthy women (n=20 vs n=75) confirmed the absence of hand flexor tendon pathology in both groups, cross-sectional and longitudinal [36].

Tenosynovitis is a complementary, but different facet of the inflammatory involvement in RA and is present from early disease stages [44-46]. In this sense, imaging evaluation could add important information to the algorithm increasing the specificity of the new ACR/EULAR classification criteria for RA, especially for early phases [44,47,48].

In order to understand how to include tendon inflammatory pathology in our clinical algorithm it is important to know about the frequency of such abnormalities in healthy subjects.

Our findings are in line with other studies focusing on tendon evaluation in healthy subjects or including

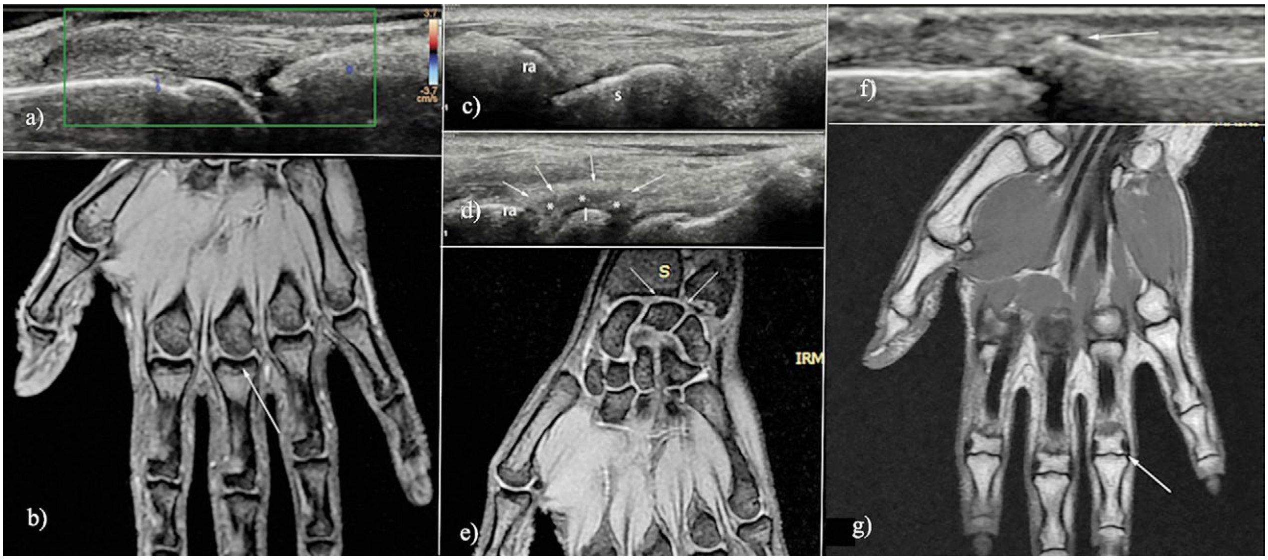

Fig 1. Female, 32 years old, 3rd MCP joint: a) longitudinal ultrasound with detection of a nutrient vessel; b) MRI, coronal plane, 2D MERGE sequence– no effusion inside the joint. Female, 26 years old, radiocarpal joint: c) longitudinal ultrasound, normal aspect between proximal radius (ra) and distal scaphoid bone (s); d) hypoechoic material distending the capsule (arrows) between proximal radius (ra) and distal lunate bone (l); e) MRI, coronal plane, 2D MERGE sequence, right hand – no pathological fluid at the radiocarpal joint, especially at lunate bone level (arrows). Female 32 years old, PIP joint: f) longitudinal ultrasound showing the sharp bony cortex- small osteophyte (arrow); g) MRI, coronal plane, T1 sequence - small osteophyte (arrow).

healthy control groups, showing a very low prevalence of pathologic findings, mostly unilateral, which correlates probably more with age and intense physical activity involving hands. A prospective MRI study focusing on the hand structures evaluation in 23 healthy subjects (range of 25-86 years) found out that only 4.3% (1 subject) presented extensor tendon involvement vs 17.4% (4 subjects) showing flexor tenosynovitis. In this study, the subjects were much older compared with our subjects [29].

Another study compared the prevalence of tenosynovitis in the hands in RA patients vs 20 controls. Tenosynovitis of the flexor tendons was present in 65% of patients vs only 1 of the 20 (5%) controls/1 tenosynovitis [32]. No tenosynovitis of the flexor tendons was found in the control group (n=10) of another study that addressed tenosynovitis as an important MRI finding in early RA [48]. In both these studies, the participants were older than in our study and tenosynovitis in the control group was assessed on gadolinium-enhanced MRI images.

Wakefield et al analysed a group of not treated early RA patients using MSUS and MRI. They found a frequency of 28% vs 64% digit flexors tenosynovitis and 14% vs 40% for the extensors, in favor of MRI evaluation. No tenosynovitis was detected in the control group of health subjects but they underwent only MSUS evaluation [49].

The largest prospective MRI study performed on 42 healthy volunteers identified fluid inside the tendon sheath as being a very common finding in at least 1 location. The authors concluded that fluid in the finger flexor tendon sheaths may be a normal finding and that one should be cautious when interpreting these findings as pathology in MRI images without gadolinium administration [31].

In our study we performed in each tendon a multiplanar and dynamic MSUS evaluation. All tendons that were evaluated as normal, not only fulfilled the morphologic normality criteria but showed also a smooth gliding pattern of the tendon in relation to the surrounding structures, with a normal range of motion; PD signal was absent in all evaluated tendons. Generally, MSUS information obtained during dynamic manoeuvre scan may be of great value when differentiating true inflammatory pathology from imaging inflammatory-like pathology. A truly inflamed tendon will show gliding abnormalities together with a variable spectrum of morphologic modifications in the tendon sheath/tendon belly. MSUS evaluation has this advantage over MRI where only morphologic information can be depicted [39,50]. At this point we could hypothesize that tenosynovitis could be a very feasible discriminative imaging parameter between healthy subjects and groups with subclinical disease.

At wrist joint level we faced the lowest concordance between the two imaging methods. MSUS depicted SH (grade 1 or 2, without PD signal) in 7/20 (35%) wrists, none being confirmed by MRI evaluation. This result raised the problem of wrist SH overestimation with MSUS, mostly in situations when the transducer is placed between the radius and lunate bone. The presence inside the joint space of hypoechoic inhomogeneous material distending the capsule may be interpreted as SH. A possible confounder could be represented by synovial folds being pushed inside the joint recess. So, in absence of any capsular distension visible at radio-scaphoid level, in absence of associated effusion or PD signal at this level one should be cautious in interpreting these modifications as MSUS radiocarpal synovitis.

MCPj evaluation was provocative. Concordance between MSUS and MRI in detecting joint effusion (grade 1 in both scoring systems) was high but joint by joint analysis revealed a total discordance between the findings' location. We concluded at this point that effusion grade 1 may be a challenge even for an experienced MSUS performer. More objective MRI findings could be explained by detecting these small quantities of effusion in the extreme lateral areas of the joint recess, a place with less accessibility for MSUS evaluation.

Regardless of the imaging method used, several other studies identified a low frequency of mild MCPj pathology (SH and/or E), mostly unilateral, sometimes associated with a low grade PDUS [25-30,34-37,40].

Detection of intra-articular nutrient vessels may generate a false interpretation for the PD signal inside the joint. It is well known by now that subclinical PD positive synovitis is linked to further joint destruction in clinical remission RA patients [2]. In fact, PD signal is encountered more often in joints that show erosions [51]. Therefore, in joints without grey scale SH, presence of true PD signal must be carefully analysed [52].

We detected no erosion and no bone marrow edema in any location suggesting that in very young healthy people these findings are absent in comparison to older healthy groups [26,27,34,52]. Osteophytes showed a lower concordance between the two imaging methods. MSUS detected very small osteophytes in 40% PIPj vs 16% detected by MRI. Firstly, we could conclude that isolated osteophytes start to be present in very young healthy population (the same trend was observed also in cortical cysts). Secondly, the very sharp phalangeal bony cortex could be misinterpreted at MS US as an incipient osteophyte.

Our study has the advantage of comparing for the first time two high resolution imaging methods in healthy subjects offering a more objective mirror regarding possible imaging abnormalities. Indeed, the discussions were focussed on potential pitfalls to be encountered/avoided in clinical practice as well as in trials.

The limits of the study were the low number of participants, suitable only for a pilot study and the MRI protocol which did not include contrast agents. Contrast enhanced MRI evaluation has shown to be superior to the native one by detecting with a high accuracy synovial hypertrophy and differentiating it from effusion, both in joints and tendons. Because of ethical reasons we did not enrol healthy subjects for this kind of protocol, several studies showing a risk for potential side effects [53]. Another limit would be the absence of an interobserver reliability exercise, both for MSUS and MRI.

In **conclusion**, MSUS has been demonstrated to be a very accurate imaging method mostly for hand tendon evaluation. This will allow a better discrimination between normal and pathologic findings, adding supplementary information. In the young population, flexor tenosynovitis coupled with wrist/MCPj synovitis should trigger the practitioners' attention for early disease detection or future flare recognition.

Acknowledgements: We would like to thank to Oana Şerban, Bianca Bălan, Iulia Papp, Bianca Pop, Andreean Relenschi, Linda Inocan, Alexandra Cherecheş, Iulia Moldovan, Jessica Trif and Mihaela Coştişor for their valuable contribution in performing this study.

References

1. Brown AK, Quinn MA, Karim Z, et al. Presence of significant synovitis in rheumatoid arthritis patients with disease-modifying antirheumatic drug– induced clinical remission: evidence from an imaging study may explain structural progression. Arthritis Rheum 2006;54:3761-3773.
2. Brown AK, Conaghan PG, Karim Z, et al. An explanation for the apparent dissociation between clinical remission and continued structural deterioration in rheu- matoid arthritis. Arthritis Rheum 2008;58:2958-2967.
3. Picchianti Diamanti A, Navarini L, Messina F, et al. Ultrasound detection of subclinical synovitis in rheumatoid arthritis patients in clinical remission: a new reduced-joint assessment in 3 target joints. Clin Exp Rheum 2018;36:984-989.
4. Kawashiri SY, Suzuki T, Nakashima Y, et al. Ultrasonographic examination of rheumatoid arthritis patients who are free of physical synovitis: power Doppler subclinical synovitis is associated with bone erosion. Rheumatology (Oxford) 2014;53:562-569.
5. Molenaar ET, Voskuyl AE, Dinant HJ, Bezemer PD, Boers M, Dijkmans BA. Progression of radiologic damage in patients with rheumatoid arthritis in clinical remission. Arthritis Rheum 2004;50:36-42.
6. Mäkinen H, Kautiainen H, Hannonen P, etal. Sustained remission and reduced radiographic progression with combination disease modifying antirheumatic drugs in early rheumatoid arthritis. J Rheumatol 2007;34:316-321.

7. Peluso G, Michelutti A, Bosello S, Gremese E, Tolusso B, Ferraccioli G. Clinical and ultrasonographic remission determines different chances of relapse in early and long standing rheumatoid arthritis. Ann Rheum Dis 2011;70:172-175.
8. Foltz V, Gandjbakhch F, Etchepare F, et al. Power Doppler Ultrasound, but Not Low-Field Magnetic Resonance Imaging, Predicts Relapse and Radiographic Disease Progression in Rheumatoid Arthritis Patients With Low Levels of Disease Activity. Arthritis Rheum 2012;64:67-76.
9. Scire CA, Montecucco C, Codullo V, Epis O, Todoerti M, Caporali R. Ultrasonographic evaluation of joint involvement in early rheumatoid arthritis in clinical remission: power Doppler signal predicts short-term relapse. Rheumatology 2009;48:1092-1097.
10. Saleem B, Brown AK, Keen H, et al. Disease remission state in patients treated with the combination of tumor necrosis factor blockade and methotrexate or with disease-modifying antirheumatic drugs: A clinical and imaging comparative study. Arthritis Rheum 2009;60:1915-1922.
11. Saleem B, Brown AK, Quinn M, et al. Can flare be predicted in DMARD treated RA patients in remission, and is it important? A cohort study. Ann Rheum Dis 2012;71:1316-1321.
12. Dohn UM, Ejbjerg B, Boonen A, et al. No overall progression and occasional repair of erosions despite persistent inflammation in adalimumab-treated rheumatoid arthritis patients: results from a longitudinal comparative MRI, ultrasonography, CT and radiography study. Ann Rheum Dis 2011;70:252-258.
13. Wakefield RJ, Green MJ, Marzo-Ortega H, et al. Should oligoarthritis be reclassified? Ultrasound reveals a high prevalence of subclinical disease. Ann Rheum Dis 2004;63:382-385.
14. Geng Y, Han J, Deng X, Zhang Z. Deep clinical remission: an optimized target in the management of rheumatoid arthritis? Experience from an ultrasonography study. Clin Exp Rheumatol 2016;34:581-586.
15. Wakefield RJ, Freeston JE, Hensor EM, Bryer D, Quinn MA, Emery P. Delay in imaging versus clinical response: a rationale for prolonged treatment with antitumor necrosis factor medication in early rheumatoid arthritis. Arthritis Rheum 2007;57:1564-1567.
16. Ozgocmen S, Ozdemir H, Kiris A, Bozgeyik Z, Ardicoglu O. Clinical evaluation and power Doppler sonography in rheumatoid arthritis: evidence for ongoing synovial inflammation in clinical remission. South Med J 2008;101:240-245.
17. Saleem B, Brown AK, Keen H, et al. Should imaging be a component of rheumatoid arthritis remission criteria? A comparison between traditional and modified composite remission scores and imaging assessments. Ann Rheum Dis 2011;70:792-798.
18. Ten Cate DF, Luime JJ, Swen N, et al. Role of ultrasonography in diagnosing early rheumatoid arthritis and remission of rheumatoid arthritis - a systematic review of the literature. Arthritis Res Ther 2013;15:R4.
19. Janta I, Valor L, De la Torre I, et al. Ultrasound–detected activity in rheumatoid arthritis on methotrexate therapy: Which joints and tendons should be assessed to predict unstable remission? Rheumatol Int 2016;36:387-396.
20. Naredo E, Valor L, De la Torre I, et al. Ultrasound joint inflammation in rheumatoid arthritis in clinical remission: how many and which joints should be assessed? Arthritis Care Res (Hoboken) 2013;65:512-517.
21. Vlad V, Berghea F, Iorgoveanu V, Popescu M, Predeteanu D, Ionescu R. Does patients' opinion of remission in rheumatoid arthritis overlap ultrasound "true" remission? - a pilot study. Med Ultrason 2018;20:328-334.
22. Möller I, Janta I,Backhaus M, et al. The 2017 EULAR standardised procedures for ultrasound imaging in rheumatology. Ann Rheum Dis 2017;76:1974-1979.
23. Colebatch AN, Edwards CJ, Ostergaard M, et al. EULAR recommendations for the use of imaging of the joints in the clinical management of rheumatoid arthritis. Ann Rheum Dis 2013;72:804-814.
24. Grassi W, Filippucci E, Farina A, Cervini C. Sonographic imaging of tendons. Arthritis Rheum 2000;43:969-976.
25. Ellegaard K, Torp-Pedersen S, Holm CC, Danneskiold-Samsøe B, Bliddal H. Ultrasound in finger joints: findings in normal subjects and pitfalls in the diagnosis of synovial disease. Ultraschall Med 2007;28:401-408.
26. Millot F, Clavel G, Etchepare F, et al; Investigators of the French Early Arthritis Cohort ESPOIR. Musculoskeletal ultrasonography in healthy subjects and ultrasound criteria for early arthritis (the ESPOIR cohort). J Rheumatol 2011;38:613-620.
27. Szkudlarek M, Klarlund M, Narvestad E, et al. Ultrasonography of the metacarpophalangeal and proximal interphalangeal joints in rheumatoid arthritis: a comparison with magnetic resonance imaging, conventional radiography and clinical examination. Arthritis Res Ther 2006;8:R52.
28. Kitchen J, Kane D. Greyscale and power Doppler ultrasonographic evaluation of normal synovial joints: correlation with pro- and anti-inflammatory cytokines and angiogenic factors. Rheumatology (Oxford) 2015;54:458-462.
29. Parodi M, Silvestri E, Garlaschi G, Cimmino MA. How normal are the hands of normal controls? A study with dedicated magnetic resonance imaging. Clin Exp Rheumatol 2006;24:134-141.
30. Padovano I, Costantino F, Breban M, D'Agostino MA. Prevalence of ultrasound synovial inflammatory findings in healthy subjects. Ann Rheum Dis 2016;75:1819-1823.
31. Agten CA, Rosskopf AB, Jonczy M, Brunner F, Pfirrman CWA, Buck FM. Frequency of inflammatory-like MR imaging findings in asymptomatic fingers of healthy volunteers. Skeletal Radiol 2018;47:279-287.
32. Rowbotham EL, Freeston JE, Emery P, Grainger AJ. The prevalence of tenosynovitis of the interosseous tendons of the hand in patients with rheumatoid arthritis. Eur Radiol 2016;26:444-450.
33. Terslev L, Torp-Pedersen S, Qvistgaard E, von der Recke P, Bliddal H. Doppler ultrasound findings in healthy wrists and finger joints. Ann Rheum Dis 2004;63:644-648.

34. Ejbjerg B, Narvestad E, Rostrup E, et al. Magnetic resonance imaging of wrist and finger joints in healthy subjects occasionally shows changes resembling erosions and synovitis as seen in rheumatoid arthritis. Arthritis Rheum 2004;50:1097-1106.
35. Zufferey P, Möller B, Brulhart L, et al. Persistence of ultrasound synovitis in patients with rheumatoid arthritis fulfilling the DAS28 and/or the new ACR/ EULAR RA remission definitions: results of an observational cohort study. Joint Bone Spine 2014;81:426-432.
36. Micu MC, Fodor D, Micu R, Bolboacă SD, Ionescu R. Pregnant versus non-pregnant healthy subjects – a prospective longitudinal musculoskeletal ultrasound study concerning the spectrum of normality. Med Ultrason 2018;20:319-327.
37. Tan AL, Grainger AJ, Tanner SF, et al. High-Resolution Magnetic Resonance Imaging for the Assessment of Hand Osteoarthritis. Arthritis Rheum 2005;52:2355-2365.
38. Wakefield RJ, Balint PV, Szudlarek M, et al. Musculoskeletal ultrasound including definitions for ultrasonographic pathology. J Rheumatol 2005;32:2485-2487.
39. Naredo E, d'Agostino MA, Wakefield RJ, et al; OMERACT Ultrasound Task Force. Reliability of a consensus based ultrasound score for tenosynovitis in rheumatoid arthritis. Ann Rheum Dis 2013;72:1328-1334.
40. Szkudlarek M, Court-Payen M, Jacobsen S, Klarlund M, Thomsen HS, Ostergaard M. Interobserver agreement in ultrasonography of the finger and toe joints in rheumatoid arthritis. Arthritis Rheum 2003;48:955-962.
41. Ostergaard M, Peterfy C, Conaghan P, et al. OMERACT rheumatoid arthritis magnetic resonance imaging studies. Core set of MRI acquisitions, joint pathology definitions, and the OMERACT RA-MRI scoring system. J Rheumatol 2003;30:1385-1386.
42. Haavardsholm EA, Ostergaard M, Ejbjerg BJ, Kvan NP, Kvien TK. Introduction of a novel magnetic resonance imaging tenosynovitis score for rheumatoid arthritis: reliability in a multireader longitudinal study. Ann Rheum Dis 2007;66:1216-1220.
43. Jäntschi L, Bolboacă SD. Exact Probabilities and Confidence Limits for Binomial Samples: Applied to the Difference between Two Proportions. ScientificWorldJournal 2010;10:865-878.
44. Navalho M, Resende C, Rodrigues AM, et al. Bilateral MR imaging of the hand and wrist in early and very early inflammatory arthritis: tenosynovitis is associated with progression to rheumatoid arthritis. Radiology 2012;264:823-833.
45. Lindegaard HM, Vallø J, Hørslev-Petersen K, Junker P, Østergaard M. Low-cost, low-field dedicated extremity magnetic resonance imaging in early rheumatoid arthritis: a 1-year follow-up study. Ann Rheum Dis 2006;65:1208–1212.
46. McQueen F, Beckley V, Crabbe J, Robinson E, Yeoman S, Stewart N. Magnetic resonance imaging evidence of tendinopathy in early rheumatoid arthritis predicts tendon rupture at six years. Arthritis Rheum 2005;52:744-751.
47. Cader MZ, Filer A, Hazlehurst J, de Pablo P, Buckley CD, Raza K. Performance of the 2010 ACR/EULAR criteria for rheumatoid arthritis: comparison with 1987 ACR criteria in a very early synovitis cohort. Ann Rheum Dis 2011;70:949-955.
48. Navalho M, Resende C, Rodrigues AM, et al. Bilateral evaluation of the hand and wrist in untreated early inflammatory arthritis: a comparative study of ultrasonography and magnetic resonance imaging. J Rheumatol 2013;40;1282-1292.
49. Wakefield RJ, O'Connor PJ, Conaghan PG, et al. Finger tendon disease in untreated early rheumatoid arthritis: a comparison of ultrasound and magnetic resonance imaging. Arthritis Rheum 2007;57:1158-1164.
50. Micu MC, Berghea F, Fodor D. Concepts in diagnosing, scoring, and monitoring tenosynovitis and other tendon abnormalities in patients with rheumatoid arthritis – the role of musculoskeletal ultrasound. Med Ultrason 2016;18:370-377.
51. Fodor D, Felea I, Popescu D, et al. Ultrasonography of the metacarpophalangeal joints in healthy subjects using an 18 MHz transducer. Med Ultrason 2015;17:185-191.
52. Vreju FA, Filippucci E, Gutierrez M, et al. Subclinical ultrasound synovitis in a particular joint is associated with ultrasound evidence of bone erosions in the same joint in rheumatoid patients in clinical remission. Clin Exp Rheumatol 2016;34:673-678.
53. Radiology and Radiation Oncology/Imaging Technology News. Available at: www.itnonline.com. Last accessed 2018 October 5.

Assessment of Cutaneous Melanoma by Use of Very-High-Frequency Ultrasound and Real-Time Elastography

Carolina M. Botar-Jid[1]
Rodica Cosgarea[2]
Sorana D. Bolboacă[3]
Simona C. Şenilă[2]
Lavinia M. Lenghel[1]
Liliana Rogojan[4]
Sorin M. Dudea[1]

OBJECTIVE. The primary objective of this study was to evaluate the usefulness of very-high-frequency ultrasound as tool for assessment of skin melanoma by investigation of the correlation between the ultrasound measurement of the thickness of a melanoma and the histopathologically measured Breslow index. The secondary objective was to assess the potential role of real-time elastography in the preoperative evaluation of skin melanoma.

SUBJECTS AND METHODS. The study included 42 cutaneous melanoma lesions in 39 adult subjects examined in the division of ultrasound of a department of radiology between September 2011 and January 2015. Gray-scale sonographic features at 40 MHz (thickness, echogenicity, contour) and real-time strain elastographic (qualitative and semiquantitative, strain ratio) characteristics were evaluated and compared with the pathologic results.

RESULTS. The melanoma lesions had a homogeneous hypoechoic appearance with a regular contour and stiff or medium consistency. The mean difference between Breslow index and ultrasound thickness was –0.05 mm (95% CI, –0.24 to 0.13 mm), sustaining the absence of significant differences between these two measurements. A strong relation was identified between real-time elastographic appearance and strain ratio for the relations between lesion and hypodermis and between lesion and neighboring dermis ($p < 0.002$) or hypodermis.

CONCLUSION. Our study showed that very-high-frequency ultrasound and real-time elastography can be useful examinations for comprehensive preoperative evaluation of cutaneous melanoma.

Keywords: cutaneous melanoma, real-time elastography, very-high-frequency ultrasound

DOI:10.2214/AJR.15.15182

Received June 17, 2015; accepted after revision October 28, 2015.

Supported by Iuliu Haţieganu University of Medicine and Pharmacy Cluj-Napoca through project no. 1494/7/28.01.2014.

[1]Department of Radiology, Iuliu Haţieganu University of Medicine and Pharmacy, Cluj-Napoca, Romania.

[2]Department of Dermatology, Iuliu Haţieganu University of Medicine and Pharmacy, Cluj-Napoca, Romania.

[3]Department of Medical Informatics and Biostatistics, Iuliu Haţieganu University of Medicine and Pharmacy, Louis Pasteur St, no. 6, 400349 Cluj-Napoca, Romania. Address correspondence to S. D. Bolboacă (sbolboaca@umfcluj.ro).

[4]Department of Pathology, Emergency County Hospital Cluj-Napoca, Cluj-Napoca, Romania.

AJR 2016; 206:699–704

0361–803X/16/2064–699

Cutaneous melanoma is one of the most severe skin diseases and has had an increasing incidence in recent decades. The global incidence is approximately 160,000 new cases every year with 48,000 deaths [1–4]. The prognosis of cutaneous melanoma depends on the vertical growth of the tumor (pathologic Breslow index) [5, 6]. This index is positively related to the probability of lymph node involvement and to the risk of distant metastasis. Other important histologic prognostic factors are the presence of ulceration, mitotic rate (number of mitoses/mm^2), and Clark level of invasion [7, 8]. Poor prognosis also correlates with increasing age, male sex, and localization (truncal and head and neck locations have a poorer prognosis than tumors on the limbs) [2, 3, 7].

Highly accurate preoperative evaluation of cutaneous melanoma lesions is essential for establishing an optimal therapeutic approach and for improving the survival rate [9, 10]. Use of very-high-frequency ultrasound (> 20 MHz) increases the accuracy of differentiation of the skin layers, improves characterization of skin lesions, and increases the accuracy of measurement of the thickness of the lesion [5].

Real-time elastography (RTE) provides data about the relative elasticity or rigidity (stiffness) of the tissues and structures being examined [11–13]. RTE measures tissue strain in response to an external force on the basis of the assumption that less deformation occurs in rigid tissues than in flexible ones. The elasticity or stiffness of tissue is color coded depending on intensity and is superimposed on a 2D image. The predominance of stiff tissue indicates a higher likelihood of malignancy [11, 14]. This method proved to be suitable in assessment of the breast [15, 16], thyroid [16, 17], malignant lesions of the prostate [18, 19], and superficial lymph nodes [14, 16, 20, 21].

Given the increasing incidence of cutaneous melanoma [22, 23], it is necessary to develop imaging techniques for noninvasive early and complex diagnoses [24]. The primary objective of our study was to evaluate the usefulness of very-high-frequency ultrasound as a tool for assessment of cutaneous melanoma by investigation of the correlation between ultrasound measurement of the thickness of melanoma and the histopathologically measured Breslow index. A secondary objective was to assess the potential role of RTE in the preoperative evaluation of cutaneous melanoma.

Subjects and Methods

A prospective study was performed between September 2011 and January 2015 in the division of ultrasound of the department of radiology at a county emergency hospital. The study included only patients with skin lesions that were clinically suspected of being malignant melanoma but who had not undergone cutaneous biopsy or surgery at the level of the identified lesion. The exclusion criteria were having undergone a specialized clinical examination, the presence of a skin lesion other than melanoma at clinical examination, having undergone any dermatologic treatment, and previous surgery in the area of the lesion.

The very-high-frequency ultrasound evaluation was performed with a Sonotouch and Tablet system (Ultrasonix Medical Corporation) with an 8–40-MHz linear transducer operating at 40 MHz and with RTE capability. Each cutaneous lesion was scanned in the transverse and longitudinal planes with compression perpendicular to the lesion. For RTE examinations, a wide color window was used in an attempt to include the lesion and surrounding normal epidermis, dermis, and hypodermis. Whenever possible, more than one-half of the ROI width containing nontumoral tissue was examined. Images with a good acquisition quality scale, defined as midrange light-green coloring, were stored. Three different images obtained with both techniques (2D ultrasound and RTE) were stored for each lesion. The following data were collected for each subject who met the inclusion criteria.

With 2D ultrasound, the thickness of the melanoma was based on the greatest thickness of the tumor; it was a quantitative variable measured in millimeters. Echogenicity was measured in comparison with that of the neighboring dermis; it was a dichotomous qualitative variable recorded as homogeneous hypoechoic or nonhomogeneous hypoechoic. Contour was recorded as a qualitative variable on a nominal scale as regular, irregular, or ulcerated surface. The ultrasound gel was in sufficient quantity that the transducer caused minimal compression to not alter tumor thickness.

With RTE, qualitative tumor elasticity (low, medium, or high) was based on intratumoral distribution of colors. Flexible tissues were coded in red, medium-elasticity tissues were coded in shades of yellow and green, and stiff tissues appeared in shades of blue. Semiquantitative assessment of tumor elasticity was performed by measuring the strain ratio, which was a semiquantitative variable. Strain ratio is a measurement of the elasticity of the tumor relative to that of normal epidermal and dermal tissue. To measure strain ratio, we used two similar ROIs that were the same size for all lesions. For each lesion, we performed three measurements, and the average value was considered for this study. Strain ratios were calculated for a lesion to neighboring dermis and for a lesion to underlying hypodermis.

The 2D ultrasound image with the greatest value for tumor thickness was retained. A single RTE image, considered by the examiner to be the most representative and reproducible for the lesion, was also retained for analysis. All very-high-frequency ultrasound and RTE examinations were performed by one radiologist with 11 years of ultrasound experience and 7 years of RTE experience. Thickness, contour, echogenicity, qualitative stiffness, and strain ratio were compared with the histopathologic results. Informed consent was obtained from each patient included in the study. The study protocol was approved by the ethics committee of the institution.

Data were summarized as mean and SD for measurements that proved normally distributed. Qualitative characteristics were summarized as percentages and 95% CI calculated with an exact method [25, 26]. The z test for proportions was used to compare pairs of groups for qualitative variables. A significance level of 5% was applied to compare two groups, and in the comparison of three groups, a significance level of 1.7% was used: $\alpha^* = \alpha/K$, where K is the number of comparisons, and $K = k \cdot (k - 1) / 2$, where k is the number of groups, three in this study.

Simple linear regression analysis was conducted to identify the relation between Breslow index and ultrasound thickness under the assumption of linearity between these two variables. The Cook distance (D_i) is used to identify subjects who significantly influence the model. Any lesion with $D_i > 4/n$, where n is the sample size, was considered influential and was withdrawn from the regression analysis. The relation between RTE and ultrasound parameters was quantified with the Spearman correlation coefficient. Statistical analysis was conducted with Statistica software (version 8.0, StatSoft).

TABLE 1: Summaries of Bidimensional, Real-Time Elastographic, and Histopathologic Examinations

Characteristic	Value	p
Two-dimensional ultrasound		
Thickness (mm)[a]	2.53 ± 1.54	
Echogenicity[b]		< 0.0001
Homogeneous hypoechogenic	69.05 (52.44–83.28)	
Nonhomogeneous hypoechogenic	30.95 (16.72–47.56)	
Contour[b]		< 0.0001[c]
Regular	57.14 (40.53–71.37)	
Irregular	38.10 (23.87–54.71)	
Ulceration	4.76 (0.01–16.61)	
Real-time elastography		
Elasticity (qualitative)[b]		< 0.0005[d]
Low	45.24 (28.63–61.85)	
Medium	42.86 (28.63–59.47)	
High	11.90 (4.82–26.13)	
Elasticity (semiquantitative)[a]		
Strain ratio, lesion vs dermal normal tissue	1.02 ± 0.49	
Strain ratio, lesion vs hypodermal tissue	2.16 ± 1.32	
Histologic examination		
Breslow index[a]	2.78 ± 1.38	

[a] Mean ± SD.
[b] Percentage with 95% CI in parentheses.
[c] Significant difference for percentage between regular versus ulceration and irregular versus ulceration.
[d] Significant difference for percentage between low versus high and medium versus high.

Results

A total of 42 cutaneous melanoma lesions in 39 subjects (21 women, 18 men; mean age, 56.56 ± 15.44 years) who met the inclusion criteria were assessed. One subject, a 49-year-old woman, had two localizations (left arm and elbow), and one subject, a 75-year-old man, had three localizations (thoracic, scapular, and lumbar). The three most frequent localizations of the lesions were leg (16.6%; 95% CI, 7.2–30.9%), lumbar or thoracic region (11.9%; 95% CI, 4.8–26.13%), and mammary region (9.5%; 95% CI, 2.4–21.4%). The other localizations of lesions were as follows: scapular (7.1%; 95% CI, 2.4–19.0%); cervical, shoulder, arm, thumb, popliteal region, foot (each with a frequency of 4.8%; 95% CI, 0.1–16.6%); and thigh, elbow, interscapular region, face (frequency, 2.4%; 95% CI, 0.1–11.8%). The main characteristics of the lesions investigated with 2D ultrasound, RTE, and histologic examination are presented in Table 1 and Figures 1–3.

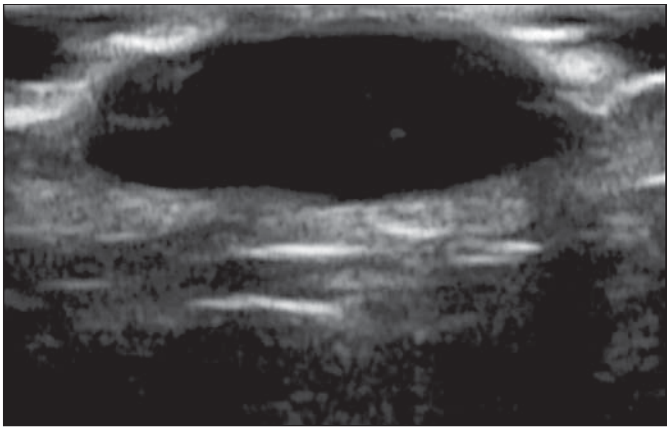

Fig. 1—37-year-old woman with cutaneous melanoma. Two-dimensional ultrasound image shows homogeneous hypoechoic lesion localized to scapular region.

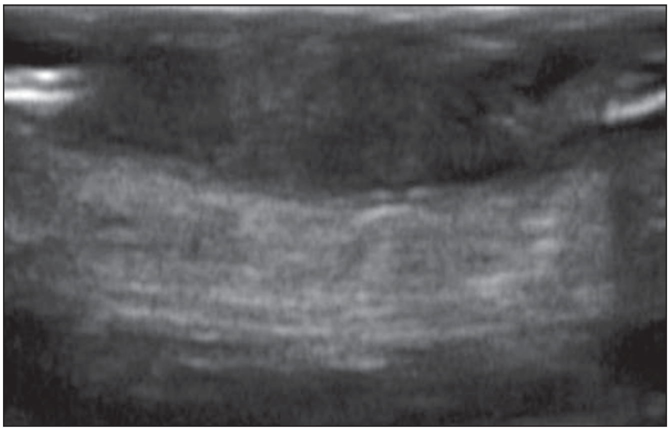

Fig. 2—71-year-old man with cutaneous melanoma. Two-dimensional ultrasound image shows nonhomogeneous hypoechoic lesion localized to lumbar region.

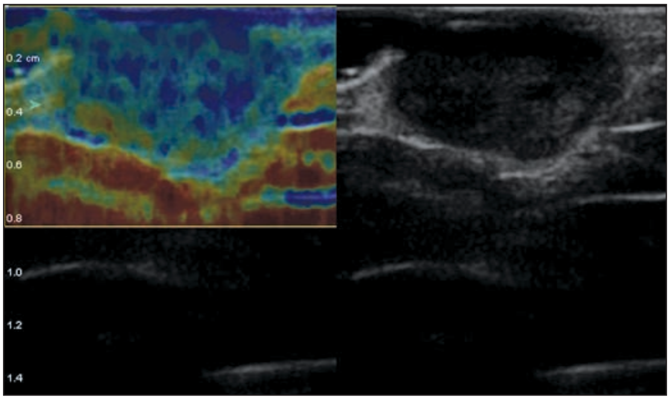

Fig. 3—43-year-old woman with cutaneous melanoma. Real-time elastogram shows stiff skin lesion.

The Breslow index could not be calculated for five lesions (11.9%; 95% CI, 4.8–26.1%), which were included in the stage in situ and excluded from the study. Thus, 37 lesions were included in the analysis in which Breslow index was calculated. Breslow index proved linearly related to ultrasound thickness. The results of regression analysis after removal of influential data (Breslow index, 5 mm; ultrasound thickness, 2.68 mm; Cook distance, 3.5 times as great as threshold) are presented in the following equation and graphed in Figure 4:

$$
\begin{aligned}
&\text{Breslow index} = 0.9495 \times \text{ultrasound thickness}\\
&R = 0.9594,\ SE = 0.3790,\ n = 36\\
&F = 405,\ p\ (F \text{ statistic}) = 1.82 \times 10^{-20}\\
&t = 47.44,\ p\ (t \text{ statistic}) = 2.33 \times 10^{-33},
\end{aligned}
$$

where R is the Pearson correlation coefficient, SE is the standard error of the estimate, n is the sample size, F is the statistic associated with the Fisher test, and t is the statistic associated with the t test.

With the value of the Breslow index as the reference standard, the mean of the difference between Breslow index and ultrasound thickness was –0.05 mm (95% CI, –0.24 to 0.13 mm). The 95% CI associated with the mean of the difference sustained the absence of significant difference between Breslow index and ultrasound thickness (t = –0.58, p = 0.5655). Figure 5 shows the similarity between ultrasound thickness and Breslow index for a male subject with cutaneous melanoma on the lumbar region. The relation between qualitative appearance of the lesion at RTE and the thickness of the lesions measured with ultrasound, the lesion to dermis strain ratio, and lesion to hypodermis strain ratio proved statistically significant (Table 2).

TABLE 2: Spearman Correlation Coefficients (ρ) and Associated Significance (*p*) of Real-Time Elastography

Characteristic	ρ	*p*
Real-time elastographic appearance and ultrasound thickness of the lesion	−0.3052	0.0494
Real-time elastographic appearance and strain ratio of lesion to normal dermis	−0.4660	0.0019
Real-time elastographic appearance and strain ratio of lesion to hypodermis	−0.5792	0.0001

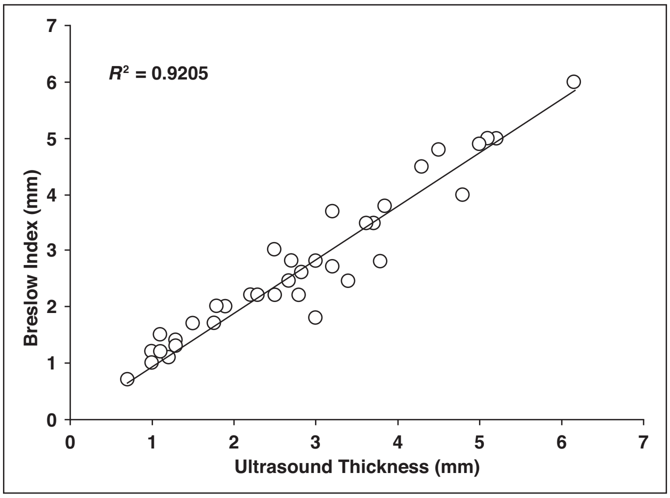

Fig. 4—Graph shows relation between Breslow index and ultrasound thickness.

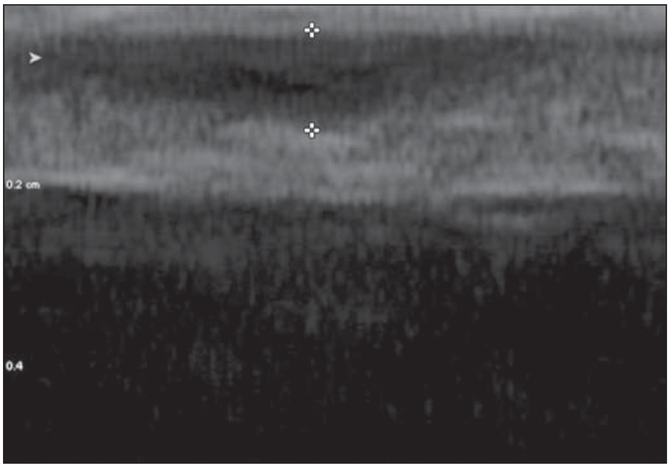

Fig. 5—68-year-old man with cutaneous melanoma of lumbar region. Ultrasound image shows ultrasound thickness is 1.09 mm. Breslow index is 1.1 mm.

Discussion

The mean age of the patients in this study was 57 years, comparable to data in the literature that show the decade with the highest frequency is 50–60 years [22] or 55–64 years [27]. In our study, the most common locations of cutaneous melanoma were the legs and the lumbar and thoracic regions. Fernández Canedo et al. [10] found that most lesions were located on the trunk and limbs. Livingstone et al. [1] and Haddad et al. [2] found the highest frequency on the back and the legs.

Our study showed that tumor echogenicity is an important parameter in the characterization and diagnosis of melanoma, most injuries (69.05%) following the homogeneous hypoechoic model ($p < 0.0001$) [2–6, 28, 29] (Table 1). Contour of the lesions was another statistically significant descriptor ($p < 0.001$) in the study group. Most tumors had a regular contour (57.14%), only 38.10% being irregular (Table 1). Only a small number of cases (4.76%) presented ulceration. Regular contour of cutaneous melanoma correlates with a favorable evolution, whereas ulceration is associated with increasing risk of lymphatic invasion and development of distant metastasis [2, 3, 5, 6]. With the foregoing considerations taken into account, favorable outcome for most of the patients in the study is expected.

The use of elastography in the evaluation of skin lesions has been the subject of research conducted to determine the benign or malignant nature of lesions. A few studies conducted in the early period of clinical elastography showed that this technique has the potential to be useful in the diagnosis of skin tumors. In reported cases, the tumors were diagnosed as malignant on the basis of color distribution on elastograms [14, 30, 31]. In our study, tumor elasticity was a statistically significant descriptor ($p < 0.0005$): 45.24% of the tumors were stiff at RTE, and 42.86% had moderate elasticity (Table 1). It is noteworthy that thicker tumors had low elasticity and thin tumors appeared more flexible. The variability of tumor thicknesses in our study may explain the larger number of tumors with medium or high elasticity.

To our knowledge, semiquantitative assessment of lesion elasticity (strain ratio) compared with the neighboring dermis and hypodermis has not been previously reported. We measured high strain ratios, which suggest that a lesion is stiffer than neighboring dermis and hypodermis. Calculation of lesion-to-dermis strain ratio may prove more reliable because the ROIs may be placed at the same depth. However, the proximity of both lesion and dermis to the transducer may induce false stiffness. In an attempt to avoid this effect, we calculated the strain ratio between the tumor and underlying hypodermis. The use of hypodermis is justifiable because the hypodermis can be considered a landmark of constant elasticity and, in the absence of surgical or local changes, has reproducible stiffness. Investigators in previous studies [32] recommended that the depth difference between the two ROIs (measured in the anteroposterior direction) should not exceed 5 mm. By following these recommendations, we attempted to avoid strain decay by depth. In all lesions, the same depth difference between the tumor and the maximal ROI of the reference tissue was observed. All of the foregoing technical considerations address method reproducibility. In our study, semiquantitative assessment of lesion elasticity compared with the elasticity of the adjacent dermis and underlying hypodermis by means of strain ratio showed averages of 1.02 and 2.16. The semiquantitative evaluation of lesion elasticity may represent an additional factor for complete characterization of the tumor. To our knowledge, the potential of this ratio has not been previously reported.

Evaluation of the lesion thickness of cutaneous melanomas is extremely important in both management and prognosis. Breslow index correlates positively with the probability of lymph node involvement and with the risk of distant metastasis. Several studies have assessed the correlation between melanoma thickness measured with ultrasound and pathologically. Most of them showed a significant statistical correlation between these two measurements [28, 29, 33]. Kaikaris et al. [34] used high-frequency ultrasound (14 MHz) to find an association between noninvasive ultrasound findings and morphologic findings in the measurement of cutaneous melanoma thickness influencing surgical strategy. They found a low correlation between ultrasound melanoma thickness and Breslow index for thin tumors (1–2 mm). However, they also found significant correlation for thicker melanomas (> 2 mm). Very-high-frequency ultrasound (20 MHz) measurements were found to correlate well with the depth of thick melanomas but were not sufficiently accurate for thinner melanomas. The evidence showed that using high frequency (lower penetrance) may be more successful in estimation of tumor size than is 20-MHz ultrasound [10, 35].

Kleinerman et al. [36], using very-high-frequency ultrasound (75 MHz), found significant correlations with Breslow depth for lesions with an average thickness of 0.4 mm. Although results of several studies suggested that preoperative 75-MHz very-high-frequency ultrasound scanning may be a reliable means of predicting lesion size [10, 35, 36], the authors recognized limitations in the use of 20-MHz ultrasound to assess tumor margins. These limitations are related to inflammatory infiltrates associated with cutaneous melanoma, which may create hypoechoic extension and cause overestimation of tumor size [36]. In our study, in which scanning was performed at 40 MHz, ultrasound thickness (2.53 ± 1.54 mm) had linear correlation with Breslow index (2.78 ± 1.38 mm), the determination coefficient being 0.9205 (Fig. 4), greater than reported by Jasaitiene et al. [35].

Other possibly useful information (Table 2) was found by analyzing the correlation between the RTE appearance and other sonographic features of cutaneous melanoma lesions. Thus, in the relation between the elastographic features and tumor thickness, we observed that elasticity of cutaneous melanoma decreases with increasing thickness, which is probably explained by increased packing of cells (melanocytes and inflammatory infiltrate).

The qualitative elastographic appearance was significantly associated with semiquantitative elastographic measurements, that is, the strain ratios between the tumor and adjacent normal dermis and the tumor and hypodermis. In this study, cutaneous melanoma lesions appeared stiffer than surrounding tissues, probably as a result of the presence of malignant infiltration.

A limitation of this study was that the number of skin lesions investigated was small because it was difficult to find the patients and acquire their consent for enrollment in the study, which was conducted at a single institution. However, we present only partial results of the study, which is ongoing. Another possible limitation might have been bias introduced by the fact that all examinations were performed by one radiologist, so interobserver and intraobserver agreement was not analyzed. This bias is not necessarily deleterious, because it becomes a constant factor. Shear-wave elastography may be a more objective way of quantifying stiffness, but the method was not available for this study.

To our knowledge, this is the first report of the combined use of elastography and very-high-frequency sonography in the assessment of cutaneous melanoma. Additional research with larger samples is necessary to certify the results presented.

Conclusions

This study showed that very-high-frequency ultrasound is useful for preoperative evaluation of cutaneous melanoma. No significant difference was found between the sonographic and histologic measurements of Breslow index. Information obtained with RTE contributes to assessment of the primary skin tumor and may be useful for complex preoperative diagnoses. Because malignant tumors are stiffer than benign ones, elastography added to high-frequency ultrasound imaging of the skin has potential for improving the accuracy of traditional clinical diagnosis of cutaneous melanoma.

References

1. Livingstone E, Windemuth-Kieselbach C, Eigentler TK, et al. A first prospective population-based analysis investigating the actual practice of melanoma diagnosis, treatment and follow-up. *Eur J Cancer* 2011; 47:1977–1989
2. Haddad D, Garvey EM, Mihalik L, et al. Preoperative imaging for early-stage cutaneous melanoma: predictors, usage, and utility at a single institution. *Am J Surg* 2013; 206:979–985
3. Garbe C, Peris K, Hauschild A, et al. Diagnosis and treatment of melanoma: European consensus-based interdisciplinary guideline—update 2012. *Eur J Cancer* 2012; 48:2375–2390
4. Eggermont AM, Spatz A, Robert C. Cutaneous melanoma. *Lancet* 2014; 383:816–827
5. Hayashi K, Koga H, Uhara H, et al. High-frequency 30-MHz sonography in preoperative assessment of tumor thickness of primary melanoma: usefulness in determination of surgical margin and indication for sentinel lymph node biopsy. *Int J Clin Oncol* 2009; 14:426–430
6. Quaglino P, Ribero S, Osella-Abate S, et al. Clinico-pathologic features of primary melanoma and sentinel lymph node predictive for non-sentinel lymph node involvement and overall survival in melanoma patients: a single centre observational cohort study. *Surg Oncol* 2011; 20:259–264
7. Scolyer RA, Prieto VG. Melanoma pathology: important issues for clinicians involved in the multidisciplinary care of melanoma patients. *Surg Oncol Clin N Am* 2011; 20:19–37
8. Patnana M, Bronstein Y, Szklaruk J, et al. Multimethod imaging, staging, and spectrum of manifestations of metastatic melanoma. *Clin Radiol* 2011; 66:224–236
9. Ferris LK, Harris RJ. New diagnostic aids for melanoma. *Dermatol Clin* 2012; 30:535–545
10. Fernández Canedo I, de Troya Martín M, Fúnez Liébana R, et al. Preoperative 15-MHz ultrasound assessment of tumor thickness in malignant melanoma. *Actas Dermosifiliogr* 2013; 104:227–231
11. Botar-Jid C, Vasilescu D, Dudea SM. Tridimensional ultrasound and sonoelastography in musculoskeletal pathology. In: Fodor D, ed. *Clinical musculoskeletal ultrasonography*. Bucharest, Romania: Editura Medicală, 2009:381–389
12. Bamber J, Cosgrove D, Dietrich CF, et al. EFSUMB guidelines and recommendations on the clinical use of ultrasound elastography. Part 1. Basic principles and technology. *Ultraschall Med* 2013; 34:169–184
13. Dancey AL, Mahon BS, Rayatt SS. A review of diagnostic imaging in melanoma. *J Plast Reconstr Aesthet Surg* 2008; 61:1275–1283
14. Hinz T, Hoeller T, Wenzel J, et al. Real-time tissue elastography as promising diagnostic tool for diagnosis of lymph node metastases in patients with malignant melanoma: a prospective single-center experience. *Dermatology* 2013; 226:81–90
15. Itoh A, Ueno E, Tohno E, et al. Breast disease: clinical application of US elastography for diagnosis. *Radiology* 2006; 239:341–350
16. Cosgrove D, Piscaglia F, Bamber J, et al. EFSUMB guidelines and recommendations on the clinical use of ultrasound elastography. Part 2. Clinical applications. *Ultraschall Med* 2013; 34:238–253
17. Rago T, Santini F, Scutari M, et al. Elastography: new developments in ultrasound for predicting malignancy in thyroid nodules. *J Clin Endocrinol Metab* 2007; 92:2917–2922
18. Correas JM, Tissier AM, Khairoune A, et al. Ultrasound elastography of the prostate: state of the art. *Diagn Interv Imaging* 2013; 94:551–560
19. Dudea SM, Giurgiu CR, Dumitriu D, et al. Value of ultrasound elastography in the diagnosis and management of prostate carcinoma. *Med Ultrason* 2011; 13:45–53
20. Lenghel LM, Bolboacă SD, Botar-Jid C, et al. The value of a new score for sonoelastographic differentiation between benign and malignant cervical lymph nodes. *Med Ultrason* 2012; 14:271–277
21. Lenghel LM, Botar Jid C, Bolboacă SD, et al. Comparative study of three sonoelastographic

scores for differentiation between benign and malignant cervical lymph nodes. *Eur J Radiol* 2015; 84:1075–1082

22. Doben AR, MacGillivray DC. Current concepts in cutaneous melanoma: malignant melanoma. *Surg Clin North Am* 2009; 89:713–725
23. Bichakjian CK, Halpern AC, Johnson TM, et al. Guidelines of care for the management of primary cutaneous melanoma. *J Am Acad Dermatol* 2011; 65:1032–1047
24. Catalano O, Siani A. Cutaneous melanoma: role of ultrasound in the assessment of locoregional spread. *Curr Probl Diagn Radiol* 2010; 39:30–36
25. Jäntschi L, Bolboacă SD. Exact probabilities and confidence limits for binomial samples: applied to the difference between two proportions. *ScientificWorldJournal* 2010; 10:865–878
26. Bolboacă SD, Jäntschi L. Optimized confidence intervals for binomial distributed samples. *Int J Pure Appl Math* 2008; 47:1–8
27. Leiter U, Buettner PG, Eigentler TK, et al. Hazard rates for recurrent and secondary cutaneous melanoma: an analysis of 33,384 patients in the German Central Malignant Melanoma Registry. *J Am Acad Dermatol* 2012; 66:37–45
28. Guitera P, Li LX, Crotty K, et al. Melanoma histological Breslow thickness predicted by 75-MHz ultrasonography. *Br J Dermatol* 2008; 159:364–369
29. Wang SQ, Hashemi P. Noninvasive imaging technologies in the diagnosis of melanoma. *Semin Cutan Med Surg* 2010; 29:174–184
30. Wortsman X, Carreño L, Morales C. Skin cancer: the primary tumors. In: Wortsman X, Jemec GB, eds. *Dermatologic ultrasound with clinical and histologic correlations*. New York, NY: Springer, 2013:249–280
31. Hinz T, Wenzel J, Schmid-Wendtner MH. Real-time tissue elastography: a helpful tool in the diagnosis of cutaneous melanoma? *J Am Acad Dermatol* 2011; 65:424–426
32. Lyshchik A, Higashi T, Asato R, et al. Thyroid gland tumor diagnosis at US elastography. *Radiology* 2005; 237:202–211
33. Machet L, Belot V, Naouri M, et al. Preoperative measurement of thickness of cutaneous melanoma using high-resolution 20 MHz ultrasound imaging: a monocenter prospective study and systematic review of the literature. *Ultrasound Med Biol* 2009; 35:1411–1420
34. Kaikaris V, Samsanavicius D, Maslauskas K, et al. Measurement of melanoma thickness: comparison of two methods—ultrasound versus morphology. *J Plast Reconstr Aesthet Surg* 2011; 64:796–802
35. Jasaitiene D, Valiukeviciene S, Linkeviciute G, et al. Principles of high-frequency ultrasonography for investigation of skin pathology. *J Eur Acad Dermatol Venereol* 2011; 25:375–382
36. Kleinerman R, Whang TB, Bard RL, et al. Ultrasound in dermatology: principles and applications. *J Am Acad Dermatol* 2012; 67:478–487

Original paper

Med Ultrason 2016, Vol. 18, no. 3, 312-317
DOI: 10.11152/mu.2013.2066.183.hgh

High-frequency sonography in the evaluation of nail psoriasis

Mihaela Elena Marina*[1], Carolina Solomon[2], Sorana-Daniela Bolboaca*[3], Corina Bocsa[4], Carmen Mihaela Mihu[1], Alexandru Dumitru Tătaru[5]

[1]Histology Department, [2]Radiology Department, [3]Medical Informatics and Biostatistics Department,[5]Dermatology Department, "Iuliu Haţieganu" University of Medicine and Pharmacy, [4]Medical-Surgical Center InterServisan, Cluj-Napoca, Romania
* the authors shared the first authorship

Abstract

Aim: To evaluate the morphostructural aspects and nail vascularity in the nail unit of patients with psoriasis, and to evaluate whether there are differences among psoriatic patients with and without nail involvement. **Material and methods:** Nail plates and nail bed changes, nailfold vessel resistance index (NVRI), power and color Doppler blood flow appearances were investigated in 23 patients with moderate-to-severe psoriasis, with and without nail involvement, and compared to those of 11 healthy participants. **Results:** Ventral nail plate deposits were present only in psoriasis patients. Irregular or totally fused nail plates and increased nail plate thickness was frequently observed in psoriasis patients compared to controls. NVRI was increased in psoriatic patients' nails compared to controls (0.62 vs. 0.57, $p<0.0001$). In the psoriasis patient group there was significant statistical difference in NVRI in patients with nail involvement compared to those without (0.66 vs. 0.55, $p<0.0001$). **Conclusions:** High-frequency gray scale sonography provides valuable information regarding morphostructural changes in nail unit structure in patients with psoriasis. Power Doppler imaging enables blood flow assessment in psoriasis nail induced changes.

Keywords: nailfold vessel resistance index (NVRI), nail psoriasis, power and color Doppler sonography

Introduction

Psoriasis is a chronic, relapsing skin disease affecting millions of people worldwide, with a general prevalence estimated to be approximately 2-3% [1]. While skin lesions are the most typical findings of psoriasis, nail involvement is an often-overlooked clinical manifestation of the disease. Nail changes were reported to occur in up to 40% of patients with mild psoriasis and 50-70% with severe disease [2,3]. Samman et al reported an 80% to 90% lifetime incidence of nail involvement in psoriatic patients [4]. Nail psoriasis, in the absence of cutaneous lesions, can be present in 5% of patients [5] and represents a special diagnostic challenge.

Traditionally, nail psoriasis is a clinical diagnosis due to the fact that nail biopsy, besides being a bleeding and painful procedure, may cause detrimental cosmetic changes such as scarring and permanent nail dystrophy [6]. Dermoscopy and videodermoscopy, generally used in describing benign and malignant tumoral skin lesions, were reported as being non-invasive, quickly applied, and easy-to-use methods that may aid in diagnosing nail psoriasis [7-10]. Capillaroscopy, usually used to study the microcirculation in collagen disease, can also be used to detect psoriasis induced microvascular changes, such as decreased capillary density and avascular areas in the periungual area [11].

High-resolution ultrasonography (HRUS) was used in assessing nail apparatus anatomy and soft tissues changes in patients with different nail pathologies and provided appropriate diagnosis and additional informa-

---

Received 09.03.2016 Accepted 30.04.2016
Med Ultrason
2016, Vol. 18, No 3, 312-317

Corresponding author: Carolina Solomon
Department of Radiology, "Iuliu Haţieganu"
University of Medicine and Pharmacy
3-5 Clinicilor Street
400006 Cluj-Napoca, Romania
Phone: +40745601976
E-mail: carolina.solomon@umfcluj.ro

tion to the clinical examination [12]. Easy to perform and having no risk of irradiation, HRUS has been proposed as a valuable imaging method in assessing the extension and activity of both nail and cutaneous psoriasis [13,14].

The aim of this study was to evaluate both the morphological appearance and blood flow changes in the nail apparatus of patients with psoriasis compared to disease free controls using gray-scale and color and power Doppler HRUS.

Material and methods

Study design

This was a single center, transversal, observational study, from July 2014 until March 2015. Twenty-three adult patients (age > 18 years old), with moderate-to-severe chronic plaque psoriasis measured by Psoriasis Area and Severity Index (PASI>10), lasting at least 6 months, with or without fingernail involvement were included in the case group. Patients with clinical psoriatic arthritis or other inflammatory conditions affecting joints, such as rheumatoid arthritis, were excluded. Patients with diabetes, arterial hypertension, smokers (patients who smoked cigarettes daily or who had stopped smoking <10 years before enrollment in the study), and patients following systemic or topical treatment on their nails (for nail psoriasis) at the time of the clinical examination or in the last 3 month prior to examination, or having a skin disease that is associated with nail involvement and those who used artificial nails in the past 6 months were also excluded. The control group consisted of eleven non-smoking healthy subjects, age and sex matched with the cases, without psoriatic arthritis, diabetes, or arterial hypertension. The University Ethics Committee approved the study and all subjects gave their written consent prior to the enrollment.

Clinical evaluation

All subjects were interviewed to collect demographical data: age, gender, age of onset and duration of psoriasis, age of onset, and duration of fingernail psoriasis. The severity of skin psoriasis was assessed using PASI (ranging from 0- no disease to 72- maximal disease), a score that combines the severity (erythema, induration, and desquamation) and percentage of affected area [15]. Onycomycosis was excluded by direct microscopic examination (10% potassium hydroxide) in patients with nail bed hyperkeratosis.

Ultrasonography assessment

Real-time HRUS was performed by an experienced sonographer with more than 15 years' experience using an Ultrasonix Sonotouch scanner (Ultrasonix Medical Corporation, Richmond, Canada) equipped with a variable-frequency transducer ranging from 8 to 40 MHz (focal range 0.2-3 cm, image field 16 mm) to visualize nail anatomy.

In order to observe the blood flow a Hitachi EUB 8500 System equipped with a variable-frequency transducer ranging from 6.5-13 MHz was used. The imaging parameters for Doppler ultrasound examinations were set to increase the detection of low-velocity, low-volume flows within the small inside of the nail bed (color Doppler: PRF 500-1000 Hz, wall filter 25-50 Hz, power Doppler: PRF 350-700 Hz, wall filter 22-50 Hz; color and power Doppler: color gain maximized for optimal sensitivity while avoiding excessive color noise, color vs. echo priority ranging from 70 to 90% and color persistence adjusted to high values).

The sonographic examinations were performed in a room with a constant controlled temperature of 24ºC, after a 20 minute rest period. The patient was seated, with the forearm in a neutral position over the table and the nails were scanned on longitudinal and transverse planes. The ultrasound gel had sufficient quantity so that the transducer exerted no compression, to avoid alteration of nail thickness or blood flow.

Each fingernail was scanned in the gray scale mode with 40MHz frequency transducer to detect morpho-structural changes (deposits in dorsal nail plate, nail plates irregularities and thickness, nail bed thickness), and afterwards with the power Doppler technique to enable blood flow visualization. Nail plate thickness represents the distance between the two nail plates. Nail bed thickness was obtained by measuring the distance from the ventral nail plate to the dorsal of the distal phalanx at 2.5 mm from the proximal nail fold.

Using Doppler examination, in the proximal third of the nail plate of each fingernail, the maximum speeds of flow in systole (Qs) and in diastole (Qd) were registered and the nailfold vessel resistance index (NVRI) was assessed as the following ratio: (Qs-Qd)/Qs. The NVRI ratio ranges from 0 (no resistance to blood flow at all: no changes in the circulation of blood in systole and diastole) to 1 (maximum resistance to blood flow circulation of blood only at systole) [16]. Color and Power Doppler spots in nail bed were registered as follows: low <25%, medium 25-50%, and multiple >50% of nail bed's area occupied by vascular structures.

Statistical analysis

Descriptive and inferential statistical methods were applied using Statistica software (version 8, StatSoft, USA). Qualitative data were summarized as percentages and associated 95% confidence interval (provided in squared brackets along the manuscript) computed with an exact method [17]. The normal distribution of quantitative data was tested using the Shapiro-Wilks test and whenever the p-value was higher than 5%, data were considered normally distributed. Quantitative data that proved normally distributed were summarized as mean±standard deviation; otherwise median and interquartile range (expressed as Q1–Q3, where Q1 is the first quartile and Q3 is the third quartile) was used. Comparisons between groups were conducted with Z test for proportions (qualitative data), student t-test for independent samples for quantitative normally distributed data, and respectively Mann-Whitney test for quantitative data when Shapiro-Wilks null hypothesis (data follow normal distribution) failed to be rejected. Inferential statistical analysis was conducted at a significance level of 5%, and any p-value lower than 0.05 was considered statistically significant.

Results

Twenty-three patients with cutaneous psoriasis (14 with nail psoriasis and 9 without nail involvement) and eleven healthy subjects were included in the study. Thus, on the sample there were evaluated 122 nails belonging to patients with psoriasis and 82 nails belonging to controls.

Mean age in the control group was 46.09 years (±11.82SD), ranging from 20 to 59 years old, without significant differences when compared with patients in the psoriasis group (52.43±14.28SD).

Demographic and disease characteristics of the patients in psoriasis group are summarized in Table I.

No statistical difference was observed between genders in the psoriasis patients, regarding mean age of onset of cutaneous psoriasis, mean duration of psoriasis or PASI score.

In the control group there were no ventral nail plate deposits or irregularities in any of the nail plates ($p<0.05$), and only a low number of spots on Color and Power Doppler imaging (fig 1) were detected.

In the psoriasis group 13.11% of the investigated nails presented deposits in the ventral plate; both of the nail plates had various degrees of involvement and the nail plates were significantly thicker compared to controls. Color and power Doppler assessment revealed an increased nail blood flow in psoriasis patients with a higher vascular resistance when compared to controls (fig 2, Table II).

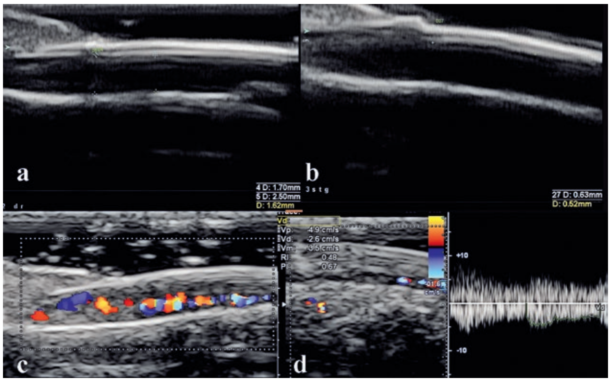

Fig 1. Normal US nail aspect in a non affected 47 years old woman: a) 2D US – thickness of the nail bed; b) 2D US – measurement of the nail plaques thickness; c) color Doppler US – aspect of the vessels in the nail bed; d) spectral Doppler – measurement of the Doppler indices in nail vessels

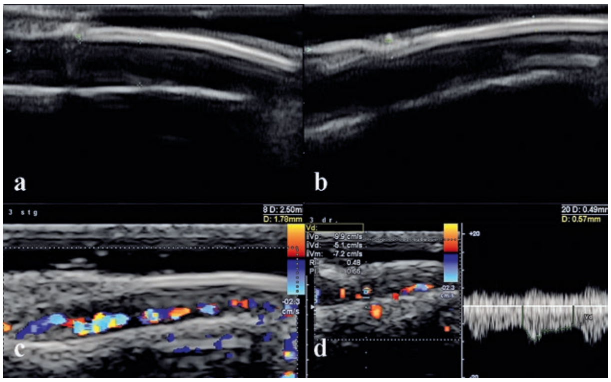

Fig 2. US aspect in a 52 years old female with psoriasis and no clinical affected nails: a) 2D US – thick-ness of the nail bed; b) 2D US – measurements of the nail plaques thickness; c) color Doppler US – tortuous vessels in the nail bed; d) spectral Doppler – Doppler indices in nail vessels

Table I. Characteristics of patients in the psoriasis group

	All (n=23)	**With nail involvement (n=14)**	**Without nail involvement (n=9)**	**p-value**
Age (years)	52.43±14.28	52.57±17.96	52.22±6.04	0.056 (0.95)
Gender[a]				|1.72| (0.08)
F	35	21	56	
M	65	79	44	
Mean age of onset of cutaneous psoriasis	36.39±12.69	32.07±12.68	43.11±9.91	-2.21 (0.03)
Mean duration of cutaneous psoriasis	15.96±13.10	20.36±14.47	9.11±6.70	2.17 (0.04)
PASI	17.81±3.64	18.79±3.37	16.29±3.70	1.67 (0.10)

Data are expressed as mean±standard deviation; [a]: %, Z-test for proportions; PASI = Psoriasis Area and Severity Index, F – female, M – male

Table II. Nail US morphostructural and blood flow characteristics: cases versus controls

	Psoriasis (n=122)	**Control (n=82)**	**Stat (p-value)**
Ventral nail plate deposits[a]	13.11 [7.38–20.49]	0 [0.00–4.86]	3.41 (0.0006)
Nail plates aspect[a]			
1 (regular)	24.59 [17.22–32.78]	100.00[95.14–100]	-10.61 (<0.0001)
2 (irregular)	34.43 [26.24–43.44]	0.00 [0.00–4.86]	5.96 (< 0.0001)
3 (pointly fused)	34.43 [26.24–43.44]	0.00 [0.00–4.86]	5.96 (< 0.0001)
4 (totally fused)	6.56 [2.47–12.29]	0.00 [0.00–4.86]	2.36 (0.0182)
CD spots[a]			
1 (low)	36.07 [27.88–45.08]	100.00 [95.14–100]	-9.21 (<0.0001)
2 (medium)	54.92 [45.91–63.93]	0.00 [0.00–4.86]	8.19 (<0.0001)
3 (multiple)	9.02 [4.11–15.57]	0.00 [0.00–4.86]	2.79 (0.0052)
PD spots[a]			
1 (low)	36.89 [28.70–45.90]	100.00 [95.14–100]	-9.12 (<0.0001)
2 (medium)	54.10 [45.09–63.11]	0.00 [0.00–4.86]	8.10 (<0.0001)
3 (multiple)	9.02 [4.11–15.57]	0.00 [0.00–4.86]	2.79 (0.0052)
Nail bed thickness[b]	1.88 (1.71–2.03)	1.89 (1.78–2.00)	-0.74 (0.4621)
Nail plates thickness[b]	0.86 (0.60–1.14)	0.63 (0.59–0.67)	5.68 (<0.0001)
NVRI[b]	0.62 (0.55–0.69)	0.57 (0.55–0.58)	4.75 (<0.0001)

CD = Color Doppler; PD = Power Doppler; NVRI = nailfold vessel resistance index; a: % [95%CI], where CI = confidence interval; comparisons done with Z-test; b: median (Q1–Q3), where Q1 = first statistic, Q3 = third statistic; Mann-Whitney test for comparison between psoriasis and control group

Table III. Nail US morphostructural and blood flow characteristics in patients with psoriasis, with and without nail involvement

	Nail involvement (n=79)	**Without nail involvement (n=43)**	**Statistic (p-value)**
Ventral nail plate deposits[a]	17.72 [10.14–27.83]	4.65 [0.05–16.23]	2.04 (0.0410)
Nail plates aspect[a]			
1 (regular)	26.58 [17.74–37.96]	20.93 [9.36–34.83]	0.69 (0.4887)
2 (irregular)	36.71 [26.60–48.09]	30.23 [16.33–46.46]	0.72 (0.4697)
3 (pointly fused)	29.11 [19.00–40.49]	44.19 [27.96–60.41]	-1.67 (0.094)
4 (totally fused)	7.59 [2.55–15.17]	4.65 [0.05–16.23]	0.63 (0.5307)
CD spots[a]			
1 (low)	34.18 [24.07–45.55]	39.53 [25.64–55.76]	-0.59 (0.5566)
2 (medium)	55.70 [44.32–67.07]	53.49 [37.26–69.71]	0.23 (0.8147)
3 (multiple)	10.13 [3.81–18.97]	6.98 [2.38–18.55]	0.58 (0.5618)
PD spots[a]			
1 (low)	34.18 [24.07–45.55]	41.86 [27.96–58.09]	-0.84 (0.4010)
2 (medium)	55.70 [44.32–67.07]	51.16 [34.94–67.39]	0.48 (0.6307)
3 (multiple)	10.13 [3.81–18.97]	6.98 [2.38–18.55]	0.58 (0.5618)
Nail bed thickness[b]	1.82 (1.66–2.00)	1.94 (1.78–2.06)	-1.82 (0.0684)
Nail plates thickness[b]	0.93 (0.69–1.24)	0.71 (0.51–0.97)	3.38 (0.0007)
NVRI[b]	0.66 (0.60–0.71)	0.55 (0.48–0.60)	4.68 (<0.0001)

CD = Color Doppler; PD = Power Doppler; NVRI = nailfold vessel resistance index; a: % [95%CI], where CI = confidence interval; comparisons done with Z-test; b: median (Q1–Q3), where Q1 = first quartile, Q3 = third quartile; Mann-Whitney test for comparison between psoriasis and control group.

Among patients with psoriasis, those who have had clinical fingernail involvement presented obvious morphostructural US modifications: ventral nail plate deposits, irregular or totally fused together nail plates were frequently observed in those with nail involvement compared to those without nail involvement.

Vascularization's assessment revealed significant differences between the two subgroups in psoriatic patients: those with clinical nail involvement displayed a great number of medium and multiple CD and PD spots, while those without nail involvement displayed more often a low number of spots on CD and PD imaging (fig 3).

The vascular resistance to blood flow measured by NVRI proved to be significantly higher in patients with psoriasis compared to controls, and among patients with psoriasis: those with nail involvement showed a higher mean±SD than those without (Table III).

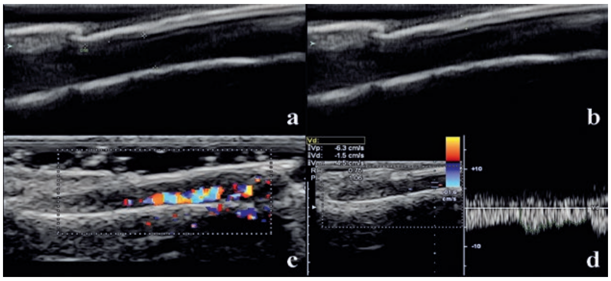

Fig 3. US aspect in a 59 years old male with psoriasis and with clinical affected nails: a) 2D US – thick-ness of the nail bed; b) 2D US – measurements of the nail plaques thickness; c) color Doppler US – tortuous vessels in the nail bed; d) spectral Doppler – Doppler indices in nail vessels

Discussions

Due to its major negative impact on the physical and social quality of life, in the last decade, there has been an increasing interest in assessing nail involvement in psoriatic patients. High-frequency ultrasonography probes and sensitive color and power Doppler technique permitted us to quantify both morphostructural and blood flow changes in the nail unit in patients with chronic moderate-to-severe cutaneous psoriasis.

Gray scale sonographic evaluation in nail apparatus showed deposits in the ventral nail plate only in patients with psoriasis, while none of the controls presented these changes. Moreover, among patients with psoriasis, the presence of ventral nail plate deposits were registered in 17.72% of the involved nails and in 4.62% of the nails without clinical signs of involvement ($p<0.05$). These changes suggest the fact that HRUS can detect subclinical modifications in ventral nail plate in patients with cutaneous psoriasis but without obvious clinical involvement.

We found increased nail plate thickness in patients with psoriasis compared to healthy controls, with a significant difference between those with and without clinical nail involvement, similar data being also reported by Gisondi et al [18]. In contrast with the same study, we did not find increased nail bed thickness in patients with psoriasis, even though this modification was expected. This fact could be explained by different anatomical sites of ultrasound measurement (we performed this measurement at 2.5 mm from the proximal nail fold) or by different stages of the nail disease (active or passive phase onichopathy). Also, the small number of enrolled patients and controls in our study could have influenced this outcome. In this matter, a histopathological investigation of nails could have helped in order to correlate high-frequency sonographic aspects with underlying anatomical changes.

Sandobal et al measured the mean distance between the ventral plate and osseous margin of the distal phalanx and reported also higher values in psoriatic arthritis patients and patients with cutaneous psoriasis compared to rheumatoid arthritis patients [19].

Elongated, twisted, and tortuous capillary loops, of the microvascular dermal plexus, lead to an increased blood flow in both the psoriatic skin and the nail bed [20]. In normal conditions, a minimal quantity of blood flow, due to thin arterial and venous vessels, can be occasionally detected by power Doppler in the nail bed [21]. Power Doppler was also reported as being a feasible highly sensitive tool in monitoring psoriatic plaque treatment response [22].

In our study color and power Doppler imaging revealed increased blood flow in the enlarged vessels in the nail bed of patients with psoriasis compared to controls ($p<0.005$). This result is in line with those reported by other studies [13,14]. When measuring NVRI, significant differences in the NVRI between patients and controls ($p<0.0001$) and among patients with psoriasis, those with clinical nail involvement had a median NVRI higher than those without nail involvement ($p<0.0001$). The same NVRI outcome was reported by Husein El-Ahmed et al in a study assessing NVRI in the fourth fingernail of the non-dominant hand in 23 psoriatic patients compared to controls. Interestingly, they stated that they observed a decreased blood supply in the nail bed in psoriatic patients, probably due to dysfunction among endothelial cells and wall vessel thickening [22]. The difference in blood flow supply reports between our study and this study could be explained by the fact that they enrolled patients with psoriasis under systemic treatment with methotrexate or biologic agents at the time of the sonographic evaluation, treatment that could have influenced measurement outcome.

We acknowledge the fact that the ultrasonographic evaluation was performed only by one evaluator and he could not be blinded to the clinical nail findings, but the statistical analysis revealed significant differences despite this limitation. Due to the synovio-entheseal inflammation that occurs in psoriatic arthritis and its anatomic proximity to the nail unit, patients with clinical psoriatic arthritis were not included in this study, in order to assess only nail psoriasis induced changes.

Our findings underline the necessity of correlating clinical modifications with ultrasound aspects in fingernail psoriasis: morphostructural changes in the nail unit could be detected in an early stage, even in clinical non-affected nails, thus enhancing a precocious diagnosis and a better disease management. Nail bed's blood flow assessment revealed important data regarding microvasculatures alterations and could be taken in consideration as an adequate area to monitor targeted antiangiogenic therapy. This is the first study to report NVRI on a greater number of fingernail psoriasis and we propose this index to be taken into account when an ultrasound evaluation of this area is required.

In conclusion, we found that patients with psoriasis have ventral nail plate deposits, irregular or totally fused nail plates and increased nail plate thickness compared to controls. In patients with psoriasis, an increased blood supply and higher resistance to blood flow were observed in patients with nail involvement compared to those without clinically nail disease. Our observations confirm that a nail unit is a suitable anatomic location for assessing blood flow changes in psoriatic onychopathy using high-frequency sonography with sensitive Power Doppler imaging.

Conflict of interest: None

Acknowledgement: This paper was published under the frame of the European Social Fund, Human Resources Development Operational Programme 2007-2013, project no. POSDRU/159/1.5/138776

References

1. Lima XT, Minnillo R, Spencer JM, Kimball AB. Psoriasis prevalence among the 2009 AAD National Melanoma/Skin Cancer Screening Program participants. J Eur Acad Dermatol Venereol 2013; 27: 680-685.
2. Augustin M, Krüger K, Radtke MA, Schwippl I, Reich K. Disease severity, quality of life and health care in plaque-type psoriasis: a multicenter cross-sectional study in Germany. Dermatology 2008; 216: 366–372.
3. Jiaravuthisan MM, Sasseville D, Vender RB, Murphy F, Muhn CY. Psoriasis of the nail: Anatomy, pathology, clinical presentation, and a review of the literature on therapy. J Am Acad Dermatol 2007; 57: 1–27.
4. Samman PD, Fenton DA. The nails in disease, 5th ed. London: Butterworth-Heinemann Ltd., 1994.
5. Gregoriou S, Kalogeromitros D, Kosionis N, Gkouvi A, Rigopoulos D. Treatment options for nail psoriasis. Expert Rev Dermatol 2008; 3: 339–344.
6. Grover C, Reddy BS, Uma Chaturvedi K. Diagnosis of nail psoriasis: importance of biopsy and histopathology. Br J Dermatol 2005; 153: 1153-1158.
7. Farias DC, Tosti A, Chiacchio ND, Hirata SH. Dermoscopy in nail psoriasis. An Bras Dermatol 2010; 85: 101-103.
8. Micali G, Lacarrubba F, Massimino D, Schwartz RA. Dermatoscopy: Alternative uses in daily clinical practice. J Am Acad Dermatol 2011; 64: 1135-1146.
9. Micali G, Lacarrubba F. Possible applications of videodermatoscopy beyond pigmented lesions. Int J Dermatol 2003; 42: 430-433.
10. Iorizzo M, Dahdah M, Vincenzi C, Tosti A. Videodermoscopy of the hyponychium in nail bed psoriasis. J Am Acad Dermatol 2008; 58: 714-715.
11. Ribeiro CF, Siqueira EB, Holler AP, Fabrício L, Skare TL. Periungual capillaroscopy in psoriasis. An Bras Dermatol 2012; 87: 550-553.
12. Singh R, Bryson D, Singh HP, Jeyapalan K, Dias JJ. High-resolution ultrasonography in assessmentof nail-related disorders. Skeletal Radiol 2012; 41: 1251–1261.
13. Wortsman X, Wortsman J, Carreño L. Sonographic Anatomy of the Skin, Appendages, and Adjacent Structures. In: Wortsman X, Jemec GBE. Dermatologic Ultrasound with Clinical and Histologic Correlations. New York, Springer 2013: 15-38.
14. Gutierrez M, Wortsman X, Filippucci E, De Angelis R, Filosa G, Grassi W. High-frequency sonography in the evaluation of psoriasis: nail and skin involvement. J Ultrasound Med 2009; 28: 1569-1574.
15. Fredriksson T, Pettersson U. Severe psoriasis—oral therapy with a new retinoid. Dermatologica1978; 157: 238–244.
16. Husein El-Ahmed H, Garrido-Pareja F, Ruiz-Carrascosa JC, Naranjo-Sintes R. Vessel resistance to blood flow in the nailfold in patients with psoriasis: a prospective case-control echo Doppler-based study. Br J Dermatol 2012; 166: 54-58.
17. Jäntschi L, Bolboacă SD. Exact probabilities and confidence limits for binomial samples: applied to the difference between two proportions. ScientificWorldJournal 2010; 10: 865-878.
18. Gisondi P, Idolazzi L, Girolomoni G. Ultrasonography reveals nail thickening in patients with chronic plaque psoriasis. Arch Dermatol Res 2012; 304: 727–732.
19. Sandobal C, Carbo E, Iribas J, Roverano S, Paira S. Ultrasound nail imaging on patients with psoriasis and psoriatic arthritis compared with rheumatoid arthritis and control subjects. J Clin Rheumatol 2014; 20: 21-24.
20. Creamer D, Allen MH, Sousa A, Poston R, Barker JN. Localization of endothelial prolife-ration and microvascular expansion in active plaque psoriasis. Br J Dermatol 1997; 136: 859–865.
21. Gutierrez M, Filippucci E, De Angelis R, Filosa G, Kane D, Grassi W. A sonographic spectrum of psoriatic arthritis: “the five targets”. Clin Rheumatol 2010; 29: 133–142.
22. Gutierrez M, Filippucci E, Bertolazzi C, Grassi W. Sonographic monitoring of psoriatic plaque. J Rheumatol 2009; 36: 850–851.

Med Ultrason 2015, Vol. 17, no. 4, 509-514
DOI: 10.11152/mu.2013.2066.174.dus

Doppler ultrasound and strain elastography in the assessment of cutaneous melanoma: preliminary results

Carolina Botar Jid[1], Sorana D. Bolboacă[2], Rodica Cosgarea[3], Simona Şenilă[3], Liliana Rogojan[4], Manuela Lenghel[1], Dan Vasilescu[1], Sorin M. Dudea[1]

[1]Department of Radiology," Iuliu Haţieganu" University of Medicine and Pharmacy, [2]Department of Medical Informatics and Biostatistics, "Iuliu Haţieganu" University of Medicine and Pharmacy, [3]Department of Dermatology "Iuliu Haţieganu" University of Medicine and Pharmacy, [4]Emergency County Hospital Cluj-Napoca, Department of Pathology, Cluj-Napoca, Romania

Abstract

Aim: To study the usefulness of color or power Doppler ultrasound (US) in the pre-surgical evaluation of skin melanoma, and to correlate the Doppler characteristics with the appearance on high frequency ultrasound strain elastography (SE) in the preoperative evaluation of cutaneous melanoma. **Materials and method:** The study included 42 cutaneous melanoma lesions in 39 adult subjects examined between September 2011 and January 2015. Doppler US features (the presence and aspect of vascularization, and the number of vascular pedicles) and elasticity by strain elastography were evaluated together with the pathological results. **Results:** The melanoma lesions presented hyper-vascularization, with multiple vascular pedicles and stiff appearance. Significant correlations between the thickness of the tumor, measured histopathologically by the Breslow index, and the degree of vascularization ($p=0.0167$), and number of vascular pedicles ($p=0.0065$) were identified. Strong correlations between the SE appearance and vascularization on one hand, and SE and the number of vascular pedicles were also identified ($p<0.001$). **Conclusion:** Our study demonstrates that Doppler US and SE offer useful information for THE preoperative evaluation of cutaneous melanoma and may contribute to better defining the long term prognosis.

Keywords: cutaneous melanoma, Doppler ultrasound, strain elastography, real time elastography

Introduction

Cutaneous melanoma (CM) is the most important skin tumor with increasing incidence in the general population, including young people, with major health and socio-economic implications [1-3]. According to Scally et al, in 2013 there were about 76,250 new cases of CM which produced 9180 deaths [4] while according to Li et al about 76,100 new cases were diagnosed in 2014 in the USA with an estimated 9710 expected deaths [5]. Patients with CM present a high risk of relapsing, the occurrence of metastases, and a low rate of long-term survival [5]. The prognosis of these patients depends not only on the thickness of the tumor (Breslow index), presence of ulceration, mitotic rate, or Clark level invasion [6,7], but also on tumor vascularization, which is correlated with the risk of recurrence, occurrence of metastasis, and reduced long-term survival [8-12].

To establish a complex, highly accurate preoperative diagnosis in patients with CM is necessary for the best therapeutic assessment in order to improve the survival rate. Ultrasound (US) has an important role in diagnosis and staging and for establishing the optimal treatment and follow-up of patients with CM [10,11]. Using high frequency transducers, US allow a good characterization of the skin tumors and assessment of the thickness of the tumor (ultrasound Breslow index) [10-12]. By using Doppler techniques, US detect the presence of vascular signal, describe the distribution and characterize intra-

Received 08.08.2015 Accepted 24.09.2015
Med Ultrason
2015, Vol. 17, No 4, 509-514

Corresponding author: Sorana D. Bolboacă
Department of Medical Informatics
and Biostatistics, "Iuliu Haţieganu"
University of Medicine and Pharmacy
6, Louis Pasteur street
400349 Cluj-Napoca, Romania
E-mail: sbolboaca@gmail.com

tumoral vessels, thus increasing the diagnostic accuracy [10-13].

Strain elastography (SE) offers information about the relative elasticity or stiffness of the tissues comparing the target lesion with surrounding normal tissues, on the assumption that stiff tissues (as in most malignancies) are less deformable than the soft tissues (basically benign) [14,15]. The degree of elasticity is color coded, the elastographic information being superimposed on the two-dimensional image.

The aim of this study was to assess the usefulness of color or power Doppler US in the pre-surgical evaluation of skin melanoma in relation with pathology results, and to correlate the information obtained by Doppler with the high frequency SE appearance in the preoperative evaluation of CM.

Material and methods

A prospective study was performed between September 2011 and January 2015. The study comprised patients with skin lesions having the clinical suspicion of malignant melanoma, without previous cutaneous biopsy or surgery at the level of the identified lesion.

The exclusion criteria were: patients without specialized clinical examination, with other type of skin lesions than melanoma at clinical examination, patients who had underwent any dermatological treatment, and patients with previous biopsy or surgery in the area of the lesion.

All images were obtained using an Ultrasonix Sonotouch scanner (Ultrasonix Medical Corporation, Richmond, Canada) with an 8-40 MHz linear transducer and the possibility to perform Doppler ultrasound and SE.

The imaging parameters for Doppler ultrasound examinations were set to increase the detection of low-velocity and low-volume flows (color Doppler: PRF 500-1000 Hz, wall filter 25-50 Hz, power Doppler: PRF 350-700 Hz, wall filter 22-50 Hz; color and power Doppler: color gain maximized for optimal sensitivity while avoiding excessive color noise, color vs. echo priority ranging from 70 to 90% and color persistence adjusted to high values). The tumors were scanned in longitudinal and transverse planes. The ultrasound gel was in sufficient quantity so that the transducer exerted no compression, to avoid alteration of tumor thickness or blood flow.

For SE investigation each skin lesion was scanned in transverse and longitudinal planes with compression applied perpendicular to the lesion. A wide color window was used in order to include both the lesion and surrounding normal epidermis, dermal, and hypodermal tissue. Whenever possible, more than half of the region of interest width contained non-tumoral tissue.

Images with a good acquisition quality scale, defined as midrange quality scale light green coloring, were stored. Three different images of Doppler US (with the most representative vascular signal) and SE (considered by the examiner to be representative and reproducible for the lesion) were stored for each lesion, for further analysis.

The following information was collected for each patient:

- *Doppler US*: the aspect of vascularization (no or low vascularization – few color spots; medium vascularization – vascular signal <50% of tumor; hypervascularization – vascular signal >50% of the tumor) and the number of vascular pedicles (single or multiple);
- *Qualitative SE*: intratumoral distribution of colors (soft tissues were coded in red, medium elasticity tissues were colored in shades of yellow and green, and stiff tissues appeared in shades of blue). We used qualitative distribution of elasticity to correlate with the degree of vascularization: low elasticity for more than 50% of blue shades in the tumor; medium elasticity for predominant shades of yellow and green and high elasticity for more than 50% red color inside of the skin tumors. For Doppler examinations the images of the most visible vascular signal were analyzed. A single SE image, considered by the examiner to be the most representative and reproducible for the lesion, was also retained for analysis. All Doppler and SE examinations were performed by the same radiologist with 12 years experience of US and 8 years experience of SE.

Informed consent was obtained from each patient included in the study. The study protocol was approved by the Ethical Committee of the institutions.

Statistical analysis

Qualitative data were summarized as percentages and associated 95% confidence intervals (CI, provided in squared brackets), confidence intervals being calculated with an exact method [16]. The Breslow index was summarized as a mean and standard deviation since it proved to be normally distributed.

The comparison between the two proportions was made using the Z-test. The association in the contingency tables was carried out with the Fisher exact test. The relationship between the Doppler characteristics and the Breslow index and respectively between the SE appearance and the Doppler characteristics was investigated using the Spearman correlation coefficient.

Statistical analysis was conducted with Statistica software (v.8) at a significance level of 5% for comparisons of two groups and of 1.67% for comparisons on three groups.

Results

A number of 42 CM lesions belonging to 39 subjects, 21 female and 18 male (one female subject, 49 years old with two localizations left arm and elbow and one male subject, 75 years old with three localizations – thoracic, scapular and lumbar), mean age of 56.56±15.44 years old achieved the inclusion criteria and were assessed in our study.

The main characteristics of the investigated lesions according to the histopathological, Doppler US and SE examinations are presented in Table I.

The Breslow index could not be calculated in 5 lesions (11.9% [4.8–26.1]), as the histopathological diagnosis was “in situ” and these cases were excluded from further analysis. Finally, 37 lesions were included in the analysis related to the Breslow index.

Overall, no statistical significant difference was observed when the Breslow index was compared with groups of vascularization (low, high, and medium vascularization) (p=0.058). However, the post-hoc test identified that the mean of the Breslow index on lesions with high vascularization was significantly higher compared to the mean of the Breslow index on lesions with low vascularization (high: 3.03±1.30; low: 1.57±0.86; p-value=0.018).

The relation between the appearance of vascularization and Breslow index, and the qualitative appearance of the lesion at SE was statistically significant (Table II) and is illustrated in figures 1 and 2.

The mean value of the Breslow index proved significantly higher whenever multiple pedicles were present compared to cases where there was a unique pedicle (multiple: 3.18±1.29, unique: 1.51±0.71, p=0.0008).

The lesions with high elasticity proved to have medium or low vascularization while low vascularization was observed in a higher number of cases in lesions with medium elasticity (fig 3). No dependence was observed between the elasticity appearance and vascularization (p= 0.058).

Table I. Summary of histopathological, Doppler US and SE examinations

Characteristics	Value	Statistics (p-value)
Histology		
Breslow index[a] (mm)	2.78±1.38	
Doppler US		
Vascularization[b]		5.0541
Low vascularization	26.47 [11.85–44.03]	(< 0.0001)
Hypervascularization	64.71 [47.14–79.32]	
No. of pedicles[b]		4.1284
Unique	29.41 [14.79–46.97]	(< 0.0001)
Multiple	61.76 [45.55–78.70]	
SE		
Elasticity[b]		> 3.5
Low	45.24 [28.63–61.85]	(<0.0005)[c]
Medium	42.86 [28.63–59.47]	
High	11.90 [4.82–26.13]	

[a] mean±standard deviation; [b] percentage [95%CI], where 95%CI = 95% confidence interval; Statistics = the statistics associated to Z test for proportions; [c] Z-statistic and associated value on pairs comparisons as low vs. high, respectively medium vs. high

Table II. Doppler US and Breslow index and elastographic appearance respectively: Spearman’s correlation coefficients (ρ) and associated significance (p)

Characteristics	ρ (p-value)
Vascularization & the Breslow index	0.4483 (0.0167)
Number pedicles & the Breslow index	0.5016 (0.0065)
SE appearance & vascularization	-0.4937 (0.0035)
SE appearance & the number of pedicles	-0.5299 (0.0015)

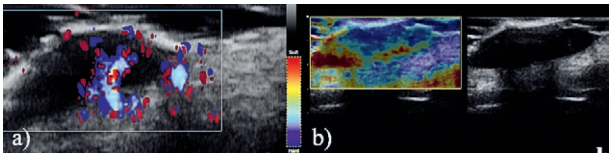

Fig 1. Cutaneous melanoma localized on the right mammary region, hypervascularized on Doppler US (a) and with stiff appearance on SE (b) in a 52 year old female. Breslow index 2.68 mm, thickness of the skin tumor measured by a 40 MHz frequency linear transducer was 2.55 mm.

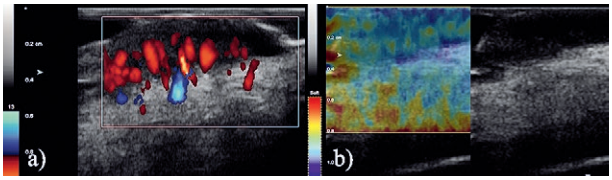

Fig 2. Cutaneous melanoma localized on the left lumbar region with multiple vascular pedicles on Doppler US (a) and stiff appearance on SE (b) in a 57 year old male. Breslow index 3.7 mm, thickness of the skin tumor measured by a 40 MHz frequency linear transducer was 3.8 mm.

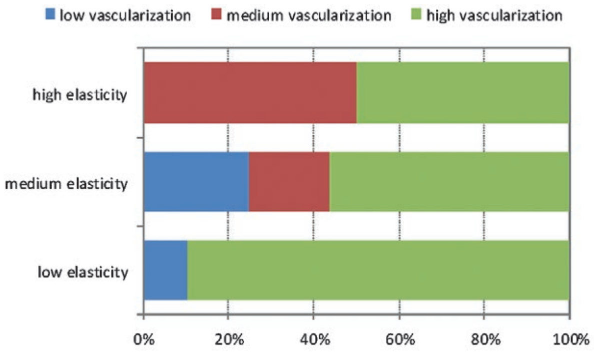

Fig 3. Distribution of SE elasticity according to vascularization

All lesions with high elasticity had multiple pedicles while the higher percentage of the unique pedicle was observed in lesions with medium elasticity.

No correlation was observed between the elasticity appearance and the number of pedicles (p=0.082).

Discussions

To the best of our knowledge this is the first study that compares Doppler US and SE in cutaneous melanoma. It is very important for patients with this pathology to benefit from complex US preoperative diagnosis by assessing not only gray scale appearance, but also vascularization and elasticity.

Doppler US is used to assess the vascularization of the skin tumors before surgical excision, high vascularization being correlated with an important risk of metastasis [17-20]. The thickness of CM lesions represents a very important element for preoperative management and prognosis, being correlated with the risk of metastasis or relapsing, as well [11,12,21,22]. Catalano et al [11] found that CMs with a thickness greater than 2 mm showing high vascularization have a high risk for a bad prognosis. In our study, the median tumor thickness was 2.78 mm, and most of the CMs were very well vascularized. These findings require wide margins of safety at surgery and the exclusion of metastases and, in time, the recurrences. In our group of patients we found that the Breslow index was significantly higher in lesions with high vascularity compared to those with low vascularity; in other words we expected that a lesion with a greater Breslow index would present hypervascularization.

Another investigated and significant factor in our study was the number of vascular pedicles: most tumors presented multiple pedicles (61.76%). Di Santolo et al [21] detected an intratumoral vascular signal in most of lesions, with one or two afferent vessels to the lesion. The presence of a greater number of vascular pedicles shows an abundant blood supply. Knowing that vascularization may be related to tumor aggressiveness, through to the metastatic potential or relapsing and reduced long-term survival [12,19,23,24], it is very important for these patients to have a good management both pre- and postoperatively.

The use of elastography in the evaluation of skin lesions has been the subject of several studies, in an attempt to differentiate between benign and malignant lesions [25-27]. Few research studies conducted in the early period of clinical elastography have demonstrated that this technique has potential in the diagnosis of skin tumors. In reported cases the tumors were diagnosed as malignant based on the color distribution on elastographic images [25-27]. In this present study, tumor elasticity represented a statistically significant factor: almost half of the tumors were stiff at SE and another important percentage had medium elasticity. In our patients thicker tumors presented low elasticity, while thin tumors appeared softer. Increased stiffness of melanomas can be explained by increased cellularity and tumor infiltration typical for malignant tumors, which can be correlated with the degree of aggressiveness. Preoperative evaluation of CM by SE is important not only for the tumor itself, but also for perilesional infiltration in order to establish the safety surgical margins.

There are several studies concerning the relationship between the thickness of skin melanomas and the presence and aspect of vascularization. Lassau et al [9] assessed the tumor vascularity using color Doppler in 111 skin melanomas before surgical resection and demonstrated intratumoral vessels in 43 lesions. Lassau et al [9] and Srivastava et al [12] found a strong positive correlation between the vascularization and Breslow tumor thickness, reporting that Breslow thickness and vascularity offer information for the prognosis of these patients. Srivastava et al [12] proposed a *"tumor vascularity database"* in countries with a high prevalence of melanoma with a detailed description of intratumoral vessels. Catalano et al [11] demonstrated that the presence of intratumoral vessels is correlated with the Breslow index and with patient survival. Di Santolo et al [20] found intratumoral vessels in 24/34 of lesions with thickness greater than 1 mm. We obtained no statistical differences when comparing the Breslow index with the three classes of vascularization but a post hoc test identified that the Breslow index is significantly higher in lesions with hypervascularization compared to those with low vascularity. This confirms that the Breslow index and hypervascularization represents negative prognostic factors for the evolution of patients with CM by increasing the risk of metastasis or relapse [5,11,21,22].

In the present work, we found a strong correlation between the tumor thickness, measured histopathologically by the Breslow index, degree of vascularization, and number of vascular pedicles. We found that as the Breslow index increases more obvious multiple vascular pedicles in the skin tumors can be detected, which demonstrate increased vascularization, consistent with a previous published study [9]. To the best of our knowledge, the relation between the elastographic appearance of CM and the aspect of vascularization and number of vascular pedicles has not been previously described. We noticed that the SE appearance of skin melanoma is strongly correlated both with the vascularization and with the number of vascular pedicles of the lesions. We found that tumors with high elasticity presented medium or low vascularization. This fact could be correlated with the aggressiveness of the tumor, assuming that an increased vascularity is associated with an increased degree of aggressiveness, and a malignant tumor tissue shows increased stiffness. In our study we could not find a model of correlation between the SE appearance of CM and their degree of vascularization and the number of vascular pedicles, probably due to the variability of the tumor thickness.

Since it has been proven that hypervascularization is a bad prognostic factor [12,20] and we have proved that there is a positive correlation between the stiffness and degree of vascularization, our results suggest that the stiffness of the tumor represents a negative prognostic factor. However, it is necessary to analyze a larger group of patients and their clinical outcome to assess the extent to which the stiffness is an independent predictor of unfavorable evolution.

One limitation of the study arises from the small number of melanoma tumors enrolled. This item represents only a part of the study, which is still ongoing. Another limitation of our work can be the bias induced by the fact that the Doppler and SE examinations were performed by the same investigator and no inter- and intra-observer could be computed. A greater degree of objectivity could be obtained by measuring the Doppler indices. Another limitation resides in the qualitative assessment of elasticity by means of SE scores. Shear wave elastography might represent another, more objective, way of quantifying stiffness, but this method was not available for this study.

To the best of our knowledge, data on the correlation between the intratumoral vascular signal and the elastographic appearance has not been previously published. Further studies on larger groups of patients are necessary to confirm and refine the results of the present work.

Conclusions

This study demonstrates that the assessment of intratumoral vascularization and stiffness in skin melanomas may contribute to a complex diagnosis before surgical excision. Both Doppler US and SE may provide useful information for the management of CM patients. We recommend the association of these techniques, whenever possible, with a two dimensional US and clinical examination for a complex and complete diagnosis of cutaneous melanoma.

Acknowledgements

The study was supported by the “Iuliu Haţieganu” University of Medicine and Pharmacy, Cluj-Napoca through project no. 1494/7/28.01.2014.

Conflict of interest: none

References

1. Tronnier M, Semkova K, Wollina U, Tchernev G. Malignant melanoma: epidemiologic aspects, diagnostic and therapeutic approach. Wien Med Wochenschr 2013; 163: 354-358.
2. Voit CA, Gooskens SL, Siegel P, et al. Ultrasound-guided fine needle aspiration cytology as an addendum to sentinel lymph node biopsy can perfect the staging strategy in melanoma patients. Eur J Cancer 2014; 50: 2280-2288.
3. Livingstone E, Krajewski C, Eigentler TK, et al. Prospective evaluation of follow-up in melanoma patients in Germany – Results of a multicentre and longitudinal study. Eur J Cancer 2015; 51: 653-667.
4. Scally CP, Wong SL. Intensity of follow-up after melanoma surgery. Ann Surg Oncol 2014; 21: 752-757.
5. Li J, Wang Y, Liang R, et al. Recent advances in targeted nanoparticles drug delivery to melanoma. Nanomedicine 2015; 11: 769-794.
6. Scolyer RA, Prieto VG. Melanoma pathology: important issues for clinicians involved in the multidisciplinary care of melanoma patients. Surg Oncol Clin N Am 2011; 20: 19–37.
7. Patnana M, Bronstein Y, Szklaruk J, et al. Multimethod imaging, staging, and spectrum of manifestations of metastatic melanoma. Clin Radiol 2011; 66: 224–236.
8. Srivastava A, Hughes LE, Woodcock JP, Laidler P. Vascularity in cutaneous melanoma detected by Doppler sonography and histology: correlation with tumor behaviour. Br J Cancer 1989; 59: 89-91.
9. Lassau N, Lamuraglia M, Koscielny S, et al. Prognostic value of angiogenesis evaluated with high-frequency and colour Doppler sonography for preoperative assessment of primary cutaneous melanomas: correlation with recurrence after a 5 year follow-up period. Cancer Imaging 2006; 6: 24-29.
10. Dancey AL, Mahon BS, Rayatt SS. A review of diagnostic imaging in melanoma. J Plast Reconstr Aesthet Surg 2008; 61: 1275-1283.
11. Catalano O, Siani A. Cutaneous melanoma: role of ultrasound in the assessment of locoregional spread. Curr Probl Diagn Radiol 2010; 39: 30-36.
12. Srivastava A, Woodcock JP, Mansel RE, et al. Doppler ultrasound flowmetry predicts 15 year outcome in patients with skin melanoma. Indian J Surg 2012; 74: 278-283.
13. Hernández C, del Boz J, de Troya M. can high-frequency skin ultrasound be used for the diagnosis and management of basal cell carcinoma? Actas Dermosifiliogr 2014; 105: 107-111.

14. Botar-Jid C, Vasilescu D, Dudea SM. Tridimensional ultrasound and Sonoelastography in musculoskeletal pathology. In: Fodor D, Clinical musculoskeletal ultrasound. București, Ro: Medical Ed, 2009: 381–389.
15. Bamber J, Cosgrove D, Dietrich CF, et al. EFSUMB guidelines and recommendations on the clinical use of ultrasound elastography. Part 1: Basic principles and technology. Ultraschall Med 2013; 34: 169–184.
16. Jäntschi L, Bolboacă SD. Exact probabilities and confidence limits for binomial samples: applied to the difference between two proportions. ScientificWorldJournal 2010; 10: 865–878.
17. Doben AR, MacGillivray DC. Current concepts in cutaneous melanoma: malignant melanoma. Surg Clin North Am 2009; 89: 713–725.
18. Leiter U, Buettner PG, Eigentler TK, et al. Hazard rates for recurrent and secondary cutaneous melanoma: An analysis of 33,384 patients in the German Central Malignant Melanoma Registry. J Am Acad Dermatol 2012; 66: 37–45.
19. Mandava A, Ravuri PR, Konathan R. High-resolution ultrasound imaging of cutaneous lesions. Indian J Radiol Imaging 2013; 23: 269-277.
20. Scotto di Santolo M, Sagnelli M, Mancini M, et al. High-resolution color-Doppler ultrasound for the study of skin growths. Arch Dermatol Res 2015; 307: 559-566.
21. Wortsman X. Common applications of dermatologic sonography. J Ultrasound Med 2012; 31: 97-111.
22. Kleinerman R, Whang TB, Bard RL, Marmur ES. Review ultrasound in dermatology: principles and applications. J Am Acad Dermatol 2012; 67: 478-487.
23. Wortsman X, Wortsman J. Clinical usefulness of variable-frequency ultrasound in localized lesions of the skin. J Am Acad Dermatol 2010; 247-256.
24. Alfageme Roldán F. Ultrasound skin imaging. Actas Dermosifiliogr 2014; 105: 891-899.
25. Hinz T, Wenzel J, Schmid-Wendtner MH. Real-time tissue elastography: A helpful tool in the diagnosis of cutaneous melanoma? J Am Acad Dermatol 2011; 65: 424–426.
26. Hinz T, Hoeller T, Wenzel J, Bieber T, Schmid-Wendtner MH. Real-time tissue elastography as promising diagnostic tool for diagnosis of lymph node metastases in patients with malignant melanoma: a prospective single-center experience. Dermatology 2013; 226: 81–90.
27. Wortsman X, Carreńo L, Morales C. Skin Cancer: The Primary Tumors. In: Wortsman X, Jemec GBE, eds. Dermatologic Ultrasound with Clinical and Histologic Correlations. New York, USA: Springer, 2013: 249–280.